The American University in Cairo

School of Sciences and Engineering

Experimental Investigation of Non-linearities in Thermoacoustic Systems: Streaming, Transition to Turbulence and Entrance Effects

Dissertation Submitted to

The Mechanical Engineering Department

In partial fulfillment of the requirements for the degree of

Doctor of Philosophy

by

ISLAM AHMED ELSAYED RAMADAN

Under the Supervision of

Prof. Ehab Abdel-Rahman
Professor, Physics Department
The School of Sciences and Engineering
The American University in Cairo

Prof. Mohamed Amr Serag Eldin
Professor, Mechanical Engineering Department
The School of Sciences and Engineering
The American University in Cairo

Dr. Abdelmaged Hafez Ibrahim Essawey
Research Postdoctoral Scholar, Physics Department
School of Sciences and Engineering
The American University in Cairo

April 2018

Abstract

Thermoacoustic systems (engines or refrigerators) convert any source of heat energy, including solar energy and waste heat, into electricity or cooling effect. These systems are reliable and durable as they operate with few or no moving parts and they employ environmentally-friendly gases without gaseous emissions. However, thermoacoustic systems suffer from many non-linearities that deteriorate the overall performance after a certain level such as streaming, turbulence generation, entrance effects and harmonic generation. This thesis focuses on first three of these non-linearities.

Streaming is a second order steady flow that convects a certain amount of heat. The convected heat does not contribute to the thermoacoustic conversion process and hence it represents a loss. In this work, the effects of the natural convection flow on Rayleigh streaming have been investigated. The first objective of this work is to investigate the distribution of the axial mean velocity inside a simple standing-wave thermoacoustic engine using both Particle Image Velocimetry and Laser Doppler Velocimetry. The engine consists of a stack heated from one side whereas the other side is left uncontrolled. The velocity measurements cover the axial distance from the cold side of the stack to the termination of the resonator. Also, dynamic pressure and mean gas temperature measurements are conducted. Three different regions are observed and named the “cold streaming” region, the “hot-streaming region” and the “end-effects” region. In the cold streaming region, the measured mean velocity distribution agrees well with the theoretical expectation of Rayleigh streaming at low acoustic level. At high acoustic level, the measured quantities deviate from the theoretical expectations reported in the literature. Also, the size of the cold streaming region was found to decrease with the increase of the acoustic level. In the hot streaming region, where the measured wall temperature gradient is non-zero, the measured mean velocity distribution does not agree with the theoretical expectation for all acoustic levels. This discrepancy was found to be caused by the natural convection flow originated by the non-uniform temperature distribution of the resonator wall. In this work, the natural convection flow is decoupled from the acoustic streaming flow in order to measure the natural convection flow distribution inside the engine. The results reveal that there is a competition between acoustic streaming flow and the natural convection flow. This competition, at some acoustic levels, results in a zero mean axial velocity distribution. In the end-effects region, the mean flow velocity is disturbed by the vortex generation near to the stack. The size of each of these three regions is determined for different acoustic levels.

As the flow inside the thermoacoustic systems has an oscillating nature, the study of the transition to turbulence in the oscillating flow is critical to understand the flow characteristics at high velocity amplitudes, which is the second objective of this work. In this work, the transition to turbulence in an oscillating flow has been studied at two different frequency ranges namely the sub-acoustic (low) frequency range (i.e. frequency $\ll$ 20 Hz) and the acoustic (high) frequency range (i.e. frequency $\geq$ 20 Hz). In the sub-acoustic frequency range, the transition to turbulence under the

oscillating flow conditions inside a square duct is investigated experimentally. For this purpose, the oscillating flow is generated by a mechanical system known as the Scotch-Yoke mechanism that is able to provide an oscillating flow with wide range of amplitudes at low frequencies. The axial velocity profile is measured using Particle Image Velocimetry and two dimensionless parameters are used to describe the oscillating flow namely the Reynolds number and the Womersley number. At low Reynolds numbers, the measured axial velocity profile in the duct agrees reasonably well with the theoretical laminar velocity profile over the complete cycle; whereas at higher Reynolds numbers, the results show that the agreement is limited to the acceleration phase. The transition to turbulence process is identified by measuring the turbulence intensities. The turbulence intensities based on both velocity components at both the center of the duct and near to the viscous penetration depth increase as the Reynolds number is increased. Also, the cycle-average Reynolds stress is estimated. Beyond a certain Reynolds number, the cycle-average Reynolds stress experiences a sudden increase indicating transition to turbulence and hence the value of the critical Reynolds number can be determined. The estimated value of the critical Reynolds number, which equals to 500, complies with the literature. The work is then extended to the acoustic (high) frequency range. In the acoustic frequency range, the mechanical Skotch-Yoke system is replaced by two powerful loudspeakers operating at 180 deg out-of-phase to produce an oscillating flow with high velocity amplitudes at the resonance frequency of the system. The same methodology is used to investigate the transition to turbulence at high frequency range. The cycle-average Reynolds stress experiences a sudden increase near the wall at Reynolds number of 270. The vorticity fields are calculated from the measured 2-D velocity field. It is found that the vorticity value increases as the Reynolds number is increased. Also, the largest vorticity value is observed near the wall. As the Reynolds number increases the largest vorticity value shifts away from the wall during the deceleration phases in the acoustic cycle. The spatial energy density spectrum is calculated at different phases for different Reynolds numbers. Also, the cycle-average spatial energy density spectrum is calculated. The slope of the decay of the spatial energy at high wavenumbers was found to be nearly equals to the universal value of -5/3.

As the thermoacoustic core of any thermoacoustic systems consists of a stack and heat exchangers, the study of the oscillating flow behavior in the vicinity of the stack is important, which constitutes the third objective of this work. The stack is usually modelled as a set of parallel plates. This work focuses on the effects of the plate-end shape on the oscillating flow morphology at high velocity amplitudes. Four different plate-end shapes namely rectangular, circular, 90^{O} triangular and 30^{O} triangular are placed inside an acoustic resonator. The temporal evolution of the vorticity field in the vicinity of the plates is investigated. The vortices originated at the beginning of the ejection stage (flow moves outwards the plates) and moves with the flow till they reach an axial distance nearly equals to one acoustic displacement amplitude. As the Reynolds number increases, the generated rounded-vortices around each plates transformed from two counter-rotating vortices attached to the plate into two elongated counter-rotating vortices. Also, the non-periodicity (cycle-to-cycle variations) of the oscillating flow in the vicinity of the plates is reported. As the Reynolds number increases, the non-periodicity of the flow does not change significantly. The 30^{O} triangular

plate-end shape reduces the non-periodicity of the oscillating flow near the plates at different axial locations whereas the other plate-end shapes have nearly similar values of non-periodicity.

Acknowledgements

The pursuit of my PhD has been a life-changing journey and it would not have been completed without the support of many persons and entities.

First and foremost, I would like to acknowledge my advisors for all the support and guidance they gave me. I am grateful to Dr. Ehab Abdelrahman who has been supportive to my career goals and who worked sincerely to secure the financial and academic support not only for me but also for the whole thermoacoustic research team. Also, I would like to say a very big "thank you" to Dr. Abdelmaged who worked actively to provide me a sincere academic, professional and personnel guidance. I am also grateful to him for the nice "walk and talk" time we spent together discussing both scientific and general-life issues.

I would like to thank Dr. Ahmed Abdel-Rahman for the fruitful discussions we had at the beginning of my PhD research. I would like to thank my colleagues in the thermoacoustic research team for the time we spent together. Also, I am thankful to my friend Khaled Elbeltagy for the sleepless nights we were working together to catchup on the deadlines of the projects.

I am grateful to the financial support received towards my PhD from Yousef Jameel PhD fellowship through the American University in Cairo. I am also grateful to the fund received from the Egyptian Academy of Scientific Research and Technology to undertake my PhD. Also, I would like to thank the European union for funding my work[*].

I greatly appreciate the support received from the collaborative research conducted with Pprime Institute, Poitiers University. I am especially grateful to Dr. Helene Bailliet for the sincere academic guidance during my stay in France. This collaborative work would not have been possible without the financial support received from both the American University in Cairo and Pprime Institute.

Last but not least, I would like to thank my family for all their love and support. For my parents who did sacrifice their time and money to raise me with a love of hard working which is the pillar for all my pursuits. Most importantly, I would like to thank my loving, encouraging and patient wife, Alaa, for the faithful support throughout all ups and downs of my PhD journey. Thank you.

[*] Part of this work has been produced with financial assistance of the European Union. The contents of this document are the sole responsibility of the authors and can under no circumstances be regarded as reflecting the position of the European Union.

Table of Contents

List of Figures

List of Tables

List of symbols

Alphabetic letters

A	Acoustic velocity amplitude at the velocity antinode, m/s
A_{Ray}	Amplitude of the Rayleigh streaming velocity, m/s
a	Flow acceleration, m/s^2
c	Speed of sound at the ambient conditions, m/s
C	Proportionality factor OR critical amplitude number
D	Hydraulic diameter of the duct, m
d_e	Effective image diameter of the seeding particle, m
d_p	Diameter of the seeding particle, m
d_s	diffraction spot size, m
E_u	Spatial turbulent energy spectrum based on the axial fluctuating velocity component, $(m^2/s^2)/(rad/s)$
E_v	Spatial turbulent energy spectrum based on the traverse fluctuating velocity component, $(m^2/s^2)/(rad/s)$
f	Frequency of oscillation, Hz
f_p	Characteristic frequency of the seeding particle motion, Hz
$f_\#$	F-number of the camera lens
g	Gravitational acceleration, m/s^2
Gr	Grashof number
I_x	Turbulence intensity based on axial velocity component, %
I_y	Turbulence intensity based on traverse velocity component, %
K_C	Keulegan-Carpenter number
k	Wave number, m^{-1}
l	Length of the duct OR resonator, m
L_p	Plate length, m
M	Magnification ratio
$\mathbf{Pr}$	Prandtl number
R	Radius of the duct, m
r	Radial position measured from the center of the duct, m
Re_D	Reynolds number based on the hydraulic diameter of the duct as a characteristic length scale
$Re_{D,s}$	Reynolds number of a steady flow
Re_{NL}	Non-linear Reynolds number
Re_{stress}	Reynolds stress
Re_δ	Reynolds number based on the viscous penetration depth as a characteristic length scale, m^2/s^2
S	Dimensionless amplitude
S_{IA}	Side length of the interrogation area, m
T	Acoustic period, s
$\mathbf{T_a}$	Temperature of the cold side of the stack, ^OC
T_{avg}	Average temperature of the cold side of the stack, ^OC
$\mathbf{T_h}$	Temperature of the hot side of the stack, ^OC

T_∞	Ambient temperature, ^{O}C
$\widehat{U}$	Cross-sectional average velocity amplitude at the center of the duct, m/s
U_{ac}	Acoustic velocity amplitude at a given location in the resonator, m/s
U_m	Mean flow velocity of a steady flow, m/s
U_{mean}	The mean flow velocity at a given location in the resonator, m/s
U_o	Velocity amplitude at the center of the duct, m/s
U_{Ray}	Theoretical Rayleigh streaming velocity at a given axial and radial location in the resonator, m/s
U_∞	Settling velocity of the seeding particle, m/s
u	Axial velocity component, m/s
$\grave{u}$	The axial component of the velocity fluctuation, m/s
V_L	Velocity lag between the fluid flow velocity and the particle velocity, m/s
v	Radial or traverse Velocity component, m/s
$\grave{v}$	The radial or traverse component of the velocity fluctuation, m/s
W	Width of the duct, m
$\grave{w}$	The third component of the velocity fluctuation, m/s
X_{Amp}	Displacement amplitude of the oscillating flow, m
x	Axial location, m
y	Traverse location, m

Greek Letters

α	Womersley number
β	Expansion coefficient of fluid at ambient conditions
Δp	Pressure drop, pa
Δt	Time between pulses of the laser light source, s
δ OR δ_v	Viscous penetration depth, m
ϵ	Rate of dissipation of turbulent kinetic energy, m^2/s^3
η	Kolmogorov length scale, m
λ	Wave length, m
μ	Dynamic viscosity of the fluid, kg/(m.s)
ν	Kinematic viscosity, m^2/s
ρ_f	Density of the fluid, kg/m^3
ρ_p	Density of the seeding particles, kg/m^3
τ_w	Wall shear stress, N/m^2
ω	Angular frequency, rad/s
ω_t	Turbulent fluctuations frequency of the flow, rad/s

Acronyms

DOF	Depth of field of the camera lens, m
FOV	Field of view, m

Chapter 1: Introduction and Literature Review

Thermoacoustic science is an interdisciplinary field which focuses on the interactions between acoustics and heat transfer. There are two types of thermoacoustic systems namely thermoacoustic engine, where heat is converted into sound wave, and thermoacoustic refrigerator, where the acoustic energy is converted into cooling effect. Based on the linear theory of Nikolaus Rott [1], the operation and design of thermoacoustic systems (i.e. engine and refrigerator) are mostly well understood but only for the low acoustic amplitudes (i.e. linear regime). At higher acoustic amplitudes, the actual performance indices deviate from the theoretical expectations. The deviation is due to many non-linearities such as acoustic streaming, turbulence generation, entrance effects and harmonic generation. Researchers attempted to investigate the effects of those non-linearities on the performance of different thermoacoustic systems. However, a lot of work is still needed to deeply understand these phenomena and their impacts on the thermoacoustic systems, in order to improve the overall conversion efficiency (or performance coefficient) as well as the power density.

In the present work, light has been shed on three types of these non-linearities which are acoustic streaming, turbulence generation and entrance effects. In the following subsections, review of the previous work, for each of these non-linearities, is discussed and the objectives of the work are stated by the end of each subsection.

1.1. Acoustic Streaming

Acoustic streaming is a second-order DC flow superimposed on the first-order oscillating flow. This steady flow is generated by the interaction of the solid walls and the acoustic waves. Acoustic streaming is considered as a mechanism of carrying heat between the segments of a thermoacoustic device. There are many types of streaming flow in thermoacoustic systems. Most of these types are harmful to the performance of thermoacoustic systems because they, generally, convect a certain amount of heat that does not contribute to the thermoacoustic conversion process itself. As shown in Fig. 1.1, there are four types of harmful acoustic streaming, namely Gedeon streaming, Rayleigh streaming, jet-driven streaming and streaming within stack or regenerator. Gedeon streaming can exist in any looped-system and hence it is only related to traveling-wave thermoacoustic systems. Gedeon streaming creates a non-zero mass flow over the loop of thermoacoustic device however, it can be suppressed by using either a jet-pump [2] or an elastic diaphragm [3]. Rayleigh streaming is a convective flow within the tube. It was proven [4] that Rayleigh streaming can be eliminated by tapering the tube. Jet-driven streaming is a time-average flow generated due to large and sudden change in the cross-sectional area. Finally, the streaming within stack or regenerator can occur due to the interaction between the solid walls of the mesh and the acoustic wave. On the other hand, it was reported in [5] that there are some types of acoustic streaming (e.g. deliberate streaming) that can be beneficial to the performance of thermoacoustic system by enhancing the heat transfer processes.

Among these types of acoustic streaming, Rayleigh streaming is the focus of the current work because it is more common in all types of thermoacoustic systems (i.e. engine or refrigerator) either standing-wave or travelling-wave system.

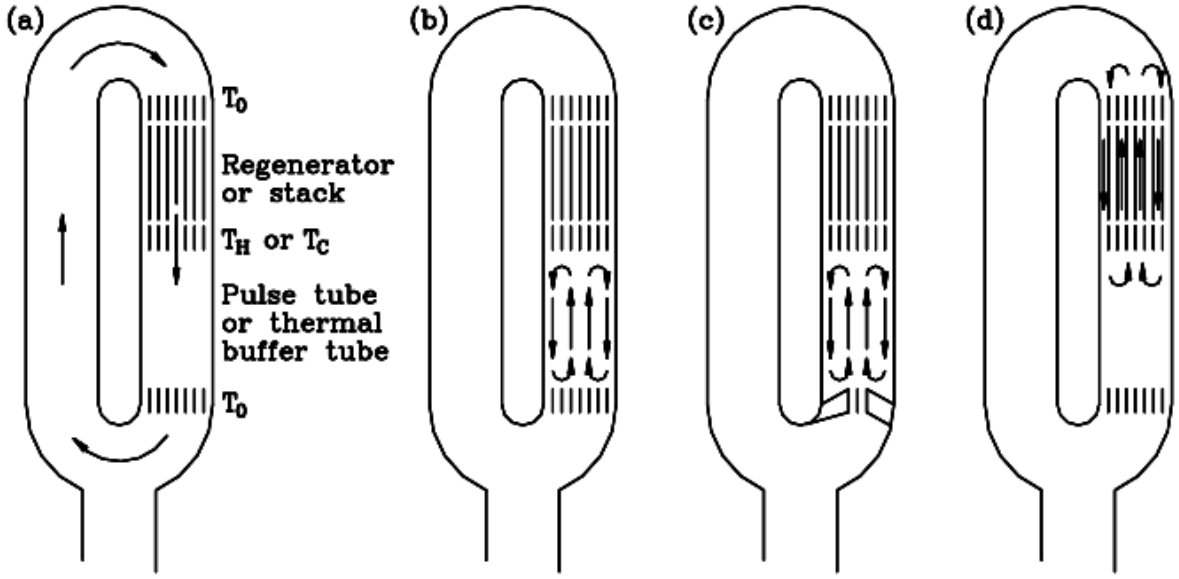

Figure 1.1: Graphical representation for the types of acoustic streaming that have a negative impact on the performance of thermoacoustic systems: (a) Gedeon streaming, (b) Rayleigh streaming, (c) Jet-driven streaming, and (d) Streaming within stack or regenerator. Adapted from [5].

Rayleigh streaming phenomenon in a standing-wave resonator was observed, long time ago, by Dvorak [6] through the observation of a gas pattern motion in Kundt's tube. He observed that there is a steady flow motion inside the resonator. An explanation for this phenomenon was presented by Rayleigh [7]. He stated that the streaming is a second-order DC flow superimposed on the first order oscillating flow. Also, he described a mathematical model to quantify this phenomenon for the case of standing-wave in a large channel (e.g. two parallel plates). His findings are employed as a theoretical reference by many of the following researchers. Rayleigh streaming is encountered in many engineering applications including thermoacoustics. In thermoacoustic applications, it is important to consider the effects of both high acoustic amplitude and heat on the Rayleigh streaming patterns. Most of thermoacoustic devices (engines or refrigerators) operate at high amplitude to maximize the output. Above a certain limit, the "slow streaming" hypothesis of Rayleigh is not valid. Menguy and Gilbert [8] defined dimensionless parameter to determine the limit of "slow streaming" hypothesis. The dimensionless parameter is known as non-linear Reynolds number which is described mathematically as following:

$$\boldsymbol{Re_{NL}} = \left(\frac{\boldsymbol{A}}{\boldsymbol{c}}\right)^{\boldsymbol{2}} \left(\frac{\boldsymbol{R}}{\boldsymbol{\delta_v}}\right)^{\boldsymbol{2}} \tag{1.1}$$

where A is the acoustic amplitude at the velocity antinode, c is the speed of sound at the ambient conditions, R is the radius of the pipe and δ_v is the viscous penetration depth ($\delta_v = \sqrt{\nu/\pi f}$, where ν is the kinematic viscosity and f is the frequency of oscillation).

For Re_{NL} less than unity the "slow streaming" hypothesis of Rayleigh is valid. Rayleigh streaming pattern at low Re_{NL} in a half wave resonator is shown in Fig. 1.2. The pattern of Rayleigh streaming is repeated each quarter wave length. Each pattern is axisymmetric and consists of two vortices namely outer and inner streaming vortex. The inner streaming vortex is located near to the wall and its direction of rotation is opposite to the direction of rotation of the outer streaming vortex. The axial streaming velocity distribution in the radial direction shows that the maximum velocity is achieved at the center of the duct and the negative maximum velocities are achieved near to the wall. Also, the cross sectional average velocity should be zero.

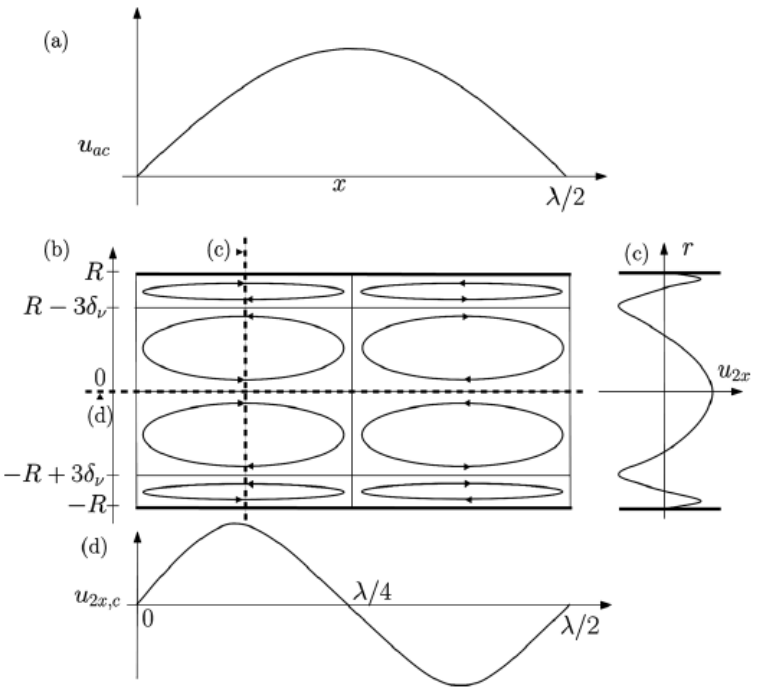

Figure 1.2: Rayleigh streaming flow pattern in a half wave resonator at low Re_{NL}: (a) Axial acoustic velocity distribution, (b) Rayleigh streaming velocity distribution, (c) Axial streaming velocity distribution in the radial direction (d) Axial streaming velocity distribution in the axial direction. Adapted from [9].

For Re_{NL} larger than unity, the "fast streaming" effects should be considered. Reyt *et al.* [9] studied the effects of high Re_{NL} on Rayleigh streaming pattern. As shown in Fig. 1.3, the measured axial streaming velocity agrees well with the theoretical expectations at $Re_{NL} = 1$ whereas the

discrepancy between the measurements and the theoretical expectations increases as the Re_{NL} is increased. At high Re_{NL}, the maximum axial streaming velocity shifts toward the streaming velocity node. The reason for this discrepancy has been investigated in many studies [10], [11], [12] and [13].

The effects of temperature on the Rayleigh streaming pattern has been theoretically investigated (i.e., [14], [15] and [16]). In addition, Thompson *et al.* [11] experimentally studied the temperature effects on Rayleigh streaming pattern. As shown in Fig. 1.4a, the effects of wall temperature conditions are not significant at low Re_{NL}. Whereas, the wall temperature effects are more significant at high Re_{NL}. As shown in Fig. 1.4b, the measured axial streaming velocity distribution agrees with the theoretical expectations in the isothermal case whereas the discrepancy increases whenever there is a temperature gradient (i.e. insulated and uncontrolled).

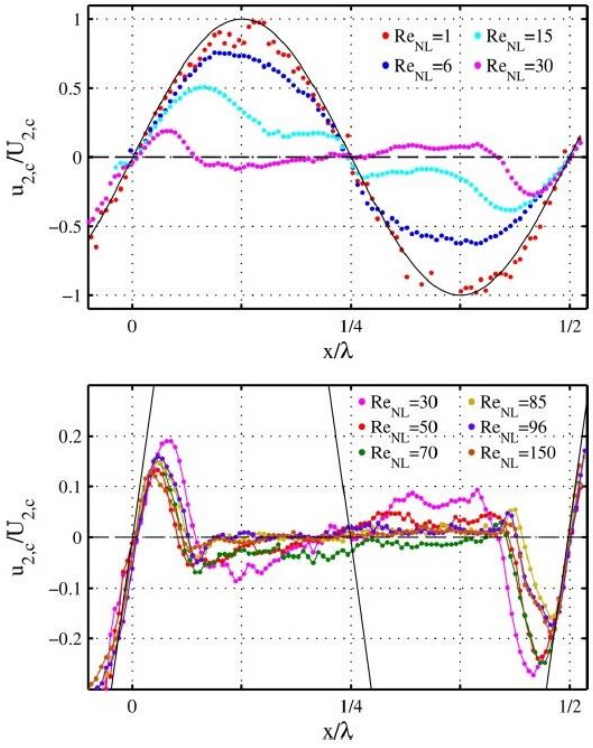

Figure 1.3: The axial distribution of the normalized axial streaming velocity at different Re_{NL}. Adapted from [9].

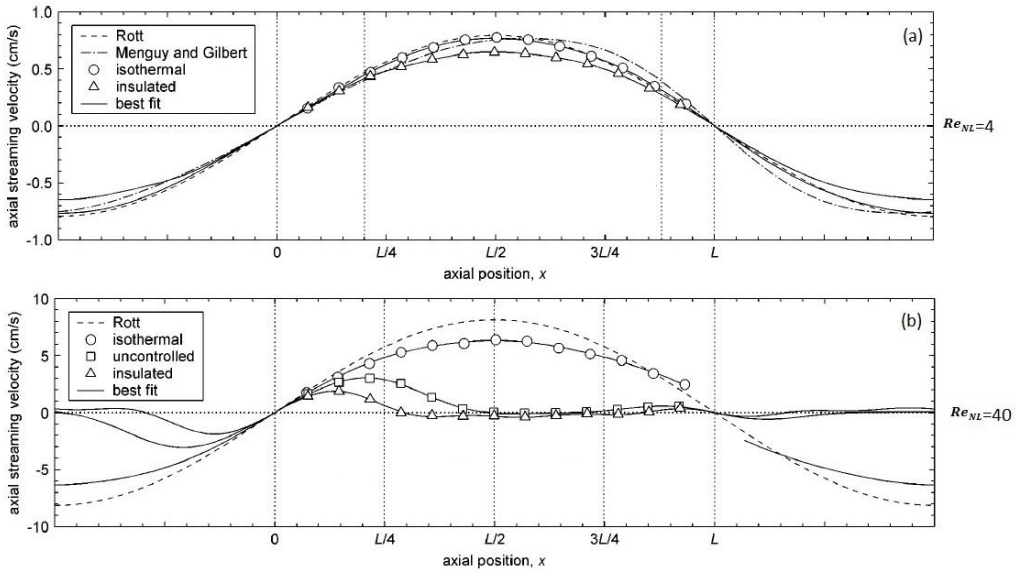

Figure 1.4: The axial distribution of the axial streaming velocity at different wall temperature conditions at two different Re_{NL}. Adapted from [11].

All the work cited above investigated the effects of different parameters on the Rayleigh streaming in simplified configurations (e.g. empty channels). However, thermoacoustic devices are more complicated than those simplified configurations.

In the course to approach the thermoacoustic devices, Moreau *et al*. [17] experimentally investigated the effect of placing a stack inside an empty resonator where the acoustic wave was generated by loudspeakers but there are no thermoacoustic process (i.e. no temperature gradient across the stack). As shown in Fig. 1.5, the stack always creates disturbances in the axial streaming velocity distribution. It was found that the disturbance is limited to a certain zone on both sides of the stack. They found that the disturbance is due to the jet-driven streaming generated at both ends of the stack. The results of this work is used in the current work to define the disturbance zone (i.e. the distance over which the jet-driven streaming affect the Rayleigh streaming distribution). Debesse *et al.* [18] measured the mean velocity in a standing-wave thermoacoustic engine but the measurements were performed at one axial location and far from the thermoacoustic core (i.e. stack and heat exchangers). Their measurements indicated that there is a mean flow inside the resonator but is totally different from the theoretical expectations of Rayleigh streaming.

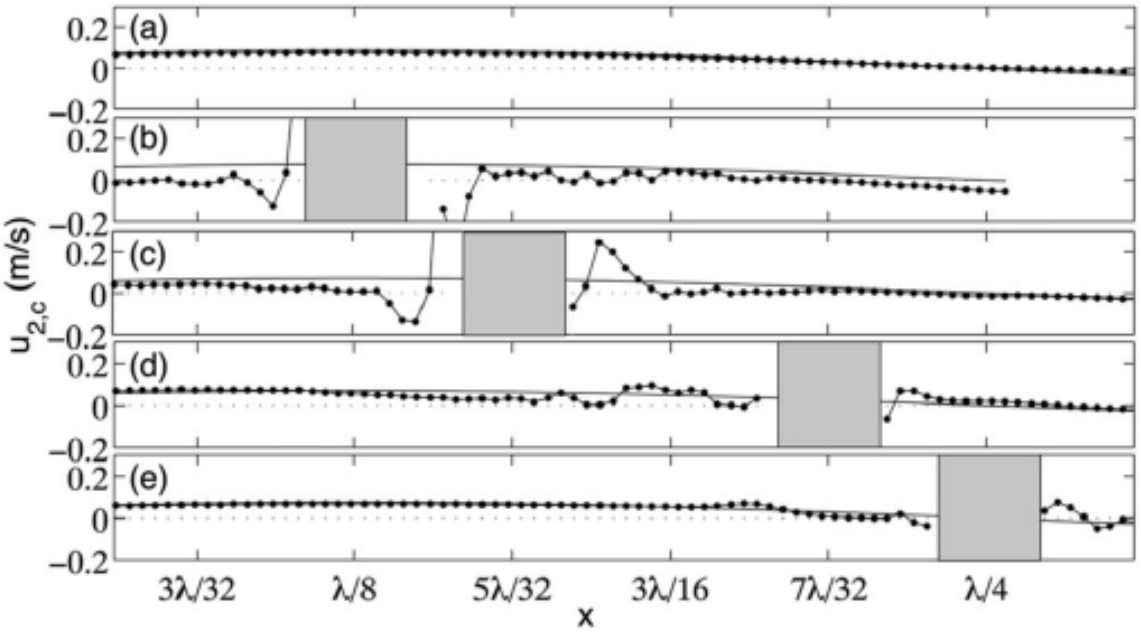

Figure 1.5: The axial distribution of the axial streaming velocity at the center of the duct with different locations for the stack inside the duct. Adapted from [17].

Heat has another effects on the Rayleigh streaming in a thermoacoustic systems. This effect is due to the natural convection flow generated by the non-uniformity of the temperature field [19]. Although the effects of natural convection flow on Rayleigh streaming seem to be crucial, very few studies can be found on that regards. Babaei and Siddiqui [20] measured the mean velocity at both sides of the stack of a thermoacoustic refrigerator. As shown in Fig. 1.6, the values of the mean velocities at both sides of the stack are not the same and the discrepancy increases with the drive ratio increase. They described the reason for this difference is as the natural convection flow created by the temperature gradient.

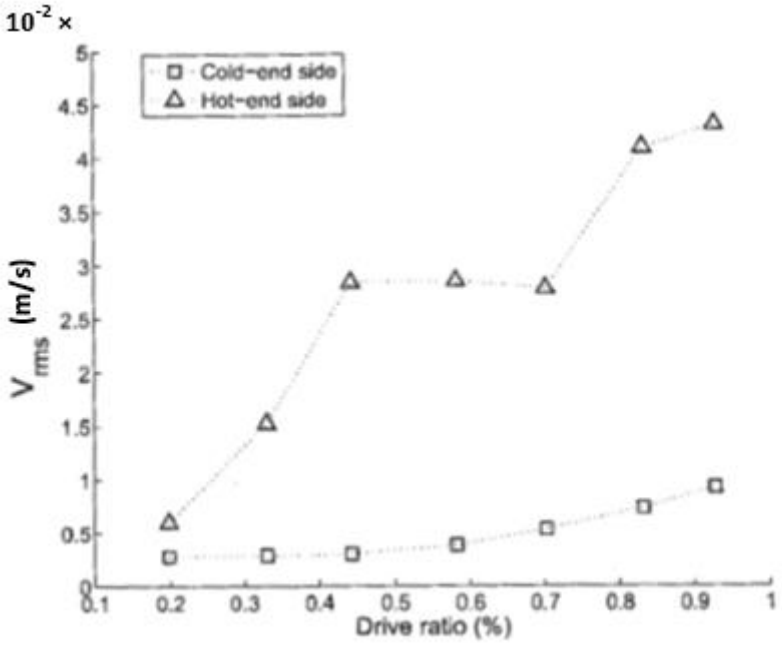

Figure 1.6: The axial mean velocity at both sides of the stack of a refrigerator at different drive ratios. Adapted from [20].

Some studies investigated the effects of the convection motion on acoustic velocities not mean velocities. Pan *et al.* [21] studied the effects of a temperature gradient on the acoustic velocity distribution inside an empty resonator in which the wave is generated by loudspeaker and the temperature gradient is imposed through two heat exchangers. As shown in Fig. 1.7, the measured acoustic velocity pattern at all phases is different from the expected velocity pattern. This difference is due to the natural convection flow created by the temperature gradient.

Moreover, Saint Ellier *et al.* [22] measured the effect of an imposed temperature gradient on the axial mean velocity distribution in the radial direction. As shown in Fig. 1.8, their results do not agree with any theoretical expectations. On the other hand, the enhancement of convective motion by acoustic streaming has been the subject of several studies, the case of differentially heated horizontal walls being generally considered (e.g., [23] and [24]). All these studies reveal a strong and complex interaction between acoustics, acoustic streaming and convective motions.

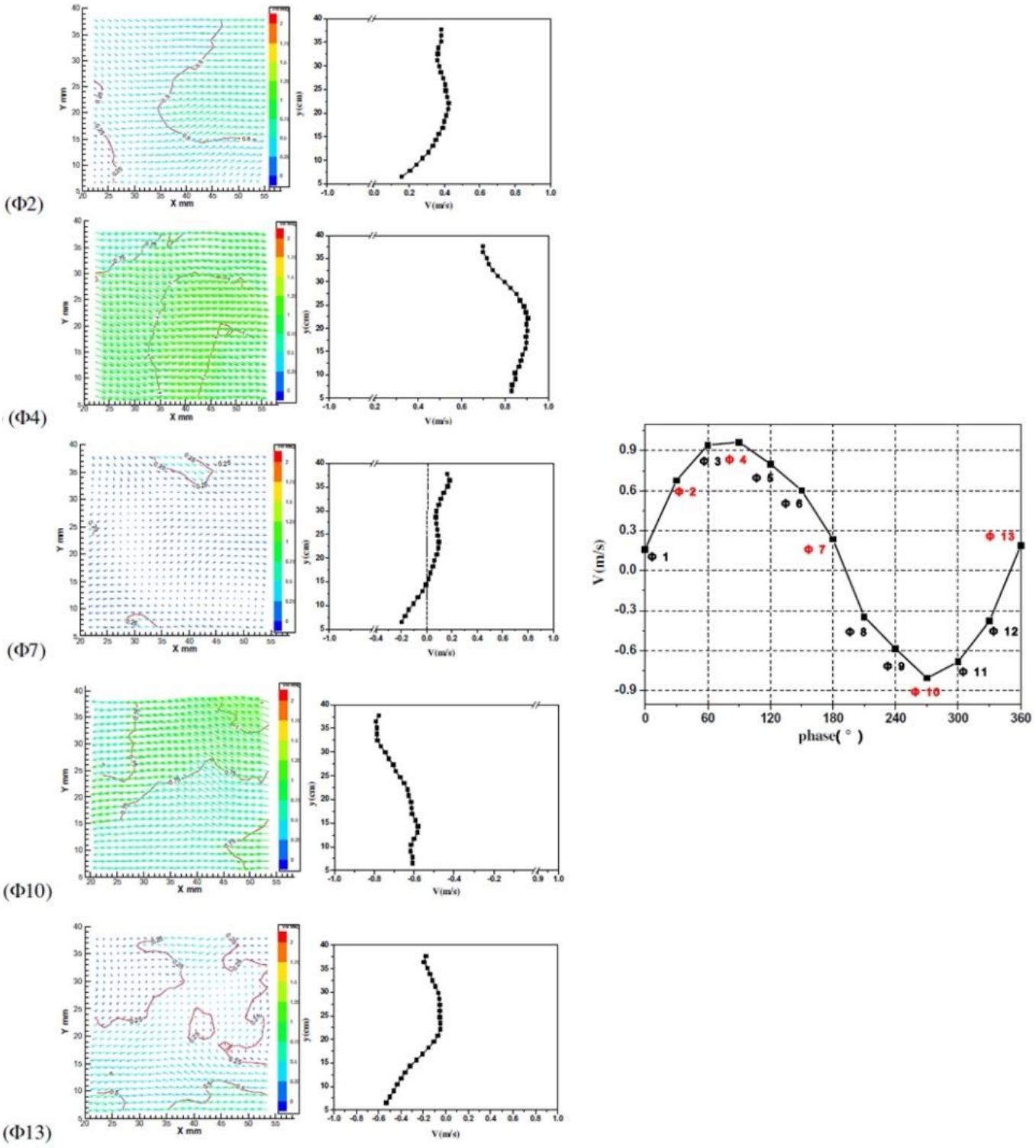

Figure 1.7: The acoustic velocity vector map at different phases over the acoustic cycle. Adapted from [21]

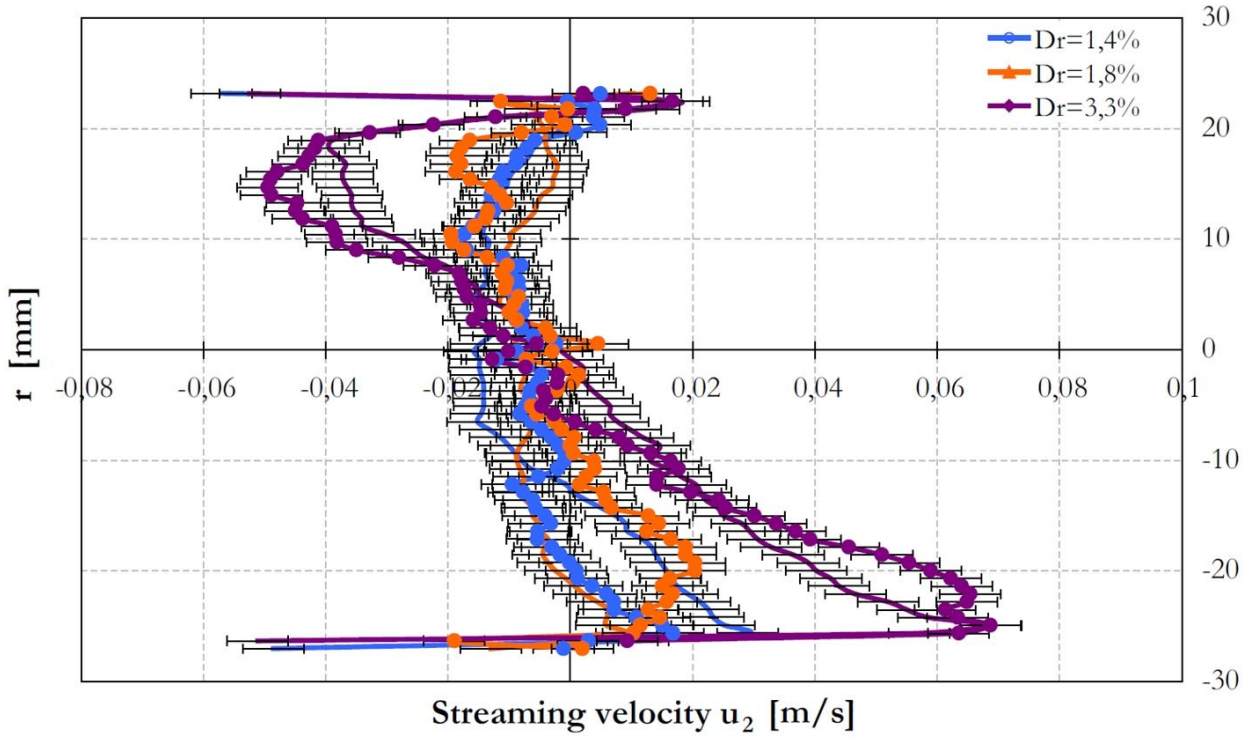

Figure 1.8: Axial streaming velocity distribution in the radial direction at different drive ratios with (●) and without (▬) temperature gradient. Adapted from [22].

The current study aims to bridge further the gap between academic configurations for which Rayleigh streaming has been studied and real thermoacoustic devices while still considering a very simple system to be able to benefit from the results of previous studies (especially, [9] and [17]) as references. Measurements of axial mean velocity are reported in a standing-wave guide in which a stack is set. The stack is heated at one end to generate a sound wave, yielding a thermoacoustic device. Measurements are performed in the heated system with and without the sound wave (that is in a thermoacoustic engine or just in a heated tube) and reveal that the mean flow in the engine results from a competition between Rayleigh streaming, jet-driven streaming and also natural convection.

Chapter 2 discusses the experimental setup, measurement techniques and signal processing tools used to study Rayleigh streaming in a real thermoacoustic device. Also, the results are discussed and conclusions are drawn by the end of the chapter.

1.2. Transition to turbulence in oscillating flow

Most of the design tools of thermoacoustic devices are mainly dependent on the linear theory of Rott [1]. Generation of turbulent flow inside some segments (e.g. inertance, resonator … etc.) of thermoacoustic devices is one type of the non-linearities that has negative effects on the overall performance, however they are not taken into consideration while designing thermoacoustic

devices due to the lack of data on this regards. Turbulence generation represents an energy loss because part of the kinetic energy of the main oscillating flow is dissipated into turbulent kinetic energy which is finally dumped as heat.

The study of oscillating flow at low frequencies (i.e. sub-acoustic range) in a pipe has been studied long time ago. For instance, Richardson and Tyler [25] used a hot wire anemometer to measure the velocity gradient near to the end of an oscillating pipe flow with different cross sectional shapes (square and oval). They noticed that the maximum velocity is achieved near to the wall rather than the center of the pipe and this phenomenon is known as annular effect, and the core flow almost has a flat profile. The annular effect was found to vanish gradually as the distance from the pipe end increases. Also, they noticed that the boundary layer thickness can be scaled with the square root of the oscillation frequency. The velocity profiles of a turbulent steady flow were captured, as well. These measurements were in agreement with the Prandtl law ($1/7^{th}$ law).

Afterwards, the issue of quantifying the transition to turbulence in an oscillating pipe flow was raised. Hence, many studies have been implemented to determine the critical Reynolds number at which the turbulent bursts start to appear during the cycle of oscillations. In the following paragraphs, a summary for the implemented work regarding this issue is presented.

Collins [26] studied the transition to turbulence in the boundary layer of periodic gravity waves at a smooth horizontal bed. Based on quasi-steady approximation, he found that the velocity at the edge of the boundary layer has a direct proportionality with the wave height in the laminar flow. So, he claimed that the onset of turbulence occurs when this proportionality is broken. Accordingly, the critical Reynolds number (Re_δ)was found to be 160. The Reynolds number (Re_δ) is defined as follows:

$$Re_\delta = U_o \delta / \upsilon \tag{1.2}$$

where U_o is the velocity amplitude at the center line of the duct, δ is the viscous penetration depth and υ is the kinematic viscosity. Also, based on the instability theory, he claimed that the first instability point in the laminar boundary layer occurs during the acceleration phase which contradicts the observations of other experiments.

However, the results of Collins [26] were not in agreement with experimental observations. For example, Sergeev [27] derived an expression for determining the value of the critical Reynolds number for oscillating flows and the expression was validated by experiments. Aluminum powder particles were added to the flow for visualization purpose and the disturbance of the flow was visually observed. He stated the value of the critical Reynolds number is a function of the Womersley number (α) which is defined as follows:

$$\alpha = \frac{D/2}{\sqrt{\upsilon/\pi f}} \tag{1.3}$$

where D is the hydraulic diameter of the duct and f is the oscillating frequency. For $(\alpha < 5.6)$, the value of the critical Reynolds number equals to $(Re_D = U_o D/\upsilon = 2500 + 13.88 * \alpha^4)$. While, for $(\alpha > 5.6)$, the value of the critical Reynolds number equals to $(Re_D = 990 * \alpha)$. Also, the friction factor of the oscillating flow was measured at different Reynolds and Womersley numbers in the turbulent flow regime and it was found to be a function of Reynolds number and it can be obtained directly from Blasius law.

Also, Ohmi and Iguchi [28] investigated experimentally the critical Reynolds number for oscillatory flow. The critical Reynolds number is defined as the value of oscillating Reynolds number (Re_D) at which the generation region is fully built up. They came up with an evaluation method for the critical Reynolds number based on the assumption that the turbulence generation region in steady flow is the same as in the oscillating flow. This evaluation method concludes that the critical Reynolds number is a function of (α), where $(Re_D = 1247 * \alpha)$ for $(\alpha > 4.9)$. This result is in agreement with the experimental data of other investigators. In addition, they mentioned that the value of the critical Reynolds number will be same as steady flow $(Re_D = 2450)$ when $(\alpha < 0.707)$. Also, the turbulence during the cycle is investigated. They concluded that the turbulence bursts appear during the acceleration phase. However, this conclusion was disproved by experiments where the turbulent bursts are observed only during the deceleration phase.

Moreover, Zhao and Cheng [29] studied the transition of oscillatory flow from laminar to turbulent by utilizing a hot-wire anemometer to record the velocity variations inside oscillatory pipe flow. Also, correlations for frictional losses are derived for both laminar and turbulent oscillating flows. The experimental data we obtained in ranges of $(332 < Re_\delta < 1193)$ and $(1.7 < \alpha < 8.2)$. They proved that the critical Reynolds number is $Re_\delta = 538$. In addition, they found that the turbulence occurs during the deceleration phase due to change from favorable pressure gradient to an adverse pressure gradient.

All of the previous studies proved the critical Reynolds number is expected to be around 500. Also, it is noted that these experiments were done at low frequencies (sub-acoustic frequency range). Hence, Merkli and Thomann [30] studied the transition to turbulence in oscillating flow using hot-wire anemometer and flow visualization. Scotch Yoke mechanism was used to generate sine wave inside a closed tube filled with air. The measurements were conducted at high frequency range up to 130 Hz. Also, the frequencies near to resonance were excluded from the study in order to avoid travelling shocks and grantee sinusoidal variation of properties with time. They proved that the transition of flow from laminar to turbulent conditions is dependent only on the Reynolds number and the reported value of the critical Reynolds number is $(Re_\delta = U_o \delta/\upsilon = 283)$. In addition, they concluded that the hot-wire measurements in the boundary layer at high frequencies are misleading because the size of boundary layer at high frequency becomes too small and hence the disturbance of the hot-wire probe becomes large enough to affect the collected data.

After quantifying the critical Reynolds number, it was important to define different patterns and structures of oscillating flow. Hence, Ohmi and Iguchi [31] described the flow patterns in an

oscillating pipe flow at different oscillating Reynolds number ($8550 < Re_D = \frac{U_o D}{\upsilon} < 67700$) and Womersley number ($3 < \alpha < 16.5$). Three characteristic parameters are used to describe the different flow patterns. These are the cross-sectional mean velocity, pressure gradient, and wall shear stress. The relationship between these parameters can be expressed in the unsteady momentum equation given as follows:

$$\rho_o \frac{d\bar{U}}{dt} + \frac{4}{D}\tau_w - \frac{\Delta p}{l} = 0 \tag{1.4}$$

where the former two terms are the inertia and the viscous terms respectively whereas the latter term is the pressure gradient. They classified the flow patterns into three categories which are quasi-steady region, intermediate region, and inertia dominant region. When the latter two terms in the previous equation are balanced, the flow is classified as quasi-steady, while the flow becomes in an intermediate region when the three terms are nearly balanced and finally when the former two terms are balanced the flow is in inertia dominant region. Also, the comparison between the measurements and turbulent quasi-steady state relations showed a favorable agreement in the whole cycle, except early stage of acceleration phase and latest stage in deceleration phase, when the flow is fully turbulent ($Re_D > 3960\alpha$). While, this agreement is limited to a portion of the cycle, mainly the deceleration phase, when the flow is conditionally turbulent ($1131\alpha < Re_D < 3960\alpha$).

Also, Hino *et al*. [32] investigated the oscillating flow characteristics at different Reynolds number ($19 < Re_\delta < 1530$) and Womersley number ($1.35 < \alpha < 6.18$). They divided the oscillating flow into three categories which are laminar or distorted laminar flow, weakly turbulent flow, and conditionally turbulent flow. The laminar flow is described as a smooth flow with no oscillations. The weakly turbulent flow is described as a flow with small fluctuations during the whole cycle. Finally, the conditionally turbulent flow is described as the flow which has violent fluctuations during deceleration phase. In laminar cases, the measured velocity distribution matches the theoretical velocity distribution. In conditionally turbulent flow, the measured velocity distributions match the theoretical velocity distribution only in acceleration phase while it deviates during the deceleration phase due to turbulence occurrence. Also, they concluded that for $\alpha < 1.6$ the critical Reynolds number is dependent on the Womersley number; while for larger Womersley number the critical Reynolds number is a constant value equals to $Re_\delta = 550$. However, Sergeev [27] mentioned that the critical Reynolds number is proportional to Womersley number only for $\alpha > 5.6$.

Moreover, Hino *et al*. [33] studied experimentally the structure of the turbulent oscillating flow. Two different techniques are used to measure instantaneous velocity of oscillating flow inside a wind tunnel has a rectangular cross section with aspect ratio of 2.6. These techniques are hot wire anemometry and laser Doppler velocimetry. The flow inside the wind tunnel is driven by a reciprocating piston with diameter of 480 mm. The frequency of oscillatory flow can be varied from 0.01886 to 0.4 Hz. As a kind of validation, the measured laminar velocity profiles at different

phases during the cycle are compared with theoretical profiles. They reported that there is an overshoot in the velocity profile near to the wall during the acceleration phase, while this overshoot is vanished during deceleration phase. Regarding the turbulent flow, the measurements showed that there is a too small overshoot in the velocity profile during the acceleration phase. Also, near to the wall above the viscous sublayer, there is a layer obeys semilog-law like in a steady flow. However, the thickness of this layer during the acceleration phase is smaller than during the deceleration phase. In addition, the total viscous layer is increased during acceleration phase till reaches to maximum value at the end of acceleration then it is suddenly decreased at the beginning of deceleration phase due to turbulence generation. Also, the turbulence intensity increases from the wall towards the center of the duct in the beginning of the acceleration phase and later in the deceleration phase. While, during the reminder part of the cycle; the turbulence intensity profile has a peak value near to the wall rather than the center of the duct. Interestingly, they reported that the value of the wall shear stress reached to the maximum value at the peak of turbulence intensity ($\omega t \cong 0.75\pi$) not at the phase of maximum axial velocity ($\omega t \cong 0.5\pi$). In addition, the turbulence energy production is increased during deceleration phase while is kept constant almost in the acceleration phase. Also, the turbulence energy dissipation rate is increased suddenly at $\omega t \cong 0.25\pi$; then it decreases suddenly at $\omega t \cong 0.75\pi$, which means the turbulence energy production is consumed mainly by the violent turbulent fluctuations during the deceleration phase.

In the previous experiments, the measurement techniques were intrusive techniques (e.g. How wire). However, such technique might have an effect on the acquired results. So, some researchers use non-intrusive techniques to study the oscillating flow. Clamen and Minton [34] studied the transition of oscillating and pulsatile flows from laminar to turbulence. The flow was described by dimensionless parameters which are the oscillatory Reynolds number (Re_D), the Womersley number (α) and the mean Reynolds number, defined as follows:

$$Re_{D,s} = U_m D/\upsilon \tag{1.5}$$

where U_m is the mean flow velocity. A hydrogen-bubble technique was used to obtain the velocity profile through the pipe cross section. Regarding pure oscillatory flow (i.e. zero mean flow), the measured velocity profiles was in agreement with the theoretical velocity profiles for low frequencies. However, at higher frequencies, there is about 10% error due to difficulties of keeping pure harmonic pipe oscillations. Also, it is worthwhile to mention that the flow regime was laminar for all experiments associated with pure oscillatory flow. On the other hand, the regime of pulsatile flow was changed from laminar to turbulent. Regarding pulsatile flow, the intermittency of the flow, defined as the percentage of the time the flow was disturbed to the total time of measurements, is used as an indicator for transition to turbulence in the flow regime. They concluded that the increase in the mean Reynolds number at a constant Womersley number leads to an increase in the intermittency. However, in some cases at a constant mean Reynolds number the increase in the Womersley number leads to a reduction in the intermittency. Also, they observed that the flow was laminar up to Re_D of 1500 and Womersley number up to 7.

Also, Eckmann *et al.* [35] utilized a Laser Doppler Velocimeter (LDV) to study the transition from laminar to turbulent in oscillating flow. They used the following parameters to describe the flow; the Reynolds number Re_δ, Womersley number (α), and the dimensionless amplitude ($S = \frac{Stroke\ distance}{tube\ radius}$). This study covers a range of Re_δ up to 1310 and Womersley number from 6.36 to 23.3. To ensure conducting measurements in a proper way; they compared the measured velocity distribution through the duct, in the laminar cases, with the result of laminar theory of oscillatory flow. Their measurements were in a good agreement with theory. The instability of the flow was observed at different radial positions. At Reynolds number less than 500 the both core and boundary layer flows are stable. For Reynolds number up to 1310, the core flow remains stable. However, the boundary layer flow show instabilities during deceleration phase and the flow appears to relaminarize again during acceleration phase. In addition, the effect of existence of the hot-wire probe inside the flow on the measurements was investigated. A dummy hot-wire probe is inserted near to the measurement location (LDV probe) and the instabilities of the flow is monitored. The instabilities in the boundary layer is observed at Re_δ above 300. This reduction in the critical Reynolds number is due to the existence of the hot-wire probe.

Moreover, Flisher and Brodkey [36] studied the transition to turbulence in oscillating pipe flow using flow visualization technique. They described a mechanism for turbulence generation in oscillating flow. The dimensionless parameters used in this study are Reynolds number Re_δ and Womersley number (α) ranged from 536 to 1340 and 4.66 to 11.74, respectively. They mentioned that series of events or flow structures are responsible for generating turbulence in oscillating flow like steady flow. However, these events in oscillatory flow are not random in time and space in contrast to steady flow turbulence. These events occurred during deceleration phase of the cycle. These events are local deceleration, local acceleration, Excitation-traverse vortex and ejection. Also, they concluded that the critical Reynolds number ranged from $650 < Re_\delta < 1000$. However, these values of the critical Reynolds number is much higher than stated values by Merkli and Thomann [30]; this discrepancy might be due to some disturbances imposed on the flow in Merkli's experimental setup. Also, Merkli used a resonance tube closed from one end while others used an oscillating pipe flow. On the other hand, the stated range of the critical Reynolds number (650-1000) is reasonable value when compared with values obtained by Hino *et al*. [32] and Sergeev [27].

Finally, Akhavan *et al*. [37] utilized the Laser Doppler Anemometer (LDA) to investigate the transition to turbulence in oscillating pipe flow for a range of Reynolds number Re_δ from 550 to 2000 and Womersley number α from 4.95 to 9.9. In order to verify their measurements, the measured velocity profiles, in laminar flow, are compared to the theoretical profiles and a good agreement is achieved. They classified the flow regimes into four types; namely, laminar flow, weakly turbulent flow, conditionally turbulent flow, and fully turbulent flow which is in agreement with the classifications of Hino *et al.* [33]. They noticed a vigorous turbulent busts during the deceleration phase while the flow is relaminarized during the acceleration phase. Also, they concluded that the turbulent oscillating flow has the same layers of the turbulent steady flow which

are a viscous sublayer, a logarithmic layer and an outer wake. On the other hand, the major difference from the steady flow is the ratio of turbulence intensities (axial and radial) and average center line velocity has a value twice larger than the value reported for the steady flow. In addition, the production rate of turbulence is found to be significant at the late stages of acceleration phase and early stages in the deceleration phase.

In addition, some experiments were conducted on pulsatile flow to understand the transition to turbulence in such flow. Trip *et al.* [38] studied experimentally the transition of water flow from laminar to turbulent in a pulsatile pipe flow. Three dimensionless parameters were employed to describe the pulsatile flow. These parameters are the mean Reynolds number ($Re_{D,s}$), the oscillatory Reynolds number ($Re_D = U_o D/\upsilon$), and the Womersley number (α) which is the ratio of the transit inertia force to the viscous force; where U_o is the axial velocity. The measurements were implemented over a range of mean Reynolds number (2000-5000) and Womersley number ranged from 7.1 to 17.67. The turbulence intensity was used as indication for the turbulence generation. Both spatial and temporal intensities were obtained simultaneously by using particle image velocimetry (PIV). In laminar cases, the measured velocity distribution in the pipe was in agreement with the theoretical velocity distribution obtained from the solution of Navier-Stocks equations for the same conditions of that case. Interestingly, they found that there is no effect for both oscillatory Reynolds number and Womersley number on the turbulence generation; however, the turbulence generation is only associated with the mean Reynolds number and the fully developed turbulent flow is achieved at $Re_{D,s} = 2761$. In addition, the turbulence intensity was measured during the different phases of the cycle. They found that during the acceleration phase the turbulence intensity is decreased and start to increase during acceleration phase. The maximum turbulence intensity is achieved at the end of deceleration phase.

Also, Carpinlioglu and Ozahi [39] derived some governing correlations, based on the available experimental data, describing the start of the transition to turbulence in both oscillating and pulsatile flows. The start of the transition is recognized by the observation of turbulent bursts during the deceleration phase. While the end of transition is marked by the spreading of these bursts in the whole cycle. Regarding oscillating flow, they found that the critical Reynolds number (Re_D) is dependent only on the Womersley number (α). For $0.707 < \alpha < 29$, the critical Reynolds number can be represented as following ($Re_D = 1060 * \alpha$) with accuracy of ± 12 %. While for $\alpha > 29$, the critical Reynolds number is represented as following ($Re_D = 565 * \alpha$). On the other hand, the critical Reynolds number in the pulsatile flow is dependent on both Womersley number and velocity amplitude ratio ($Re_D/Re_{D,s}$).

Regarding numerical work in this subject, Ahn and Ibrahim [40] evaluated the performance of high Reynolds $k - \varepsilon$ model for turbulent oscillating flow in a pipe. They compared the measured normalized velocity distribution and phase difference with the numerical simulation data. For laminar flow regime, the oscillating flow can be simulated numerically with high accuracy. For

fully developed turbulent flow, the $k-\varepsilon$ model predicts the oscillating flow with an acceptable error. However; for transition regime, the numerical data deviates from the experimental one.

Also, Akhavan *et al*. [41] investigated numerically the transition to turbulence in oscillating flow inside a channel. The stability of the flow to different disturbances is studied using direct numerical simulations of the Navier-Stokes equations. Different disturbances such as infinitesimal and finite amplitude in two and three dimensions are imposed to the main oscillating flow and the evolution of such disturbances is monitored and compared with the experimental results. Out of this work, they found that the transition to turbulence in oscillating flow can be captured by a secondary instability mechanism of disturbances have two-dimensional finite-amplitude and three-dimensional infinitesimal amplitude. This method shows a good agreement with experimental results.

Finally, some theoretical work was implemented regarding this subject. For instance, Womersley [42] established a method for determining the velocity profile and viscous drag in a circular pipe when the pressure gradient varies with time. He expressed the pressure gradient as an exponential function of time. So, the real part of this pressure gradient is equivalent to the oscillating pressure gradient.

Drake [43] derived mathematical expressions to predict the velocity profile and skin-friction of oscillating flow inside a rectangular duct. He concluded that the velocity profile at too low frequencies (dimensionless frequency parameter) is the same as that for a steady flow. While, at high frequencies the velocity profile is changes and the maximum velocity is achieved near to the walls rather than at the center of the duct. This phenomenon is known as an annular effect. Also, the mathematical expression for the velocity profile at high frequencies is divided into two expressions where, one is valid near the walls while other is valid near the center of the duct.

Tsangaris [44] presented the exact solution for of the Navier-Stokes equations for pulsatile flow inside a rectangular duct. This solution contains the effect of both steady and oscillating flow on the velocity profile. Also, the result of this solution, when only oscillating flow is considered, is equivalent to Fan (1965) and Drake (1964) solutions.

Fan [45] solved the equations of motion and continuity for laminar, incompressible, and fully developed flow in a rectangular duct under am axial pressure gradient which is an arbitrary function of time. Solutions for four different pressure gradient functions are obtained. Those functions are impulsive pressure gradient, Heaviside unit step pressure gradient function, harmonic oscillating pressure gradient and purely harmonic motion superimposed on a steady slow.

Kerczek and Davis [46] studied the stability of the Stokes layer in an oscillating flow against two and three-dimensional disturbances. The approach of energy method is employed to investigate the stability criteria. Based on two-dimensional disturbances, the criterion for stokes layer stability is ($Re_{\delta} < 38.9$).

From the previous review, it can be concluded that the selection of the characteristic length of the Reynolds number is important to define the value for the critical Reynolds number. In other words, when the diameter of the duct(D) is chosen as a characteristic length; the critical Reynolds number is proportional to Womersley number ($Re_D = C * \alpha$) and the proportionality factor or the critical amplitude number (C) ranges from 990 to 1247. However, for those who use the viscous penetration depth $\delta_v = \sqrt{2v/\omega}$ as a characteristic length, the value of the critical Reynolds number becomes constant because the effect of the Womersley number is included in the Reynolds number itself, where $Re_\delta = \frac{U_o \delta_v}{v} = \frac{Re_D}{2*\alpha} = \frac{C}{2}$. Also, it can be noted that the critical Reynolds number depends on the frequency range. Many research postulated that the critical Reynolds number for sub-acoustic frequency is about 500. On the other hand, the experimental work done to quantify the critical Reynolds number in the high frequency range (i.e. acoustic frequency range) is scare. Also, the available numerical models cannot predict the transition to turbulence in oscillating flows.

Also, it is noted that PIV system was not used in studying the pure oscillating flow [47]. Although, PIV is a good tool for such measurements because we can get 2D velocity field which means the velocity distribution in the duct will be measured at all points simultaneously. So, the results of the PIV system will be more realistic when compared with other techniques. The reason for not using PIV system in the previous experiments is due to the limited sampling frequency of the old PIV system (up to 10 Hz). Nowadays, the sampling frequencies of the PIV system reached up to 5000 Hz. Hence, in this work; PIV system will be utilized to study the oscillating flow inside the rectangular duct at sub-acoustic frequency range to validate the methodology applied in this work then the study will be extended to the acoustic frequency range.

Chapter 3 discusses the experimental setup, measurement techniques and signal processing tools used to study the transition to turbulence in oscillating flow at both sub-acoustic and acoustic frequency ranges. Also, the results are discussed and conclusions are drawn by the end of the chapter.

1.3. Entrance/exit effects

In steady flows, the entrance/exit effects are well described and understood. On the other hand, there are lack of studies focused on these effects in oscillating flows. The entrance/exit effects in steady flow cause an energy loss usually referred as minor loss. Also, these effects extend to a certain distance known as a development length. In thermoacoustic devices, where the main flow has an oscillating behavior, the acoustic displacement at high amplitudes becomes comparable to the length of some components of thermoacoustic devices (e.g. heat exchangers). So, the entrance/exit effects may extend over the whole length of the heat exchanger. Some studies have pointed out to the effects of entrance/exit on the performance of thermoacoustic devices. For instance, Swift [48] noticed a discontinuity in temperature measurements between the hot heat exchanger duct and the empty duct next to it. Also, Storch *et al*. [49] reported that the temperature distribution over the pulse tube of pulse tube refrigerator exhibits an overshoot near to the both

ends of the tube. As shown in Fig. 1.9, there is an overshoot in the temperature distribution near to the both ends of the pulse tube. They concluded that this overshoot is due to the entrance/exit effects.

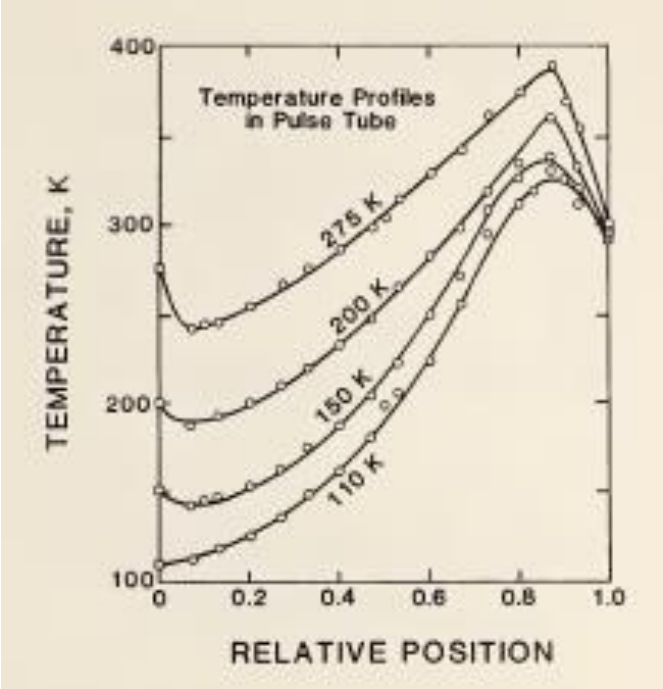

Figure 1.9: Gas temperature distribution over the whole length of the pulse tube in thermoacoustic refrigerator at different cold end temperatures. Adapted from [49].

Although it seems that the entrance/exit effects are important, the available design tools do not consider them. In these design tools, it is assumed that the flow properties (e.g. temperature and pressure) at the beginning of the segment is the same as the properties at the end of the preceding adjacent segment. This joining assumption will not be appropriate wherever the minor losses exist. Lately, the design tools added a lumped element to deal with the minor losses. However, this lumped element deals with the minor loss from the perspective of the steady flow. This assumption lacks of the experimental validation.

As the thermoacoustic core of engines and refrigerators consist of stack/regenerator and heat exchangers, it is important to understand the effects of entrance/exit on the flow characteristics near to the end of the stack/regenerator. The stack can be simplified as a set of parallel plates. Most of the researchers have followed this simplification in order to easily describe the effects of the stack on the flow morphology. For instance, Benon *et al.* [50] experimentally studied the effects of the plate thickness on the formation of vortices at the end of the parallel plate stack. As shown in Fig. 1.10, two elongated vortices are formed in the case of thin plate thickness. Whereas, two encounter vortices impinge at the end of the plate with the case of thick plate thickness. Also, they compared these results with numerical model they developed. The numerical model results agree

with the measurements. It is worthwhile to mention that the vortex generation at the inlets/exits of the stack region due to sudden contraction/expansion is one of the main mechanisms of viscous dissipation. Some numerical studies [51], [52], [53] have tempted to model the oscillating flow over the parallel plates.

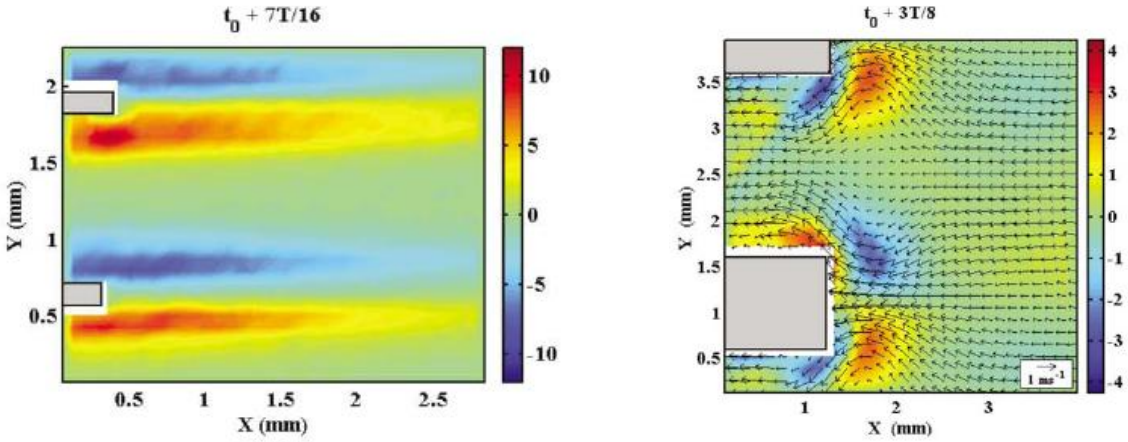

Figure 1.10: The vorticity field at a certain phase around the stack plates for different plate thicknesses: (left) Thin, (Right) Thick. Adapted from [50].

Also, part of viscous dissipation occurs near to the walls due to the formation of the boundary layer [54]. Berson *et al.* [55] measured the velocity field inside an oscillating boundary layer between the parallel plates of the stacks using PIV and compared the results with a simple numerical model. They found that the generated vortex is attached to the plate at low amplitudes. Whereas at high amplitudes the vortices detached from the plates. However, they concluded that this detachment does not indicate any transition to turbulence as Re_δ was much less than the critical value $Re_\delta = 280$ [30]. Moreover, some studies [56] [57] have found that the flow over stack plates is non-periodic flow and the non-periodicity increases with high amplitudes.

Some studies have attempted to investigate the evolution process of the vortex generation around the parallel plates. Shi *et al*. [58] described different phenomena occurring during the ejection phase. They found that at low velocity amplitudes, two symmetric (with respect to the plate centerline) vortices are formed and attached to the plate. These two vortices are either elongated or concentrated based on the plate spacing. These findings are in agreement with [50]. At higher velocity amplitudes, the elongated vortices break up to form vortex street, as shown in Fig. 1.11. At much higher velocity amplitude, the flow turned to be more chaotic, as shown in Fig. 1.12.

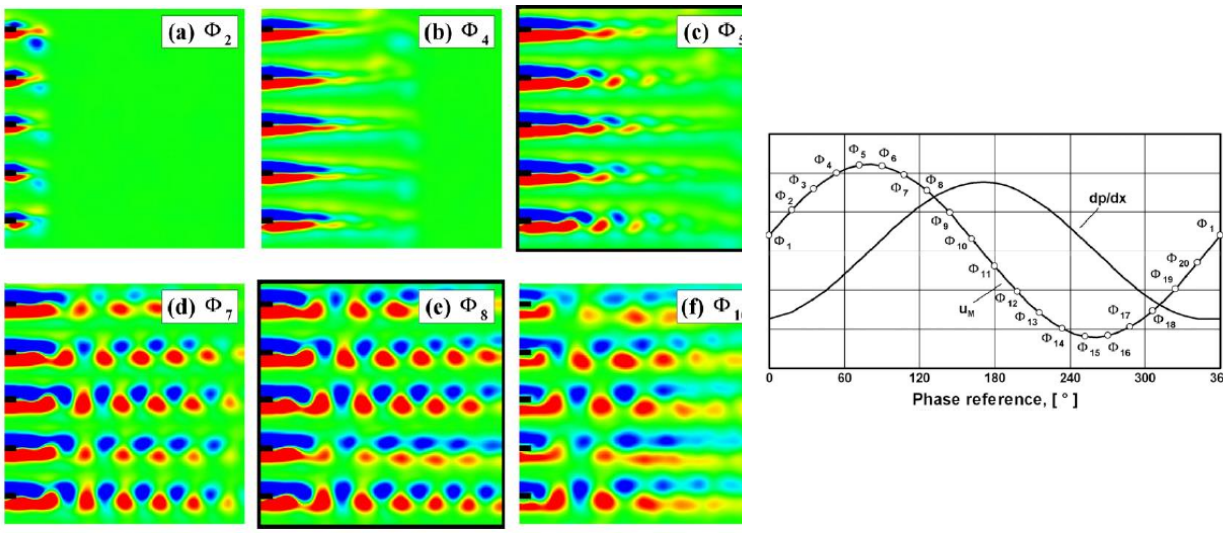

Figure 1.11: Vorticity field past the stack plates at different phases at $Re_\delta = 172$. Adapted from [58].

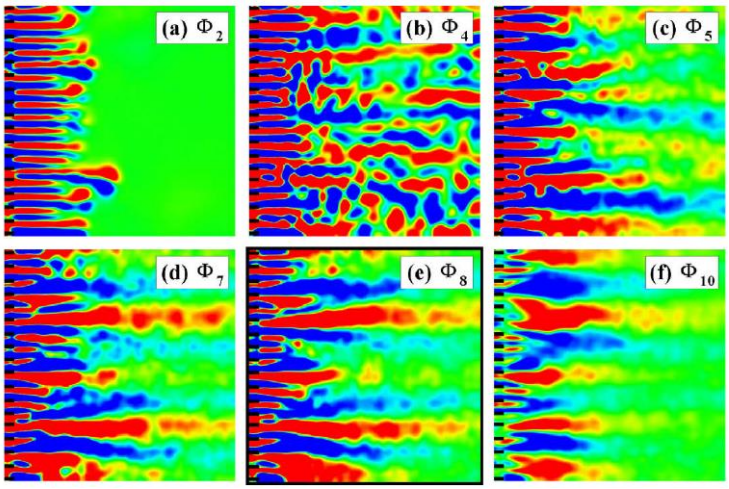

Figure 1.12: Vorticity field past the stack plates at different phases at $Re_\delta = 337$. Adapted from [58].

Rezk *et al.* [59] studied the effects of plate spacing, plate thickness and drive ratio on the flow morphology on the oscillating flow over parallel-plate stack. They found that the size of the vortex and the associated disturbance zone increase as the thickness of the plate is increased. Also, the interaction between vortices increases as the plate separation decreases.

Shi *et al.* [60] studied the relation between Reynolds number and Strouhal number in oscillating flow over parallel plate stack using LDA. As shown in Fig. 1.12, Strouhal increases with the increase of Reynolds number up to a certain level, after which Strouhal number saturates.

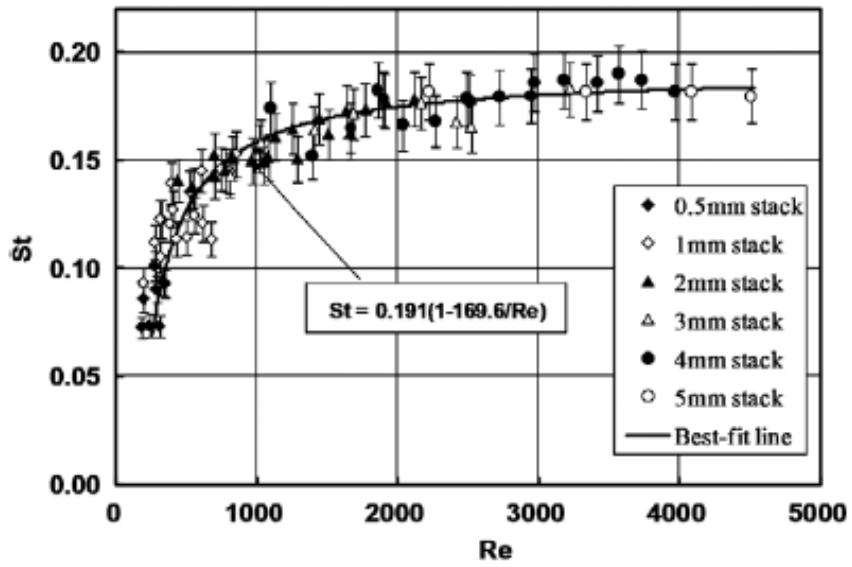

Figure 1.13: Effect of Reynolds number on Strouhal number in oscillating flow past a parallel-plate stack. Adapted from [60].

Most of the studies mentioned above were concerned with the ejection phase (i.e. moving the flow out of the stack). In other words, they studied the flow interactions outside the stack. So, Jaworski *et al.* [61] focused on the suction phase (i.e. moving the flow into the stack). They have tempted to define an entrance length inside parallel-plate stack placed inside an acoustic resonator. They defined the entrance length as the distance after which the velocity profile becomes nearly constant. They pointed out the entrance length changes over the acoustic cycle.

One of the trends to minimize the disturbance occurred at the inlet/exit of the stack is using a stack with different end-plate shapes (i.e. circular and triangular). Aben *et al.* [62] have investigated experimentally utilizing PIV some characteristics of the fluid (vortices and streaming velocity) around parallel stacks inside a standing wave resonator. Also, they have studied the effects of the drive ratio, the plate thickness, the plat spacing, and the end-plat end on the vortex shedding at the entrance of the parallel plate stacks. As shown in Fig. 1.14, the vortex generation with a plate has a circular end is smoother than the rectangular end and triangular end with right angle. However, the plate with triangular end and small angle reduces the vorticity which indicates less dissipation of the flow energy.

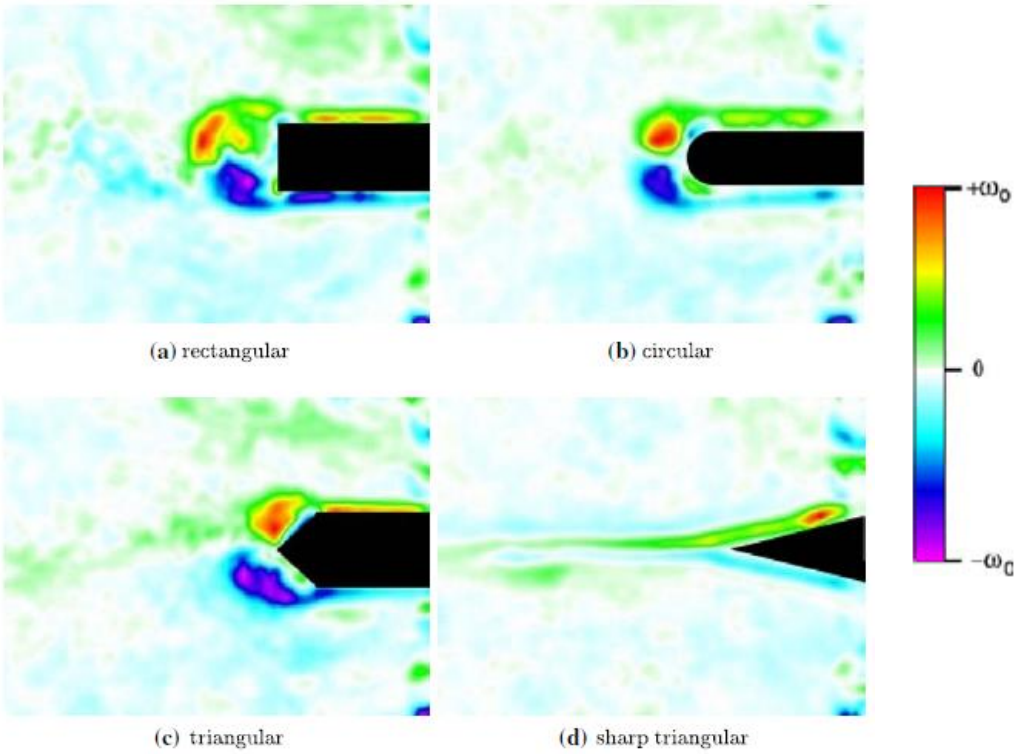

Figure 1.14: Vorticity field over parallel-plate stack with different end-shape ($\omega_o = 10^4\ s^{-1}$). Adapted from [62].

All the previous studies have investigated the effects of several parameters on the flow morphology around parallel-plate stack. However, all of these studies have been implemented at low velocity amplitudes [63]. Since most of thermoacoustic systems work at high pressure and velocity amplitudes, it is important to study the effects of previously mention parameters on the flow morphology at high velocity amplitude.

In this study, the effects of different end-plate shapes on the flow morphology and on the flow vorticity and turbulence intensities at a wide range of Reynolds number will be investigated experimentally using PIV system. Chapter 4 discusses the experimental setup, measurement techniques and signal processing tools used to study the effects of different end-plate shapes at a wide range of Reynolds number. Also, the results are discussed and conclusions are drawn by the end of the chapter.

Chapter 2: Streaming in a Thermoacoustic Engine

"This chapter is Reproduced from [Ramadan, Islam; Bailliet, Helene; and Valiere, Jean-Christophe, "*Experimental investigation of the influence of natural convection and end-effects on Rayleigh streaming in a thermoacoustic engine", J. Acoust. Soc. Am.*, Vol. **143** (1), p 361, 2018.], with the permission of the Acoustical Society of America."

As mentioned in the introduction section, this chapter focuses on the effects of the natural convection flow on Rayleigh streaming flow inside a standing-wave thermoacoustic engine. The following subsections discuss the experimental setup, measurement techniques and signal processing tools used in this part of the study. Also, the results are discussed and conclusions are drawn by the end of the chapter.

2.1. Experimental setup

As previously mentioned, the aim of this part of the study is to bridge further the gap between the academic configurations in which the steaming phenomenon has been investigated and the real thermoacoustic engine. So, a simple yet real thermoacoustic engine is proposed in the current study. Particle Image Velocimetry (PIV) and Laser Doppler Velocimetry (LDV) are used to measure the streaming velocity distributions inside the engine. Also, pressure and temperature measurements are performed. The construction of the engine and the different measurement techniques are discussed in the following subsections.

2.1.1. Thermoacoustic engine

A schematic for the standing-wave thermoacoustic engine used in this study is presented in Fig. 2.1a. The resonator is made of a glass tube, to grant an optical access for the laser measurements, with inner diameter $(2R)$ of 39 mm and length (l) of 740 mm. As shown in Fig. 2.1b, the engine core consists of an electric heater attached to a 400 CPSI (Cell Per Square Inch) ceramic stack that has a length of 60 mm. The electric heater is 0.6 mm diameter Ni-Cr wire and has an electric resistance of 2.1 ohm. The engine core is inserted inside the resonator tube so that the heater is located at distance of 129 mm from the left end of the resonator. The heat is supplied to the engine through the heater wire connected to a DC-power supply (model: FI3610). In such an engine, applying high enough temperature gradient along the stack generates sustainable acoustic waves with a specific frequency (f) that depends on the boundary conditions and on the working fluid. Since here the resonator is closed at both ends and filled with air at ambient conditions, the $\lambda/2$ mode is excited and hence the resonance frequency is $f \approx c/2l$. A DeltaEc model (see Appendix A.1) is built to predict the performance of the engine.

In order to deeply understand the mean flow patterns in this device, measurements for three different parameters (pressure, temperature and velocity) are conducted. A condenser pressure microphone (GRAS – model: 40BP) is set at the right end of the resonator to measure the dynamic pressure oscillations. The pressure signal is fed to a data acquisition card (model: NI 9234). The temperatures at both sides of the stack on the axis of the guide are measured using two type-K

thermocouples (identified by the green dots in Fig. 2.1a and further called T_h and T_a). In addition, the temperatures at different axial and radial locations are measured. Four type-K thermocouples (identified by the red dots in Fig. 2.1a) are used either to measure the azimuthal temperature distribution of the outside wall along two perpendicular axes ($A1\ (\Theta = 0)\ and\ A2\ (\Theta = \frac{\pi}{2})$) at two different axial locations (at $x = -140\ and - 180\ mm$) or to measure the axial temperature distribution (at $x = 0, -100, -140\ and - 180\ mm$). The signals of all thermocouples are fed to a data acquisition card (model: NI 9213) to be stored on the computer. The fluid velocities are measured using both Laser Doppler Velocimetry (LDV) and Particle Image Velocimetry (PIV). For this purpose, coffee smoke is used to seed the fluid. The coffee is burnt in a closed cavity; the smoke that escapes from one hole in this cavity is filtered and cooled down before being introduced in the engine. The closed ends of the resonator both have a hole used to introduce the smoke. These holes are closed by plugs for normal operation of the engine. The LDV and PIV measurements and data processing are described in the following subsections.

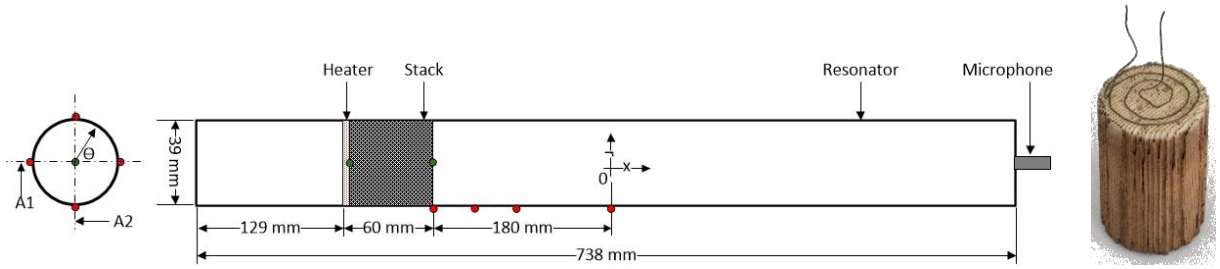

(a) **(b)**

Figure 2.1: (a) Schematic for the thermoacoustic engine, (b) Photo for the electric heater attached to the stack.

2.1.2. Experimental procedure

In this study, the mean flow velocity is estimated by performing a time average of the particle velocity. It is therefore necessary to ensure that the engine has reached its steady-state (defined by the variation of the measured quantity not exceeding 5% over the measurement period) so that the amplitude of acoustic velocity does not change along the averaging time. In particular, the coordination between the processes of heating one side of the stack and of seeding the fluid has to be considered carefully so that the engine operating state is as steady as possible during laser measurements. When the heater is turned on while both sides of the stack are at ambient temperature (normal operation), the temperatures T_h and T_a increase until they become nearly constant. As shown in Fig. 2.2 (left column), the temperature difference (T_h-T_a) becomes constant after about 500 seconds. Also, as shown in Fig. 2.3 (left column), the acoustic pressure measurements can be considered as steady after about 500 seconds. However, if the measurements are started after that time (500 seconds), most of the seeding particles will be settled down to the bottom of the resonator and hence the velocity measurements will not be satisfactory due to the

low seeding particle density. So, another procedure is followed to shorten the time required to achieve steady-state operation. The heater is turned on while the plugs at both ends of the resonator are removed, to preheat the engine. Doing so the resonator is not a λ/2 one and the thermoacoustic process does not lead to any wave generation. The heating process lasts for about 10 minutes and then seeding particles are introduced into the engine. After seeding, the plugs are closed and hence the engine starts immediately. Henceforth, this procedure is referred as "Preheating operation". It should be noted that the zero time in the preheating operation refers to the time at which the plugs at both ends of the engine are closed.

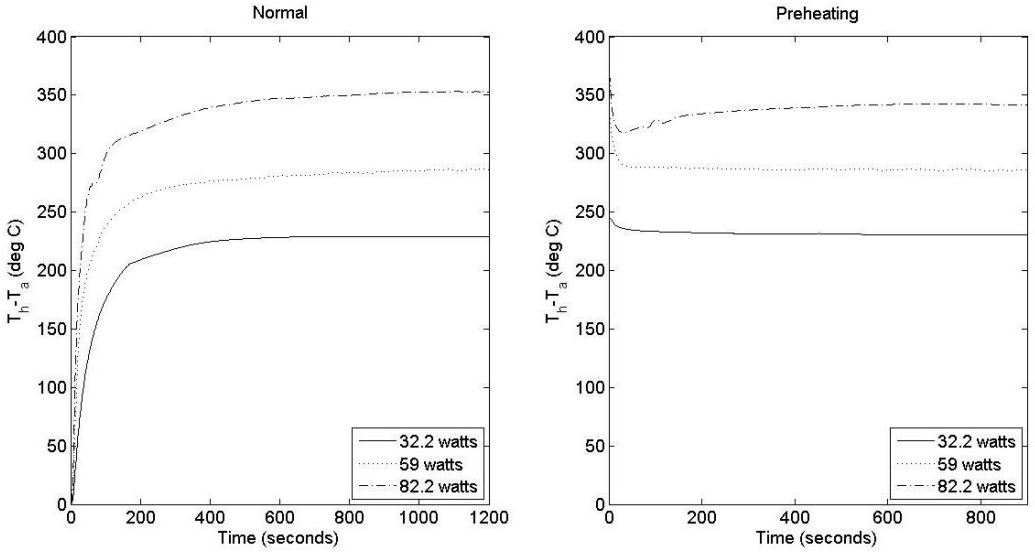

Figure 2.2: The evolution of the temperature difference (T_h-T_a) over time for three different input electric power for two different cases: normal operation (left), preheating operation (right).

As shown in Fig. 2.2 (right), the temperature difference reaches its steady-state operation after about 300 seconds. In addition, as shown in Fig. 2.3 (right), the acoustic pressure reaches its steady state after about 150 seconds. Also, preliminary measurements for the time evolution of both acoustics and mean velocities are conducted. As shown in Fig. 2.4, the acoustic velocity reaches its steady-state value after about 100 seconds, while the streaming velocity reaches the steady-state value after about 300 seconds. This is explained by the fact that the temperature field influences acoustic streaming [11] and hence the streaming transient time is linked to the temperature field transient time. Accordingly, the velocity measurements are started 300 seconds after closing the plugs; also, the measurement period does not exceed 3 minutes to ensure that there are enough seeding particles.

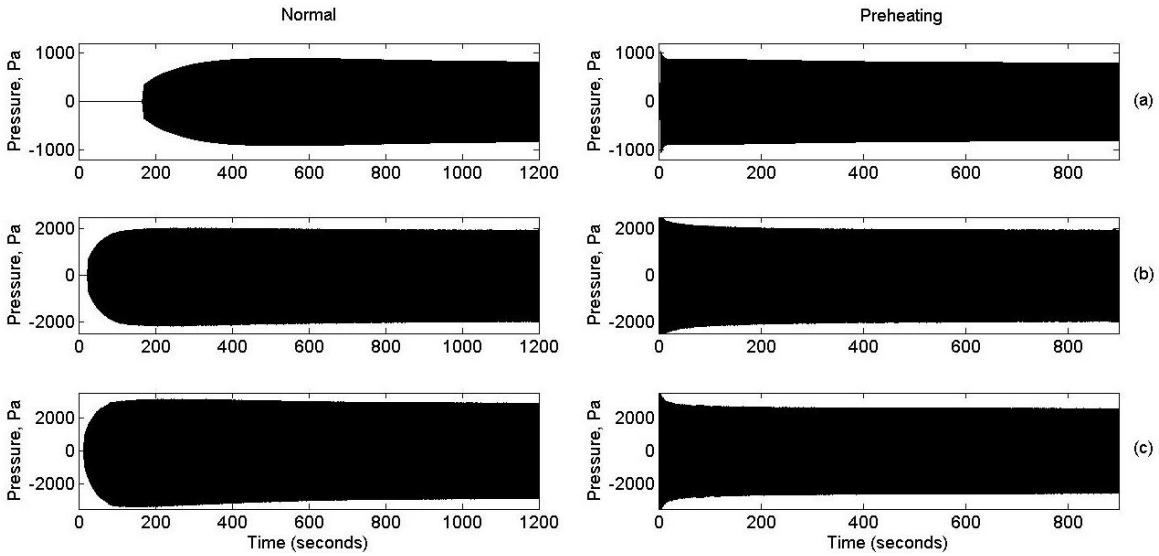

Figure 2.3: Evolution of the acoustic pressure over time at the right end of the engine for two different cases: Normal operation (left), preheating operation (right) and for three different input electric powers: (a) 32.2 W, (b) 59 W and (c) 82.2 W.

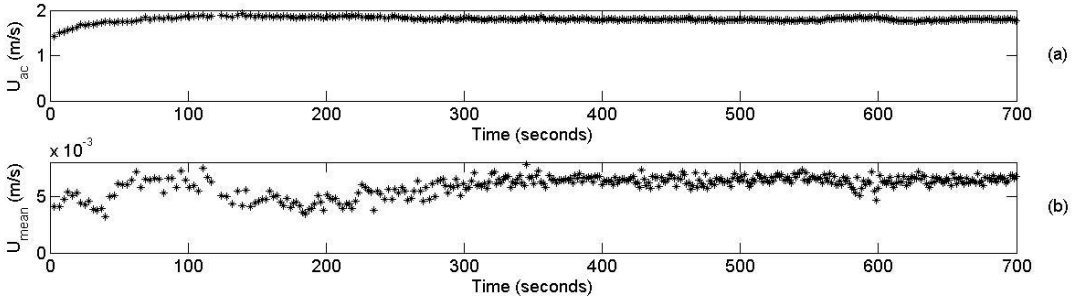

Figure 2.4: Evolution of (a) the acoustic velocity and (b) the mean velocity over time at the center of the resonator and at axial location x = 180 mm for 32.2 watts input electric power (preheating operation).

2.1.3. LDV measurements and signal processing

The LDV used to estimate the axial particle velocity is a 1-D LDV system with an argon-krypton laser source (Spectra Physics – model: Stabilite 2017) that has 514.5 nm wavelength. As shown in Fig. 2.5a, the laser beam passes through a beam splitter to be split into two beams. To overcome the problem of the directional ambiguity, the frequency of one of the beams is shifted by a certain value in the Bragg cell. The two beams are intersected to form an elliptically-shaped probe volume with length of 0.4957 mm and diameter of 0.047 mm; the fringe spacing being 2.694 μm. To achieve high sampling rate, the transmitter and the receiver are configured to collect the forward-scattered light (see Fig. 2.5c). As shown in Fig. 2.5b, the intersection of the probe volume and the volume detected by the receiver forms the measurement volume. Both the transmitter and the receiver are mounted on a traverse mechanism to facilitate the displacement in both axial and radial

directions. The step between two measurement points is set to 10 mm and 2 mm for the axial and the radial measurements, respectively. The measurements cover the zone from very near the stack (i.e. x = -175 mm) to near the right termination of the resonator (i.e. x = 340 mm).

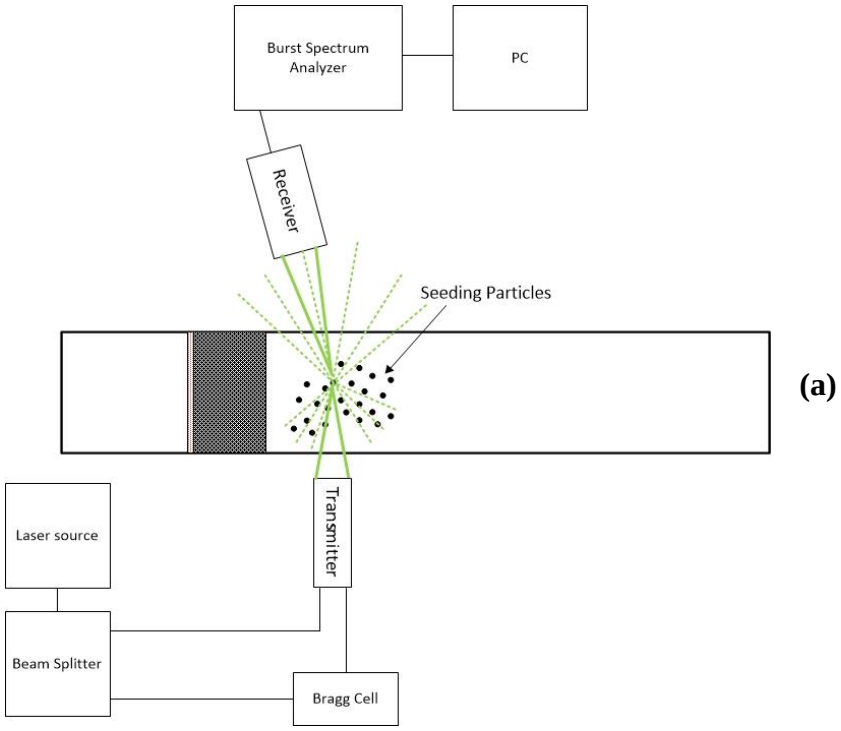

(a)

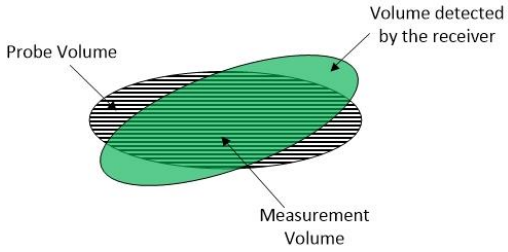

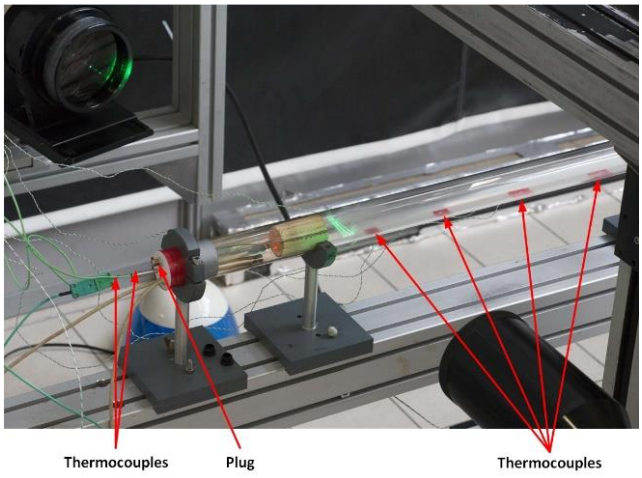

(b) **(c)**

Figure 2.5: (a) A schematic for the LDV measurement setup, (b) The probe volume and measurement volume, and (c) Photo for LDV and temperature measurements setup.

A burst spectrum analyzer (Manufacturer: Dantec Dynamics – Model: BSA-F80) is used to analyze the signal acquired by the LDV receiver. The velocity of any seeding particle crossing the

measurement volume, along with its arrival time are stored on the computer. The processing technique presented in [64] is used to get both the acoustic and the mean velocities.

A typical data set acquired from LDV measurements is shown in Fig. 2.6a. The first step is to remove the outlier data points by setting an upper and lower limits. For instance, the upper and lower limits for data shown in Fig. 2.6a are 5 m/s and -5 m/s so that any data point outside these limits is removed from the data set. The following step is to bring back all the data points into one acoustic cycle by estimating the exact oscillating frequency (see Fig. 2.6b). Then, the data is averaged over a fixed time step (see Fig. 2.6c) and hence the acoustic velocity amplitude can be obtained. Finally, in order to get the mean (streaming) velocity; the data points over the acoustic cycle are averaged. A Matlab code is used to make all the calculations mentioned above (see appendix C.1).

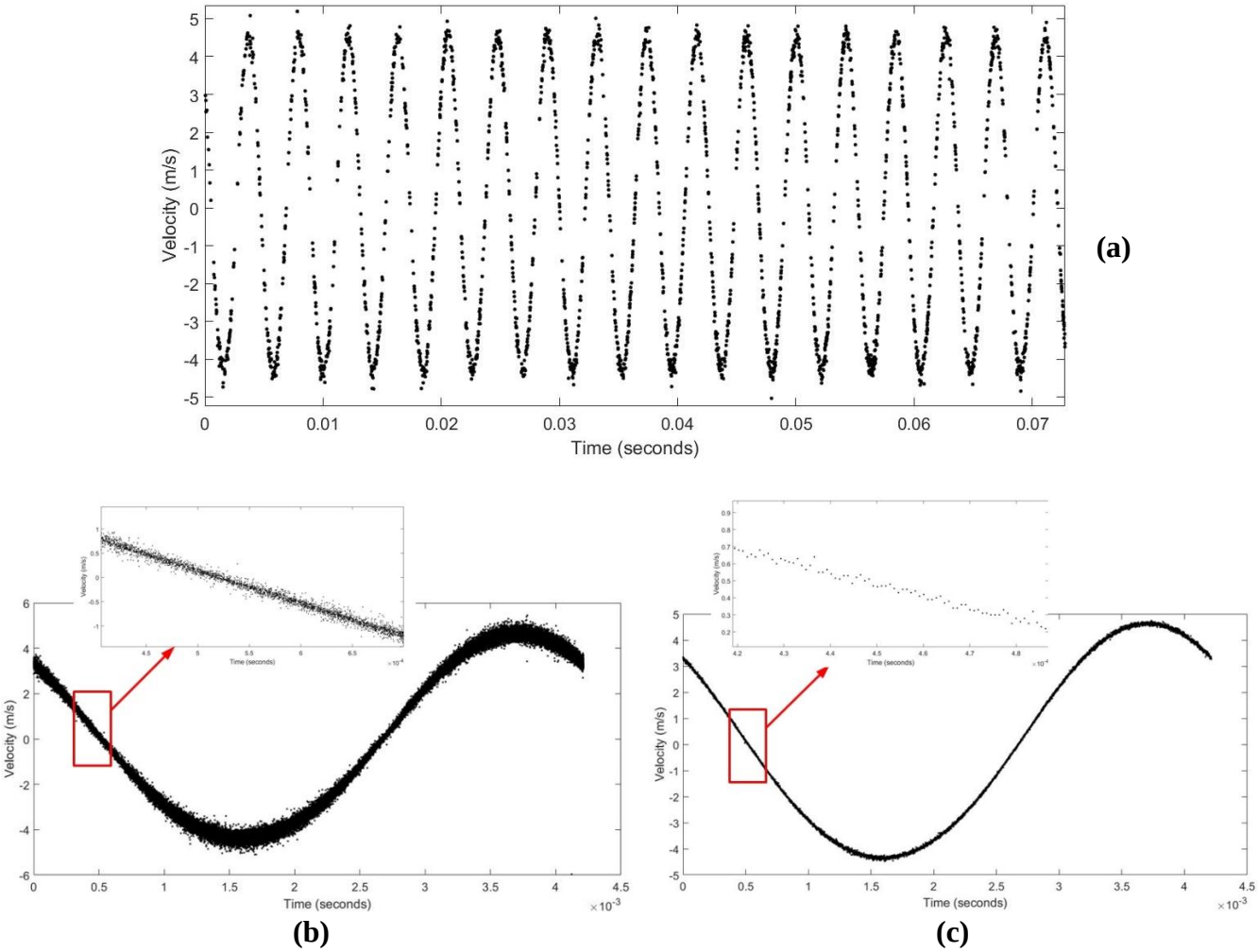

Figure 2.6: (a) A typical data set acquired from LDV, (b) Data points are brought back into one acoustic cycle, and (c) Data points are averaged over a fixed time step.

Preliminary measurements were conducted to determine the number of samples required to reach convergence of the estimation. The deviation from the steady-state value of the mean velocity estimated using 70,000 samples versus the number of samples is plotted for different experiments in Fig. 2.7. The deviation can be estimated as follows:

$$Error = \frac{|U_{mean}(N) - U_{mean}(70{,}000)|}{U_{mean}(70{,}000)} * 100 \quad (2.1)$$

As shown in Fig. 2.7, the deviation from the steady-state value decreases to about 5 % when the number of samples exceeds 35,000 samples. Therefore, it is decided to acquire data until the number of samples reaches 40,000.

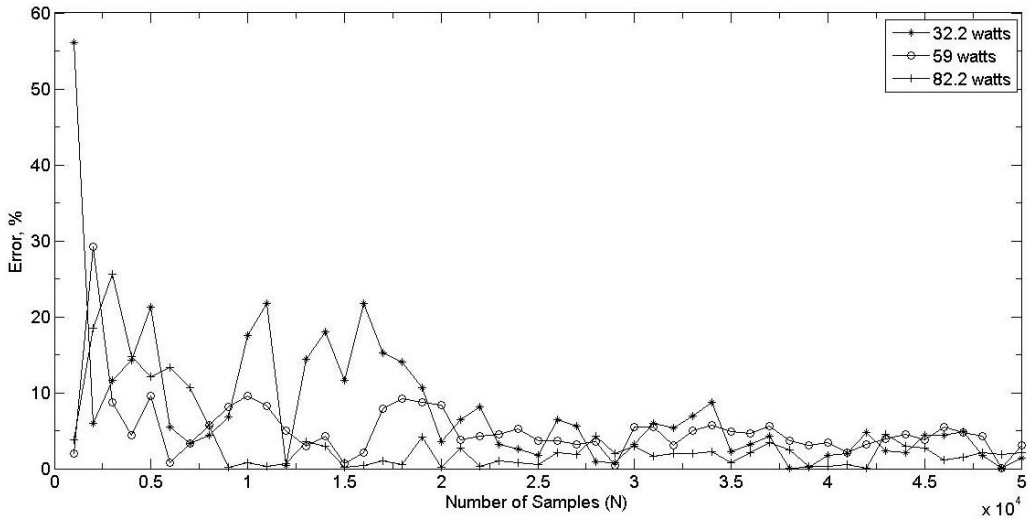

Figure 2.7: The effect of the number of samples on the estimated value of the axial mean velocity at the center of the resonator at three different acoustic levels (x = 180 mm).

2.1.4. PIV measurements and data analysis

To complement the LDV measurements, PIV was also used. PIV was set to provide an overall mapping of the mean flow velocity. Therefore, the comparison with LDV measurements, that offers precise punctual measurements of the whole velocity field, allows one to have quite a complete description of the mean flow structure. A double pulse 120 mJ Nd:YAG laser with maximum repetition rate of 15 Hz is used to illuminate the measurement plane. The images are recorded by two adjacent CMOS cameras (Model: CMC-4000) with 2320 Pixels x 1726 Pixels resolution. A Nikon lens (Model: Sigma 150 mm) is connected to each camera. The PIV system is externally triggered by a TTL signal generated by a lock-in amplifier using the pressure signal from the microphone as a reference signal. A schematic diagram for the PIV system is shown in Fig. 2.8 and more detailed connection diagram can be found in Appendix B.1.

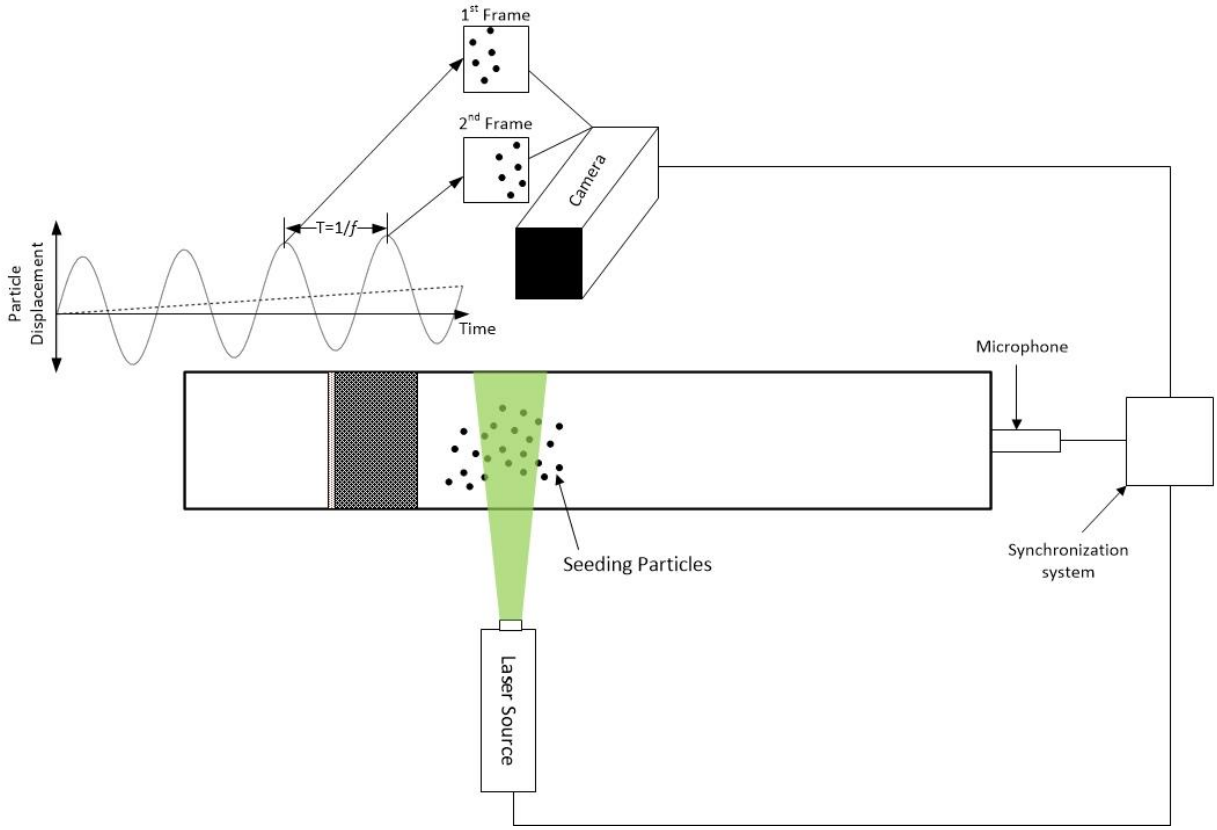

(a)

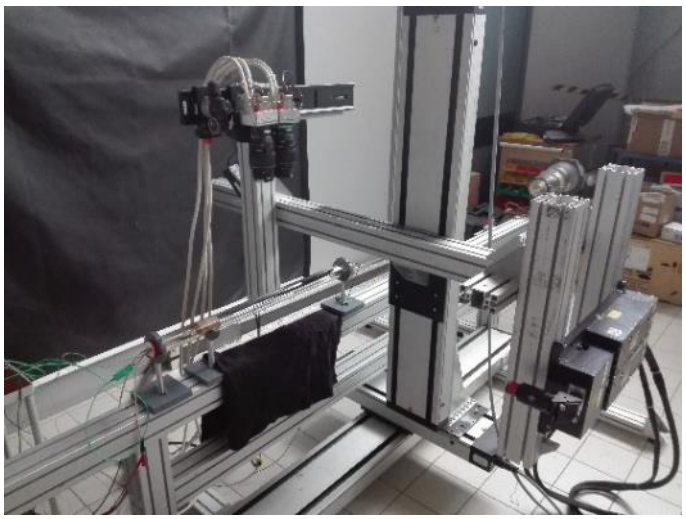

(b)

Figure 2.8: (a) Schematic diagram for PIV measurement system, (b) Photo for PIV measurements setup.

In order to improve the quality of the measurements, the light reflections (from walls and surroundings) are removed before analyzing the acquired images. So, a low-pass filter is applied

to the acquired images in order to get the reflections (see Fig. 2.9b). Then, the reflection images are subtracted from the raw images to get images nearly free from the reflections (see Fig. 2.9c).

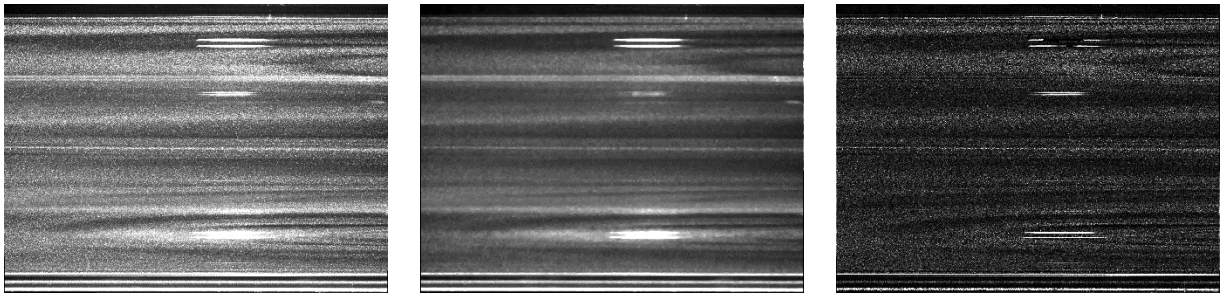

(a) **(b)** **(c)**

Figure 2.9: (a) Typical Raw image, (b) Reflection image obtained by applying low-pass filter, (c) Final image obtained by subtracting (b) from (a).

PIV was set to measure the mean flow velocity only according to the method developed by Nabavi *et al.* [65] as applied in [9]. The principle of this method is to set the time between pulses to the same value as the acoustic period ($T = \frac{1}{f}$) or to multiples of T (see Fig. 2.8a). In this case, the correlation between images provides the particle displacement over the acoustic cycle that is the mean velocity over the acoustic cycle. In our study, we want to scan the mean velocity over several streaming cells but with a good spatial resolution to obtain precise radial profiles of the velocity. Since the field of view of the two cameras is shorter than the length of the associated measurement area, several successive sets of measurements are performed, the laser and camera being moved axially among these sets to cover the whole measurement area; then the collected data are merged to get the distribution of the mean velocity within the whole measurement area.

2.2. **Results and discussion**

2.2.1. Description of the experiments

In this study, seven experiments under different operating conditions, shown in Table 2.1, were conducted. The objective of the first three experiments (1 to 3) is mainly to measure the axial mean velocity distributions in both axial and radial directions in the region from $x = -175\ mm$ to $x = 340\ mm$. These three experiments correspond to different input electric powers and hence different acoustic levels. One goal of our study is also to approach the natural convection flow generated in the system. For this purpose, it was necessary to cease the acoustic waves to avoid the generation of acoustic streaming. So, in the following three experiments (referred to as 4, 5 and 6), the plugs at both ends of the resonator were removed to prevent the acoustic oscillations; hence the measured mean velocity was associated to heat transfer. These experiments were implemented at input electric power similar to the first three experiments (1 to 3). Finally, in order to validate that opening the plugs will not affect the measured convection velocity; the last experiment (7) was conducted with closed plugs but at input electric power just below the critical value associated with the generation of acoustic oscillations. The results of this experiment (7) are to be compared with the results of experiment 4 because they have close heating conditions, though one has "open plugs" while the other has "closed plugs". The precision in the measurements of the electrical input power and the temperatures were estimated and are given in Table 2.1.

Also, the uncertainty in the measurements of both acoustic and mean velocities (partly due to the fact that the mean temperature is not constant throughout the data acquisition) has been estimated by repeating the measurements under the same conditions and calculating the standard deviation of these repeated measurements. The uncertainty in the value of the acoustic velocity were estimated to be ± 1 %, ± 3.5 % and ± 2 % in experiments# 1, 2 and 3, respectively. The uncertainty in the measured mean velocity in experiments# 1, 2 and 3 were found to be ± 12 %, ± 5.8 % and ± 8.5 %, respectively (see appendix F.1).

Table 2.1: The operating conditions for experiments

Exp. #	Electrical input power (Watts)	Re_{NL}	Pressure Amplitude (Pa)	Oscillating Frequency (Hz)	Stack ends temperatures (^{O}C)		Plugs
					$x = -180\ mm$	$x = -240\ mm$	
1	32.2 ± 1%	0.87	820	234	52 ± 9.9%	283 ± 1.5%	Placed
2	59.0 ± 1%	3.59	1950	238	91 ± 5.6%	378 ± 1%	Placed
3	82.2 ± 1%	7.20	2600	241	120 ± 7.4%	457 ± 3.5%	Placed
4	32.2 ± 1%	-	-	-	36.5 ± 2%	282 ± 2%	Removed
5	59.0 ± 1%	-	-	-	46.2 ± 2%	376 ± 2%	Removed
6	82.2 ± 1%	-	-	-	54.6 ± 2%	455 ± 2%	Removed
7	28.1 ± 1%	-	-	-	39 ± 2%	201 ± 2%	Placed

2.2.2. Mean flow velocity at different acoustic levels

Before studying the mean velocity, itself, it was verified that the estimation of acoustic velocity is correct. The distribution of the acoustic velocity amplitude at the center of the resonator along the axis was estimated from LDV measurements. Figure 2.10 shows the distribution of the acoustic velocity amplitude (U) normalized by the value of the acoustic velocity amplitude (A) at the velocity antinode ($i.e.\ x = 0$) for experiments 1 to 3, that is for three different acoustic levels. Also, the results from previous study [9] are plotted on Fig. 2.10 and compared with Exp#3 as it has nearly the same Reynolds number. In [9] Rayleigh streaming in an empty guide of the same diameter as the one used here was studied. The wave pattern was similar to the present case but the wave was generated by loudspeakers at both ends of the resonator. Also, the theoretical distribution given by:

$$U/A = \cos(\frac{\pi x}{l}) \tag{2.2}$$

is depicted in Fig. 2.10. This figure shows that the distributions in all cases correspond to the λ/2 resonance of the guide although there is a little deviation near to the stack. This may be due to the combined effects of both the heat convection [21] and the end-effects [55].

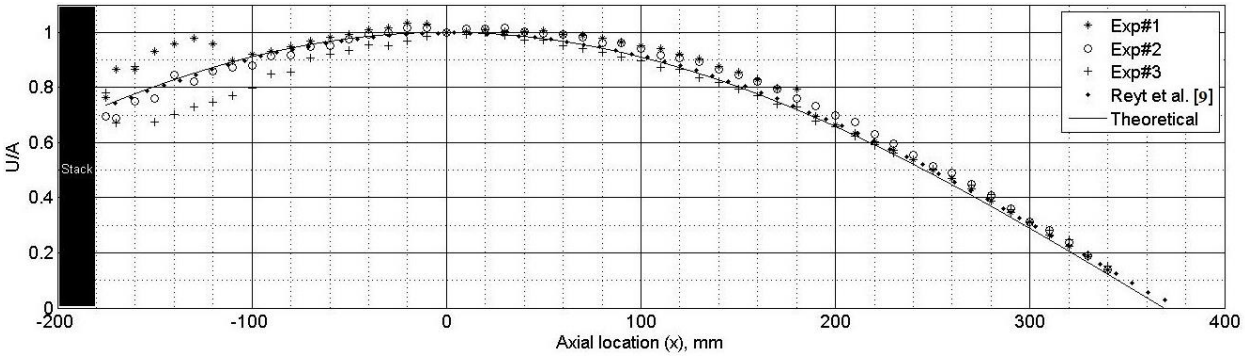

Figure 2.10: Axial acoustic velocity amplitude along the axis of the resonator at different acoustic levels.

Figure 2.11 shows results for the axial mean velocity estimate by LDV and by PIV for experiments 1 to 3, together with results from [9] and theoretical expectation of axial velocity for Rayleigh streaming. The latter, initially developed by Lord Rayleigh [7] for the flow between two parallel plates, is written for the case of a cylindrical tube as follows:

$$U_{Ray}(x,r) = \frac{3A^2}{8c}\sin\left(\frac{2\pi x}{l}\right)\left(1 - 2\left(\frac{r}{R}\right)^2 + \frac{e^{-\psi}}{3}\gamma\right), \tag{2.3a}$$

$$\gamma = \left(2 + \frac{\delta_v}{r}\right)\cos(\psi) + \left(4 + \frac{\delta_v}{r}\right)\sin(\psi) + e^{-\psi}\left(1 + \frac{\delta_v}{2r}\right), \tag{2.3b}$$

Where r is the radial distance measured from the axis of the tube and $\psi = (R + r)/\delta_v$. The mean velocities plotted in Fig. 2.11 were normalized by the value of the amplitude of the Rayleigh

streaming $A_{Ray} = \frac{3A^2}{8c} = U_{Ray}(l/4\ ,0\ )$. Figure 2.11 shows that the streaming pattern can be separated in three different regions. The first region is bounded by the right end of the resonator and the solid-vertical line, the second region extends from the solid-vertical line to the dashed-vertical line and the last region lies between the dashed-vertical line and the right end of the stack.

In the first region, at low acoustic levels (Fig. 2.11a and b), there is a good agreement between the measured axial mean velocity distribution and the theoretical expectations of Rayleigh streaming. At higher acoustic level (Fig. 2.11c), a discrepancy between the measurements and the theoretical expectations is observed. Both results of PIV and LDV measurements agree with results of [9] which allow us to state that the deviation from Rayleigh streaming in this region is due to non-linearity in the acoustic streaming. This is confirmed by results shown by Fig. 2.12 that gives the radial distributions of the axial mean velocity at different axial locations for all acoustic levels. At low acoustic levels (Fig. 2.12a and b), the distribution of the axial mean velocity indeed has a parabolic shape in agreement with the Rayleigh streaming pattern. It should be noted that the bump in the measured velocity profile at x= 275 in Fig. 2.12a is due to a local lack of seeding particles. At higher acoustic level (Fig. 2.12c), the radial distribution shows a deviation from the parabolic pattern that characterizes non-linear Rayleigh streaming as was found by Reyt *et al*. [9]. Color maps for the axial component of the mean velocity (left part of Fig. 2.12) also agree with results of Rayleigh streaming in an empty guide [9].

In the first region, we can therefore conclude that the measured mean velocity is due to acoustic Rayleigh streaming only. The extent of this region can be determined using Fig. 2.11. To determine more accurately this extent, the radial distributions of the measured axial mean velocity at different axial locations in the left half of the resonator are plotted along with the theoretical expectations of Rayleigh streaming. As shown in Fig. 2.13, the measured mean axial velocity distribution agrees with the theoretical expectations up to a certain axial distance and this distance decreases as the acoustic level is increased. This distance limits the end of this region and it was found to be -60 mm, -40 mm and -20 mm for experiments 1, 2 and 3 respectively. Figure 2.14 shows that the maximum increase in the temperature at the left-limit of this region is about 2 ^{O}C. It was checked that the temperature of the rest of this region is almost constant and equal to the ambient temperature; therefore, this region is further called the “cold streaming region”.

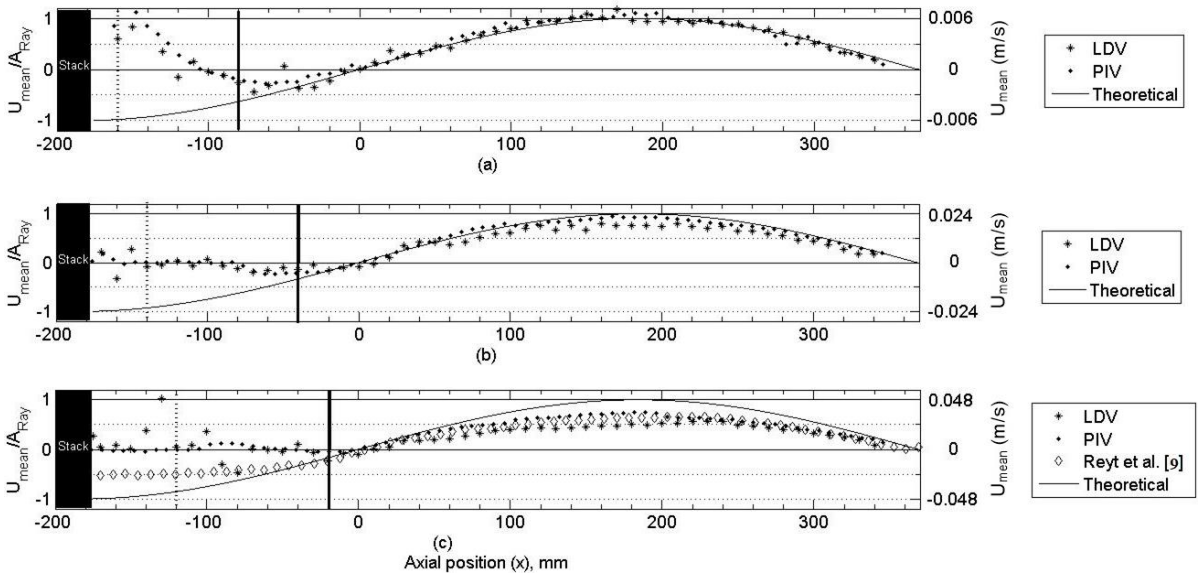

Figure 2.11: Axial mean velocity normalized by Rayleigh streaming velocity amplitude along the axis of the guide at different acoustic levels (a) Exp# 1, (b) Exp# 2 and (c) Exp# 3.

The part of the resonator closer to the stack, in which the mean flow pattern differs from Rayleigh streaming expectation for reasons other than high amplitudes affects, can be further divided in two regions, based on the literature on end effects and especially on [17]. Flow disturbances generated at the end of a thermoacoustic stack have been the subject of several studies (e.g., [55] and [56]) that generally investigated the end effects region from the point of view of acoustics, determining the distance over which the acoustic velocity is affected by the flow disturbances generated near to the stack ends. However, the dissymmetry of oscillating flow going out of and in a constriction, is associated to the generation of a mean flow - known as "jet-driven streaming" - so that we can expect that close to the stack the measured mean velocity (partly) results from end effects. In order to set the limit between the associated "end-effects region" close to stack and the "hot streaming region" results of a previous study [17], that ranges the distance over which the mean velocity is modified by introducing a stack, are used. In [17] a stack similar to the one used in the present study was set in a guide of the same diameter as the present one. The stack was kept at ambient temperature; the wave being generated at a frequency of 88 Hz by loudspeakers. LDV measurements showed that placing a stack in the resonator locally modifies the streaming pattern. This modification depends on the position of the stack in the streaming pattern and on the acoustic amplitude, the distance over which the streaming pattern is modified being almost proportional to the particle displacement amplitude. To estimate the right-limit of the "end-effects region" for case #2 (vertical dotted line in Fig. 2.11b), we used the fact that in [17], for $Re_{NL} = 4$, the streaming pattern was modified over a distance of 12 times the particle displacement amplitudes from the stack end. For a 238 Hz working frequency at similar Re_{NL} the right-limit of the "end-effects region" should be 4cm from the stack end. Then the limits for experiments #1 and #3 are set by using the proportionality to particle displacement amplitude.

In the second region, the measured mean velocity differs from the theoretical expectations of Rayleigh streaming. The objective of the next subsection is to investigate the contribution of natural convection in the mean velocity measurements conducted in this “hot streaming region”.

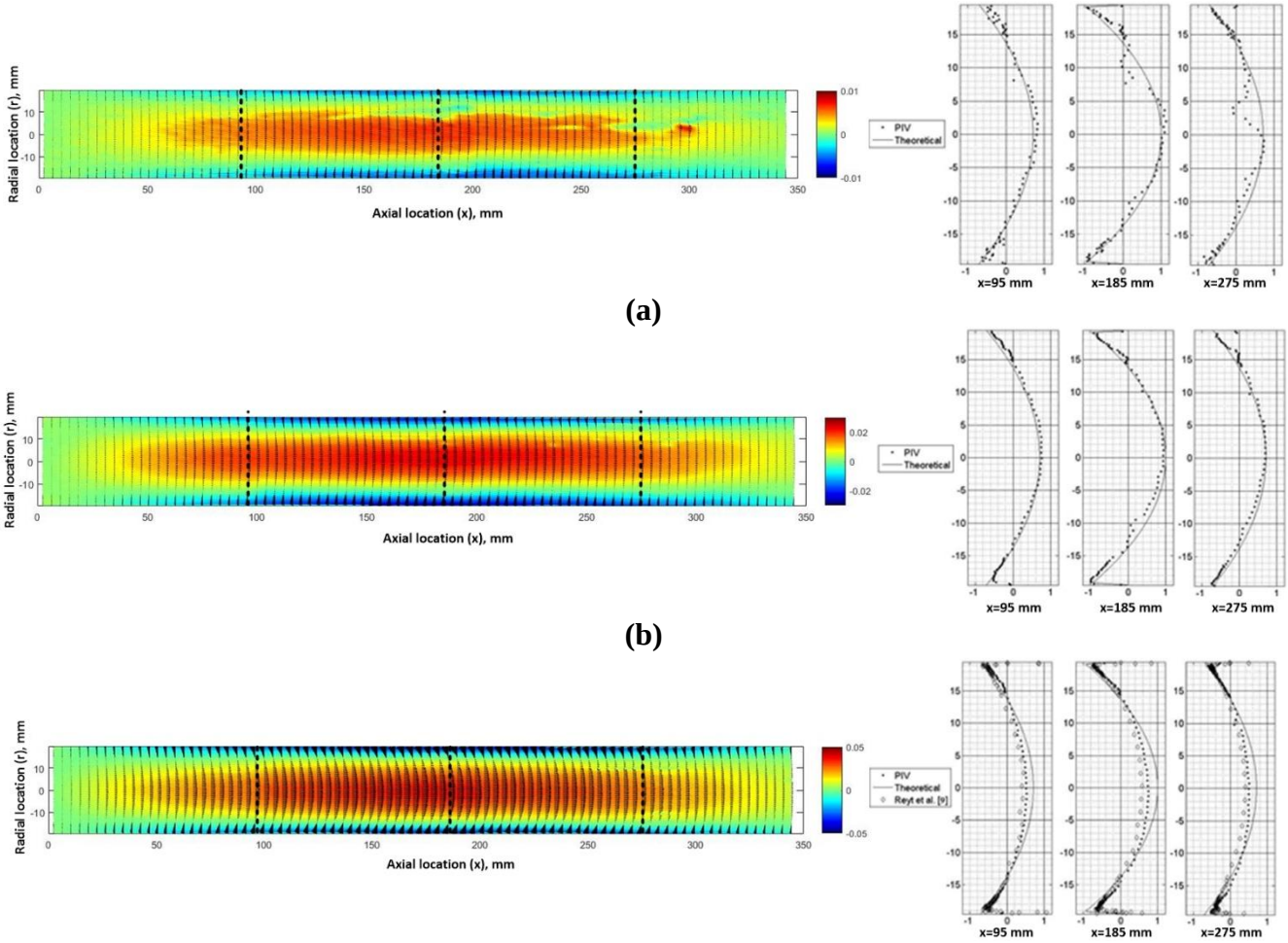

Figure 2.12: Left: Vector map of the streaming velocity and normalized color map of the axial component of the streaming velocity. Right: Radial distributions of the axial streaming velocity measured by PIV at different experimental conditions (a) Exp# 1, (b) Exp# 2 and (c) Exp# 3.

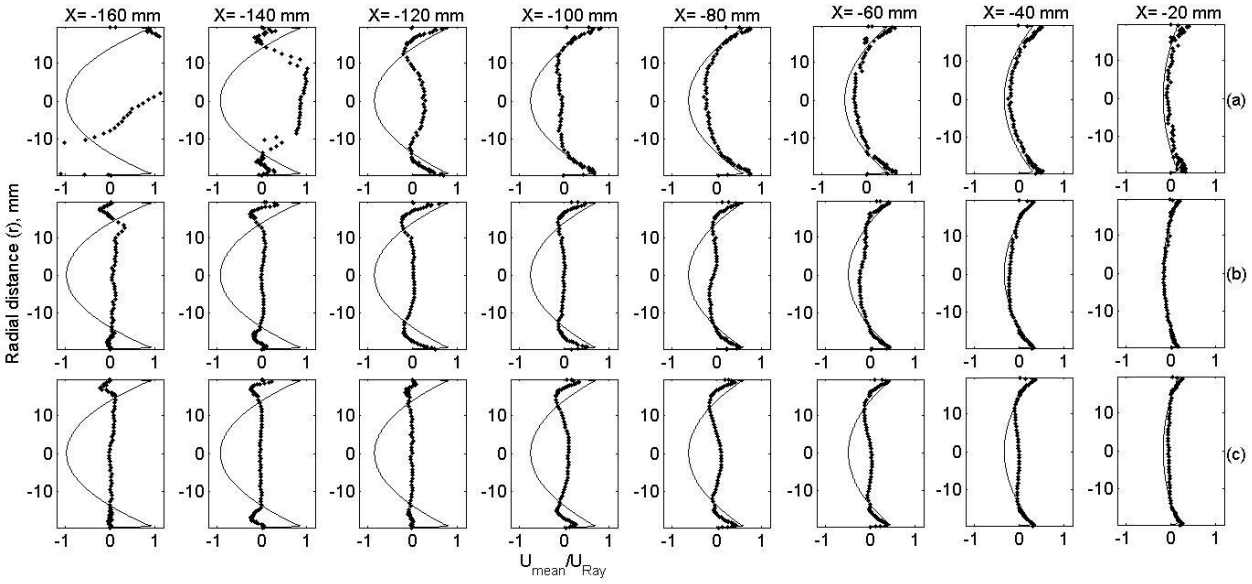

Figure 2.13: Radial distribution of the axial mean velocity obtained by PIV at different axial locations and at different experimental conditions: (a) Exp# 1, (b) Exp# 2 and (c) Exp# 3.

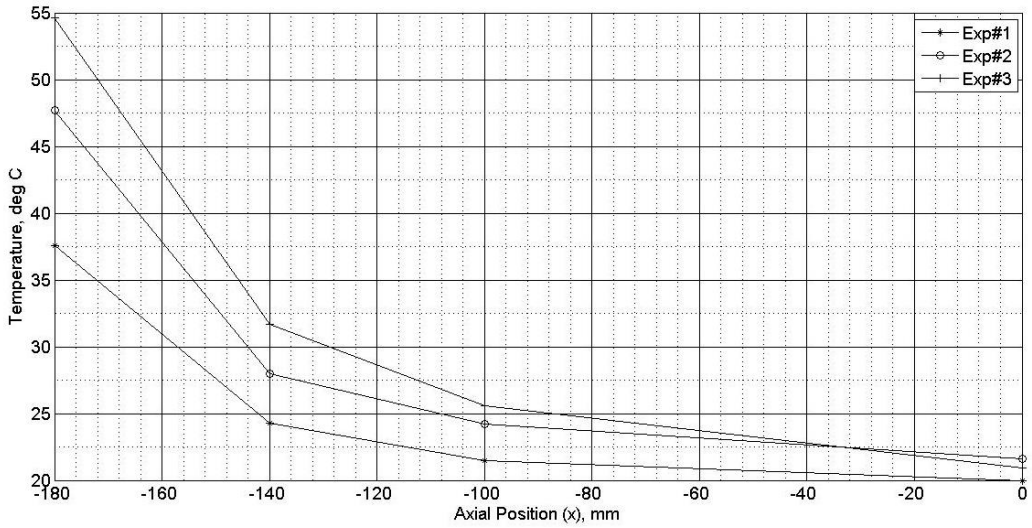

Figure 2.14: The axial distribution of the outside wall temperature at different input electric powers.

2.2.3. Natural convection velocity at different input electric powers

As explained in the previous section, the measured mean velocity in both the "hot streaming region" and the "end-effects region" does not agree with the theoretical expectations. In the present study, we want to show that one reason for this disagreement is the axial temperature distribution along with the non-uniform temperature distribution over the cross section of the resonator that is associated with natural convection and thus, with the generation of a mean flow that is further

called the "natural convection" flow. As a first approach to quantify the importance of the natural convection flow (due to buoyancy force) in the present study, the natural convection flow in a horizontal cavity with different end temperatures [66] is considered. The aim of this approach is to answer to the question: does natural convection induce a significant flow for temperature distributions encountered in our set up? Therefore, neither acoustics not streaming flow are described here. The equivalent horizontal cavity is bounded on one side by the cold end of the stack and on the other side by the right termination of the duct. In such cavity, the non-dimensional momentum equation in the radial direction can be written as following [66]:

$$u\frac{\partial \mathrm{v}}{\partial x} + v\frac{\partial \mathrm{v}}{\partial r} = -\mathrm{Pr}\frac{\partial P}{\partial r} + Gr + \mathrm{Pr}\left(\frac{\partial^2 \mathrm{v}}{\partial^2 x} + \frac{\partial^2 \mathrm{v}}{\partial^2 r}\right) \tag{2.4}$$

where Pr is Prandtl number and Gr is Grashof number:

$$Gr = \frac{8g\beta(T_{avg} - T_\infty)R^3}{\nu^2} \tag{2.5}$$

where g is the gravitational acceleration, β is the expansion coefficient of air at ambient conditions, T_{avg} is the average temperature of the cold side of the stack (shown in Fig. 2.16) and T_∞ is the ambient temperature. The estimated value of the Grashof number in all experiments (see Fig. 2.16) is much larger than unity that indicates the buoyancy has a crucial role in setting the distribution of the mean flow in the "hot streaming" region.

In order to experimentally determine the contribution of the natural convection flow to the measured mean flow velocity in the engine, it is necessary to decouple the natural convection flow field and the acoustic streaming field. To get the natural convection velocity field only, the acoustic oscillations should be stopped while the input electric power is supplied to the heater for heating purposes. This is achieved by removing the plugs at both ends of the resonator to cease the oscillations. The associated experiments are numbered 4, 5 and 6 (see Table 2.1).

In order to validate the approach of removing the plugs to cease the acoustic oscillations, the results of both experiments 4 (plugs off) and 7 (plugs on) are compared. As shown in Fig. 2.15, the measured mean velocities of experiments 4 and 7 are quite similar, revealing that removing plugs does not affect the generation of a natural convection flow. Figure 2.15 also shows that the mean velocity for experiments 4 to 7 (that are without sound generation) is almost zero in the cold streaming region. This can be seen as the reason for the good agreement previously discussed between the measured mean velocity and the Rayleigh streaming expectations in this region. Away from the cold steaming region, it is observed that the magnitude of the mean velocity globally increases as the wall temperature gradient increases (see Fig. 2.14).

Figure 2.15 shows that the natural convection flow velocity decreases as it approaches the stack, which partially blocks the flow. Figure 2.16 gives results of wall temperature measurements for different positions along the guide circumference and for different axial positions. It reveals that the temperature is not uniform over the section of the guide and that the temperature non-

uniformity increases as the stack is approached. This non-uniformity along with the temperature increase can be considered as the origin of the free convection flow.

The natural convection velocity can be roughly estimated to linearly increase over the hot streaming region. Comparing Fig. 2.11 and Fig. 2.15 then it appears that the axial evolution of the natural convection velocity is roughly similar to the expected Rayleigh streaming over this region but with opposite sign ($3A^2/8c$ is equal to 0.025 m/s for Exp #2). Hence, it can be inferred that the nearly zero measured mean velocity given by Fig. 2.11 in the hot streaming region is, qualitatively, the superposition of the Rayleigh streaming expectations and of the free convection velocity distribution given by Fig. 2.15. However, quantitative analysis cannot be provided as the temperature distributions in the sets (1 to 3) are quite different from the ones for sets (4 to 6). As shown in Fig. 2.16, the measured temperatures when the acoustic oscillations are ceased (Exp# 4 to 6) have much lower values than in the cases where the acoustic oscillations exist (Exp# 1 to 3). The reason for this is the thermoacoustic heat pumping: Acoustic oscillations carry heat from the hot side of the stack to its cold side and hence the temperature of the fluid close to the cold side of the stack is higher when the engine is running (Exp# 1 to 3).

Figure 2.17 shows the vector map of mean velocity for Exp. #4 and #5 together with the color map for the axial mean velocity (left part) and the radial distribution of the axial mean velocity at $x = -120\ mm$. This figure shows the structure of the free convection flow. The maximum velocity is observed at the center of the duct and there is a reverse flow near to the walls. This may refer to the existence of a vortex; however, the radial distributions (right part of the figure) show that the cross-sectional average is not zero, meaning that the vortex is not a complete one.

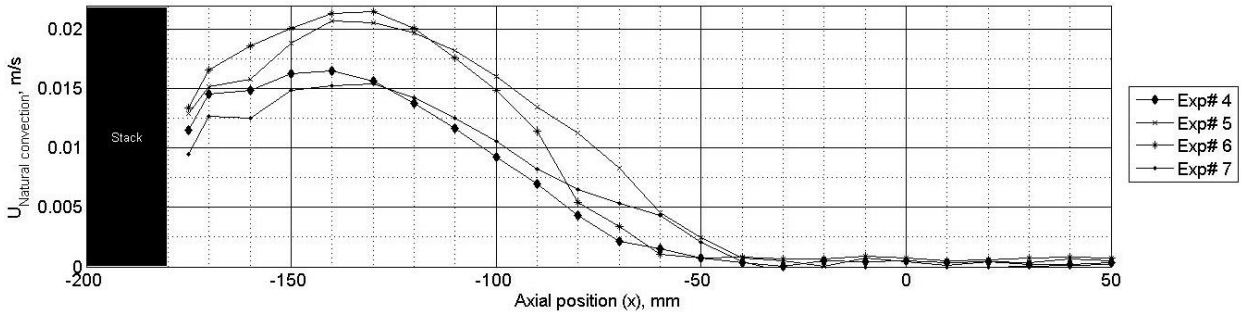

Figure 2.15: Natural convection velocity (mean velocity with no sound) measured along the axis of the resonator for different experimental conditions.

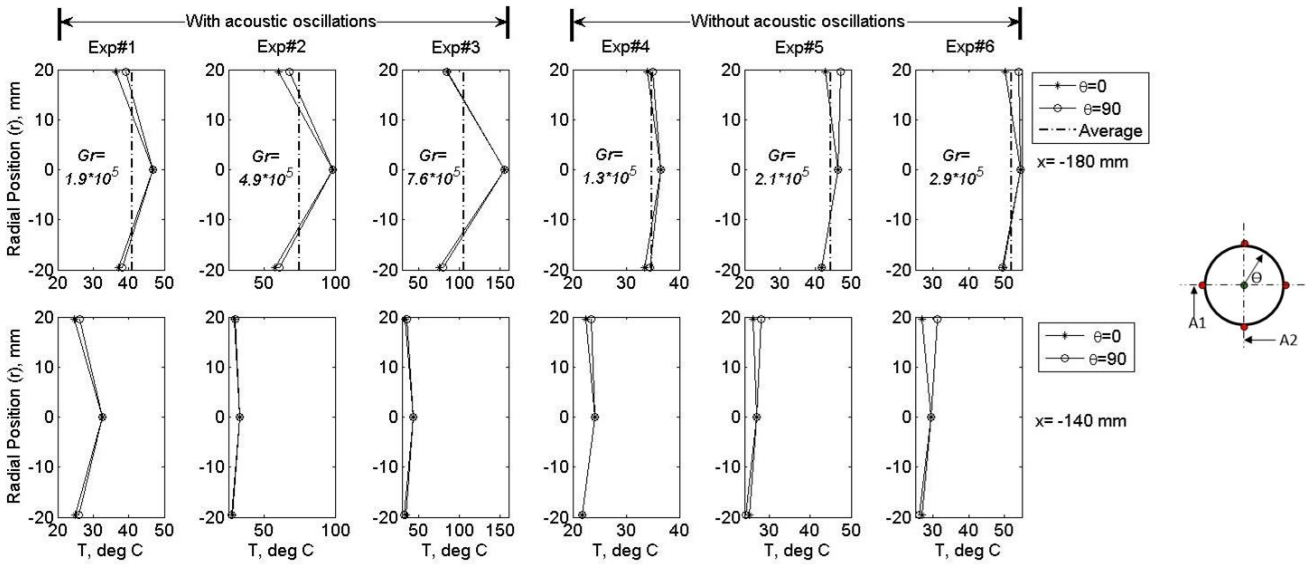

Figure 2.16: Radial temperature distribution along the two perpendicular axes A1 and A2 ($\theta = 0$ *and* 90 deg) at two different axial locations (x=-180mm top and x=-140mm bottom) for experiments #1 to 6.

The vortex observed is not axisymmetric and the measurement plane is not the most appropriate to approach its structure. The observed discontinuity is due to the fact that the natural convection flow is driven by buoyancy and hence the complete vortex could be observed in a plane perpendicular to the measurement plane (i.e. parallel to the ground). However, performing measurements in that plane was not feasible with the current facility. Therefore, Fig. 2.17 depicts a cross section in the natural convection vortex in the measurement plane.

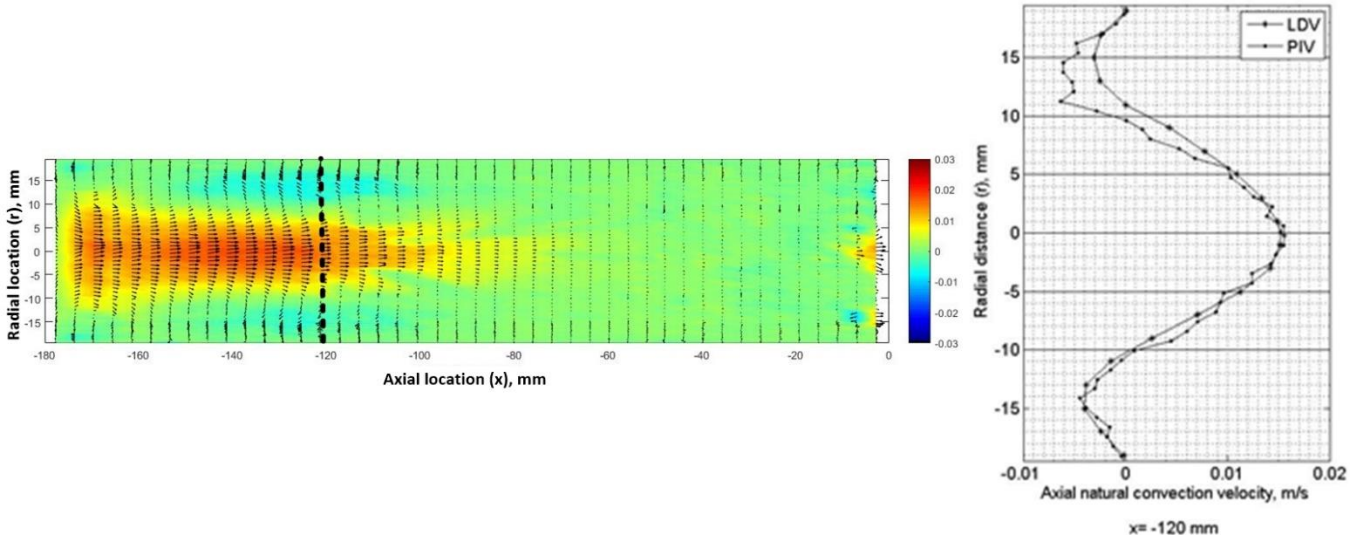

(a)

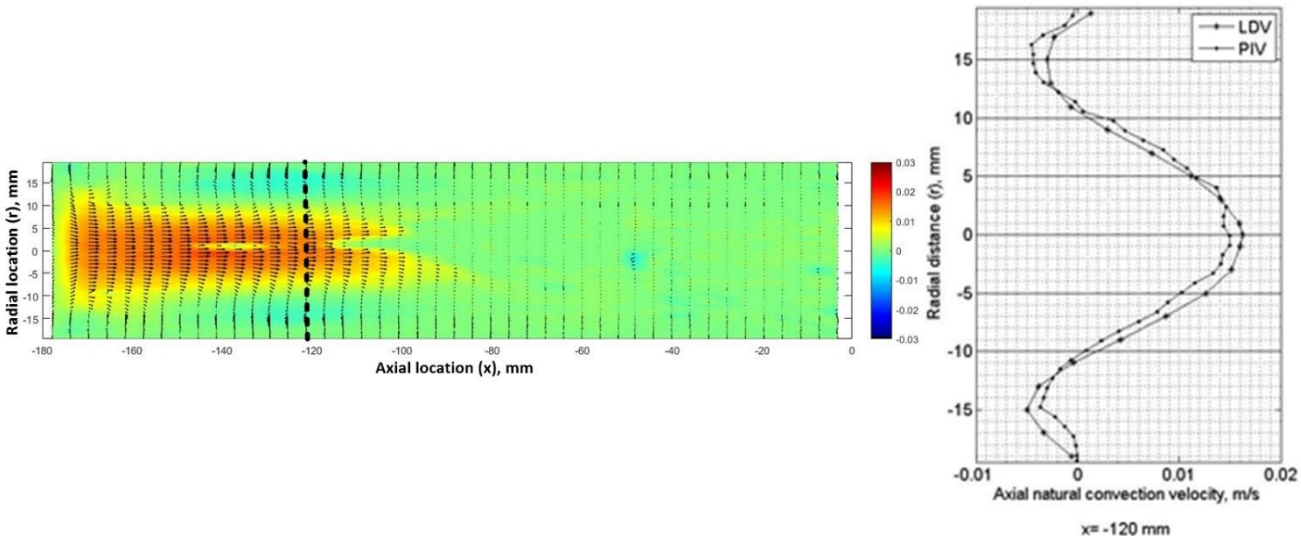

(b)

Figure 2.17: Left: Vector map of the natural convection velocity together with color map of the axial component of the natural convection velocity, right: Radial distributions of the axial natural convection velocity at $x = -120$ mm for different experimental conditions (a) Exp# 4 and (b) Exp# 5.

2.3. **Conclusions**

The effects of both the natural convection and the end-effects on the Rayleigh streaming pattern in a simple standing-wave thermoacoustic engine was investigated experimentally. The axial mean velocity field over the resonator was measured for different acoustic levels. The results reveal that the mean velocity pattern changes over three different regions, namely the cold streaming region, the hot streaming region and the end-effects region. In the cold streaming region, the measured axial mean velocity agrees with the theoretical expectations of Rayleigh streaming at low acoustic level, whereas it deviates from theoretical expectations as the acoustic level is increased due to high amplitude effects, which agrees with the literature. Also, measurements performed when the engine is turned off showed that the natural convection velocity is almost zero over this region, explaining the reason for agreement between the measured mean velocity and the theoretical expectations of Rayleigh streaming. In the hot streaming region, the measured mean velocity disagrees with Rayleigh streaming expectation. Measurements performed when the engine is turned off showed that one reason for this disagreement is the non-uniformity of the temperature over the cross section, generating a natural convection flow that superimposes the acoustic streaming. In the last region, the measurements do not agree with the theoretical expectations due to the combined effect of both natural convection and end-effects at the exit of the stack.

Finally, this study shows that in a simple engine, such as the one under study, for which the radial distribution of the temperature is not uniform, the mean velocity results not only from acoustic streaming (Rayleigh and jet-driven streaming) but also from natural convection.

2.4. **Recommendations for future work**

As mentioned above, it is believed that the effects of the natural convection on the mean flow distribution inside a thermoacoustic engine is a three-directional problem. In the current study, the effects of the natural convection were investigated as a two-dimensional problem (due to some limitations in the used facility) so that further investigations are required to complement the findings of the current work.

As the natural convection phenomenon is driven by the buoyancy force and hence gravity plays a role in the natural convection flow, the tilting of the engine (between horizontal and vertical positions) will change the pattern of the natural convection flow inside the thermoacoustic engine. Therefore, it is important to investigate the effects of the different positions on the convection flow pattern.

Chapter 3: Transition to Turbulence in Oscillating Flow

As mentioned in the introduction section, this chapter discusses the transition to turbulence in the oscillating flow at sub-acoustic and acoustic frequency ranges. The following subsections discuss the experimental setup, measurement techniques and signal processing tools used in this part of the study. Also, the results are discussed and conclusions are drawn by the end of the chapter.

3.1. Experimental Setup

As mentioned previously in the introduction section, the main objectives of this part of the study are to validate the using of the PIV tool in studying the transition to turbulence of an oscillating flow at sub-acoustic (i.e. <20 Hz) frequency range and to extend the work to the acoustic frequency range (i.e. >20 Hz). Therefore, the experimental setup is designed to generate an oscillating flow for two different frequency ranges (i.e. sub-acoustic and acoustic). For the sub-acoustic frequency range, a mechanical system (i.e. Scotch-yoke mechanism) is utilized to generate an oscillating flow with frequencies ranged from 0.5 Hz to 1.5 Hz that correspond to Womersely numbers (α) of 7.1 and 12.3, respectively. As for the acoustic frequency range, an electromechanical system (i.e. acoustic loudspeakers) is used to generate an oscillating flow at the resonance frequency of the system to achieve high velocity amplitudes. DeltaEc codes for both systems are built to predict the range of Reynolds numbers (Re_δ) that can be achieved by each system. It is found that the Reynolds number varies from 140 to 607 and from 200 to 630 for the system driven by the Scotch-yoke mechanism (see appendix A.2) and by the speakers (see appendix A.3), respectively. However, the actual measured ranges of the Reynolds number varies from 140 to 510 and from 205 to 466 for the Scotch-yoke's system and the speakers' system, respectively. The discrepancy between the measured and the predicted values is mainly due to the inability of the DeltaEc code to model the non-linear losses generated at high velocity amplitudes.

In the following subsections, each part in the experimental setup will be explained in details.

3.1.1. Driving mechanism of the oscillating flow

3.1.1.A. Scotch Yoke Mechanism

To generate an oscillating flow with very low frequencies (i.e. up to 2 Hz), it was not feasible to use speakers because they have very limited displacement amplitude and hence, at very low frequencies, they will not generate high enough velocity amplitudes to achieve turbulent flow. So, a mechanical system is used to generate the oscillating with low frequencies and large displacement amplitudes. There are two common mechanical mechanisms for generating the oscillating flow namely the crank-slider mechanism and Scotch Yoke mechanism. Merkli and Thomann [30] stated that Scotch Yoke mechanism is nearly free of harmonics comparing with the crank-slider mechanism. Hence, in the current work a Scotch Yoke mechanism is built. The Scotch Yoke mechanism is used to convert the rotary motion to a linear motion and vice versa. In this setup, the Scotch Yoke mechanism is driven by 4 Kw AC-electric motor (Manufacturer: ELMA-TROYAN, Model: T 132MA 6 B3). The rated rotational speed of this motor was selected to be

low (i.e. 960 rpm) in order to achieve high torque at low speeds which will enable us to work at very low frequencies (i.e. down to 0.3 Hz).

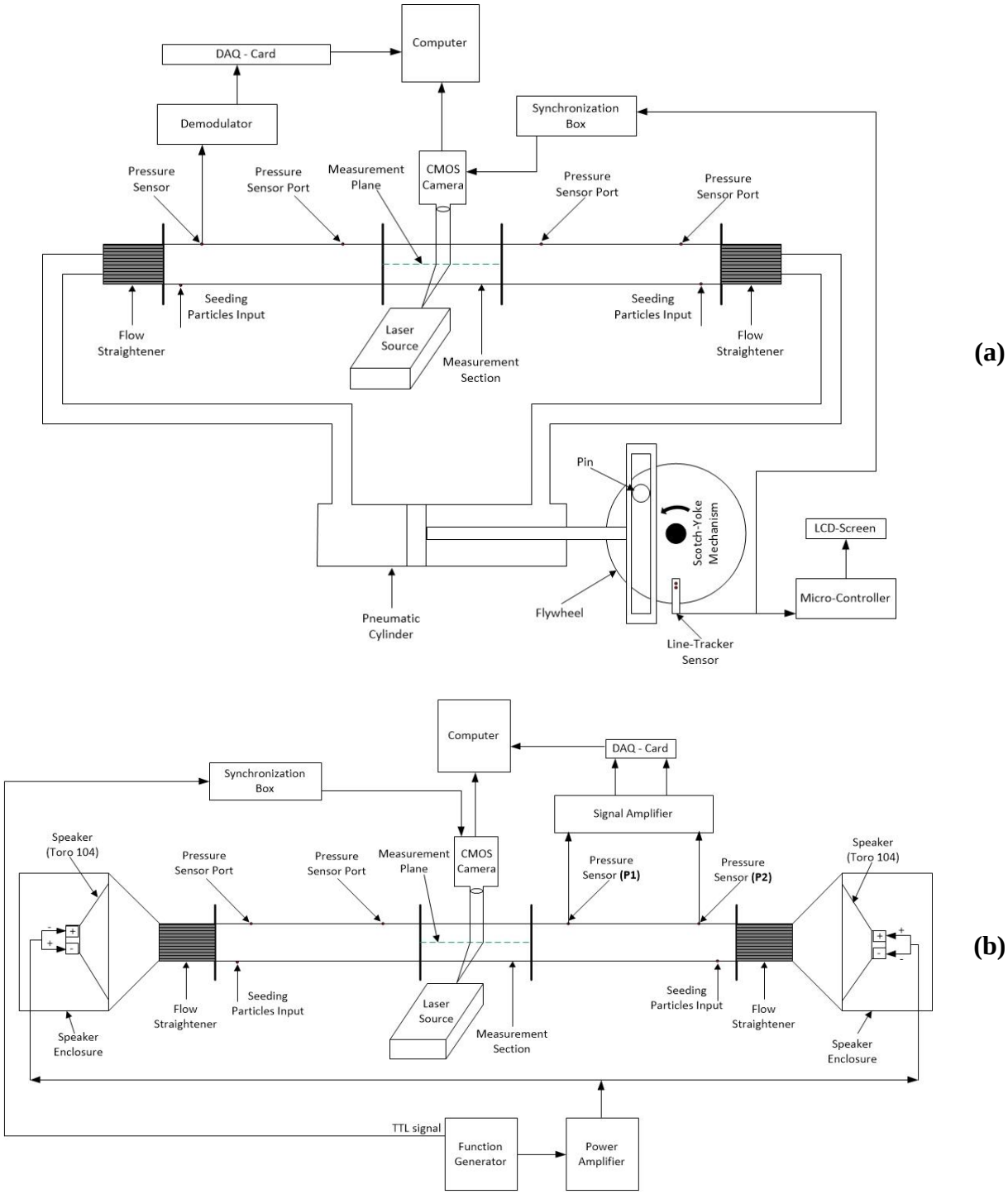

Figure 3.1: Schematics for the experimental setup including the measurement systems: (a) Oscillating flow is generated by Scotch-yoke mechanism, (b) Oscillating flow is generated by two opposite speakers. Appendices B.2 and B.3 present the exact connection diagrams for both experimental setups. Images for both systems are presented in appendix D.1 and D.2.

The frequency of this motor is governed by a variable speed driver (Manufacturer: Schneider-Electric, Model: ATV312HU40N4). A pneumatic piston-cylinder assembly (Manufacturer: JELPC, Model: S125X300) is connected to the mechanism in order to generate the oscillating flow inside the resonator. The pneumatic cylinder has a piston with diameter of 125 mm and the stroke limit of 300 mm. This cylinder has two gas inlets/outlets each is ½ inch in diameter. Each of these inlets/outlets are connected to one end of the resonator through 1500 mm flexible pipe with diameter of 1 inch. In addition, the piston displacement amplitude can by changed from 35 mm to 100 mm through changing the pin location in the flywheel. The mechanical drawings of different parts of the mechanism are presented in appendix D.7.

3.1.1.B. Loudspeakers

To generate an oscillating flow with a frequency above the acoustic frequency limit (i.e. >20Hz), the scotch Yoke mechanism was not suitable in that case as the maximum rotational speed of the electric motor is 16 Hz. Hence, two opposite powerful speakers (Massive Toro-104, maximum power rating of each is 1200 watts) were utilized for that purpose. To achieve maximum velocity amplitude at the center of the resonator (i.e. velocity antinode and dynamic pressure node), the electric poles of one of the speakers is reversed (see appendix B.3). By reversing the poles of one of the speakers, the speakers (in such configuration, 180^{O} out of phase) will move in the same direction achieving maximum velocity amplitude at the center of the resonator. To harvest the maximum possible velocity amplitude, the speakers are operated at the resonance frequency. To specify the resonance frequency of the system, the dynamic pressure (at the location P2, see Fig. 3.1b) is recoded over a certain frequency range. As shown in Fig. 3.2, the dynamic pressure peaks at frequency of 23.3 Hz. It is worthwhile to mention that the discrepancy between the measured dynamic pressure, near the resonance frequency, and the value of the numerical simulation is mainly due to the assumptions of the linear theory [1] used in DeltaEc which are not valid at high pressure amplitudes. Hence, the values of the numerical simulation agree well with the measured values at low pressure amplitudes (i.e. away from the resonance frequency).

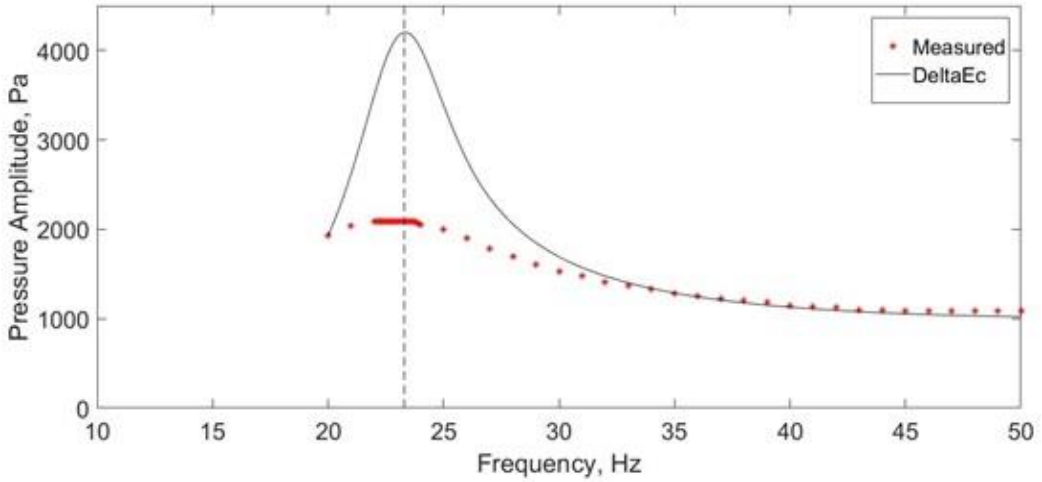

Figure 3.2: The variation of the dynamic pressure (at location **P2**) with the operating frequency.

3.1.2. Resonator

The resonator is made of 1900 mm stainless steel tube with square cross section (the outer and inner side lengths of the square are 50 mm and 44 mm, respectively). At the middle of the resonator, 500 mm of the stainless steel tube is replaced by a glass tube to grant an optical access for the PIV measurements. Also, at both ends of the resonator; flow straighteners are inserted in order to suppress any disturbances created due to the end effects. The flow straightener is made of 100 CPSI (cell per square inch) ceramic stack and has length of 25 mm. Also, Gerrard and Hughes [67] postulate that the flow turns to be fully developed at length $(L) = 0.03 * D * Re_{\delta}$. Based on the literature, the flow is considered to be laminar till $Re_{\delta} = 500$ and thus the maximum development length required is 660 mm; accordingly, the measurement section (i.e. glass tube) is placed 700 mm away from the both ends of the resonator. In addition, four threaded holes are made in the resonator to facilitate the pressure measurements. The locations of these holes are 100 mm, 600 mm, 1300 mm and 1800 mm away from one end of the resonator. Also, two threaded holes are drilled at distances of 50 mm and 1850 mm to feed seeding particles through one of them.

3.2. Measurement systems

3.2.1. Dynamic pressure measurements

The dynamic pressure measurements were implemented mainly to verify that the systems used to generate oscillating flow are working properly (i.e. produce pure sine-wave with minimum harmonics). Since there are two different systems used to generate the oscillating flow at different frequency ranges, two different pressure measurement techniques are used to monitor the pressure oscillations. The techniques are described in the following subsections.

3.2.1.A. Low-frequency pressure measurement

At very low frequencies, the system operates away from the resonance frequency and hence the produced dynamic pressure is too low. So, a reluctance pressure sensor is used for measuring the oscillating pressure. The reluctance pressure sensor (Manufacturer: Validyne – Model: D45) is connected to a demodulator (Manufacturer: Validyne – Model: CD15) that amplifies and interprets the signal of the pressure sensor. The output signal from the demodulator is fed to a data acquisition card to be stored and analyzed via the computer. A flexible tube is used to connect between the pressure port in the resonator and the positive port of the pressure sensor. As shown in Fig. 3.3a, the pressure signal in the positive part of the cycle exhibits a sinusoidal behavior whereas the negative part is deformed. The reason for this deformation is the positive port of the sensor can measure only pressures higher than the mean pressure (atmospheric pressure in this study) while the negative pressures are not measured properly. Also, to make sure that this explanation is correct, the pressure port in the resonator is connected to the negative port of the sensor. As shown in Fig. 3.3b, the measurements show that same deformation observed in Fig. 3.3a but with the positive part. So, to overcome this problem, the pressure port in the resonator is always connected to the positive port of the sensor and the positive part of the measurements is only considered and the negative part is a mirror for the positive part.

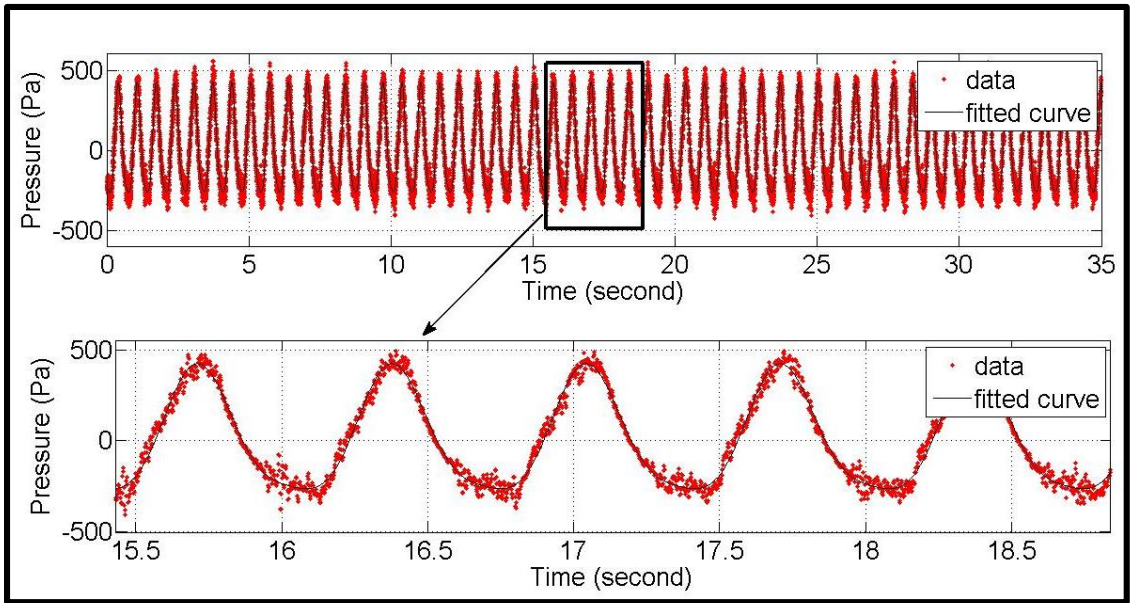

(a)

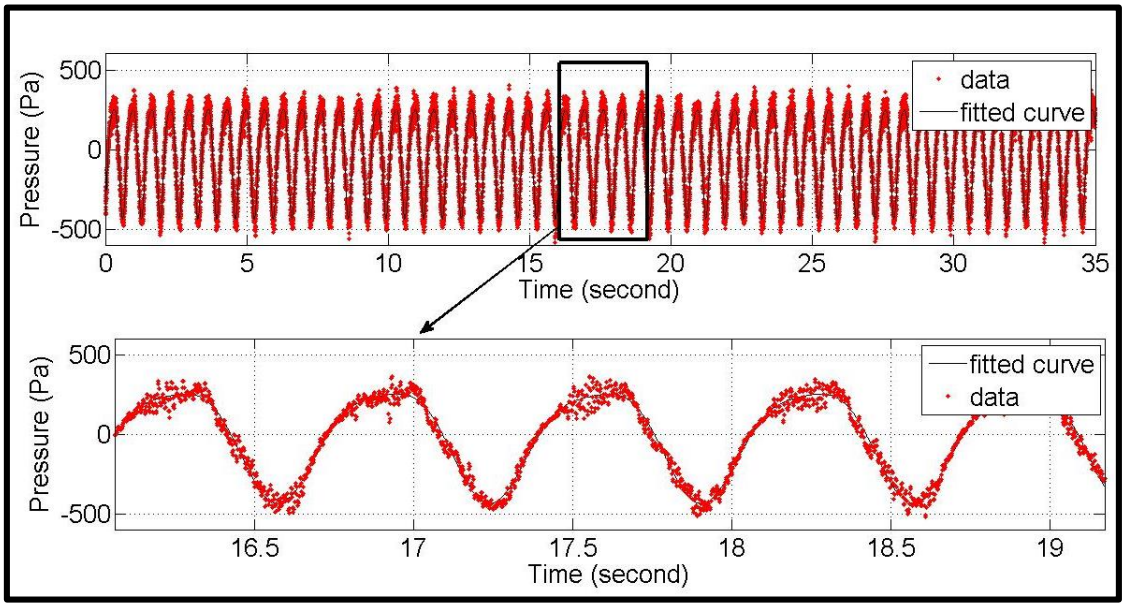

(b)

Figure 3.3:The pressure signal of the oscillating flow with frequency of 1.5 Hz when the pressure port in the resonator is connected to (a) the positive port in the pressure sensor and (b) the negative port in the pressure sensor.

The pressure measurements were conducted at three different amplitudes at the same frequency (0.5 Hz). As shown in Fig. 3.4, the pressure measurements show a sinusoidal behavior for all amplitudes. Also, an FFT analysis is performed for the pressure signals to observe the frequency content and investigate the harmonics generated in the flow. The matlab code used to perform the FFT analysis is presented in appendix C.2. As shown in Fig. 3.4, the value of the spectral density

has a peak value at the oscillating frequency while the amplitude of the spectral density at the 1st harmonic frequency is much smaller than the value at the oscillating frequency which reveals that the contribution of the harmonics to the signal is null.

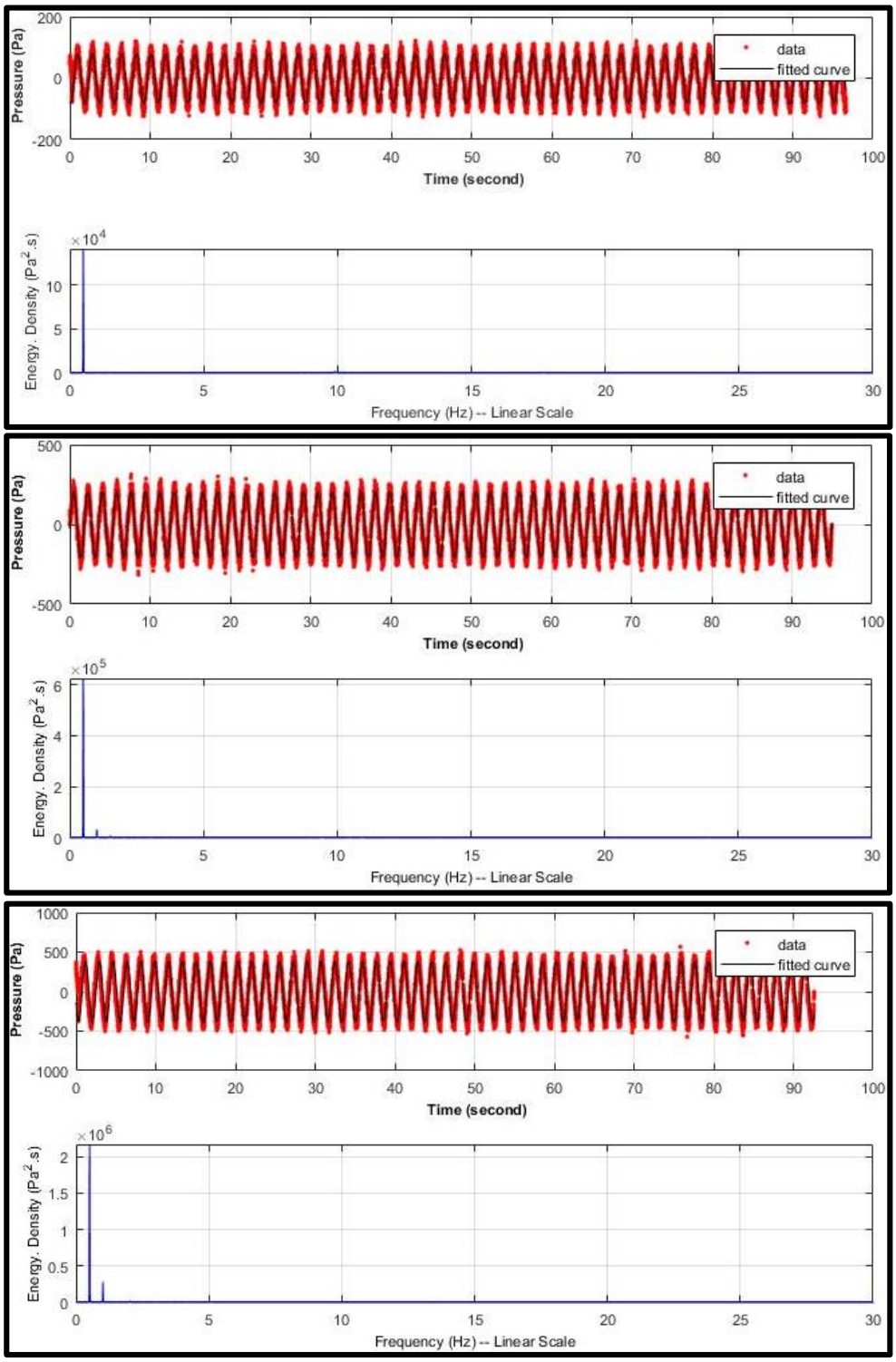

Figure 3.4: The pressure signal and spectral density of the pressure signal at oscillating frequency of 0.5 Hz and at three different pressure amplitudes: (a) 100 pa, (b) 200 pa and (c) 450 pa.

3.2.1.B. High-frequency pressure measurements

At the acoustic frequency range, the system operates at the resonance frequency and hence it produces high dynamic pressure amplitudes. So, a piezo-resistive pressure transducer is used to measure the dynamic pressure. The microphone is connected to a signal amplifier and the amplified signal is supplied to a data acquisition card to be recorded on the computer. As shown in Figure 3.1b, the pressure is measured at two different axial locations namely P1 and P2.

The results of the pressure measurements at high frequency range can be found in appendix E.1 along with some spectral analysis for the signals.

3.2.2. PIV system description

The PIV system consists of three main parts, namely the laser light source, a high speed camera, and the synchronizer (timer box). Each of these parts are described in the following subsections.

3.2.2.A. Light source and seeding particles

The laser light sheet is generated using an Nd: YLF laser (Dantec Dynamics model LDY303-PIV) with a wave length of 527 nm (i.e. green laser). As shown in Fig. 3.1, the light sheet with a thickness of around 3 mm illuminates the seeding particles at the center of the measurement section. A jet-atomizer (Manufacturer: TSI and Model: 9306) is used to atomize the seeding liquid which is olive oil. Olive oil is commonly utilized as seeding particles for PIV measurements in air because it has many advantages. First, the produced seeding particles are homogenous in shape (i.e. spherical particles). Second, the produced particles do not agglomerate like in solid-seeding particles; and hence the size distribution of the particles is narrow. Third, the mean particle diameter (d_p) is about 0.6 microns and the density (i.e. $\rho_p = 900$ kg/m^3) is much lower than solid particles and thus the seeding particles have good dynamic properties (i.e. the seeding particle are able to follow the flow with almost no slipping). Fourth, the refractive index of the olive oil seeding particles (i.e. 1.47 at 527 nm-wave length) is plausible which means the amount of the reflected light is enough to be detected by the sensor of the camera. Finally, olive oil is commercially available and inexpensive when compared with other alternatives and it is also chemically inert and non-corrosive.

3.2.2.B. High speed camera and lens

A Complementary Metal-Oxide Semiconductor (CMOS) camera (Photron SA1.1, maximum frame rate of 5400 frames/s, a resolution of 1024 X 1024 Pixels^2, 8 GB internal memory and is mounted on a 3D traverse mechanism) is used to capture and record the images for the seeded flow. In the current study, two different lenses are used with the camera. Each lens provides a certain spatial resolution and field of view. Images for both lenses are presented in appendix D.3.

For the low-frequency oscillating flow, the minimum viscous penetration depth is around 1.8 mm and hence a prime lens (60 mm Nikon AF macro) is connected to the camera providing a spatial resolution of 0.33 mm and field of view of approximately 44 mm. At the higher frequency range, the viscous penetration depth is around 0.46 mm and hence a zoom lens (Navitar: 1-60135AD,

Zoom 6000) is connected to the camera providing a spatial resolution of 0.078 mm and a field of view of 10 mm.

3.2.2.C. Synchronization

A synchronization box (National Instruments, Model: 80N77) is used to synchronize between the laser light pulses and the frames of the CMOS camera. In other words, the camera should capture the image and the laser light illuminates the flow field simultaneously. Also, in order to start the PIV measurements at a certain phase (i.e. phase-locked PIV measurements), the synchronization box is triggered by an external signal. For the Scotch-Yoke mechanism, the trigger signal is provided by the line-tracker sensor, see appendix B.2. For the loudspeakers case, the trigger signal is provided through the TTL output of the function generator, see appendix B.3. However, the TTL output of the function generator is not a pulse signal and hence a pulse generator is needed to generate a pulse signal for triggering. Since we don't have a pulse generator, the acquired data is processed and the starting phase was determined using matlab code (see appendix C.4). It is worthwhile to mention that the camera is a timer box slave and hence the maximum frame rate of the camera is reduced to two third of the rated frame rate (i.e. $\frac{2\times5400}{3} = 3600$ frames/s).

3.2.3. Adjusting the parameters of the PIV system

PIV measurement process requires many precautions in order to get accurate results. In the following subsections, the adjustment of all measurement parameters will be explained in details.

3.2.3.A. Parameters of the imaging system (camera and lens)

The imaging system should be calibrated in order to specify its magnification ratio. The magnification ratio (M) is defined as:

$$Magnification\ ratio\ (M) = \frac{The\ size\ of\ the\ camera\ sensor}{The\ actual\ size\ of\ the\ FOV} \tag{3.1}$$

The size of the camera sensor is a fixed value and equals to 20 mm × 20 mm. A calibration plate (see appendix D.4) is placed at the measurement plane, in order to determine the actual size of the field of view (FOV).

The depth of field, which is the thickness of the focused measurement plane, can be determined as following:

$$Depth\ Of\ Field\ (DOF) = 4 * (1 + \frac{1}{M})^2 * {f_\#}^2 * \lambda \tag{3.2}$$

Where, λ is the wave length of the laser light source, $f_\#$ is the ratio of the focal length of the lens to the aperture diameter. Most of the modern lenses have $f_\# = \sqrt{2}^n$ where $n = 0, 1, 2, ...$ The value of the DOF should be small enough to focus the image within the laser sheet thickness yet large enough to avoid losing seeding particles due to out of plane motion.

In addition, the object distance (od), which is the distance between the camera sensor and the measurement plane, can be calculated as well.

$$Object\ distance\ (od) = Focal\ length\ of\ the\ camera\ lens\ (fl) * \ (1 + \frac{1}{M}) \qquad (3.3)$$

3.2.3.B. Parameters of the seeding particles

Seeding particle characteristics have to be specified in order to make sure that the appropriate seeding particles are used. The rule of thumb in seeding particle selection process is that the particle diameter should be small enough to follow the flow but yet large enough to reflect plausible amount of light.

One of the most important characteristics of the seeding particle is to determine the effective image diameter (d_e) of the particle at the measurement plane. To determine this value; both geometric and diffraction effects have to be considered. The diffraction spot size (d_s) can be calculated as following:

$$d_s = 2.44 * \left(1 + \frac{1}{M}\right) * f_\# * \lambda \qquad (3.4)$$

And hence, the effective particle diameter can be calculated as follows:

$$d_e = \sqrt{\left(M * d_p\right)^2 + {d_s}^2} \qquad (3.5)$$

The first term in the equation above represents the physical size of the particle on the camera sensor. If the second term is the dominant (i.e. $M * d_p \ll d_s$), the effective particle diameter is defined by the diffraction limit. Hence, the physical size of the seeding particle can be increased without any significant change in the value of the effective particle diameter. Increasing the physical particle diameter, increases the amount of reflected light however the dynamic performance of the particle decreases. On the other hand, if the first term is the dominant (i.e. $M * d_p \gg d_s$), the effective particle diameter is defined by both the magnification ratio and the physical particle diameter.

The dynamic performance is the ability of the seeding particle to follow the flow with no slip even if the flow is accelerating or decelerating and also, its ability to follow the turbulent fluctuations in the case of turbulent flow. The following calculations will show how to estimate the dynamic performance characteristics of the seeding particle.

The velocity lag between the fluid flow velocity and the particle velocity can be estimated as follows:

$$V_L = {d_p}^2 * \frac{\rho_p - \rho_f}{18\mu} * a \qquad (3.6)$$

Where, $\rho_f, \mu \; and \; a$ are the fluid density, dynamic viscosity and acceleration, respectively. As V_L becomes smaller the ability of the particle to follow the flow will improve.

In turbulent flows, the ability of the seeding particle to follow the turbulent fluctuations can be estimated by determining an important parameter known as the characteristic frequency (f_p) of the particle motion.

$$f_p = \frac{18\mu}{\rho_p {d_p}^2} \tag{3.7}$$

The value of the characteristic frequency should be much higher than the turbulent fluctuations frequency (f_f), in order to make sure that the particles follow the turbulent fluctuations. The relation between the turbulent velocity fluctuations of the flow ($\overline{U}_f^2$) and the particle velocity fluctuations ($\overline{U}_p^2$) can be calculated as follows [68]:

$$\frac{\overline{U}_p^2}{\overline{U}_f^2} = \frac{1}{1+\frac{f_f}{f_p}} \tag{3.8}$$

The settling velocity (U_∞), which is the velocity of the particle due to the gravity, is an important seeding particle characteristic.

$$U_\infty = {d_p}^2 * \frac{\rho_p - \rho_f}{18\mu} * g \tag{3.9}$$

Where, g is the gravitational acceleration.

The value of the settling velocity should be small enough in order to make sure that the seeding particles do not leave the measurement plane during the measurement duration and hence the out of plane motion error will be reduced. In other words, the settling velocity should be less than the ratio between the DOF and the measurement duration (i.e. $U_\infty < \frac{DOF}{time \; of \; the \; measurement}$).

3.2.3.C. Parameters of the laser light source

As stated previously, the laser source used with the PIV system has wavelength (λ) of 527 nm and the light sheet thickness is about 4 mm. The laser source consists of two different laser heads. The two laser heads should produce nearly the same power and hence thermal sensor (Manufacturer: Ophir, Model: 30(150)A-LP1-18) connected to power meter (Manufacturer: Ophir, Model: Nova II) are used to measure the laser power produced by each head.

In order to get the velocity field, two laser pulses separated by a certain time illuminate the flow field while the camera captures two frames, simultaneously. The time between the two pulses (Δt) is an important parameter and should be optimized well. Because, If the time between pulses is too large, the particles in the interrogation area will travel distance larger than the length of the interrogation area and hence proper correlation between the two frames will not be possible. Also, the correlation always presumes that the flow velocity is constant over that (i.e. Δt) period of time

and therefore in the transient flows (i.e. velocity changes with time) the time between pulses should be as minimum as possible in order to avoid the acceleration/deceleration error. On the other hand, if the time between pulses is too short; the particle displacement within the interrogation area will be too small; consequently, the distinguishing between particle displacement and the random error (σ_{rand}) becomes impossible. The random error is equal to:

$$\sigma_{rand} = K * d_e \tag{3.10}$$

Where K is a constant ranged from 0.05 to 0.1 based on the experimental conditions.

Accordingly, it was found that the optimum time between pulses is:

$$\Delta t_{opt} = \sqrt{\frac{2\sigma_{rand}}{Ma}} \tag{3.11}$$

Based on the time between pulses and the number of interrogation areas (e.g. 16 × 16 pixels^2) in the FOV; both the maximum and the minimum detectable velocities can be determined as follows:

$$V_{max} \leq \frac{0.25 * N_{interrogation} * d_{pitch} * M}{\Delta t} \tag{3.12}$$

$$V_{min} \leq \frac{2 * M * d_e}{\Delta t} \tag{3.13}$$

Where, $N_{interrogation}$ is the number of interrogation areas is one direction (e.g. 16 pixels) and d_{pitch} is the distance between the sensors of the CMOS camera and can be calculated as follows:

$$d_{pitch} = \frac{The\ size\ of\ the\ camera\ sensor\ (20\ mm)}{number\ of\ pixels\ in\ one\ direction\ (1024)} \tag{3.14}$$

It is preferred that the measured flow velocity to be within the range bounded by the maximum and minimum detectable velocities. However, the minimum flow velocity limit can be pushed down by suing subpixel interpolation technique and thus increasing the dynamic range of the measurements.

All of the parameters mentioned above are considered for each measurement. An example for the calculations of theses parameters is presented in appendix D.5.

3.2.4. Processing of the PIV images

In order to produce the velocity vector map, the images captured by the PIV system have to be processed. The image processing technique includes several steps. First, the light reflections have to be removed from the raw images. For any PIV measurement, there are many reflections. These reflections can be reduced physically during the measurement process, see appendix D.6 for more details about the techniques of reflections removing. However, some reflections will always remain in the captured raw images (see Fig. 3.5a). To remove these reflections, a low-pass filter is

applied on the images to extract the reflections from the raw image (see Fig. 3.5b). By subtracting the reflection image from the raw image, an image for the seeding particles only can be obtained (see Fig. 3.5c).

The seeding particles images are then analyzed. Each pair of images are analyzed to produce a velocity vector map. Each image is divided into a certain number of interrogation areas where the size of the interrogations area is predefined (e.g. 16×16 pixels^2). Then an adaptive correlation is used to get the velocity vector for each interrogation area. Also, it is preferred that the seeding particle density to be within 5 to 10 particles per interrogation area in order to get proper correlation. The size of the interrogation area represents the spatial resolution of the measurements.

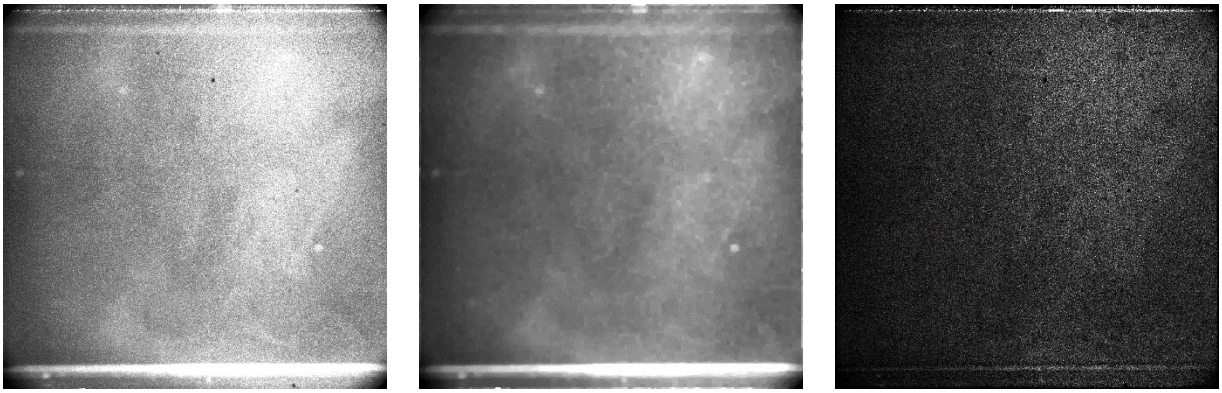

(a) **(b)** **(c)**

Figure 3.5: (a) Typical raw image, (b) Reflection image obtained by applying low-pass filter, (c) Final image obtained by subtracting (b) from (a).

3.2.5. Experimental procedure

Before starting the measurements, the imaging system is calibrated (as explained previously) to determine the size of the field of view and the magnification ratio. Then the measurement section (glass duct) is cleaned well to remove any seed contamination from the previous measurements. Afterwards, seeding particles are injected inside the resonator duct through a certain port near to one end of the resonator while another port near to the other end of the resonator is open to make sure that the seeding particles are dispersed all over the resonator. Then, the ports are closed firmly to avoid any leaks. The seeding particles are left inside the resonator for about 3 minutes to make sure that the flow motions created due to the injection of the seeding particles ceases. Then, the driving system of the oscillating flow (i.e. Scotch Yoke mechanism or speakers) is turned on and the PIV measurements started after about 1 minute to make sure that the flow characteristics are stabilized. Finally, the images are stored on the computer and analyzed (as explained previously). The post-processing of the data to produce the final results is explained in the following section.

3.3. Results and discussion

As mention at the beginning of this chapter, there are two main objectives. The first one is to validate the using of the PIV tool in studying the transition to turbulence of an oscillating flow at sub-acoustic (i.e. <20 Hz) frequency range. The second objective is to extend the work to the acoustic frequency range (i.e. >20 Hz). Accordingly, the results section has been divided into two subsections.

3.3.1. Sub-acoustic frequency range

As shown in Fig. 3.6, the PIV field of view covers the whole width (W) of the duct. However, the data is presented over one half of the duct width because the data is symmetric around the axis. The sampling frequency of the PIV system is adjusted to be multiple ($A = 50$) of the frequency of the oscillating flow. Also, the measurement duration is adjusted to cover a total number of cycles of $B = 50$. Hence, the total number of the velocity vector maps per measurement is $A \times B = 2500$. The time between pulses is adjusted, as explained previously, to allow the seeding particles to move a distance nearly equal to a quarter of the interrogation window length.

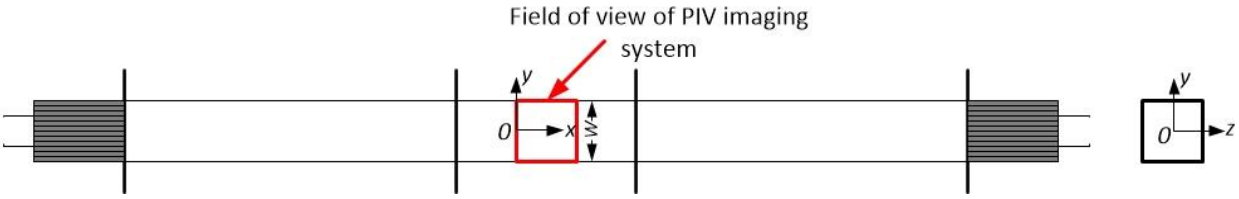

Figure 3.6: Schematic representing the field of view of the PIV imaging system.

The method of analyzing the measured data to get the velocity distribution over the cross section is quite similar to the method used in [38]. The velocity vectors in each map is spatially averaged along the x-direction because the velocity is almost constant in that direction. Then, phase averaging is implemented to get the velocity distribution over one cycle of oscillations.

A graphical representation for the method of the analysis is depicted in Fig. 3.7. The total number of vectors in each map is $N \times M$, where $N\ and\ M$ are the total number of interrogation areas in x-direction and y-direction and equals to 127 and 127, respectively. The total number of velocity vectors maps are indexed from $i = 1$ to $i = A \times B$. The velocity vector at each interrogation area within the velocity map is referred as $U_i(n,m)$ and includes both x-direction $u_i(n,m)$ and y-direction $v_i(n,m)$ velocity components. Then, the velocity vectors at the same y-position are averaged along x-axis and hence the spatial-average velocity distribution can be expressed as

$$\bar{\boldsymbol{U}}_{\boldsymbol{i}}(\boldsymbol{m}) = \frac{\mathbf{1}}{\boldsymbol{N}}\sum_{\boldsymbol{n=1}}^{\boldsymbol{N}} \boldsymbol{U}_{\boldsymbol{i}}(\boldsymbol{n},\boldsymbol{m}) \tag{3.15}$$

Finally, the maps of those 50 oscillating cycles are averaged to get the phase-average velocity vector distribution over one oscillating cycle that can be expressed as

$$\bar{\bar{U}}_{\emptyset}(m) = \frac{1}{B}\sum_{i=0}^{B-1} U_{Ai+\emptyset}(m) \quad (3.16)$$

where $\emptyset$ is the phase number in the cycle and is ranged from $\emptyset = 1$ to $\emptyset = A$.

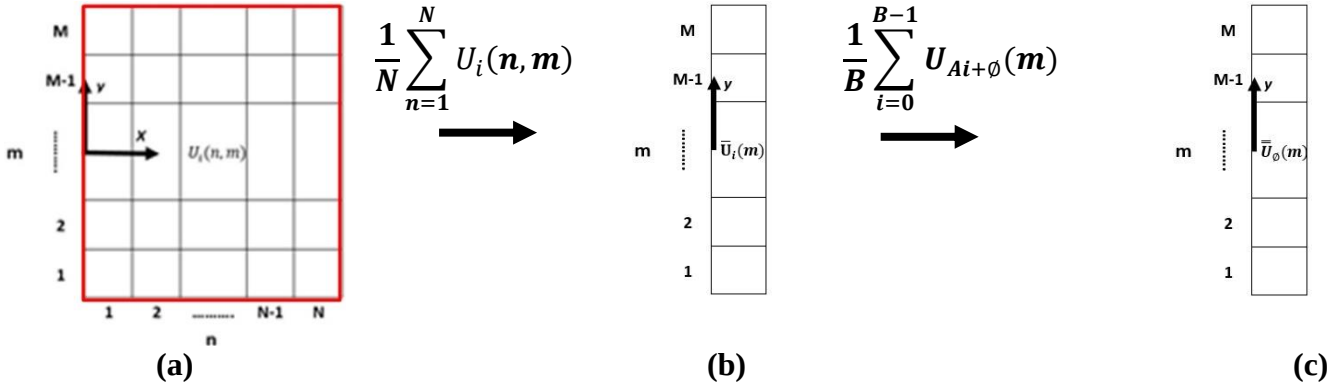

Figure 3.7: (a) An example for velocity vectors map. (b) Spatial-average velocity distribution. (c) Phase-average velocity distribution.

3.3.1.A. Experimental conditions

Nine experiments are conducted at different conditions, as shown in Table 3.1. For all experiments the resonator is filled with air at atmospheric pressure and temperature (25° C). The experiments cover a range of Reynolds numbers (Re_δ) between 141 and 510 and a range of Womersley number (α) between 7.1 to 12.3.

Table 3.1: Operating conditions for different experiments at sub-acoustic frequency range

Experiment #	f (Hz)	U_o (m/s)	δ (mm)	Re_δ	α
1	0.5	0.7	3.16	141	7.1
2	1	1.4	2.2	196	10
3	1.5	2.0	1.8	230	12.3
4	0.5	1.3	3.16	262	7.1
5	1	2.5	2.2	350	10
6	1.5	3.6	1.8	412	12.3
7	0.5	2.2	3.16	442	7.1
8	1	3.5	2.2	490	10
9	1.25	4.0	2.0	510	11.3

3.3.1.B. Results

As mentioned in section 3.3.1. the total number of phases per cycles (A) is fifty and the number of the averaged-cycles per phase (B) is fifty as well. In order to make sure that the used number of averaged images per phase is enough for the stationarity of the data, the number of averaged-cycles is changed and its effects on the flow characteristics are investigated. As shown in Fig. 3.8, as the

number of averaged-cycles is increased, the value of the mean velocity at any phase becomes nearly constant. It is found that the number of cycles required to get a stable mean velocity data is more than 30 cycles at a high Reynolds number (i.e. $Re_\delta = 490$). However, the 30-cycles criterion may be insufficient for the stability of the higher moment like velocity fluctuations and hence the turbulence intensities based on *x* and *y* velocity components are calculated using different numbers of averaged-cycles (B). The turbulence intensities based on *x* and *y* velocity components at any phase, $I_{x_\emptyset}$ and $I_{y_\emptyset}$, respectively can be calculated as follows:

$$\boldsymbol{I_{x_\emptyset}(m) = \sqrt{\frac{1}{B}\sum_{i=0}^{B-1}[\overline{u}_{Ai+\emptyset}(m) - \overline{\overline{u}}_\emptyset(m)]^2}} \tag{3.17}$$

$$\boldsymbol{I_{y_\emptyset}(m) = \sqrt{\frac{1}{B}\sum_{i=0}^{B-1}[\overline{v}_{Ai+\emptyset}(m) - \overline{\overline{v}}_\emptyset(m)]^2}} \tag{3.18}$$

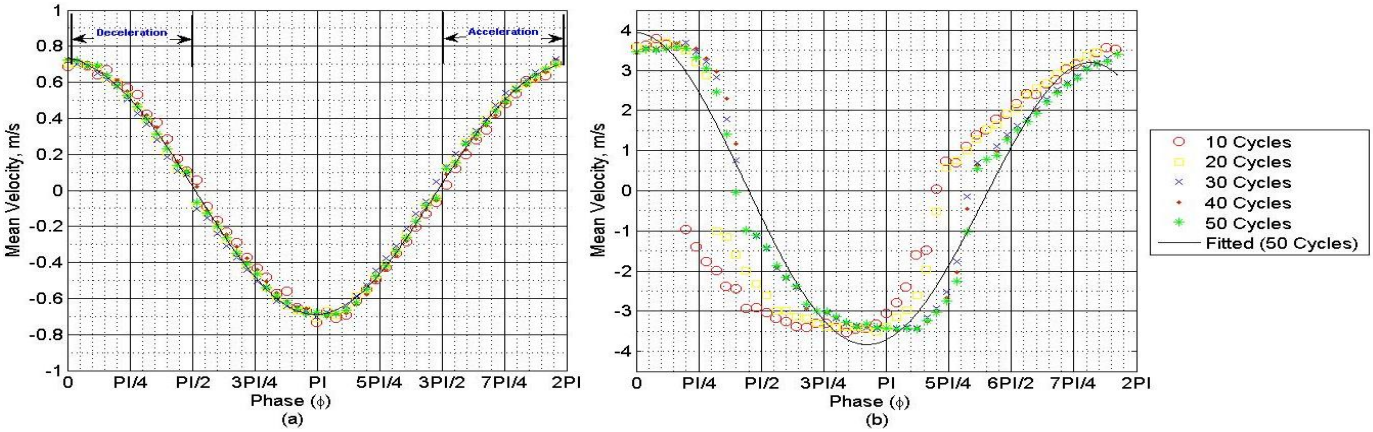

Figure 3.8: The effect of the number of the averaged-images on the value of the mean velocity over the cycle at two different Reynolds numbers: (a) Experiment# 1 and (b) Experiment# 8

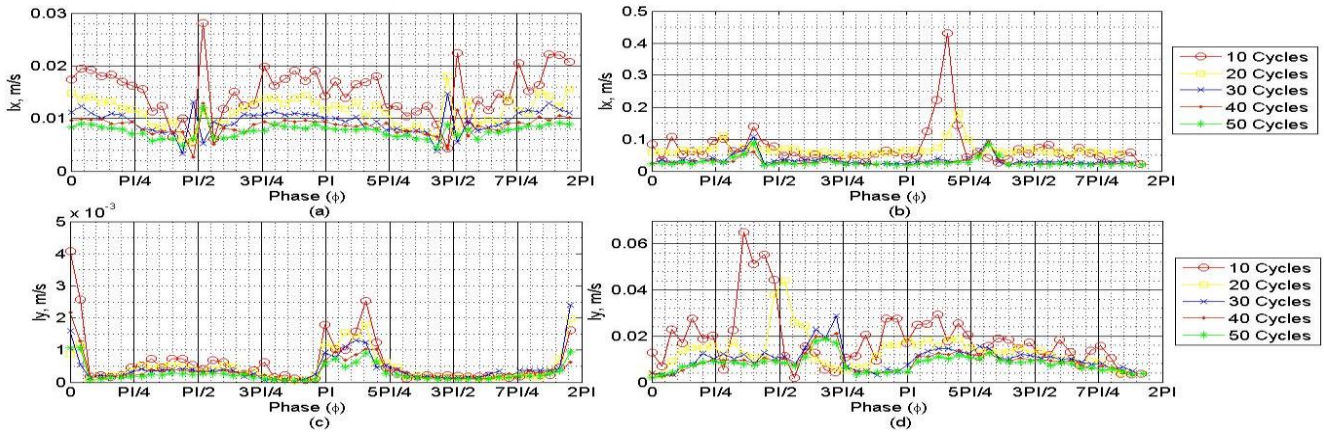

Figure 3.9: The effect of the number of the averaged-images on the values of the turbulence intensities (based on x and y velocity components) over the cycle at the center of the duct ($y = 0$) at two different experimental conditions: (a, c) Experiment# 1 and (b, d) Experiment# 8.

As shown in Fig. 3.9, the values of the turbulence intensities over the cycle becomes stable when the number of the averaged-cycles exceeds 40 images; and hence 50 images are sufficient to get converged velocity data which is in agreement with the findings of [38]. Hereinafter, the presented data are based on averaging 50 cycles.

In order to validate the measurement procedure explained above; the measured distribution of the axial velocity over the half width of the duct is compared with the theoretical expectations derived in [45] and expressed as follows:

$$u(y,z,t) = \frac{16U_o}{\pi}\sum_{l=0}^{\infty}\sum_{k=0}^{\infty}\frac{(-1)^{l+k}}{(2l+1)(2k+1)}cos\frac{(2l+1)\pi}{2W}y \times cos\frac{(2k+1)\pi}{2W}z \times \sigma \tag{3.19}$$

where,

$$\sigma = \frac{\gamma\left(\frac{\pi^2}{4}\right)\left[(2l+1)^2+(2k+1)^2\right]\cos(2\pi ft)+\varphi^2\sin(2\pi ft)}{\varphi^2+\left(\frac{\pi^2}{16}\right)\left[(2l+1)^2+(2k+1)^2\right]^2} \tag{3.20}$$

and,

$$\varphi = \frac{2\pi fW^2}{\nu} \tag{3.21}$$

As the theoretical expectations were derived for the flow in the laminar regime; the comparison is done at the lowest Reynolds number (Exp.#1). As shown in Fig. 3.10 (Exp.#1), there is a good agreement between the measured and the theoretical values over the whole cycle. It should be noted that the positive half of the cycle is only considered since the negative and positive halves are identical.

In order to recognize the end of the laminar regime; the measured distributions of the axial velocity at different Reynolds numbers are compared with the theoretical expectations. As shown in , as the Reynolds number is increased up to 230; the measured values agree well with the theoretical expectations over the whole cycle. For Reynolds number higher than 230, the agreement with theory is valid over the whole cycle except at the deceleration phase ($\emptyset = \pi/4$). This behavior is observed up to Reynolds number of 412. For Reynolds number higher than 412, it is observed that the deviation from theory in the boundary layer extends to the acceleration phase as well. For Reynolds number higher than 500, there is a large deviation from theory in the boundary layer at the phases where the velocity direction is reversed. Also, the discontinuity in the velocity distribution at these phases may be due to the increase of the acceleration error inherited in PIV technique.

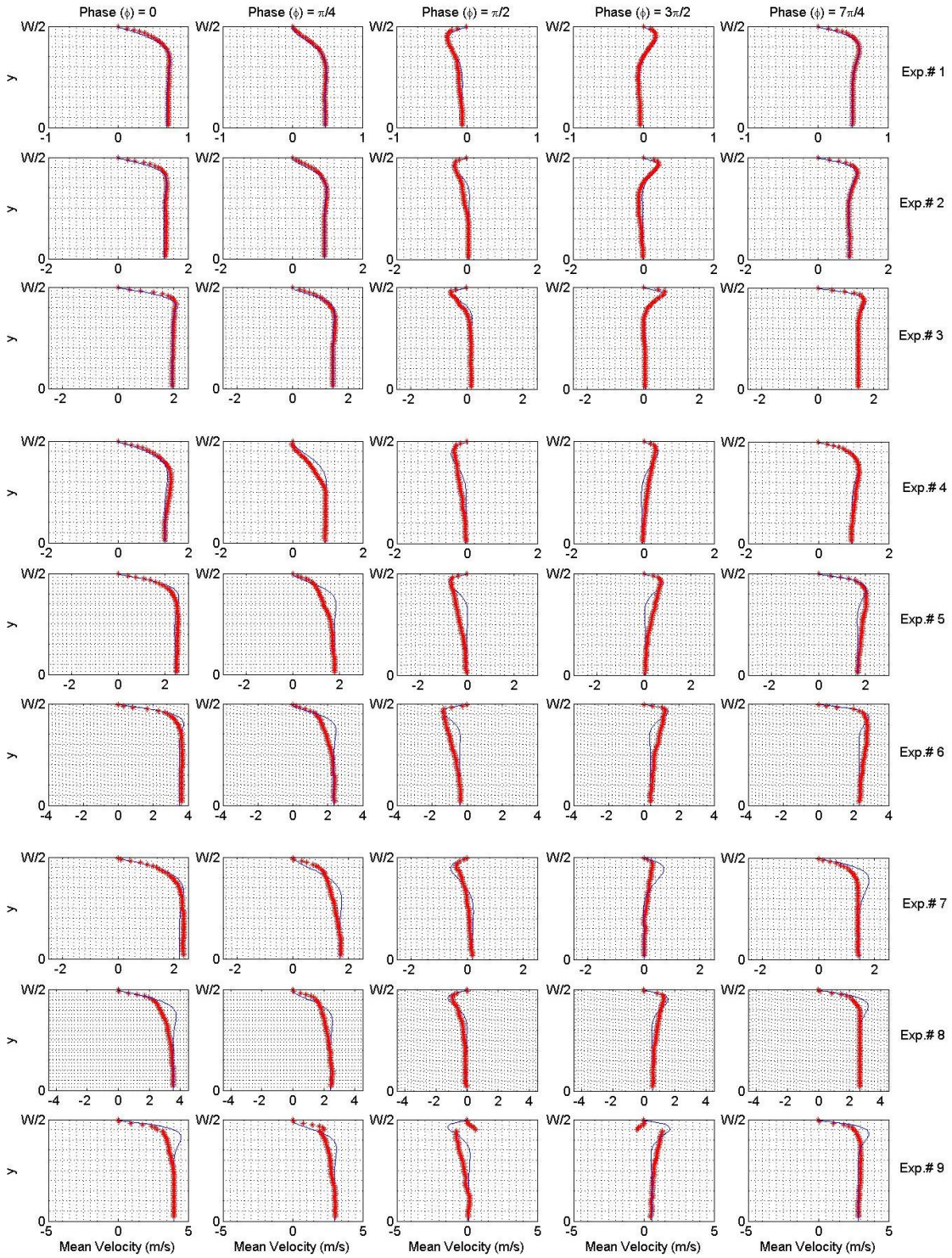

Figure 3.10: The measured (*) and the theoretical (—) distributions of the axial velocity over the half width of the duct at different phases during the cycle at different experimental conditions.

The phase-average turbulence intensities in both directions normalized by the centerline axial velocity amplitude (U_o) are calculated. Also, the value of the Reynolds shear stress divided by the flow density is calculated as follows:

$$Re_{stress_{\emptyset}}(m)/\rho = \frac{1}{B}\sum_{i=0}^{B-1}[\bar{u}_{Ai+\emptyset}(m) - \bar{\bar{u}}_{\emptyset}(m)] * [\bar{v}_{Ai+\emptyset}(m) - \bar{\bar{v}}_{\emptyset}(m)] \quad (3.22)$$

As shown in Fig. 3.11a, the phase-average turbulence intensity based on x-velocity component increases as the Reynolds number is increased. Also, the maximum value is achieved near to the wall rather than the center of the duct. In Fig. 3.11b, the phase-average turbulence intensity based on y-velocity component increases as the Reynolds number is increased. In Fig. 3.11c, the phase-average Reynolds stress divided by the density increases as the Reynolds number is increased. Also, it is obvious that the value of the phase-average Reynolds stress increases significantly when the Reynolds number exceeds 500. The sharp increase in the value of the Reynolds stress beyond a certain value of Reynolds number characterizes the transition to turbulence process. So, it can be concluded that the critical Reynolds number is about 500 which is in agreement with the literature [27], [28].

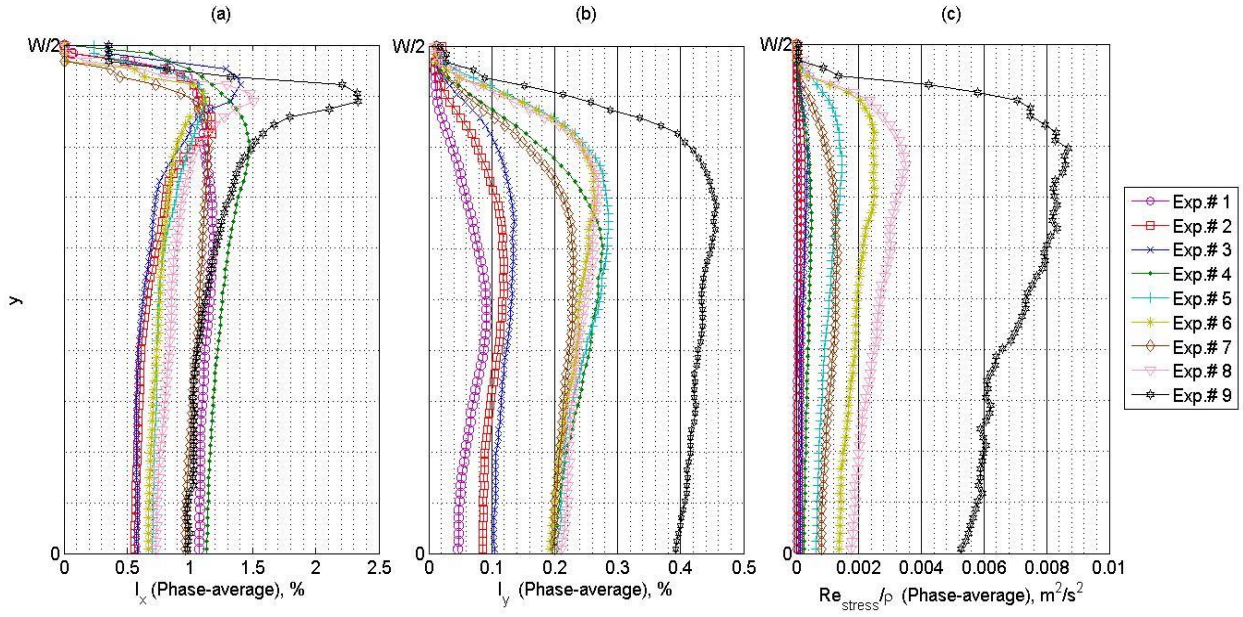

Figure 3.11: The distribution of the Phase-average turbulence intensity normalized by the centerline axial velocity amplitude over the half width of the duct based on: (a) x-velocity component and (b) y-velocity component. (c) The distribution of the phase-average Reynolds stress divided by the density over the half width of the duct.

3.3.2. Acoustic frequency range

As the frequency of the oscillating flow gets higher, the size of the viscous penetration depth becomes smaller (i.e. 0.46 mm). Hence, in order to capture sufficient points inside the viscous penetration depth a zoom lens is used. The zoom lens provides a field of view of 10 mm and a

spatial resolution of 0.078 mm. As shown in Fig. 3.12, the PIV field of view covers a certain part of the duct width. The side length of the covered area is 10 times the size of the viscous penetration depth. The sampling frequency of the PIV system is adjusted to be an integer multiple ($A = 25$) of the frequency of the oscillating flow. Also, the measurement duration is adjusted to cover a total number of cycles of $B = 100$. Hence, the total number of the velocity vector maps per measurement is $A \times B = 2500$. The time between pulses is adjusted, as explained previously, to allow the seeding particles to move a distance nearly equal to a quarter of the interrogation window length.

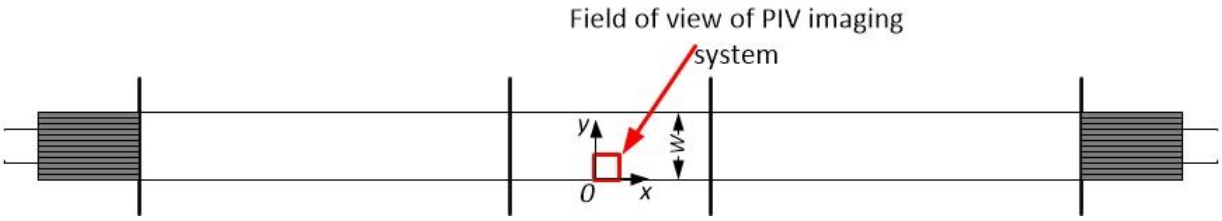

Figure 3.12: Schematic representing the field of view of the PIV imaging system.

3.3.2.A. Experimental conditions

Nine experiments are conducted at different conditions, as shown in Table 3.2. For all experiments the resonator is filled with air at atmospheric pressure and temperature (25° C). The experiments cover a range of Reynolds numbers (Re_δ) between 205 and 466.

Table 3.2: Operating conditions for different experiments at acoustic frequency range

Experiment #	f (Hz)	U_o (m/s)	δ (mm)	Re_δ	α
1	23.3	7	0.46	205	48.5
2	23.3	8.2	0.46	240	48.5
3	23.3	9.25	0.46	272	48.5
4	23.3	10.3	0.46	302	48.5
5	23.3	11.46	0.46	336	48.5
6	23.3	12.78	0.46	375	48.5
7	23.3	14.3	0.46	418	48.5
8	23.3	15.2	0.46	445	48.5
9	23.3	15.9	0.46	466	48.5

3.3.2.B. Results

3.3.2.B.1. Stationarity of the data

In order to calculate the different quantities (e.g. velocity distribution, turbulence intensities, … etc.) from the PIV data, the same post-processing technique presented in section 3.3.1. is used here. However, as the oscillating frequency gets much higher, the number of averaged-cycles required to achieve the stationarity of data has to be checked. Hence, 200 vector maps are captured

for a certain phase at $Re_\delta = 240$, to investigate the effects of the number of the averaged-cycles on the stationarity of the data.

As shown in Fig. 3.13, the deviation of the velocity components from the stationary values (estimated based on 200 vector maps) is plotted versus the number of the averaged-cycles. The deviation can be calculated as follows:

$$Error\ (\%) = \frac{|Value(N) - Value(200)|}{Value(200)} * 100 \tag{3.23}$$

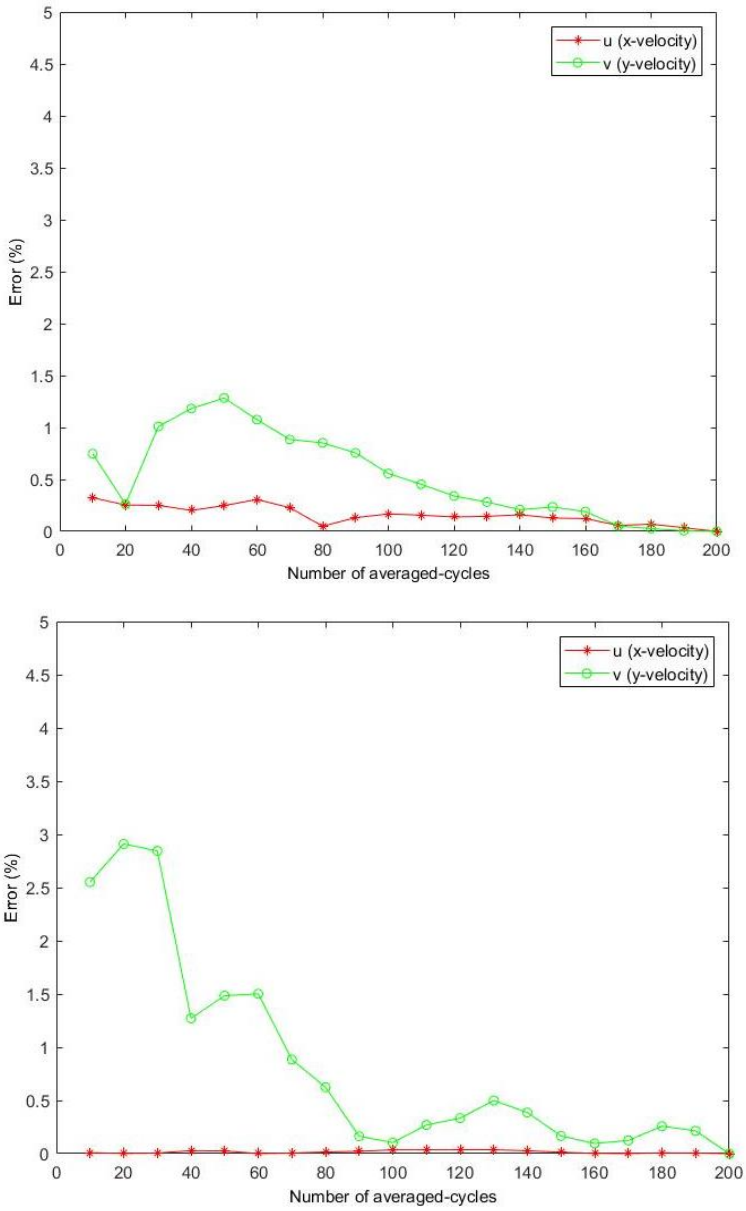

Figure 3.13: The effect of the number of the averaged-cycles on the values of the velocity components (x and y) at $Re_\delta = 240$ for different traverse locations of the resonator: a) $y = 2\delta_v$ and b) $y = 5\delta_v$

The error decreases with increasing the number of the averaged-cycles. At traverse location $y = 2\delta_v$ (Fig. 3.13a), the maximum error is less than 1.5 % which is very small value. Whereas the maximum error reaches up to 3 % at traverse location $y = 5\delta_v$ (Fig. 3.13b). These values of error are acceptable; and hence as long as the number of the averaged-cycles is more than 10 cycles, the measured mean velocity components are acceptable. However, the 10 cycles criterion may be not sufficient for the convergence of the higher moment quantities (e.g. turbulence intensities). Therefore, the effect of the number of the averaged-cycles on the turbulence intensities is investigated.

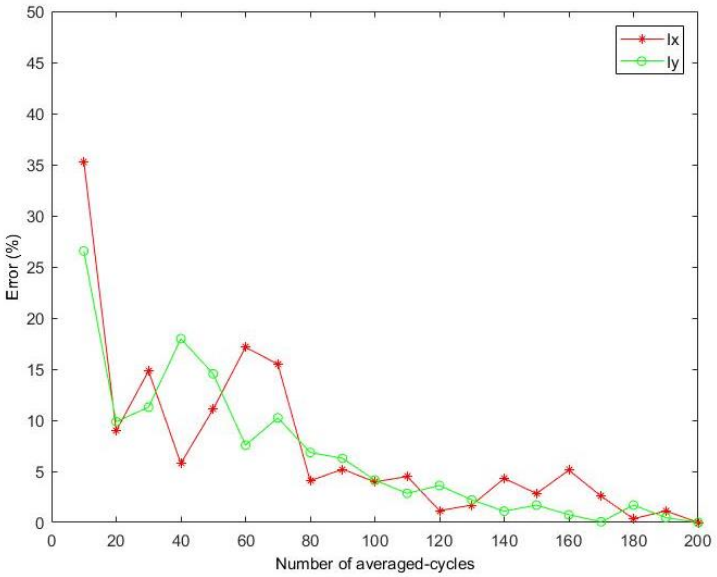

(a)

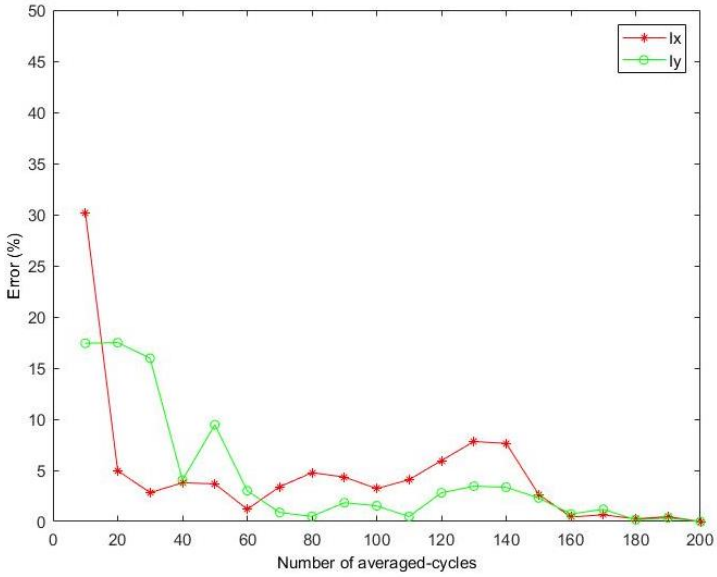

(b)

Figure 3.14: The effect of the number of the averaged-images on the values of the turbulent intensities (x and y) at $Re_\delta = 240$ for different traverse locations of the resonator: a) $y = 2\delta_v$ and b) $y = 5\delta_v$

As shown in Fig. 3.14a, the maximum value of the error is about 35 % and it drops down to 5% as the number of the averaged cycles exceeds 100 cycles. Also, at traverse location $y = 5\delta_v$ (Fig. 3.14b), the maximum error is about 30 % and it drops down to 5 % as the number of the averaged cycles exceeds 100 cycles. It is assumed that the data is stationary if the error is less than 5 % and hence the 100 cycles are sufficient for data convergence. Hereinafter, the presented data are based on averaging 100 cycles.

As the PIV camera memory cannot store more than 2700 double-images (i.e. vector maps), the total number of vector maps per measurement is selected to be 2500 (i.e. less than the limit of the camera memory). Hence, the number of the vector maps captured per cycle is 25.

3.3.2.B.2. Axial Velocity distributions

In order to validate the measurements, the measured axial velocity distribution is plotted and compared with the theoretical axial velocity distribution at low Reynolds number. The theoretical velocity distribution given by equation 3.19 is used here, however, this theoretical solution is mainly used for low frequency oscillating flow. Hence, another theoretical solution (used in [69]) is used to check the validity of the former solution at higher frequencies. As shown below, both theoretical solutions are identical. Hence, both solutions are used in this study to check the validity of the measurements.

As shown in Fig. 3.15, the measured and the theoretical axial velocity distributions are plotted for different Reynolds numbers and at five different phases (see appendix C.5 for the matlab code used to calculate and plot the data). These five phases are selected to cover one half of the acoustic cycle because both halves are similar. At low Reynolds numbers (up to $Re_\delta = 240$), the measured velocity distributions agree well with the theoretical expectations at the traverse locations (y) more than $3\delta_v$ for all phases. At traverse locations less than $3\delta_v$, there is also an agreement between the measurement and the theoretical expectations for some phases (e.g. 45, 90 and 135 deg) whereas the measurements deviate from the theoretical expectations at the other phases (0 and 180 deg). This deviation exists for all Reynolds numbers. This discrepancy is mainly due to the acceleration error associated with the PIV technique (When analyzing the PIV images, it is assumed that the measured velocity is constant over the time between the two images (i.e. time between pulses)). At these phases (0 and 180 deg), the flow experiences the maximum acceleration (i.e. $2\pi f U_o$) and therefore the maximum error is expected to occur at these phases. This error was not significant when the measurements were conducted at low frequency range (see Fig. 3.10) because the maximum acceleration of the flow (i.e. $2\pi f U_o$) is much less than the current case.

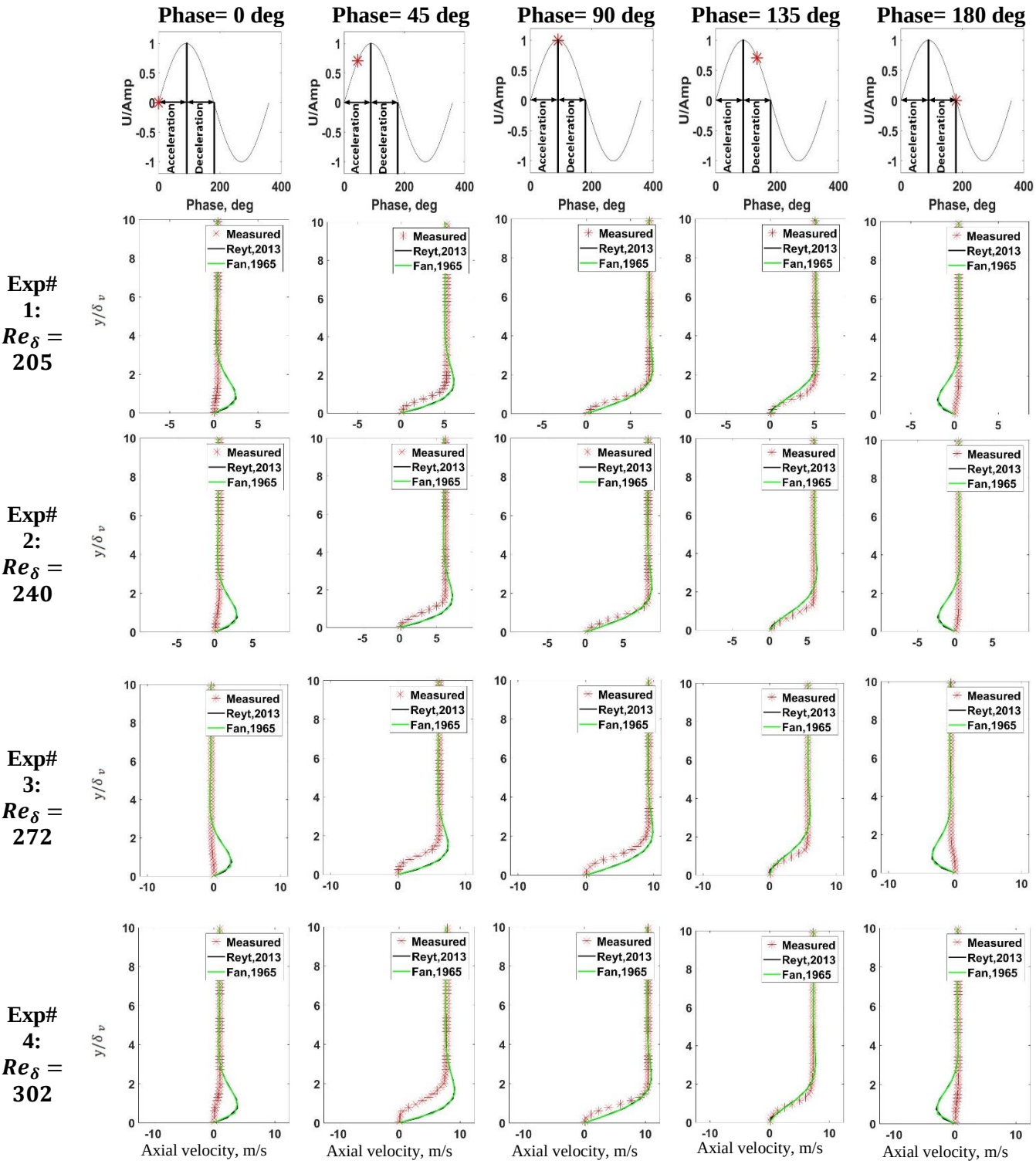

****Continued in the following page**

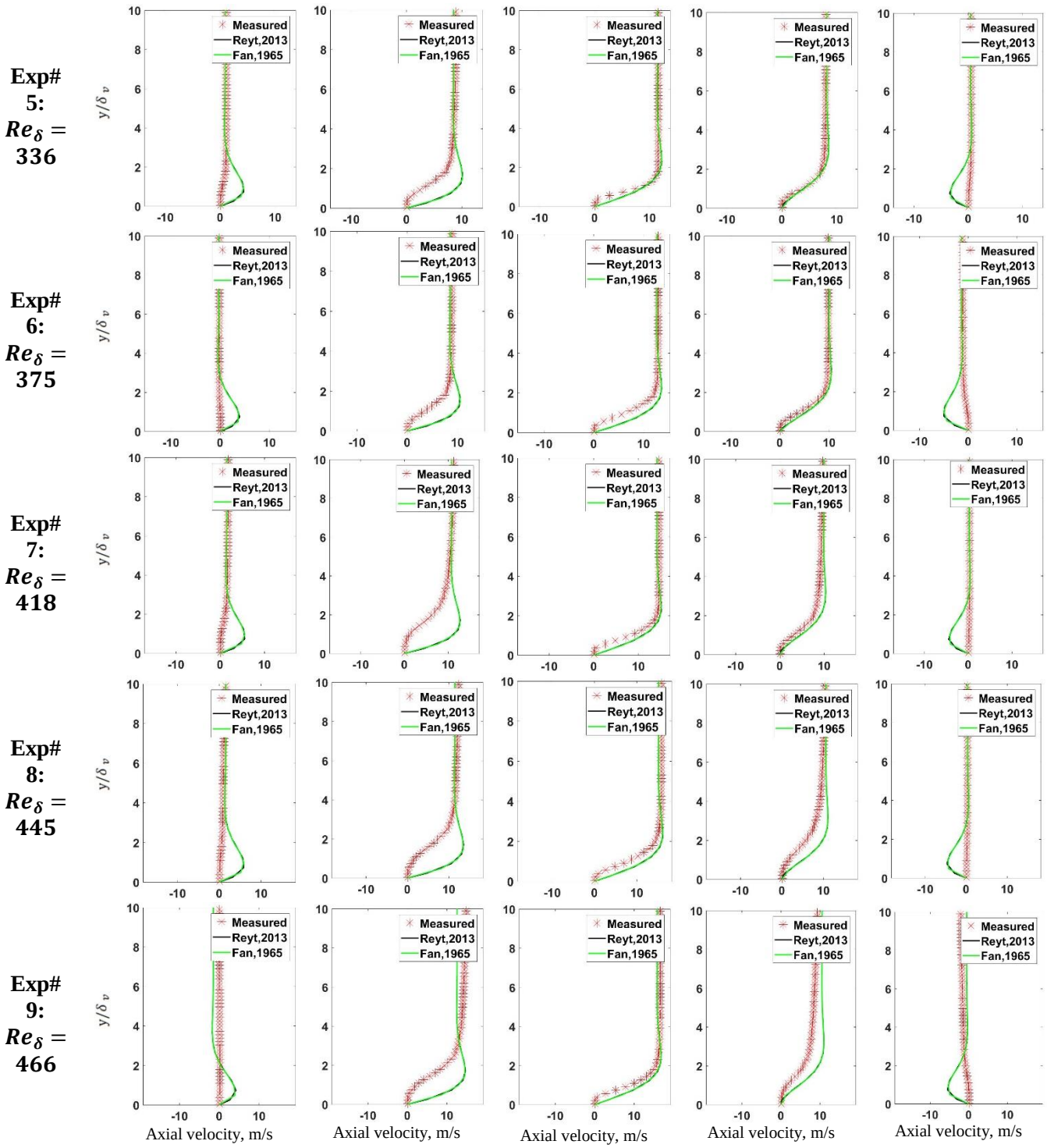

Figure 3.15: The ensemble-average measured (red dots) and the theoretical (solid lines) axial velocity distributions at different phases within the acoustic cycle for different Reynolds numbers.

As the Reynolds number increases ($272 \leq Re_\delta \leq 418$), the measured axial velocity distribution deviates from the theoretical expectations at the acceleration phase (i.e. 45 deg) for traverse locations (y) less than $3\delta_v$. For higher Reynolds number up to 466, the discrepancy between the measurements and the theoretical expectations extends to the deceleration phase (i.e. 135 deg) as well. This discrepancy may be regarded as an indication for the transition to turbulence as concluded in [69]. Hence, it can be assumed that the critical Reynolds number, at which the flow is considered non-laminar, is around 270 which agrees with the previous literature [30], [69]. However, using the axial velocity distribution as a criterion for the occurrence of turbulence is not strong enough. Hence, it is necessary to use some turbulence tools or parameters to make a strong evidence for the occurrence of turbulence. In the following subsections, some turbulence parameters will be used for that purpose.

3.3.2.B.3. Turbulence Intensities and Reynold stress

Turbulence intensity and Reynold stress are good tools to investigate the occurrence of turbulence and they have been used in some studies [33] [38] to investigate the turbulence occurrence in the oscillating flow. In the current work, turbulence intensities are calculated as presented previously in equations 3.17 and 3.18 and normalized by the velocity amplitude U_o. Also, Reynolds stress is calculated as presented in equation 3.22 and normalized by U_o^2 (see appendix C.6 for the matlab code used to calculate the turbulence intensities and Reynolds stress).

As shown in Fig. 3.16, the turbulence intensity based on the axial velocity component (Ix) is almost zero at traverse locations (y) more than $2\delta_v$ for all phases and at low Reynolds number (up to $Re_\delta = 272$). At traverse locations (y) less than $2\delta_v$, the turbulence intensity (Ix) is almost zero at phases with zero mean velocity (i.e. 0 and 180 deg) whereas it shows an overshoot at traverse location (y) equals nearly δ_v for other phases (i.e. 45, 90 and 135 deg). This overshoot is reported in [38] and [70], this can be due to the significant change in the velocity gradient near to the wall at these phases which significantly increases the turbulence intensity based on the axial velocity component (Ix). To overcome this overshoot, it was recommended in [38] to consider the turbulence intensity based on the traverse velocity component (Iy) because the mean value of the traverse velocity is always zero.

As shown in Fig. 3.16, the distribution of the turbulence intensity based on the traverse velocity component (Iy) is almost flat and equals to zero for all phases and at low Reynolds numbers (up to $Re_\delta = 272$). As the Reynolds number increases ($302 \leq Re_\delta \leq 375$), the turbulence intensity (Ix) at the acceleration phase (i.e. 45 deg) started to increase up to traverse location (y) of $7\delta_v$. Also, the turbulence intensity (Iy) slightly increases at all phases. At higher Reynolds number ($Re_\delta \geq 418$), the turbulence intensity (Ix) increases up to traverse location (y) of around $10\delta_v$. Also, the turbulence intensity (Iy) continues to increase for all phases.

As explained above, the turbulence intensities (Ix and Iy) started to increase at Reynolds number above 272 that indicates occurrence of turbulent bursts at some phases and hence it can be concluded that the critical Reynolds number is around 272. In order to support this finding, the

normalized Reynolds stress is calculated as well. As shown in Fig. 3.17, at low Reynolds number (up to 240), the distribution of the normalized Reynolds stress is almost flat and equals to zero for all phases. At Reynolds number of 272, the distribution of the normalized Reynolds stress is still flat and equals to zero for all phases except at the phase of the maximum velocity (i.e. 90 deg). At this phase, the value of Reynolds stress peaks at traverse location (y) of around $2\delta_v$. As the Reynolds number increases (up to 375), the distribution of the Reynolds stress peaks at traverse location (y) of around $2\delta_v$ for some phases (i.e. 45, 90 and 135 deg). At higher Reynolds numbers ($Re_\delta \geq 418$), the distribution of Reynolds stress becomes random and has non-zero value for some phases and also it extends up to traverse location (y) of around $10\delta_v$, similar behavior is reported in [33].

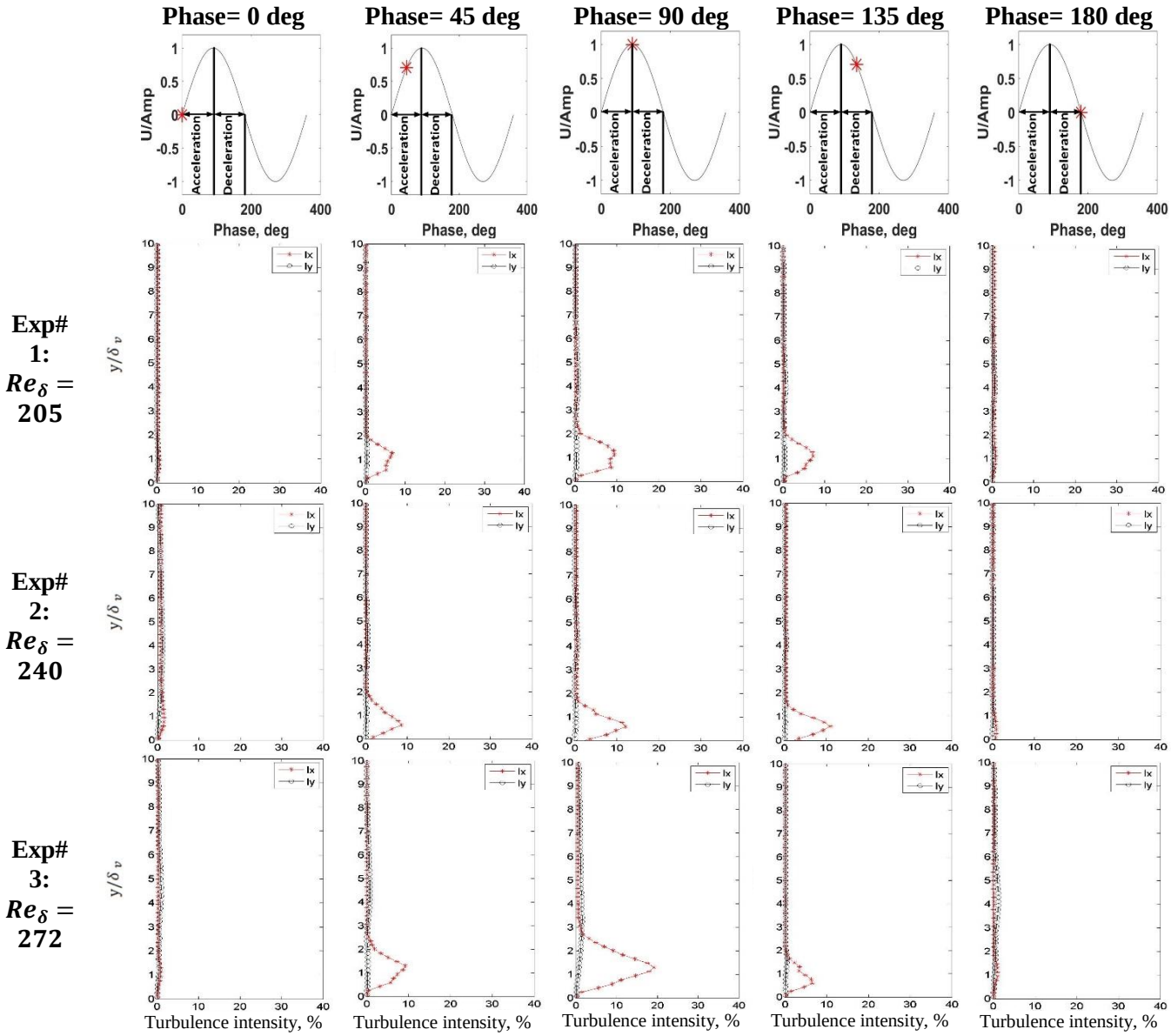

**** Continued in the following page**

Exp# 4: $Re_\delta =$ 302

Exp# 5: $Re_\delta =$ 336

Exp# 6: $Re_\delta =$ 375

Exp# 7: $Re_\delta =$ 418

Exp# 8: $Re_\delta =$ 445

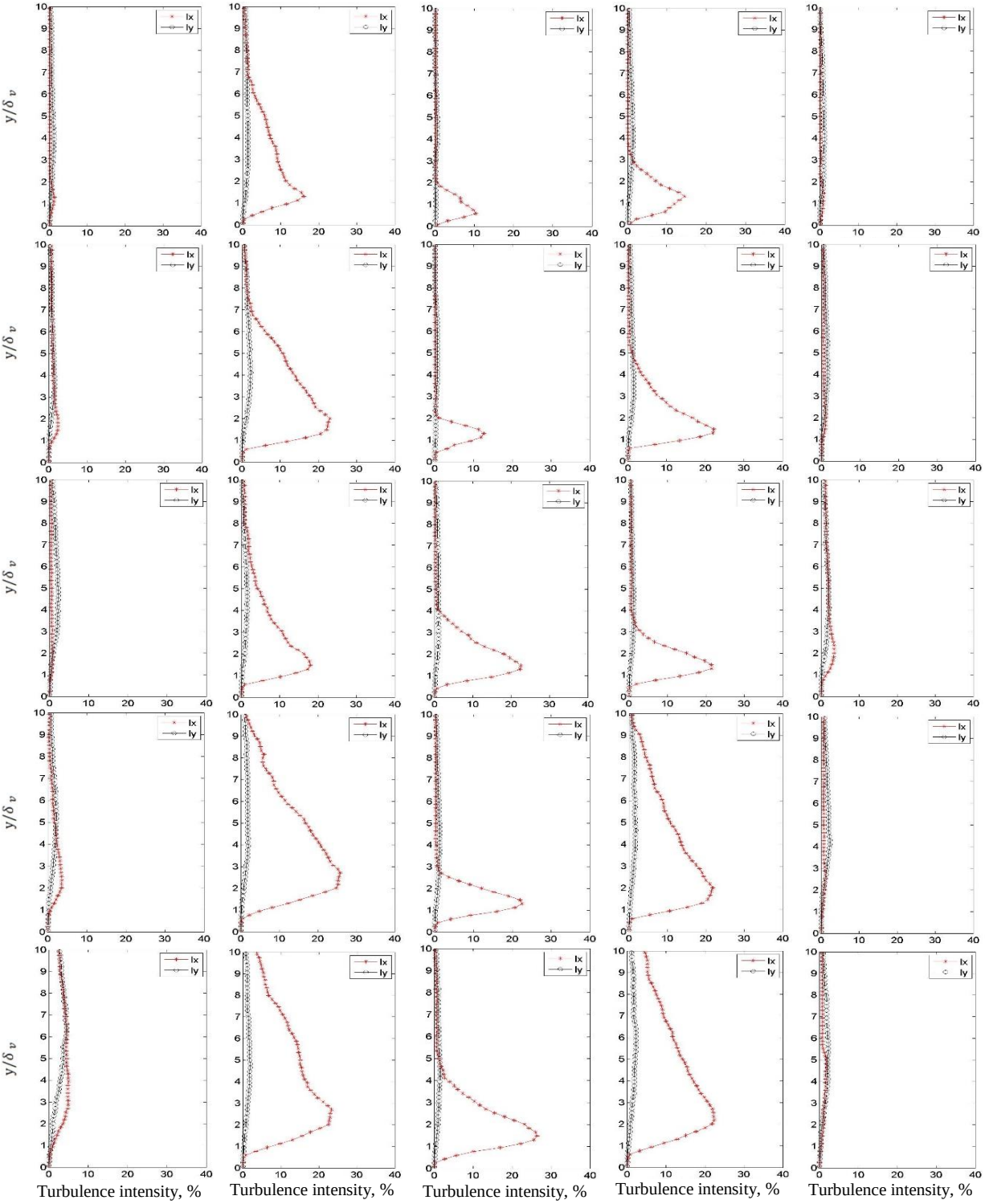

**** Continued in the following page**

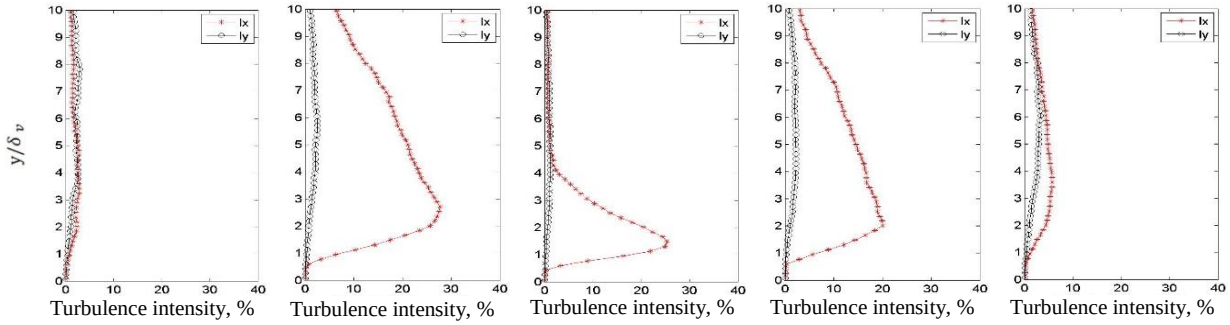

Figure 3.16: The measured turbulence intensities distribution based on axial (red dots) and traverse (black dots) at different phases over the acoustic cycle for different Reynolds numbers.

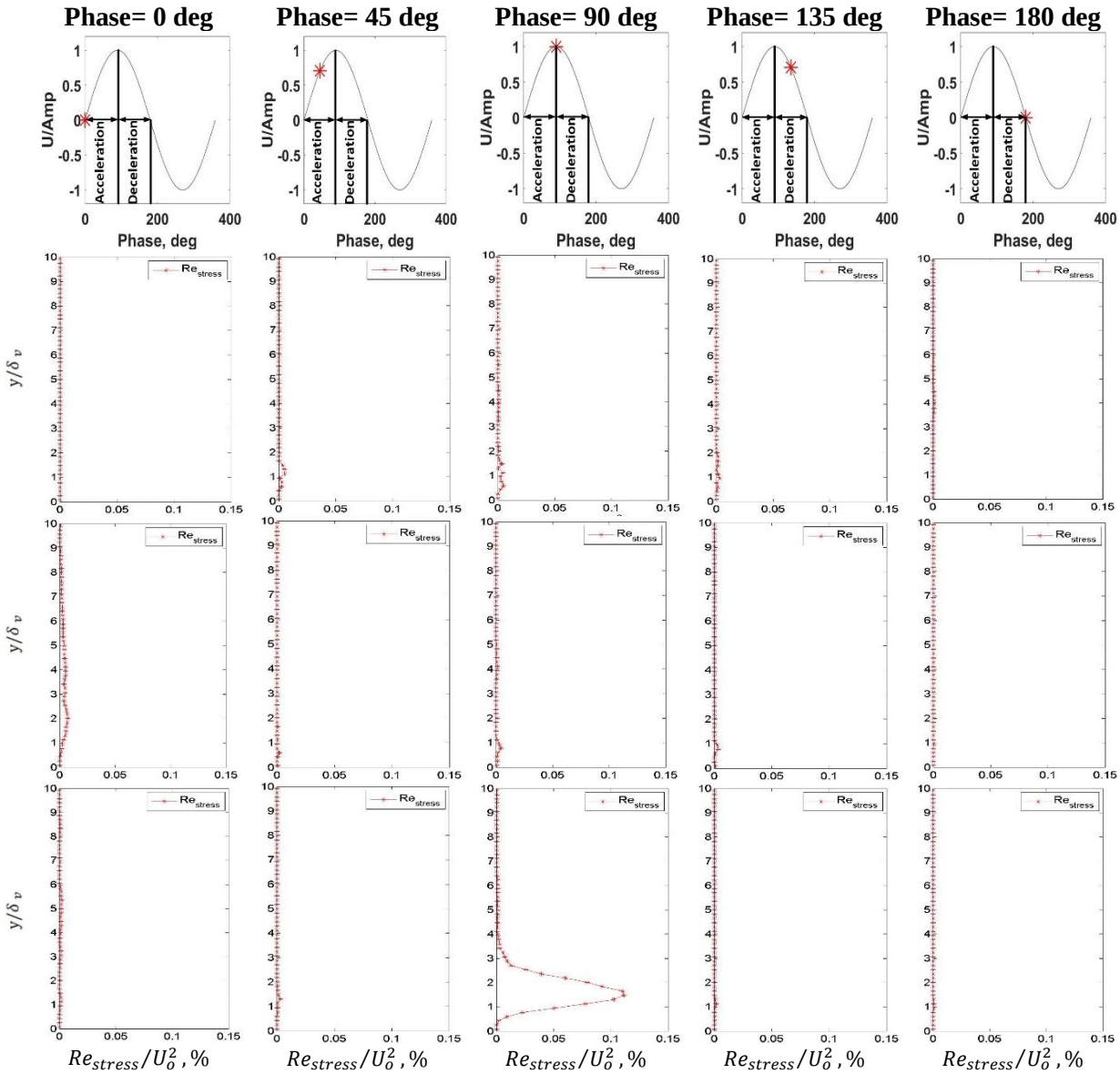

** Continued in the following page

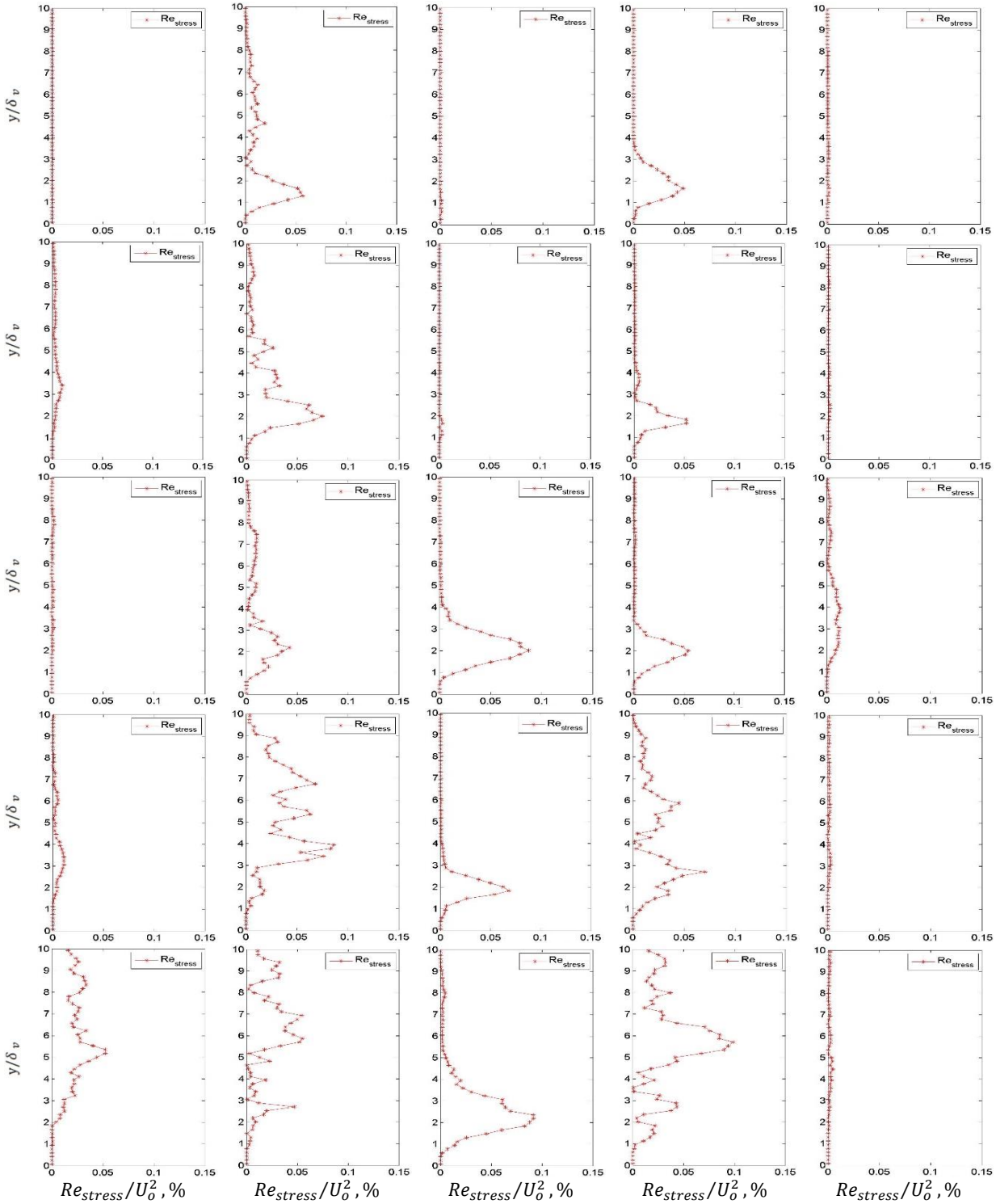

**** Continued in the following page**

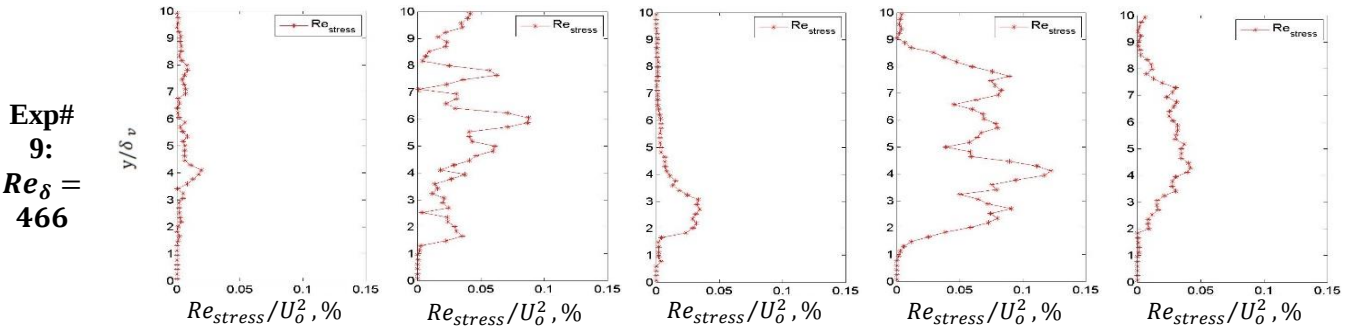

Figure 3.17: The distribution of the normalized Reynolds stress at different phases over the acoustic cycle for different Reynolds numbers.

In order to summarize the results discussed above, the phase-average turbulence intensities and the Reynolds stress are calculated. As shown in Fig. 3.18a, the turbulence intensity based on the axial velocity component (Ix) increases as the Reynolds number is increased. Also, the distribution peaks at a certain axial location (y). The peak location shifts away from the wall as the Reynolds number is increased. Moreover, the turbulence intensity based on travers velocity component (Iy) increases as the Reynolds number is increased, as shown in Fig. 3.18b.

Finally, the distribution of the phase-average normalized Reynolds stress (see Fig. 3.18c) is almost flat for Reynolds number up to 240. At Reynolds number of 272, the distribution is flat except for the traverse locations between δ_v and $2.5\delta_v$ where it peaks at a traverse location of around $1.5\delta_v$. This sudden peak in the distribution indicates the occurrence of turbulence and hence it can be concluded that the critical Reynolds number is around 272 which agrees with the previous literature [30], [69]. Also, As the Reynolds number increases, the location of the peak shifts gradually away from the wall. At Reynolds number higher than 418, a sudden increase in the level of the Reynolds stress is observed which may indicate the existence of fully turbulence features over the whole cycle.

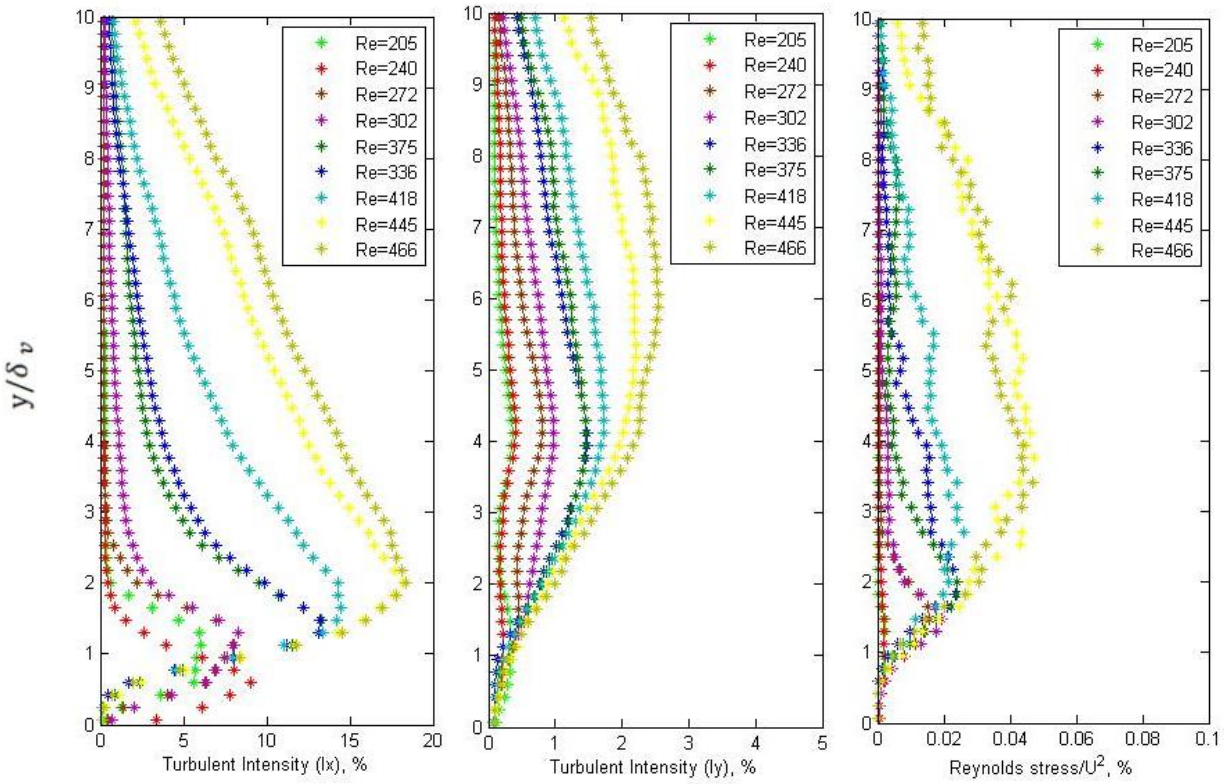

(a) **(b)** **(c)**

Figure 3.18: The distribution of the phase-average turbulence intensity based on axial velocity component (Ix), (b) The distribution of the phase-average turbulence intensity based on traverse velocity component (Iy), (c) The distribution of the normalized Reynolds stress.

3.3.2.B.4. Vorticity field

The vorticity field usually is used to describe the rotational characteristics of the flow. The vorticity field is mathematically defined as the curl of the velocity vector and can be expressed as follows:

$$\zeta \equiv \nabla \times \vec{V} \tag{3.24}$$

where $\vec{V}$ is the velocity vector. As the PIV system provides only two-dimensional velocity field, the vorticity field, perpendicular to that velocity field, can be calculated as follows:

$$\zeta_z = \frac{\partial \mathrm{v}}{\partial x} - \frac{\partial \mathrm{u}}{\partial y} \tag{3.25}$$

where u and v are the axial and the traverse velocity components at a given location, respectively. In the current work, the ensemble-average velocity fields are used to calculate the vorticity field numerically at different phases over the cycle (see appendix C.7 for the matlab code used). The data is produced for 25 different phases, however, only 5 phases are presented covering one half of the cycles because both halves are symmetric but with opposite directions.

As shown in Fig. 3.19, at low Reynolds number, the vorticity field shows a near zero value (i.e. green color) all over the domain except near to the wall ($y \leq 2\delta_v$). At traverse locations $y \leq 2\delta_v$, the intensity of the vorticity has a maximum value at the phase with maximum axial velocity at the center of the duct (i.e. 90 deg) because at this phase the velocity gradient near to the wall has a maximum value. At the phases where the axial velocity is zero at the center of the duct (i.e. 0 and 180 deg), the velocity distribution near to the wall has non-zero values (see Fig. 3.15) and hence there is a velocity gradient near to the wall which generates a non-zero vorticity field. Also, it can be observed that the vorticity field is nearly the same over the axial direction because the velocity distribution is almost constant over the axial distance within the measurement area.

As the Reynolds number is increased (up to 375), the intensity of the vorticity increases for traverse locations $y \leq 2\delta_v$, whereas the rest of the field still shows a zero value of vorticity. At higher Reynolds numbers ($Re_\delta \geq 418$), the vorticity has maximum values at the phase with maximum velocity at the center of the duct (i.e. 90 deg) and limited to the traverse location $y \leq 2\delta_v$. As the velocity decreases (phase 0, 45, 135 and 180), the vortex structure starts to move away from the wall and towards the center of the duct which explains why the turbulence intensities and the Reynolds stress peak at different traverse locations for different Reynolds number (see Fig. 3.18).

As the vorticity field describes the large turbulent structures, it is necessary to look for the small turbulent structures of the flow. In the following section, the Kolmogrov length scale will be calculated over the whole field of view.

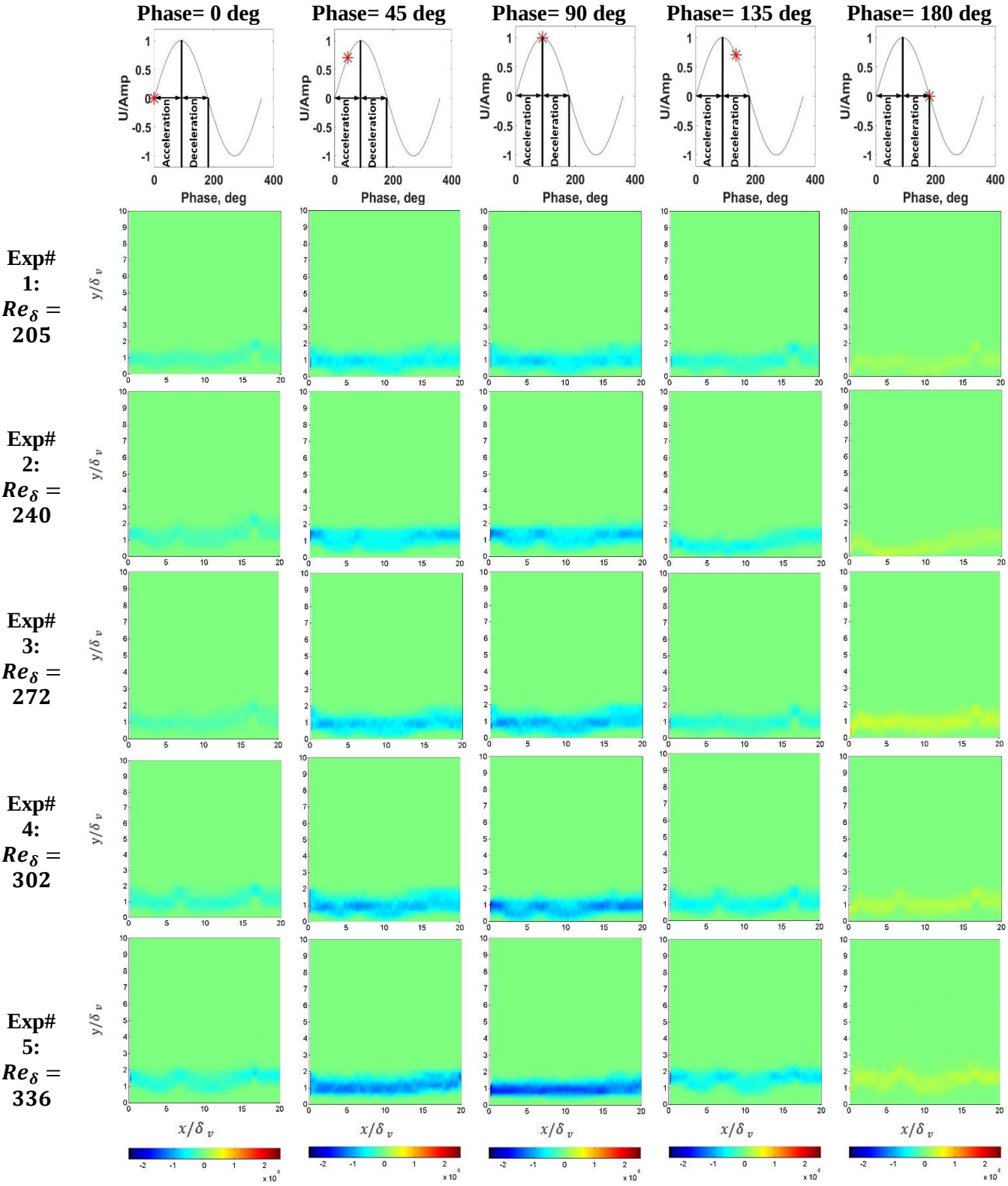

**** Continued in the following page**

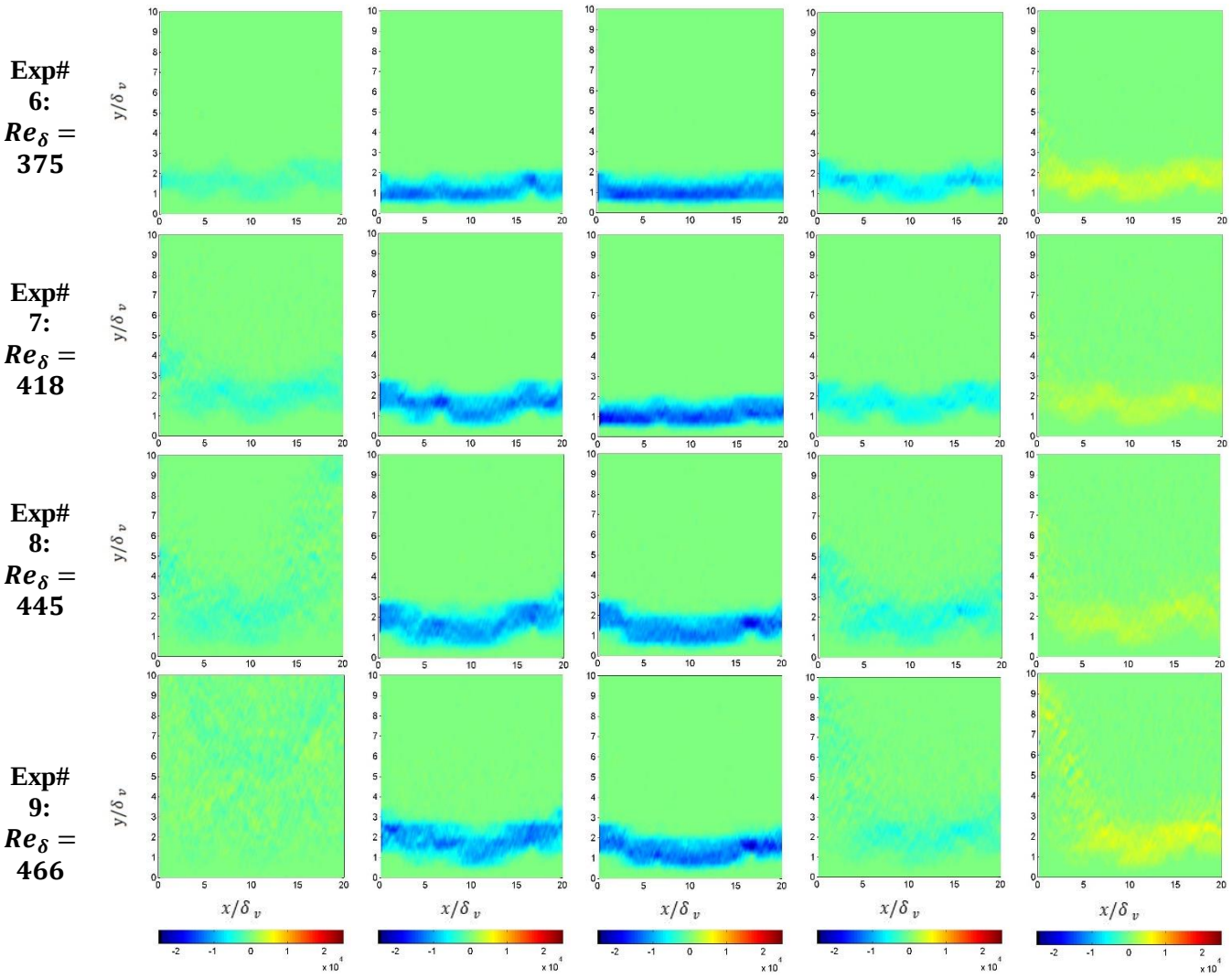

Figure 3.19: The vorticity field (in s^{-1}) at different phases for different Reynolds numbers.

3.3.2.B.5. Kolmogorov Length scale

Kolmogorov length scale defines the size of the smallest turbulence structure in the flow. At this smallest scale the turbulent kinetic energy is converted into heat via viscosity. The Kolmogorov length scale is mathematically described as follows [71]:

$$\eta = \left(\frac{\nu^3}{\epsilon}\right)^{\frac{1}{4}} \tag{3.26}$$

where ν is the kinematic viscosity and ϵ is the rate of dissipation of turbulent kinetic energy. In order to calculate ϵ, the nine components of the fluctuating velocity gradient $\left(\frac{\partial \dot{u}}{\partial x}, \frac{\partial \dot{u}}{\partial y}, \frac{\partial \dot{u}}{\partial z}, \frac{\partial \dot{v}}{\partial x}, \frac{\partial \dot{v}}{\partial y}, \frac{\partial \dot{v}}{\partial z}, \frac{\partial \dot{w}}{\partial x}, \frac{\partial \dot{w}}{\partial y}, \frac{\partial \dot{w}}{\partial z}\right)$ have to be available. Since these components cannot be

obtained for a typical 2D PIV measurement, some assumptions have to be made. If the flow is assumed to be homogeneous and isotropic then only one of these nine components is needed. However, this assumption does not employ the available four components that can be obtained from 2D PIV measurements. So, another assumption is made to utilize the available four components of the PIV measurement. This assumption is local isotropy of the flow, which can be expressed mathematically, as follows [72]:

$$\left(\frac{\partial \dot{u}}{\partial z}\right)^2 = \left(\frac{\partial \dot{w}}{\partial x}\right)^2 = \left(\frac{\partial \dot{v}}{\partial z}\right)^2 = \left(\frac{\partial \dot{w}}{\partial y}\right)^2 = \frac{1}{2}\left[\left(\frac{\partial \dot{u}}{\partial y}\right)^2 + \left(\frac{\partial \dot{v}}{\partial x}\right)^2\right] \tag{3.27}$$

$$\left(\frac{\partial \dot{u}}{\partial z}\frac{\partial \dot{w}}{\partial x}\right) = \left(\frac{\partial \dot{v}}{\partial z}\frac{\partial \dot{w}}{\partial y}\right) = \left(\frac{\partial \dot{u}}{\partial y}\frac{\partial \dot{v}}{\partial x}\right) \tag{3.28}$$

Hence, for 2D PIV measurements the rate of dissipation of turbulent kinetic energy can be calculated as follows [73]:

$$\epsilon = 3\nu\left[\left(\frac{\partial \dot{u}}{\partial x}\right)^2 + \left(\frac{\partial \dot{v}}{\partial y}\right)^2 + \left(\frac{\partial \dot{u}}{\partial y}\right)^2 + \left(\frac{\partial \dot{v}}{\partial x}\right)^2 + 2\left(\frac{\partial \dot{u}}{\partial y}\frac{\partial \dot{v}}{\partial x}\right)^2 + \frac{2}{3}\left(\frac{\partial \dot{u}}{\partial x}\frac{\partial \dot{v}}{\partial y}\right)^2\right] \tag{3.29}$$

where, $\dot{u}$ and $\dot{v}$ are the axial and traverse fluctuating velocity components, respectively.

When the PIV data is used to calculate the dissipation rate, the effect of the size of the interrogation area should be considered. Xu *et al.* [72] stated that the size of the interrogation area has a significant effect on the calculated value of ϵ. As the size of the interrogation area increases, the results deviate from the correct value. This deviation is mainly due to the fact that each velocity vector is obtained by averaging the velocity of the seeding particles within the interrogation area and thus the obtained velocity is a spatially filtered velocity. Also, they found that if the size of the interrogations area is twice the smallest length scale, there is an error of around 10 % in the calculated value of ϵ with the assumption of local isotropy. The error decreases as the size of the interrogation area decreases. In the current work, the size of the interrogation area is about 0.076 × 0.076 mm^2 which is less than the smallest length scale and hence this error is expected to be very small. The ensemble-average fluctuating velocity fields at different phases are used to calculate the distribution of the Kolmogorov length scale over the flow field (see appendix C.8 for the matlab code used). The data is produced for 25 different phases, however, only 5 phases are presented to cover one half of the cycles because both halves are symmetric.

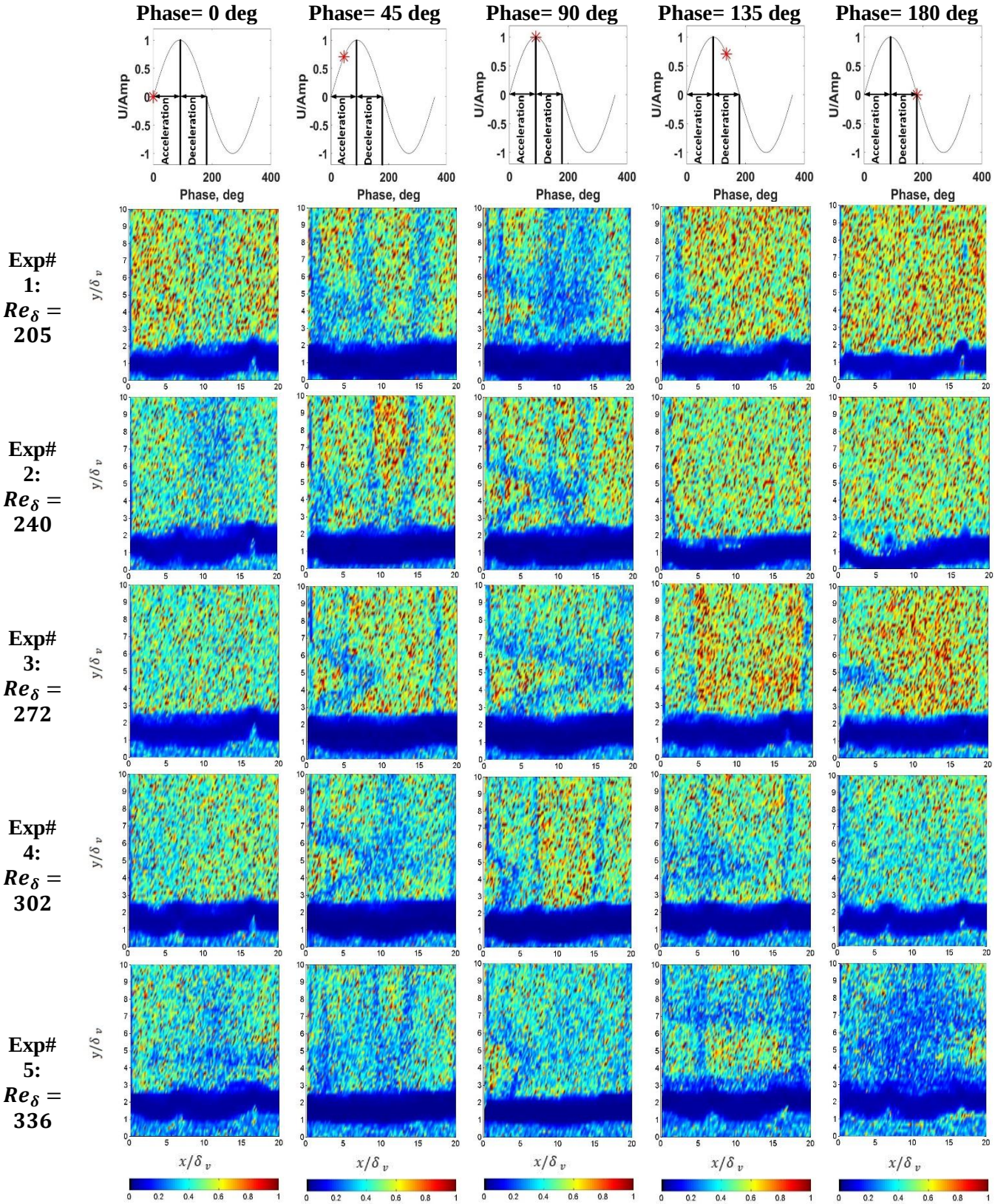

**** Continued in the following page**

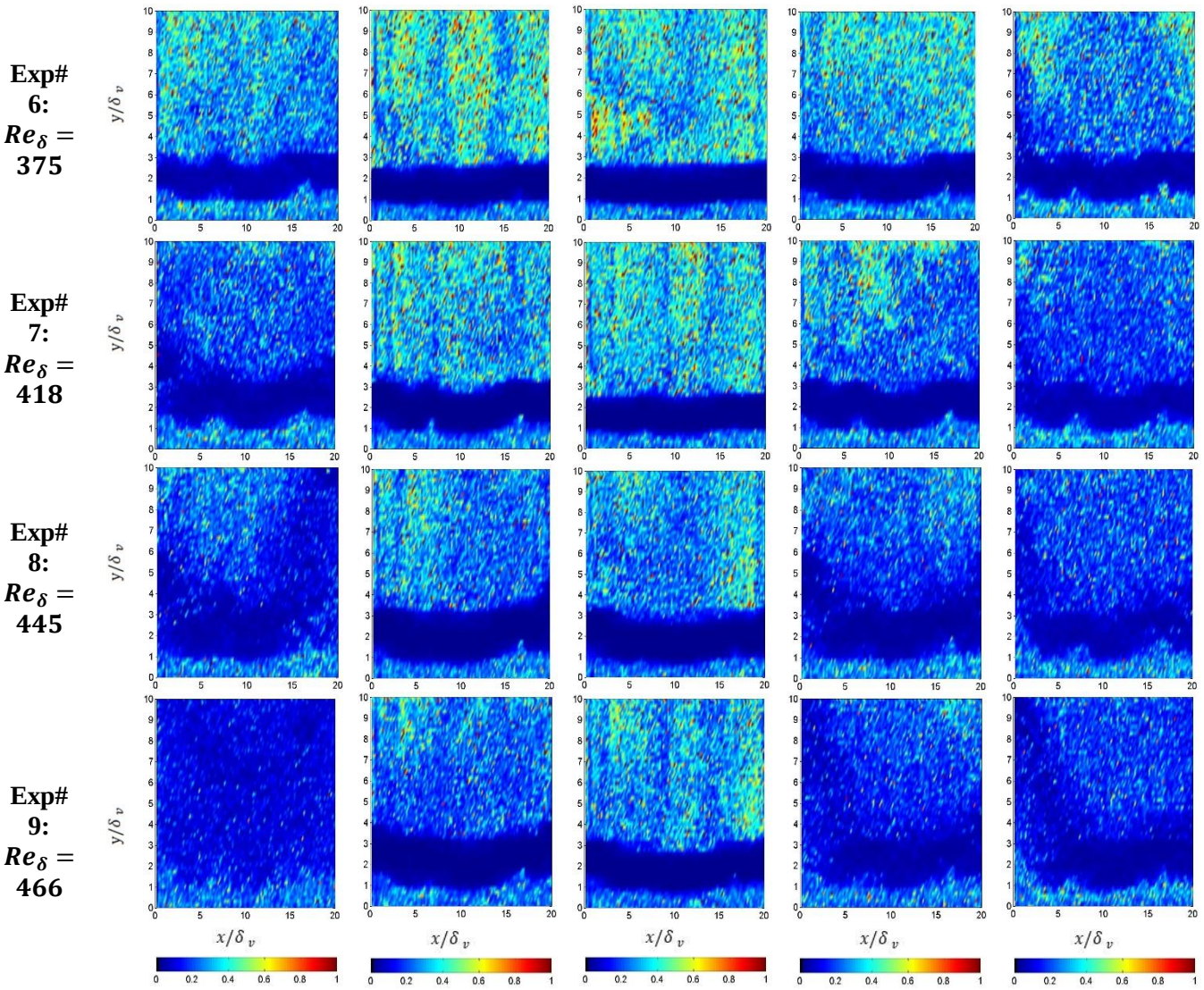

Figure 3.20: The Kolmogorov length scale (in mm) over the whole field of view at different phases for different Reynolds number.

As shown in Fig. 3.20, at low Reynolds number (i.e. 205), the smallest length scale (i.e. bluish-color) is limited to the traverse locations near to the wall (i.e. $y \leq 2\delta_v$). At the phase with the maximum velocity (i.e. 90 deg) the small length scales can be found at traverse locations (y) even larger than $2\delta_v$. As the Reynolds numbers increases (up to 302), the small length scales are mainly limited to the traverse locations (y) less than $2\delta_v$. For higher Reynolds number ($302 \leq Re_\delta \leq 466$), the small scales continue to spread in the whole field of view near the deceleration phases (i.e. 0, 135 and 180 deg), that may be an indication for the turbulence occurrence.

3.3.2.B.6. Spatial Energy spectra

The turbulent energy spectrum is one of the tools that describes the characteristics of the turbulent flows such as the decay of the turbulent kinetic energy across the different eddies. The most common energy spectrum is the temporal energy spectrum that gives an indication of the decay of the turbulent kinetic energy at different frequencies and it can be calculated from one-point time resolved measurement (e.g. LDA or hot wire). The other type of energy spectra is the spatial energy spectrum that describes the decay of the turbulent kinetic energy at different wavenumbers. The wavenumber (k_i) is defined as follows:

$$k_i = \frac{2\pi}{i \times S_{IA}} \tag{3.30}$$

where i is the interrogation area number and ranges from 2 to N (the total number of the interrogation areas in one direction) and S_{IA} is the side length of the interrogation area.

The spatial energy spectrum cannot be directly calculated from one-point measurement unless Taylor hypothesis of frozen turbulence [74] is utilized. This hypothesis assumes that the temporal turbulent energy spectrum at one fixed point is similar to the spectrum at different location due to the advection of the turbulent structures from one location to another with the mean flow velocity, known as convection velocity. However, using this hypothesis to calculate the spatial energy spectrum from one-point measurement leads to error especially at higher wave numbers [75]. Since the PIV technique provides the spatial distribution of the velocity in two dimensions, the spatial turbulent energy spectrum can be calculated directly without using the Taylor hypothesis.

In the current work, the PIV data is used to calculate the spatial turbulent energy spectra E_u and E_{v} based on the axial and the traverse fluctuating velocity components, respectively. The method used to calculate the spatial energy spectra are described in [76]. The ensemble-average data are used to calculate the energy at different wavenumbers (k). The maximum wave number corresponds to twice the size of the interrogation area (see appendix C.9 for the matlab code used to calculate the spatial energy spectra).

As shown in Fig. 3.21, the spatial turbulent energy spectra based on the axial fluctuating velocity component are plotted at different phases and for different Reynolds numbers. Also, the data is compared with the cycle-average spatial energy spectrum and the universal slope of the turbulent energy spectrum (-5/3). At all Reynolds numbers, it is observed that the spatial energy spectrum has a wavy pattern (i.e. fluctuating around a constant value) up to a certain wavenumber after which the energy level decays with a constant rate. The rate of the decay agrees well with the universal decay slope (-5/3). This wavy pattern may be due to the oscillating nature of the flow. Also, for all Reynolds numbers, it is observed that the cycle-average spatial energy spectrum is higher than the energy spectrum at the deceleration phases (0, 135 and 180 deg). During the acceleration phases (45 and 90 deg), the spatial energy spectrum is higher than the cycle-average spectrum. At any given phase, the energy level increases as the Reynolds number is increased.

As shown in Fig. 3.22, the spatial turbulent energy spectra based on the traverse fluctuating velocity component are plotted at different phases and for different Reynolds numbers. Also, the data is compared with the cycle-average spatial energy spectrum and the universal slope of the turbulent energy spectrum (i.e. -5/3). At a given Reynolds number, it is observed that the energy level is almost the same for all phases and hence, the cycle-average energy spectrum equals to energy spectrum at any phase.

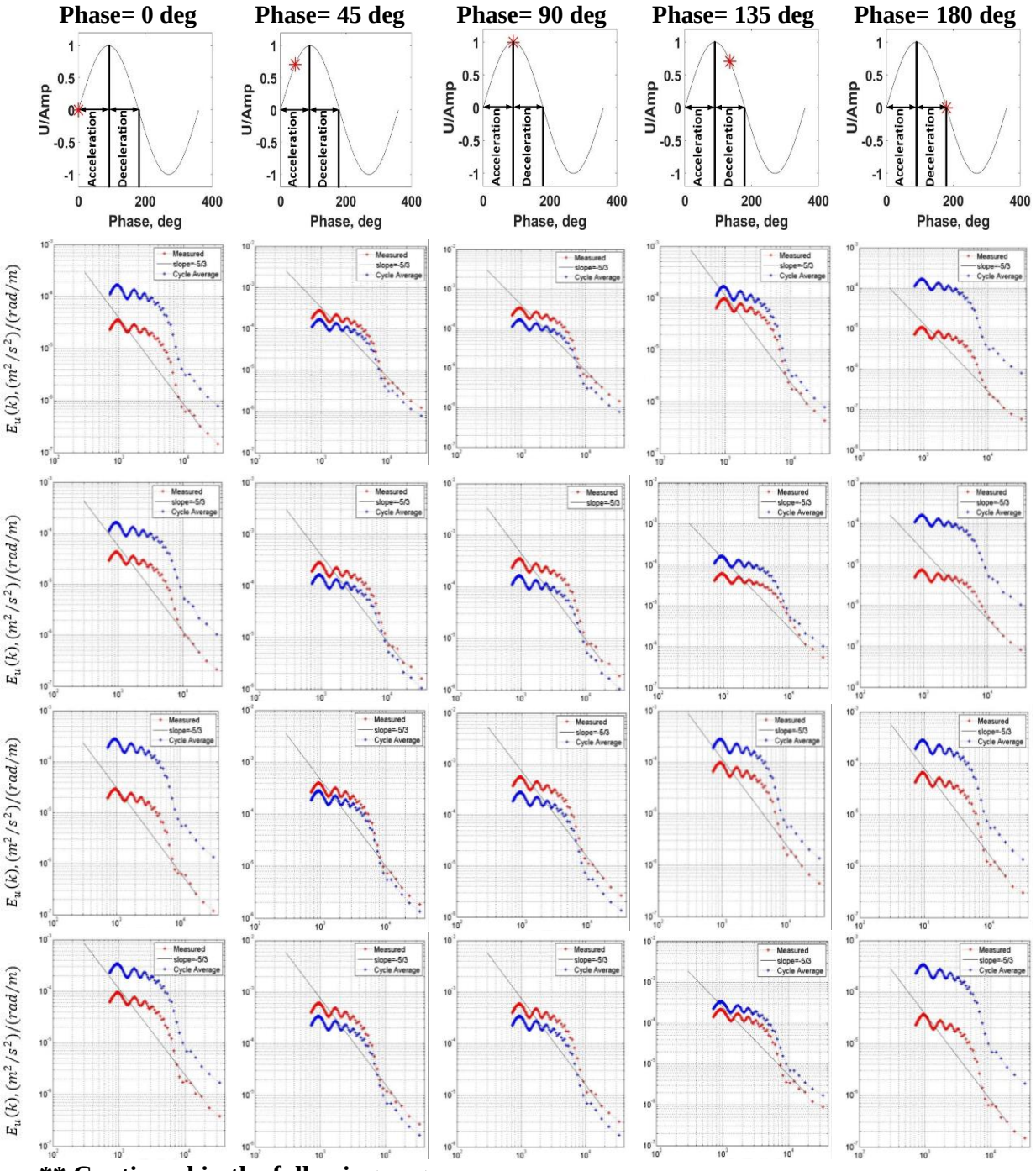

** Continued in the following page

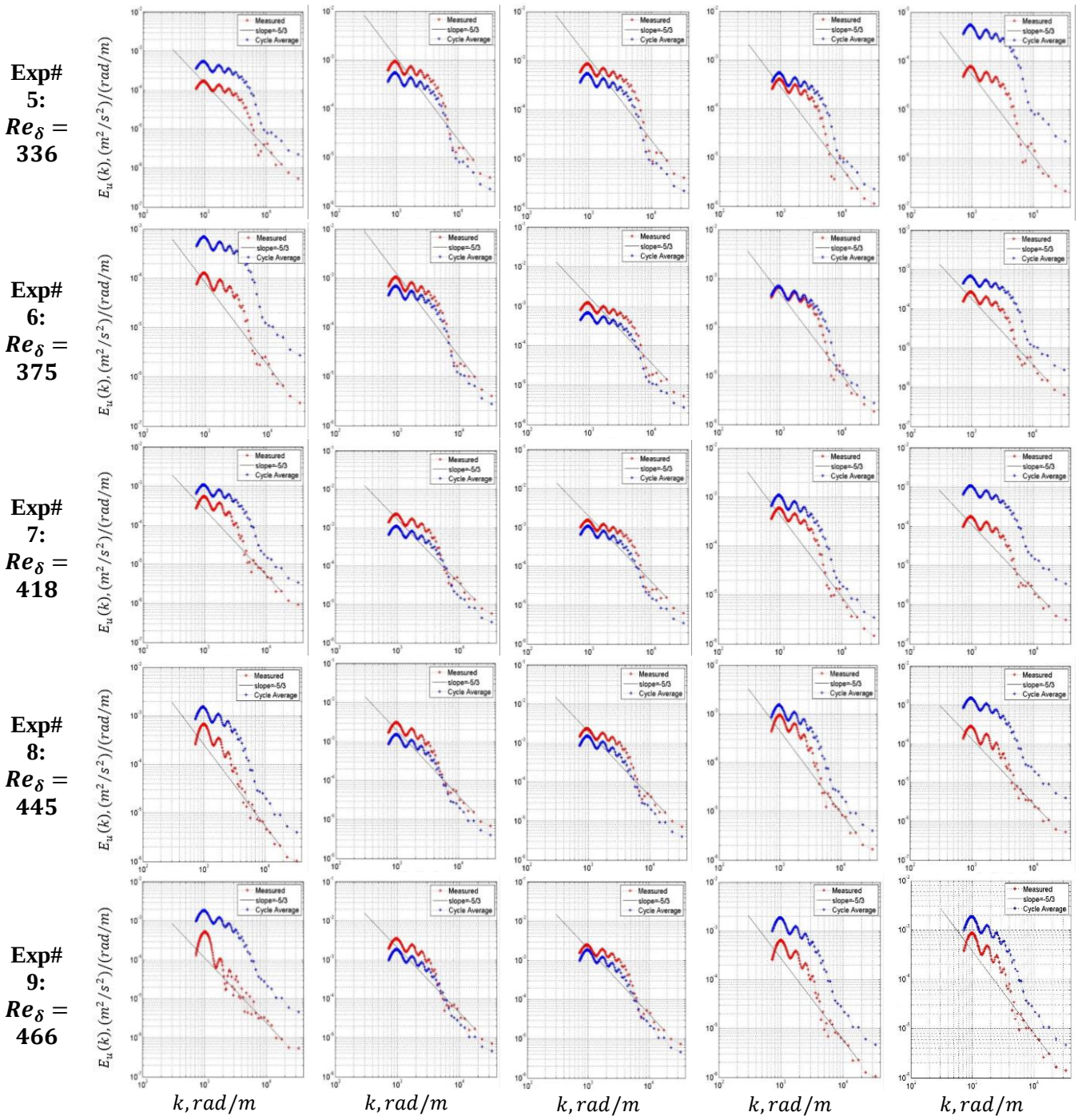

Figure 3.21: The spatial energy density spectra based on axial velocity component (red dots) at different phases compared to the cycle-average spatial energy spectra (blue dots) and the universal slope of -5/3 (solid line).

This is unlike the spatial energy spectra based on the axial fluctuating velocity component (see Fig. 3.21) because the main flow doesn't have obvious oscillating behavior in the traverse direction compared to the axial direction. Also, the wavy-pattern presented in Fig. 3.21 is not obvious with

the spectrum based on traverse velocity component. The decay of the energy with wave number has a slope similar to the universal slope (-5/3). Also, the energy level increases as the Reynolds number is increased.

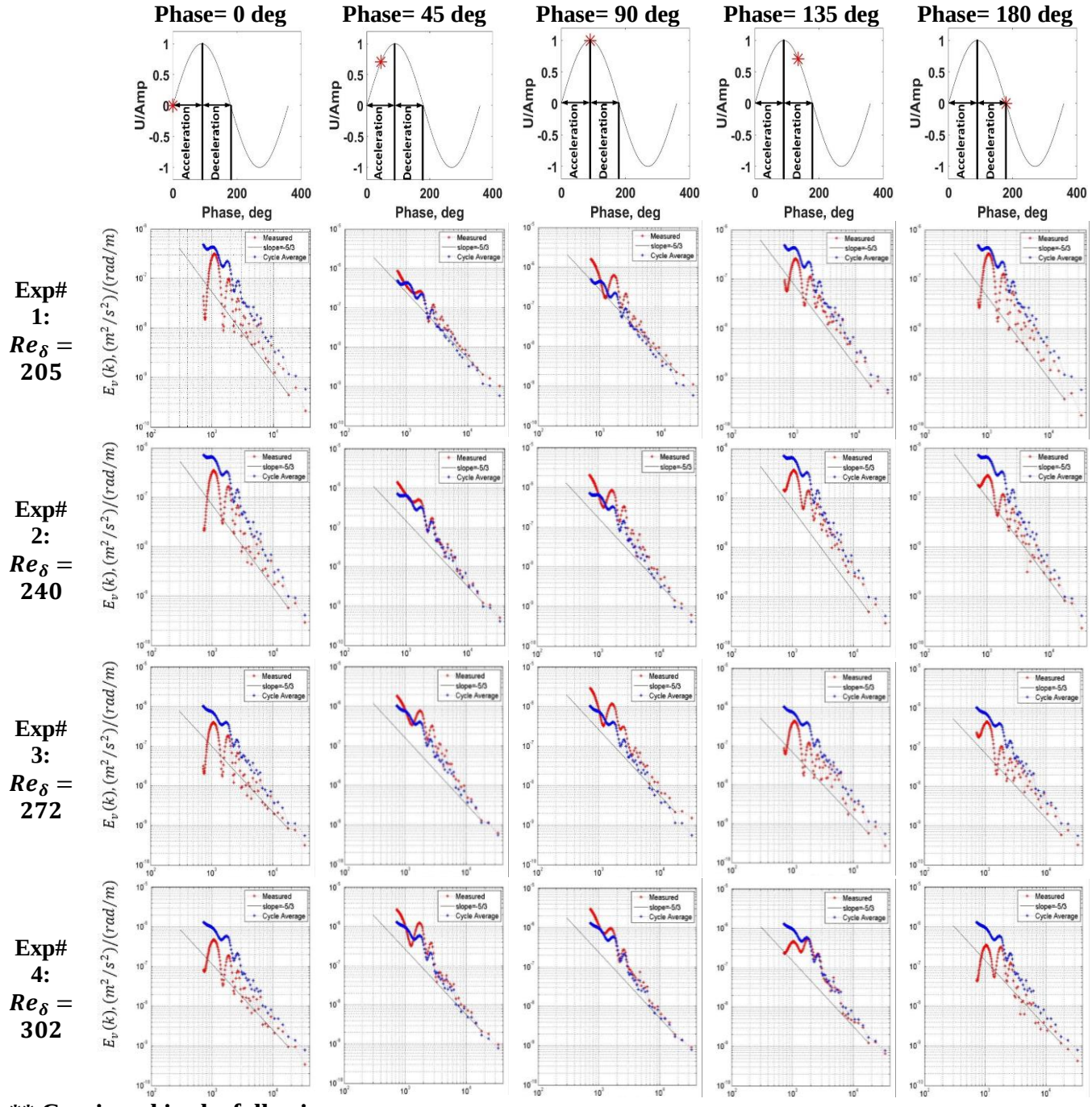

**** Continued in the following page**

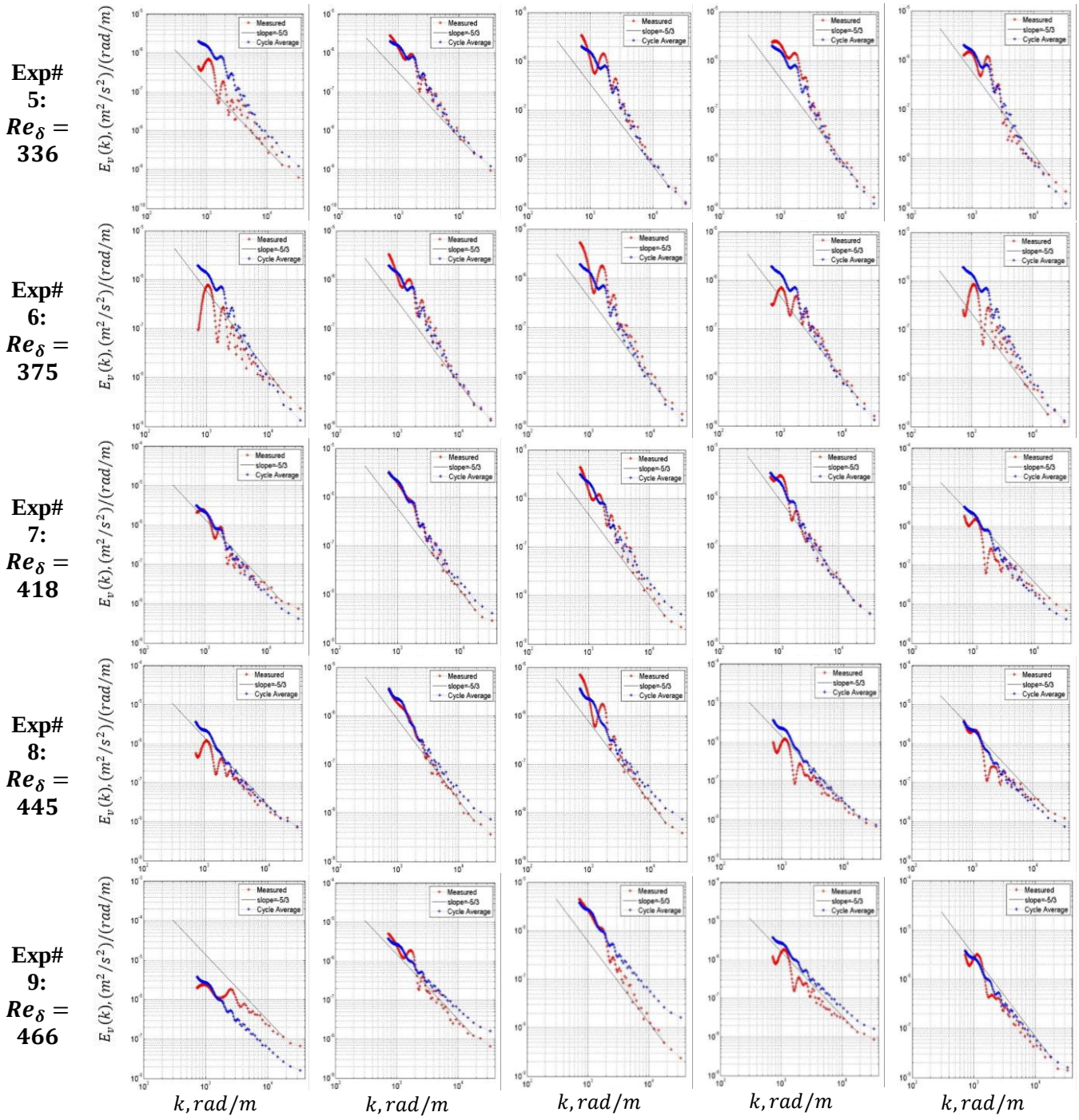

Figure 3.22: The spatial energy density spectra based on traverse velocity component (red dots) at different phases compared to the cycle-average spatial energy spectra (blue dots) and the universal slope of -5/3 (solid line).

In order to summarize the results, the cycle-average energy spectra for different Reynolds number are plotted in Fig. 3.23. The cycle-average spatial energy spectra E_u at small wavenumbers have wavy-pattern which may be due to the oscillating behavior of the flow because in steady turbulent

flows, this phenomenon (wavy pattern of the spatial energy spectrum) was not observed [76]. At larger wavenumbers, the energy spectra decay with slope of -5/3 which means that there is no difference between the decay of the turbulent fluctuations in the oscillating flow and steady flow at high wavenumbers. Also, the energy level of the spectra increase as the Reynolds number is increased.

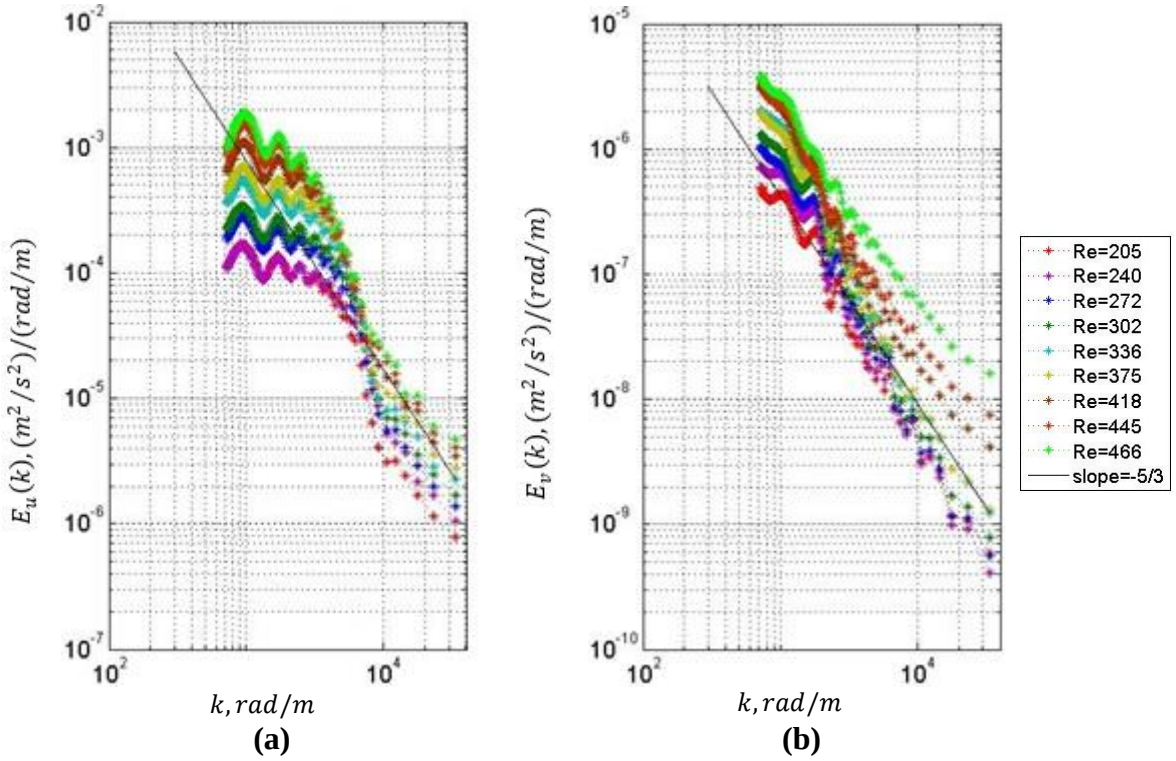

Figure 3.23: (a) The cycle-average spatial energy density spectra of axial velocity component. (b) The cycle-average spatial energy density spectra of traverse velocity component.

3.4. Conclusions

The transition to turbulence in oscillating flow at low frequencies has been investigated experimentally using PIV measurements. The axial velocity distribution in a square duct is measured at different Reynolds numbers and Womersley numbers and compared with the theoretical expectations based on the analytical solution of the Navier Stokes equations. At low Reynolds number, the measured values are in agreement with the theoretical expectations. As the Reynolds number is increased the agreement is violated in the deceleration phase first and then in more phases during the cycle. At the critical Reynolds number of around 500, it is observed that there is a sudden jump in the level of the axial turbulence intensity. These findings comply with the previous literature and hence they validate the use of the PIV system to study the transition to turbulence in oscillating flow. Therefore, the work is extended to high (i.e. acoustic) frequency range.

At high (acoustic) frequency range, the transition to turbulence has been investigated using PIV measurements. The Reynolds stress distribution is utilized as a criterion for the occurrence of turbulence. At low Reynolds number, it is observed that the Reynolds stress distribution is flat and equals to zero. At Reynolds number of 272, a sudden increase in the Reynolds stress value is observed at a traverse location of around $1.5\delta_v$. This sudden increase is due to the occurrence of turbulence. As the Reynolds number increases, the location of the peak in the Reynolds stress distribution moves gradually away from the wall. At Reynolds number higher than 418, another sudden increase in the level of the Reynolds stress is observed which may indicate the end of the transition to turbulence regime and the start of fully turbulent oscillating flow. Figure 3.24 summarizes the findings of the current work and compares it with the findings of the previous literature. Also, the spatial energy spectra of the flow are investigated. It shows an increase in the turbulent kinetic energy level as the Reynolds number increases. Also, at a given Reynolds number, the decay of the turbulent kinetic energy with the wavenumber complies with the universal slope (-5/3) in the Taylor region.

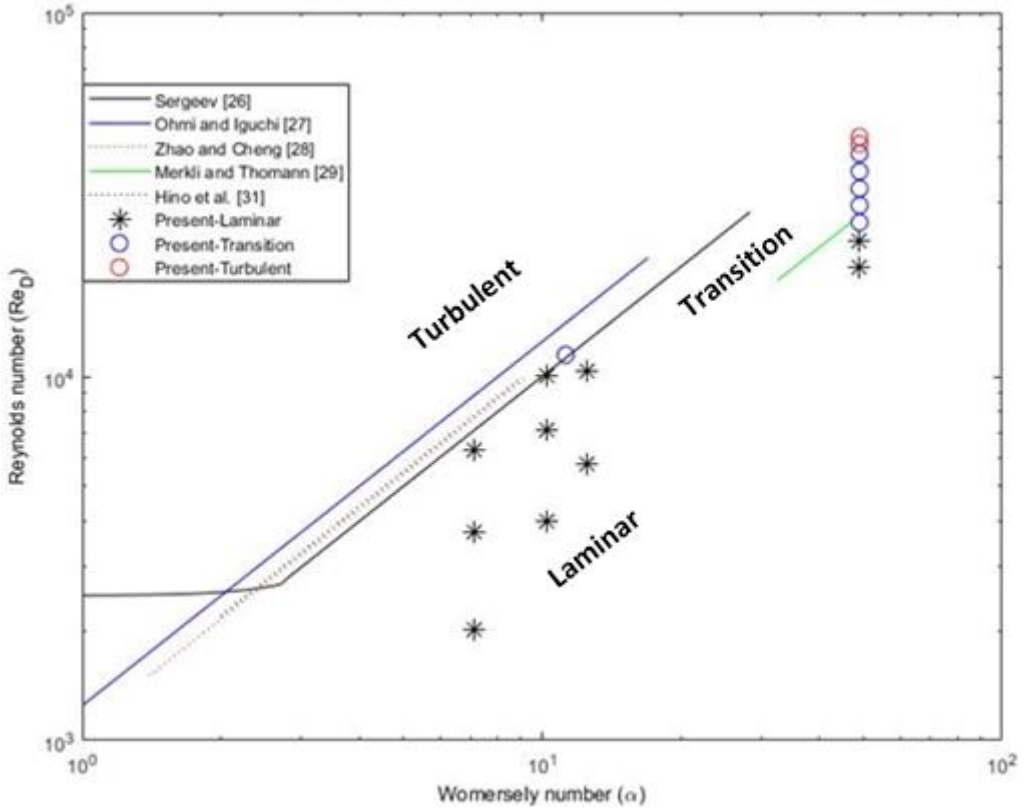

Figure 3.24: Graphical representation for the findings of the present work as compared to the previous literature.

3.5. Recommendations for future work

The transition to turbulence in the oscillating flows is an important topic in many applications such as thermoacoustic systems (i.e. engine and refrigerator). In the current work, the transition to turbulence is investigated using PIV system inside an empty resonator at ambient conditions. However, the real thermoacoustic systems have many components and mean temperature varies inside these systems and hence it is important to study the turbulent characteristics of the flow inside high amplitude real thermoacoustic systems. Also, the current study investigated the transition to turbulence at only one frequency in the acoustic frequency range. Hence, it may be necessary to investigate how the higher frequencies affected the transition to turbulence.

Chapter 4: Effects of the plate-end shape on the oscillating flow morphology

As mentioned in the introduction section, this chapter focuses on the effects of the plate-end shape on the oscillating flow characteristics such as vorticity and turbulence intensities. The following subsections discuss the experimental setup, measurement techniques and signal processing tools used in this part of the study. Also, the results are discussed and conclusions are drawn by the end of the chapter.

4.1. Experimental setup

In the previous chapter, the transition to turbulence in the oscillating flow inside an empty resonator has been investigated at low and high frequency ranges. In thermoacoustic devices, the thermoacoustic process occurs in the thermoacoustic core which consists of stack and heat exchangers. So, the effects of these components on the oscillating flow characteristics (e.g. vorticity, non-periodicity or turbulence intensity) have to be investigated. For simplicity, the stack is usually modelled as a set of parallel plates separated by a certain distance.

In the current study, the effects of the plate-end shape on the flow morphology have been investigated experimentally using PIV measurements. As shown in Fig. 4.1, the plates are placed at the center of the resonator (see section 3.1.2. for detailed description of the resonator). The oscillating flow is generated by two opposite loudspeakers (see section 3.1.1.B. for detailed description of the loudspeakers) operating at the resonance frequency of the system (i.e. 23.3 Hz).

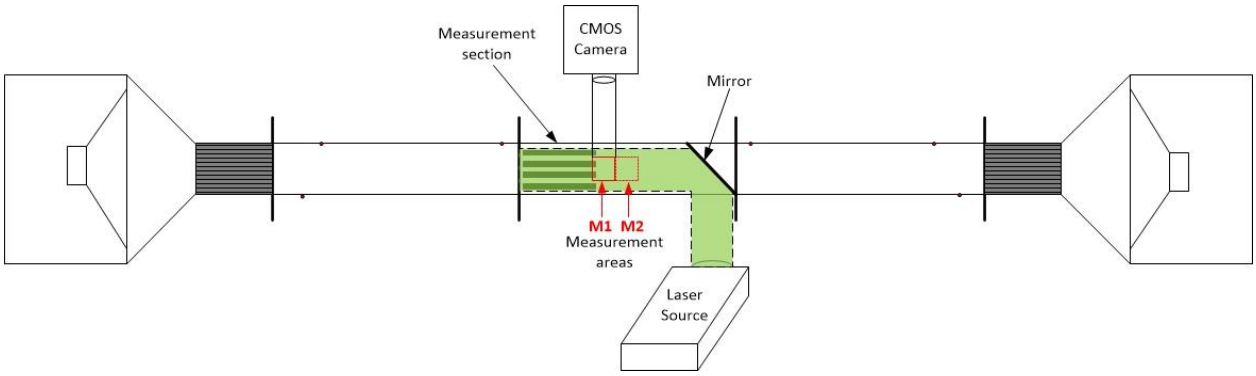

Figure 4.1: Schematic for the experimental setup showing the position of the plates and the PIV measurement system.

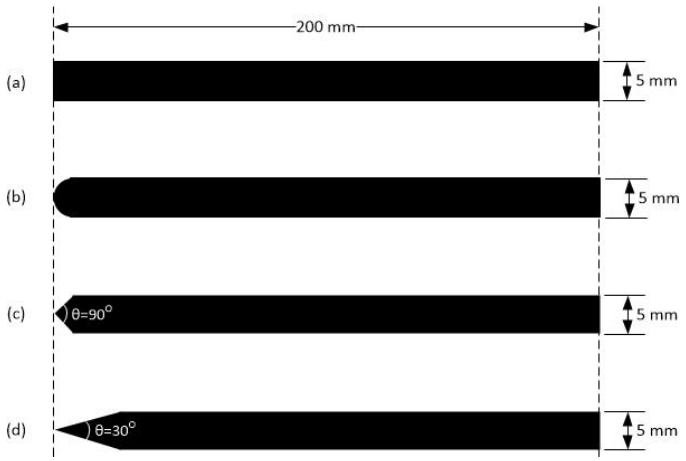

Figure 4.2: Schematic for the different plate-end shapes: (a) Rectangular, (b) Circular, (c) Triangular with cone angle of 90^O and (d) Triangular with cone angle of 30^O.

Four different plate sets are used. Each set consists of four parallel plates separated by a distance of 5 mm and have the same plate-end shape. As shown in Fig. 4.2, four different plate-end shapes (i.e. rectangular, circular, 90^O triangular and 30^O triangular) are used. Each plate has a width of 5 mm and a height of 43 mm (a bit less than the side length of the resonator, 45 mm). In order to eliminate the effects of one end of the plate on the other end, the length of the plate ($L_p = 200\ mm$) is chosen to be longer than the displacement amplitude of the oscillations. Hence, the Keulegan-Carpenter number (K_C), which is defined as follows:

$$K_C = \frac{U_o}{2\pi f L_p} \tag{4.1}$$

should be less than 1 to avoid interactions between the disturbances before and after the plates. As shown in Table 4.1, the maximum Keulegan-Carpenter number in the current study is 0.351.

It is worthwhile to mention that the four plate-end shapes used in the current study are similar to the shapes used in [62]. In that study the effects of the plate end-shape on the vorticity field were reported at one acoustic velocity amplitude. Also, the maximum Reynolds number (Re_δ) achieved in that study was about 67. However, it is important to investigate the effects of the plate-end shapes at high acoustic amplitudes and hence the current study focuses on these effects at higher Reynolds numbers (up to 302). As shown in Table 4.1, eight different experimental conditions are tested for each set of plates (4 sets) which results in total number of experiments of 32.

Table 4.1: Experimental conditions used for different plate-end shape.

Experimental Condition#	$\boldsymbol{f}$ (Hz)	$\boldsymbol{U_o}$ (m/s)	$X_{Amp} = \frac{\boldsymbol{U_o}}{2\pi f}$ (mm)	$\boldsymbol{\delta}$ (mm)	$\boldsymbol{Re_\delta}$	$\boldsymbol{\alpha}$	K_C
1	23.3	2.4	16.4	0.46	70	48.5	0.082
2	23.3	3.7	25.3	0.46	108	48.5	0.126
3	23.3	5.1	34.8	0.46	150	48.5	0.174

4	23.3	5.9	40.3	0.46	173	48.5	0.202
5	23.3	7.5	51.2	0.46	219	48.5	0.256
6	23.3	8.3	56.7	0.46	245	48.5	0.283
7	23.3	9.2	62.8	0.46	270	48.5	0.314
8	23.3	10.3	70.3	0.46	302	48.5	0.351

4.2. PIV measurements

The PIV measurements are performed to visualize the oscillating flow around the plates. For detailed description of the PIV system, refer to section 3.2.2. Also, the adjustment of the PIV system parameters are explained in section 3.2.3. As shown in Fig. 4.1, a mirror is used to divert the laser light sheet with 90 degrees in order to illuminate the measurement area. In order to avoid the interactions of the disturbances generated from mirror with the flow in the measurement area, the mirror is placed away from the plates with a distance (250 mm) much longer than the largest displacement amplitude of the oscillations (i.e. 70.4 mm).

In order to determine the furthest distance at which the disturbances can travel away from the plates, a prime lens (60 mm Nikon AF macro) is attached to the camera to provide a larger field of view. The size of the field of view is $54 \times 54\ mm^2$ with spatial resolution (i.e. size of the interrogation area) of 0.42 mm. However, the size of the field of view is not enough to cover large axial distance (i.e. 1.5 times the displacement amplitude) for some of the experimental conditions. For these experimental conditions ($Re_\delta \geq 150$), the camera is traversed axially to cover the required axial distance (i.e. 1.5 times the displacement amplitude). As shown in Fig. 4.1, there are two axial locations at which the measurements are performed namely M1 and M2.

Based on the findings presented in the previous chapter (see section 3.3.2.B.1. , the number of the averaged-cycles required to achieve the stationarity of the data is 100 cycles which also agrees with the findings of [77]. Hence, the measurement duration covers 100 cycles with 25 phases per cycle. So, the total number of velocity maps per measurement is 2500 maps.

4.3. Results and discussion

4.3.1. Vorticity field and velocity vector map

The vorticity field is an important measure for the rotational characteristics of the flow and it has been used in different studies, as mentioned in the introduction, to describe the oscillating flow around the parallel plates.

The ensemble-average velocity fields are used to get the vorticity fields. The calculations of the vorticity field are presented in section 3.3.2.B.4. The total number of the velocity vectors per map is 16129 (127 × 127) vectors. This number of vectors is a huge number and hence the individual vector will not be visible if the data is presented with the full resolution. Hence, each three columns are spatially-averaged to keep the velocity vector visible. The matlab code used to calculate and plot both the vorticity fields and vector maps is presented in appendix C.11.

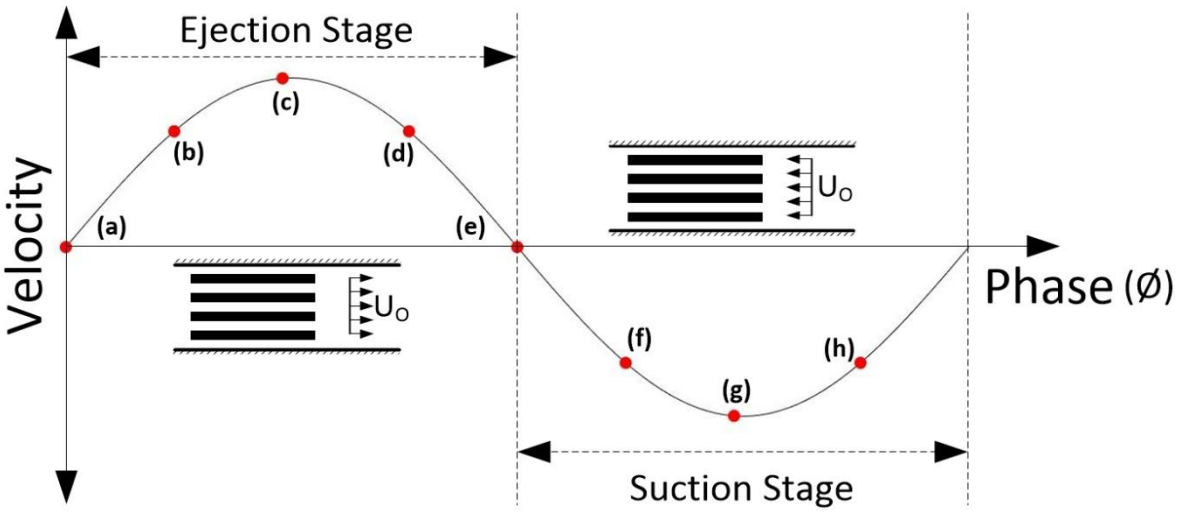

Figure 4.3: Representation for the selected phases over the acoustic cycle.

In the previous chapter, the vorticity fields are presented for only one half of the cycle because both halves are similar. However, in this part of the study, the vorticity field around the plates changes throughout the whole cycle because of the different flow morphology during the ejection and suction stages. As shown in Fig. 4.3, the first half of the cycle represents the ejection stage in which the flow moves outwards the plates. Whereas the other half of the cycle represents the suction stage in which the flow moves inwards the plates. Hence, the data are calculated for the whole 25 phases but only 8 phases (red dots), shown in Fig. 4.3, are selected to be presented in the current work. Furthermore, appendix E.2 includes a link for the videos that present the vorticity fields at the whole 25 phases and for all cases. In the following subsections, the results are presented for some cases only (see appendix E.2 for the results of all cases).

4.3.1.A. Vorticity field as a function of phase

The vorticity field changes throughout the whole cycle and hence, it is important to study the evolution of the vorticity field with time (i.e. phase). Figure 4.4 presents the vorticity field at different phases at Re_δ of 70 for the rectangular-plate end shape. As shown in Fig. 4.4a, the mean flow velocity is zero and the vorticity field has nearly zero value as well. As the velocity increases, the vorticity field start to develop in the boundary layers around the plates as shown in Fig. 4.4b. On one side of each plate there is a positive vorticity field whereas on the other side a negative vorticity field. As shown in Fig. 4.4c, there are two counter-rotating vortices attached to the plate-edge. As the velocity increases (see Fig. 4.4d), the vortices are transformed in two elongated vortices which is observed in [56]. The generated vortices are transported with the flow till they reach an axial distance nearly equals to one acoustic displacement amplitude (i.e. $^{x}/_{X_{Amp}} = 1$), as shown in Fig. 4.4d. As shown in Fig. 4.4e, the mean flow velocity is almost zero and there are two counter-rotating vortices attached to the edge of each plate. Afterwards, the flow direction is reversed (i.e. the flow moves inwards to the plates) and hence the vorticity is limited to the boundary layers around the plates, as shown in Fig. 4.4f. As the velocity increases, the intensity

magnitude of the vorticity (i.e. the intensity of the colors in the map) in the boundary layer increases, as shown in Fig. 4.4g.

The evolution of the vorticity field has been studied for different plate-end shapes at the same Re_δ of 70. As shown in Fig. 4.5, the evolution of the vorticity field for the circular plate-end shape with time is reported. For most of the phases, the vorticity field is similar to the rectangular plate-end shape presented in Fig. 4.4. However, at phase d (see Fig. 4.5d) the two counter-rotating vortices are not elongated as presented with the rectangular plate-end shape (see Fig. 4.4d). For the 90^O triangular plate-end shape (see Fig. 4.6), the generated vortices reach to an axial distance of about $x/X_{Amp} = 0.7$ which indicates that the triangular plate-end shape reduces the axial distance over which the flow is disturbed. Decreasing the cone angle of the triangular (see Fig. 4.7) makes further reduction in the distance over which the flow is distributed by the generated vortices (i.e. $x/X_{Amp} = 0.5$). This finding has direct impact on the optimum design of the stack shape in order to reduce the non-linear loss associated with the flow separation at the inlet/exit of the stack in a thermoacoustic engine and refrigerators.

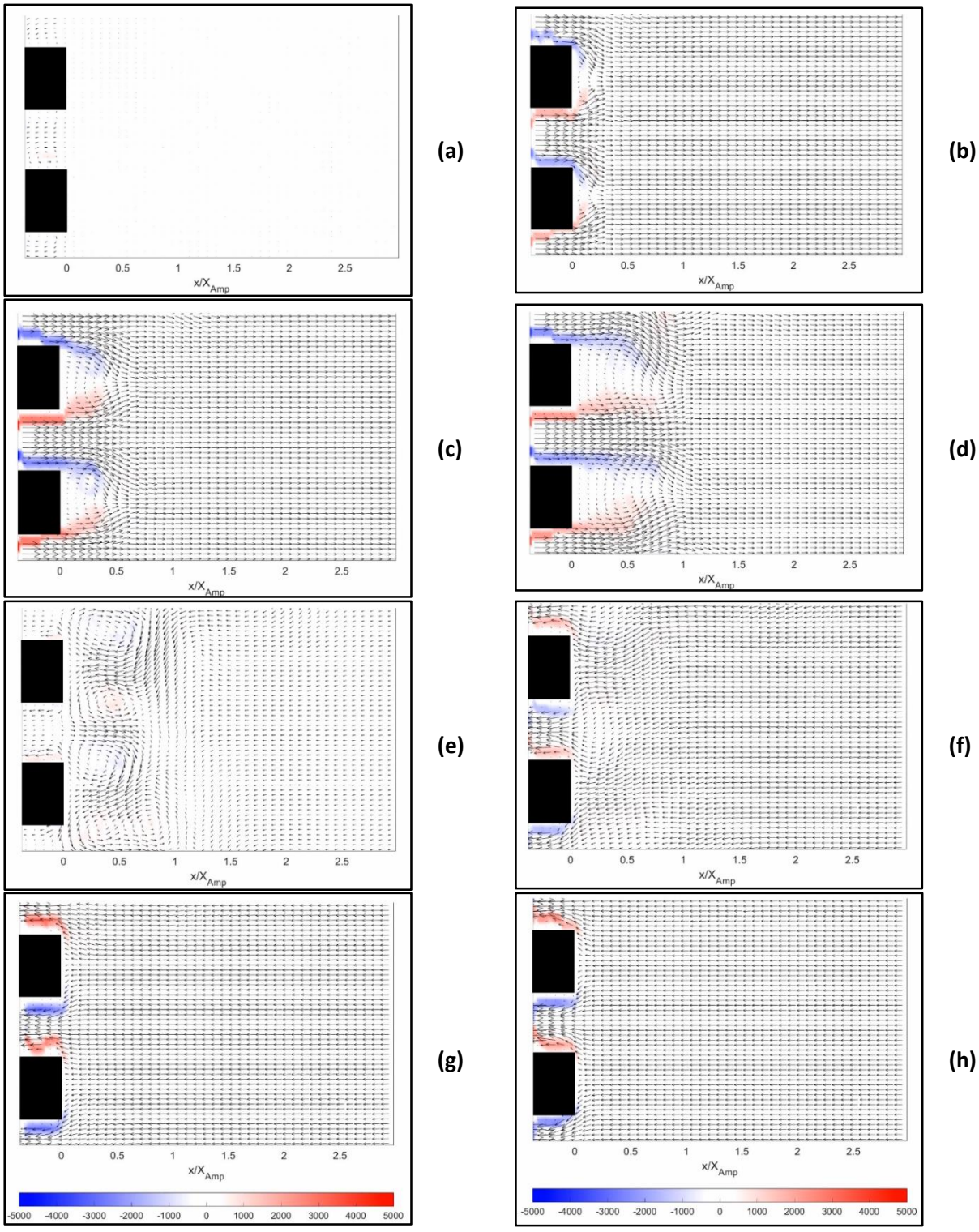

Figure 4.4: Vorticity field and vector map around the plates with rectangular end shape in the measurement area (M1) at different phases (a-h, see Fig. 4.3) over one acoustic cycle for Reynolds number (Re_δ) of 70.

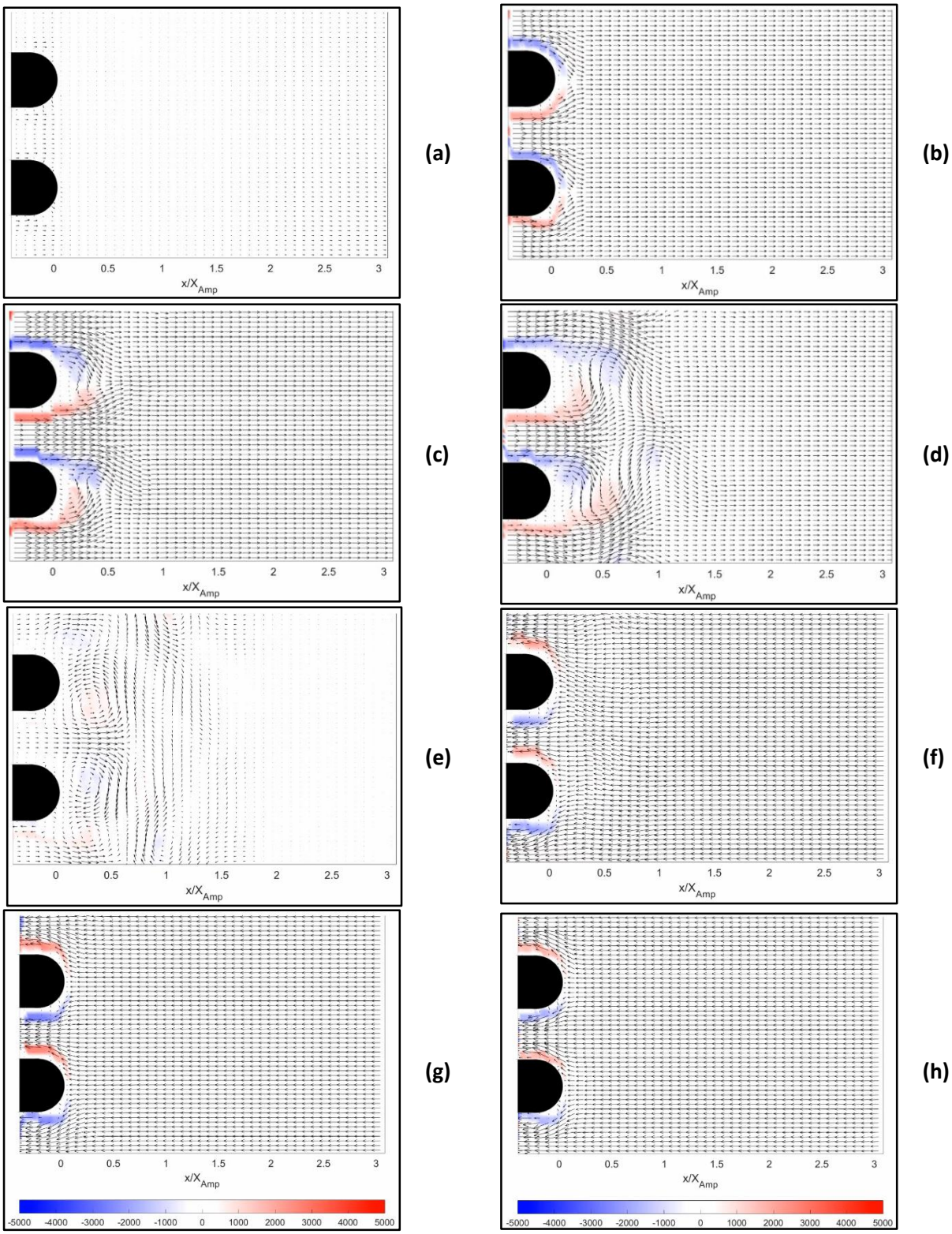

Figure 4.5: Vorticity field and vector map around the plates with circular end shape in the measurement area (M1) at different phases (a-h, see Fig. 4.3) over one acoustic cycle for Reynolds number (Re_δ) of 70.

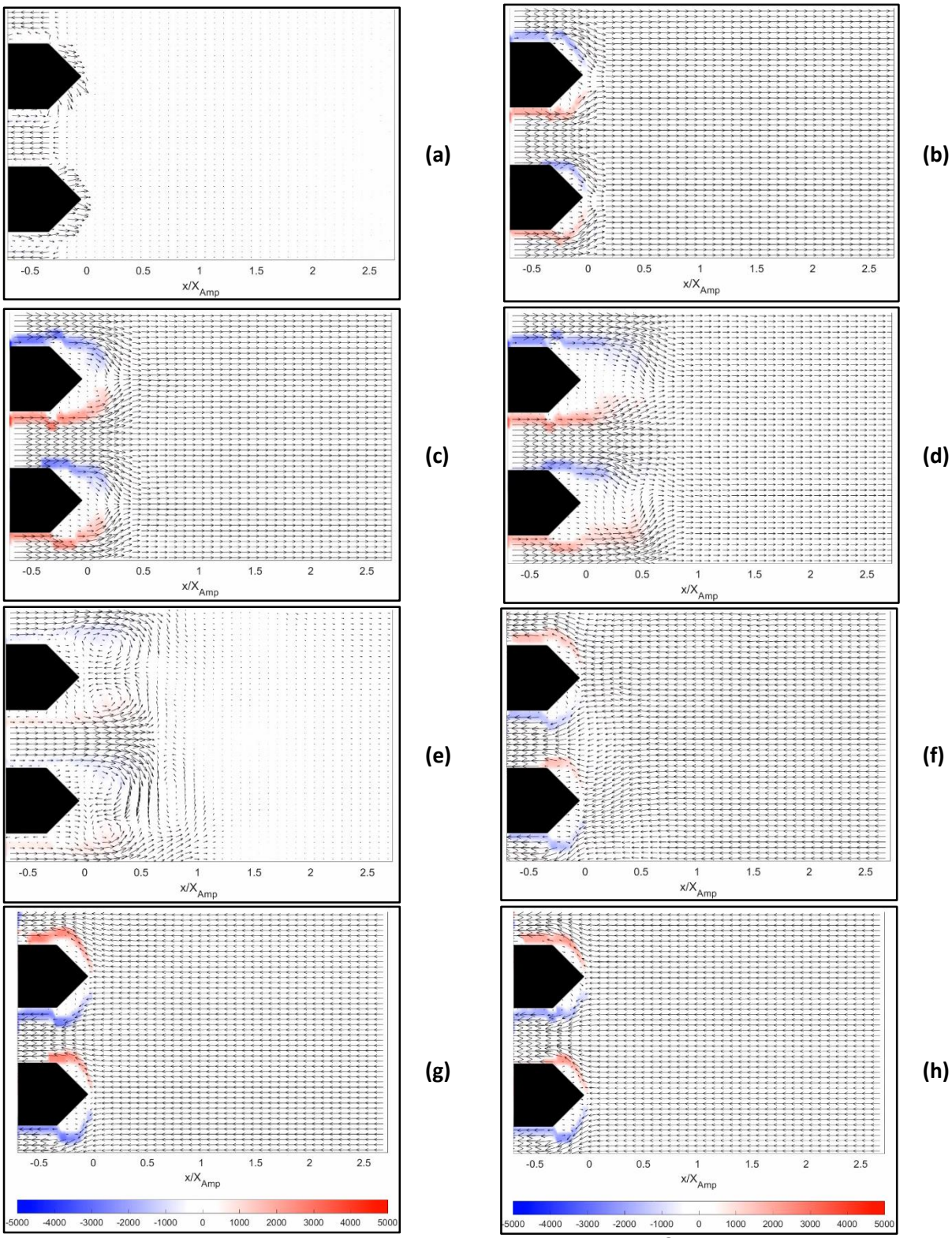

Figure 4.6: Vorticity field and vector map around the plates with 90^{O} triangular end shape in the measurement area (M1) at different phases (a-h, see Fig. 4.3) over one acoustic cycle for Reynolds number (Re_{δ}) of 70.

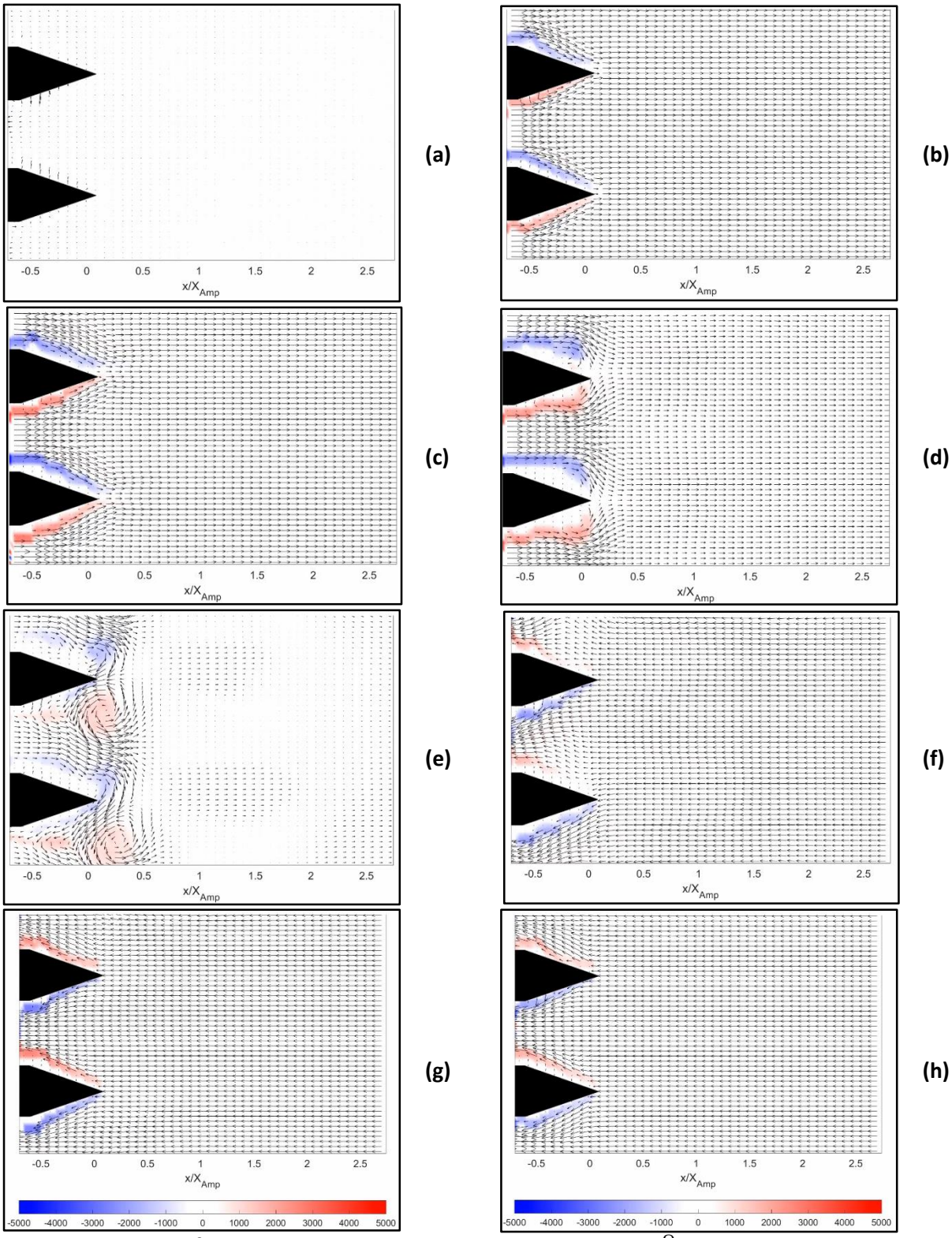

Figure 4.7: Vorticity field and vector map around the plates with 30^{O} triangular end shape in the measurement area (M1) at different phases (a-h, see Fig. 4.3) over one acoustic cycle for Reynolds number (Re_{δ}) of 70.

4.3.1.B. Effects of Reynolds number

The Reynolds number represents the ratio between the inertia force and viscous force and hence, this ratio affects the flow patterns around the plates. However, Aben *et al.* [62] found that not only the Reynolds number affects the flow patterns around the plates but also the Strouhal number (St), which is defined as follows:

$$St = \frac{Plate\ thickness * f}{U_O}. \tag{4.2}$$

In this work the Strouhal number (St) varies from 0.011 to 0.048. As shown in Fig. 4.8, the vorticity fields and vector maps are presented for three different Reynolds number at different phases (a-h) for the plates with rectangular end-shape. At the beginning of the ejection stage (i.e. phase a), the mean flow velocity is almost zero and also the vorticity in the vicinity of the plates has a very weak value (i.e. almost zero). At phase c, the intensity of the vorticity field increases as the Reynolds number is increased. At low Reynolds number (i.e. $Re_\delta = 70$), two counter-rotating vortices are attached to the plate end. As the Reynolds number increases the vortices transformed into two elongated vortices attached to the plate end. In addition, two separated vortices are observed at the end of the elongated vortices. As the velocity ejection stage decreases (phase d), the two separated vortices are disappeared. Also, the disturbance in the flow extends to an axial distance nearly equals to one acoustic displacement amplitude. During the suction stage (phases e-h), the vorticity in limited to the boundary layers around each plate. Same phenomena are observed with the case of circular-plate end shapes (see Fig. 4.9). For the 90^O triangular plate end-shape (see Fig. 4.10), two counter-rotating vortices are observed at low Reynolds number. At higher Reynolds numbers, two elongated vortices are observed and there are no separated vortices observed unlike the case of rectangular plate end-shape. Same observations are recorded for the 30^O triangular plate-end shape. However, the disturbances in the case of 30^O triangular (see Fig. 4.11) plate-end shape extend to a smaller axial distance (i.e. less than one acoustic displacement amplitude). Generally, there is no much change in the vortex patterns at different Reynolds numbers because the range of the Strouhal number (St) in the current study is very low and also the Reynolds number range is very high. According to the findings of [62], the vortex pattern tends to the elongated vortex pattern for high Reynolds number and low Strouhal number.

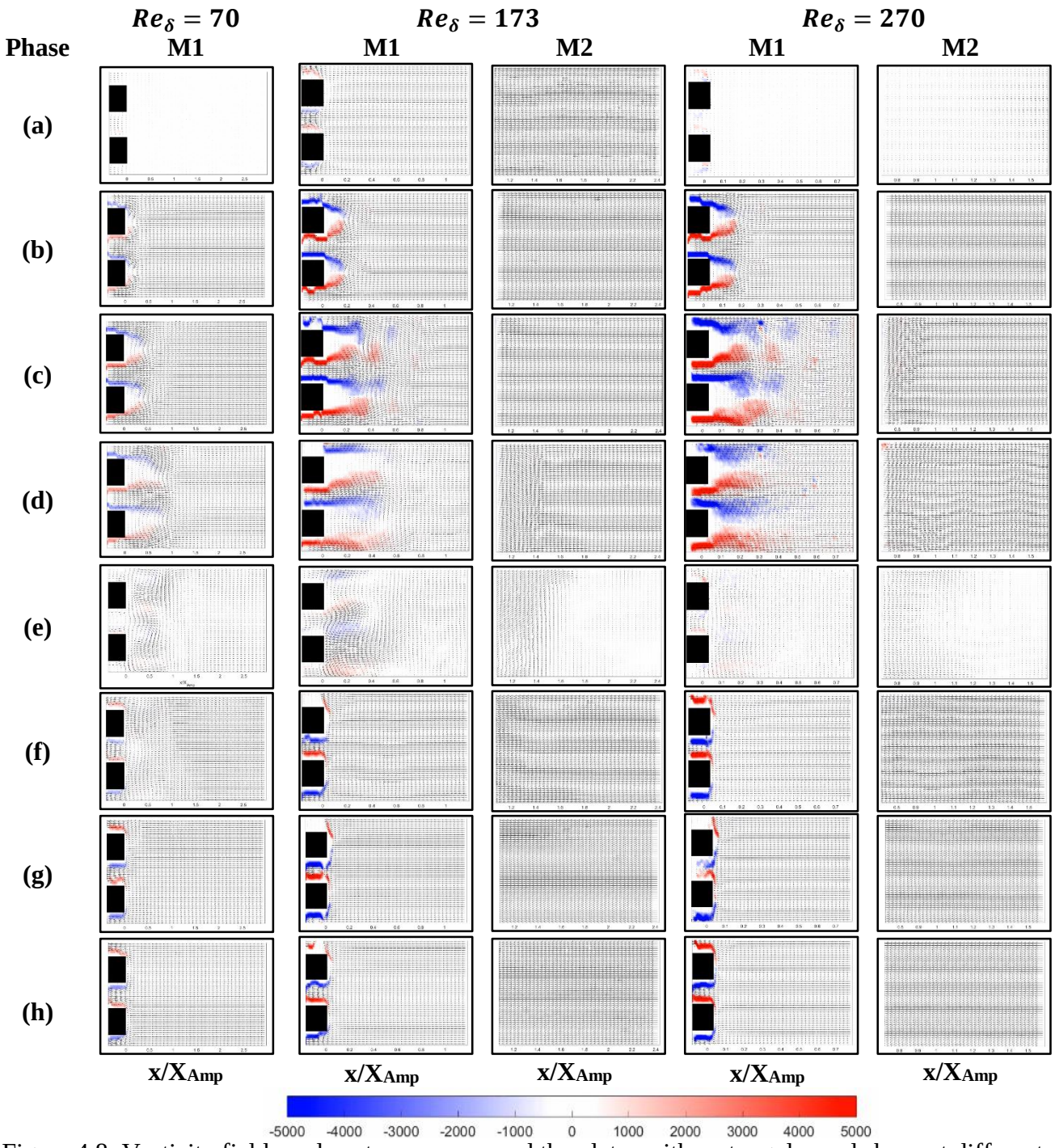

Figure 4.8: Vorticity fields and vector maps around the plates with rectangular end shape at different phases (a-h, see Fig. 4.3) for three different Reynolds.

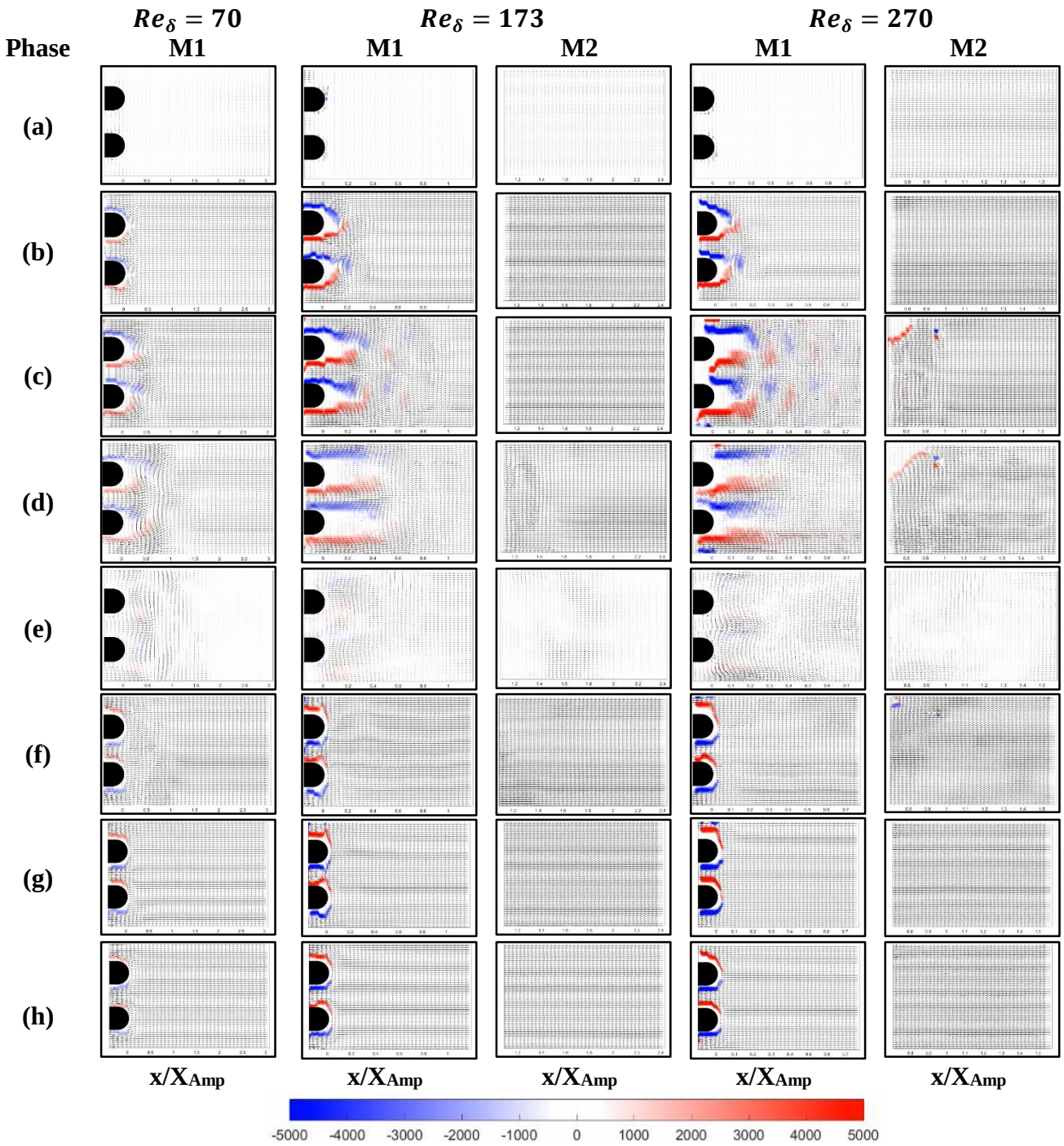

Figure 4.9: Vorticity fields and vector maps around the plates with circular end shape at different phases (a-h, see Fig. 4.3) for three different Reynolds.

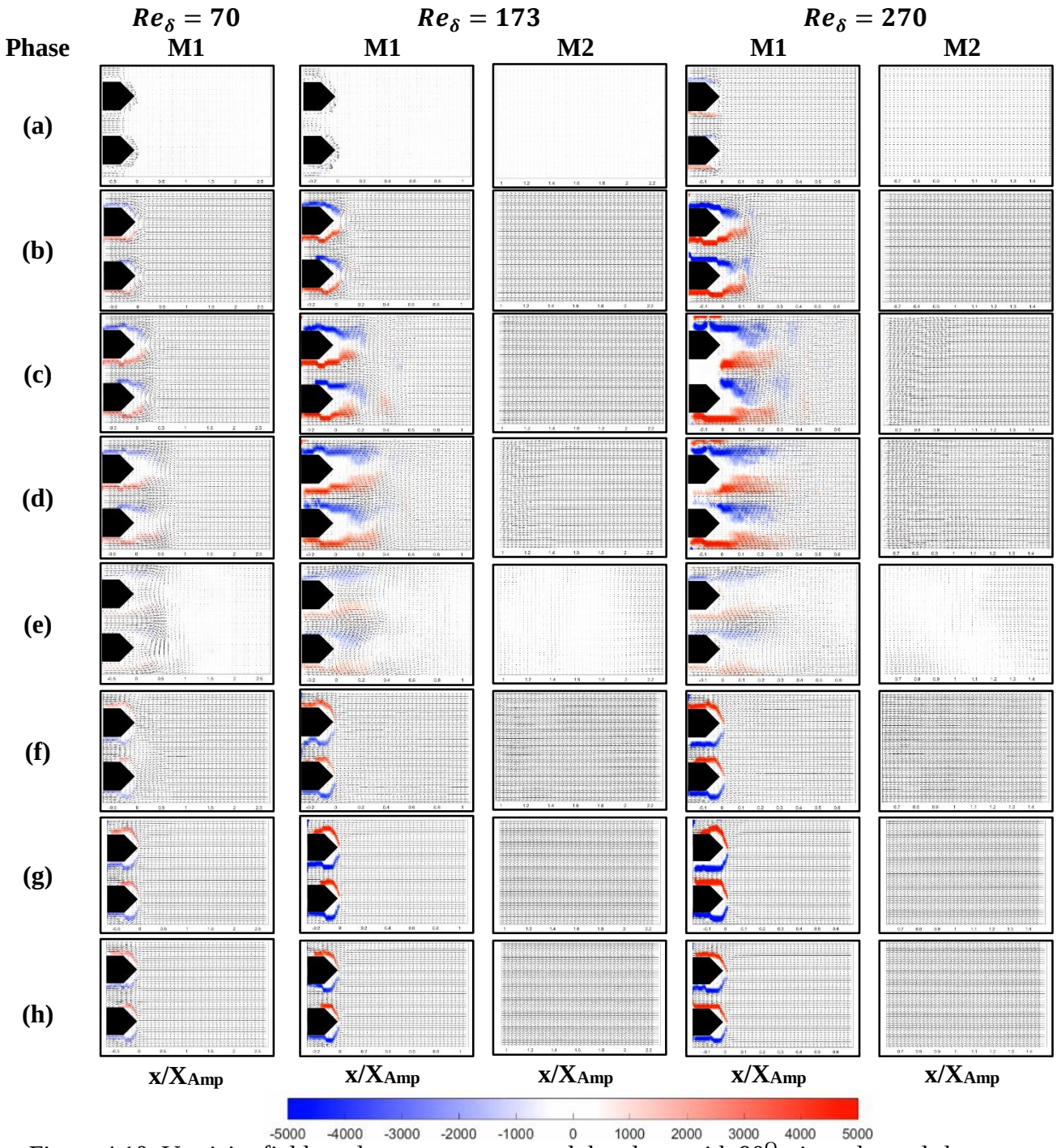

Figure 4.10: Vorticity fields and vector maps around the plates with 90^O triangular end shape at different phases (a-h, see Fig. 4.3) for three different Reynolds.

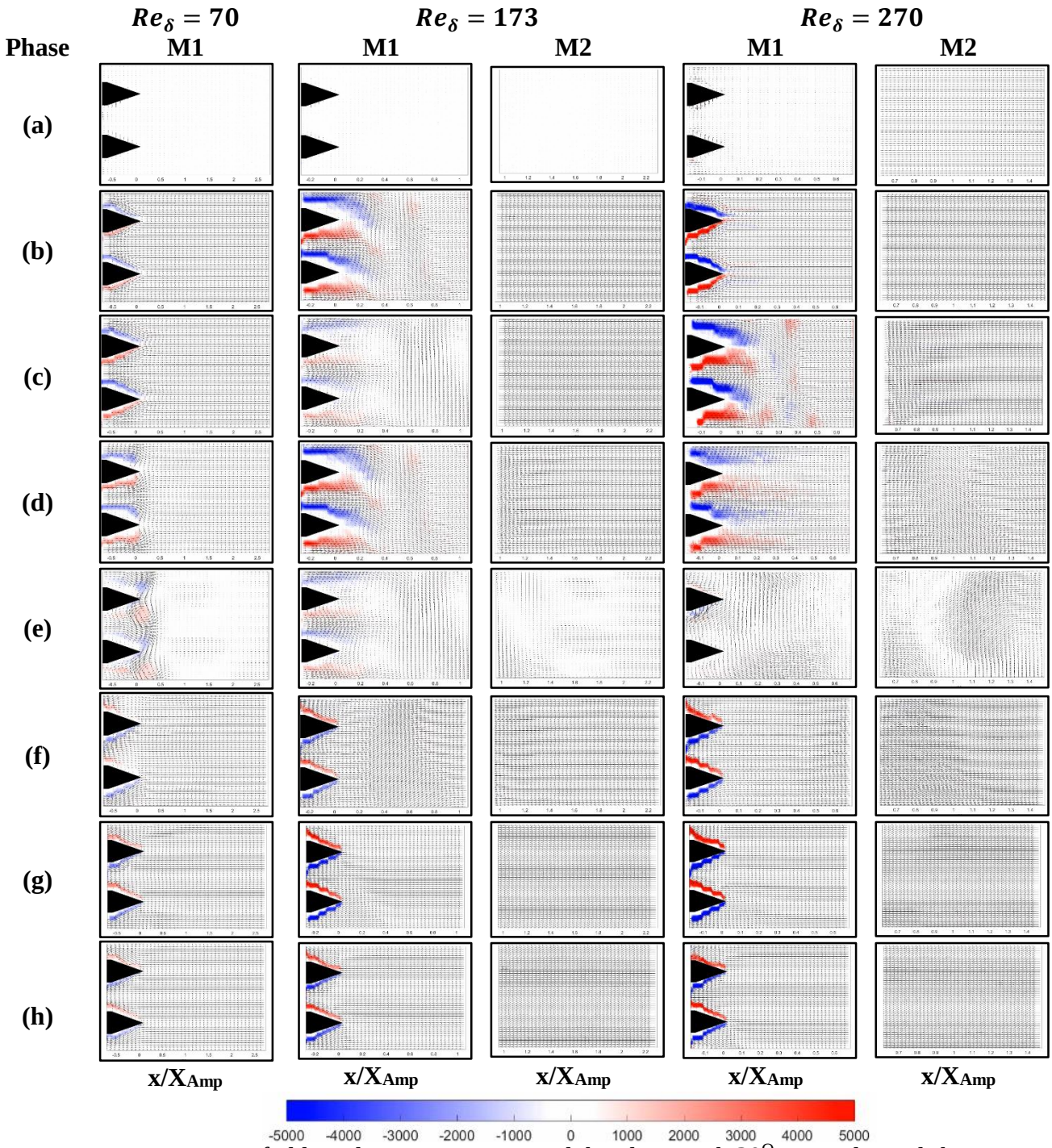

Figure 4.11: Vorticity fields and vector maps around the plates with 30^O triangular end shape at different phases (a-h, see Fig. 4.3) for three different Reynolds.

4.3.2. Turbulence intensities

The heat transfer processes in thermoacoustic systems are affected by the flow patterns in the vicinity of the stack. The analysis usually relays on the mean flow characteristics such as the vorticity fields. It was believed that the flow patterns around the plates in the oscillating flow are cyclic. However, Berson *et al.* [56] found that the flow near to a thermoacoustic stack is non-periodic. The non-periodicity of the flow is a statistical quantity that can be characterized by the turbulence intensity. The turbulence intensity represents the fluctuations of the velocity around a mean (ensemble-average) value. In the current study, the turbulence intensities based on both velocity components (u, v) are calculated over the whole measurement area. The normalized turbulence intensities are calculated as follows:

$$I_x(x, y, \emptyset) = \frac{100}{U_o}\sqrt{\frac{1}{N}\sum_{i=1}^{N=100}[u(x, y, \emptyset, i) - \bar{u}(x, y, \emptyset)]^2} \tag{4.3}$$

$$I_y(x, y, \emptyset) = \frac{100}{U_o}\sqrt{\frac{1}{N}\sum_{i=1}^{N=100}[v(x, y, \emptyset, i) - \bar{v}(x, y, \emptyset)]^2} \tag{4.4}$$

where $\emptyset$ is the phase number which is ranged from 1 to 25, U_o is the velocity amplitude at the centerline, N is the total number of cycles and

$$\bar{u}(x, y, \emptyset) = \frac{1}{N}\sum_{i=1}^{N=100} u(x, y, \emptyset, i), \tag{4.5}$$

$$\bar{v}(x, y, \emptyset) = \frac{1}{N}\sum_{i=1}^{N=100} v(x, y, \emptyset, i) \tag{4.6}$$

It is worthwhile to mention that the term "turbulence intensity" usually refers to the velocity fluctuations due to small incoherent structures in the flow. However, in this work, the term "turbulence intensity" takes into account the total fluctuations due to larger coherent structures (i.e. vortices) and the small incoherent structures as well. Also, the calculated turbulence intensities include the measurement uncertainty. However, the value of the measurement uncertainty does not exceed 3%, as described in the following section. The matlab code used to calculate and plot the turbulence intensities is presented in appendix C.12.

4.3.2.A. Turbulence intensity as a function of phase

The turbulence intensities distributions are plotted around the plates over the whole field of view for different Reynolds numbers. Also, for the sake of quantitative comparisons, the turbulence intensities profiles are plotted for one plate (as the turbulence intensities patterns are similar for both plates) at four axial locations namely X1, X2, X3 and X4. As shown in Fig. 4.12, these axial locations X1, X2, X3 and X4 correspond to $^{x}/_{X_{Amp}}$ of 0.25, 0.5, 1 and 1.5, respectively for all Reynolds numbers except for Reynolds number of 302, the axial location X4 corresponds to $^{x}/_{X_{Amp}}$ of 1.3.

As shown in Fig. 4.13, at the beginning of the ejection stage (phase a), both turbulence intensities (I_x and I_y) distributions are almost zero in the whole field of view. At phase b, the turbulence intensities start to develop and extend to an axial location less than $^{x}/_{X_{Amp}}$ of 0.5. At phase c, the turbulence intensities reach to the maximum value at the axial location of $^{x}/_{X_{Amp}}$ =0.25 (see Fig. 4.17). Then the location of the maximum turbulence intensities shifts to an axial location of $^{x}/_{X_{Amp}}$ =0.5 at phase d. At phase e, the turbulence intensities profiles are nearly similar for all axial locations up to $^{x}/_{X_{Amp}}$ =1. During the suction stage (phases f-h), the generated turbulence moves towards the plates till the values become very small at phase h. The monitoring of the turbulence intensities at phase h is important because the value of the turbulence intensities far from the plates represent the value of the measurement uncertainty as there is no flow structures during this phase. Also, at phase h the flow moving towards the plates reach to the maximum displacement amplitude and hence if there are any disturbances generated due to the reflecting mirror (see Fig. 4.1) they should appear during this phase. Also, it should be noted that both turbulence intensities (I_x and I_y) are almost similar which implies that the generated turbulence is homogenous.

The turbulence intensities distributions are also plotted for different plate-end shapes, as shown in Fig. 4.14 to Fig. 4.16. Generally, the same phenomena are observed for the different plate-end shapes. However, the axial distance at which the generated turbulence reaches is nearly similar for both rectangular and circular cases. This distance becomes smaller in the case of the 90^{O} triangular and even smaller for the 30^{O} triangular plate-end shape.

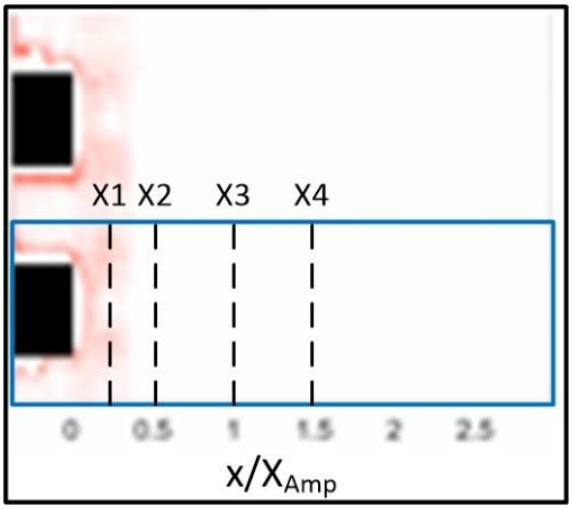

Figure 4.12: Representation for the axial locations at which the turbulence intensities distribution are plotted.

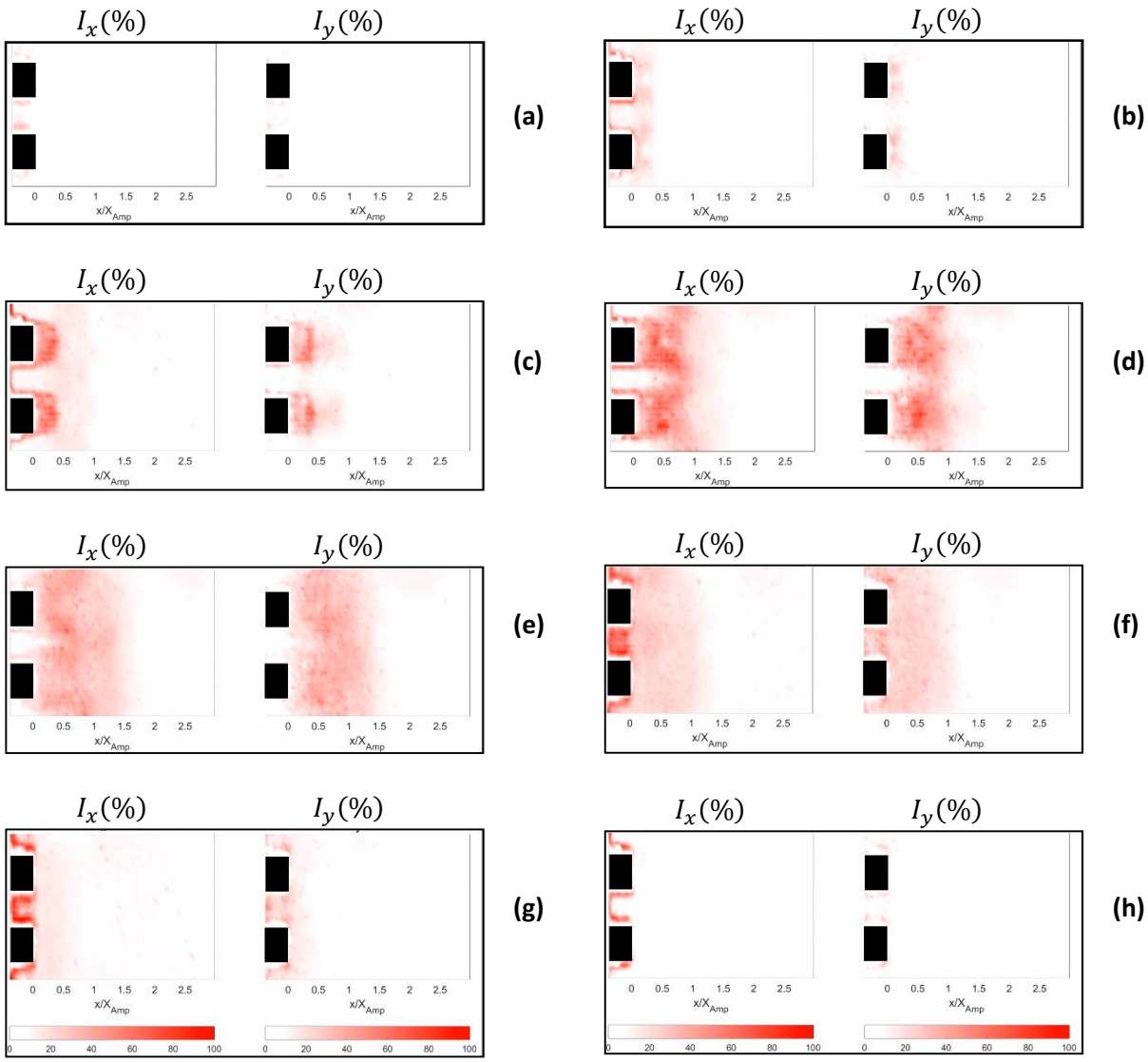

Figure 4.13: Distribution of the turbulence intensities around the plates with rectangular end shape in the measurement area (M1) at different phases (a-h, see Fig. 4.3) over one acoustic cycle for Reynolds number (Re_δ) of 70.

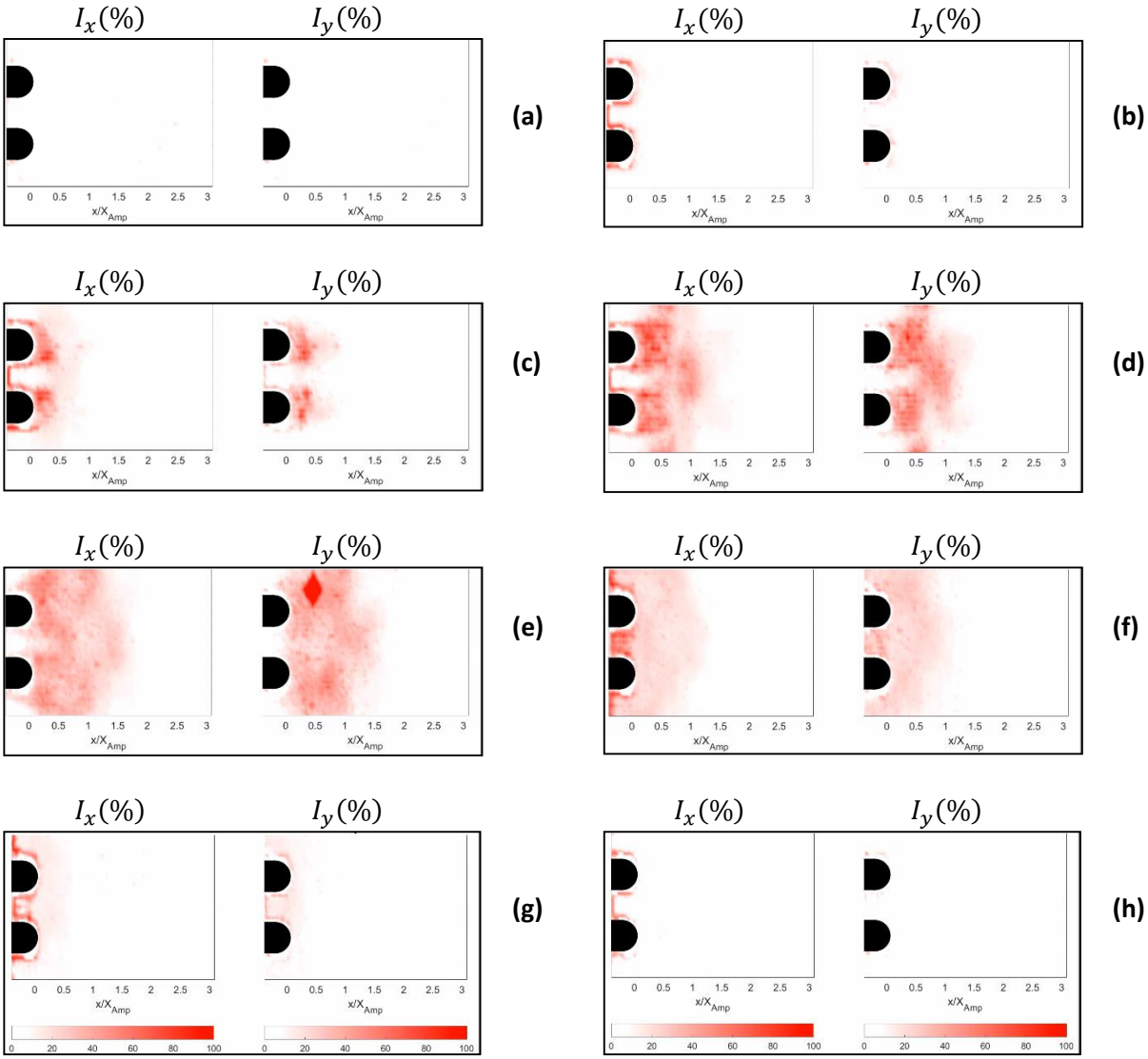

Figure 4.14: Distribution of the turbulence intensities around the plates with circular end shape in the measurement area (M1) at different phases (a-h, see Fig. 4.3) over one acoustic cycle for Reynolds number (Re_δ) of 70.

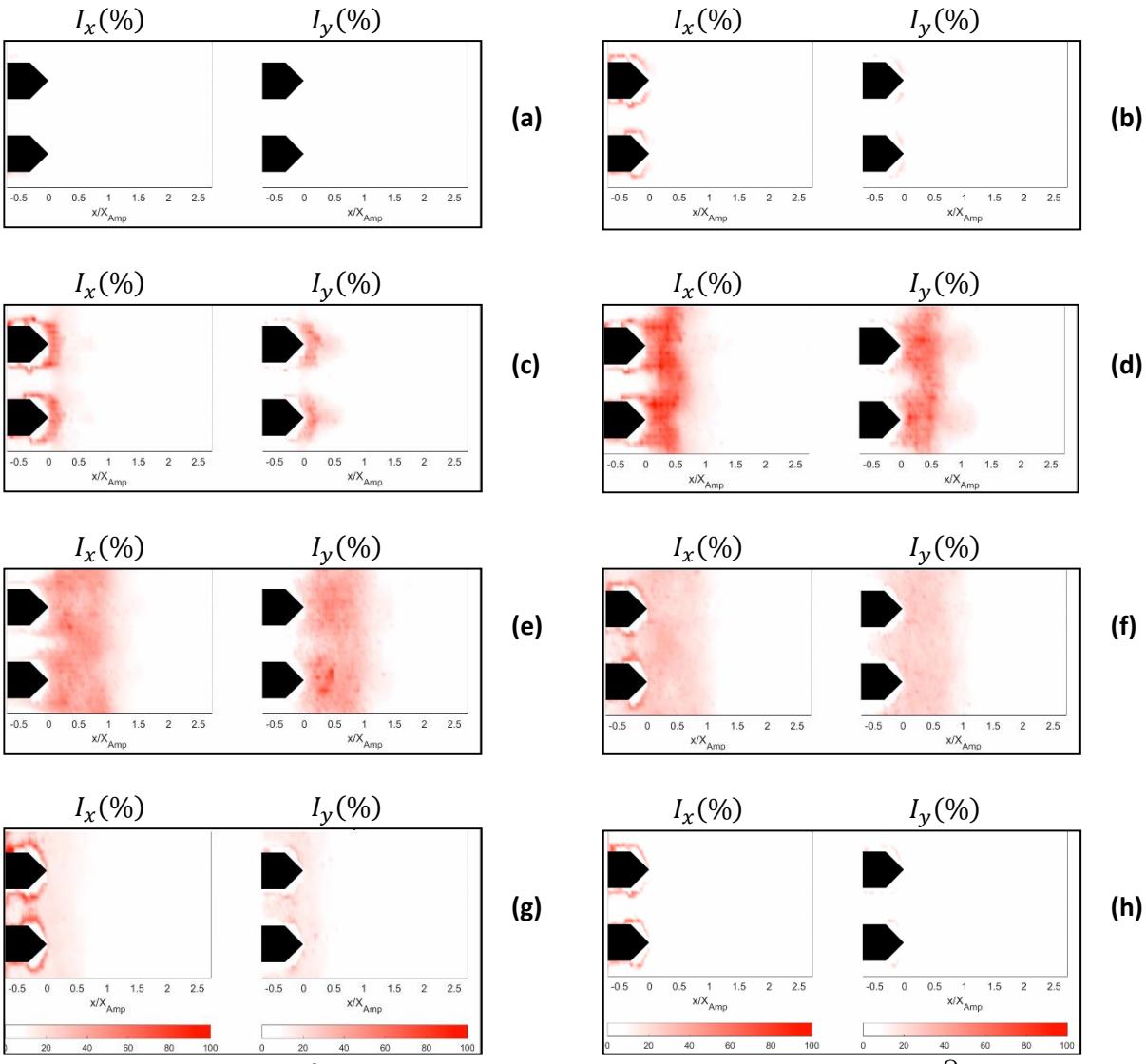

Figure 4.15: Distribution of the turbulence intensities around the plates with 90^O triangular end shape in the measurement area (M1) at different phases (a-h, see Fig. 4.3) over one acoustic cycle for Reynolds number (Re_δ) of 70.

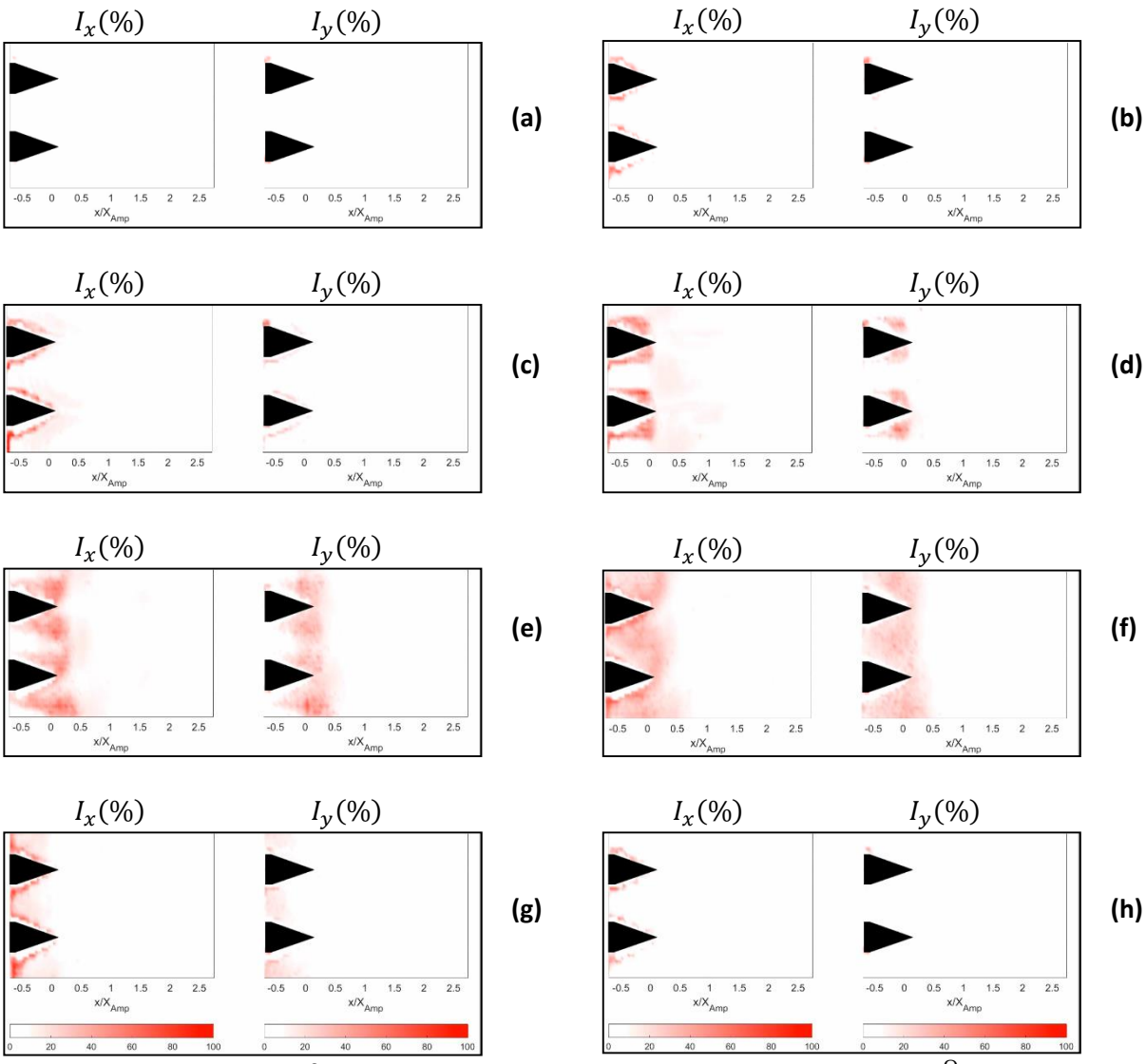

Figure 4.16: Distribution of the turbulence intensities around the plates with 30^{O} triangular end shape in the measurement area (M1) at different phases (a-h, see Fig. 4.3) over one acoustic cycle for Reynolds number (Re_{δ}) of 70.

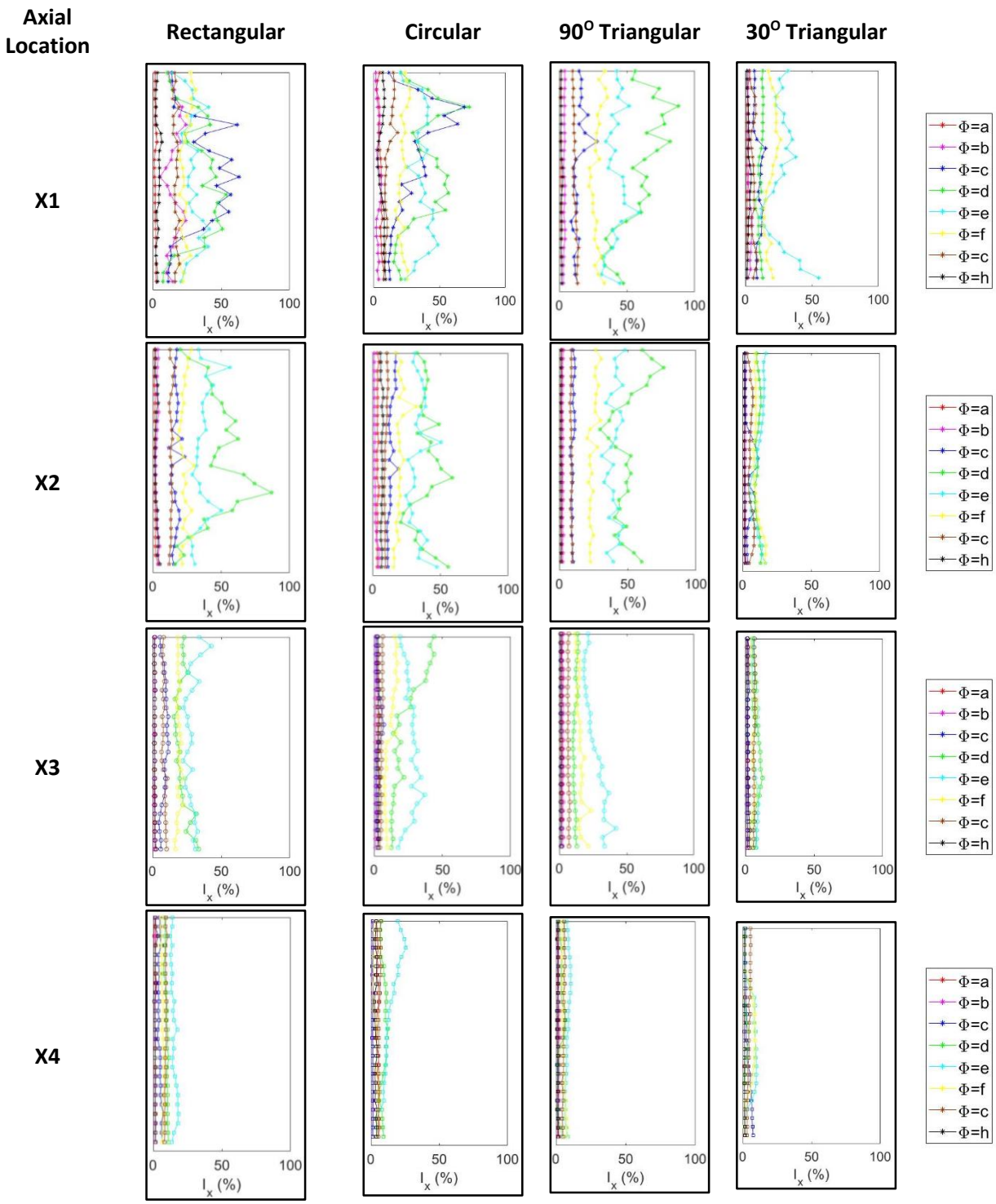

Figure 4.17: Turbulence intensity (I_x) distribution at different phases (a-h, see Fig. 4.3) at four different axial locations (X1, X2, X3 and X4) and for different plate-end shapes at Reynolds number (Re_δ) of 70.

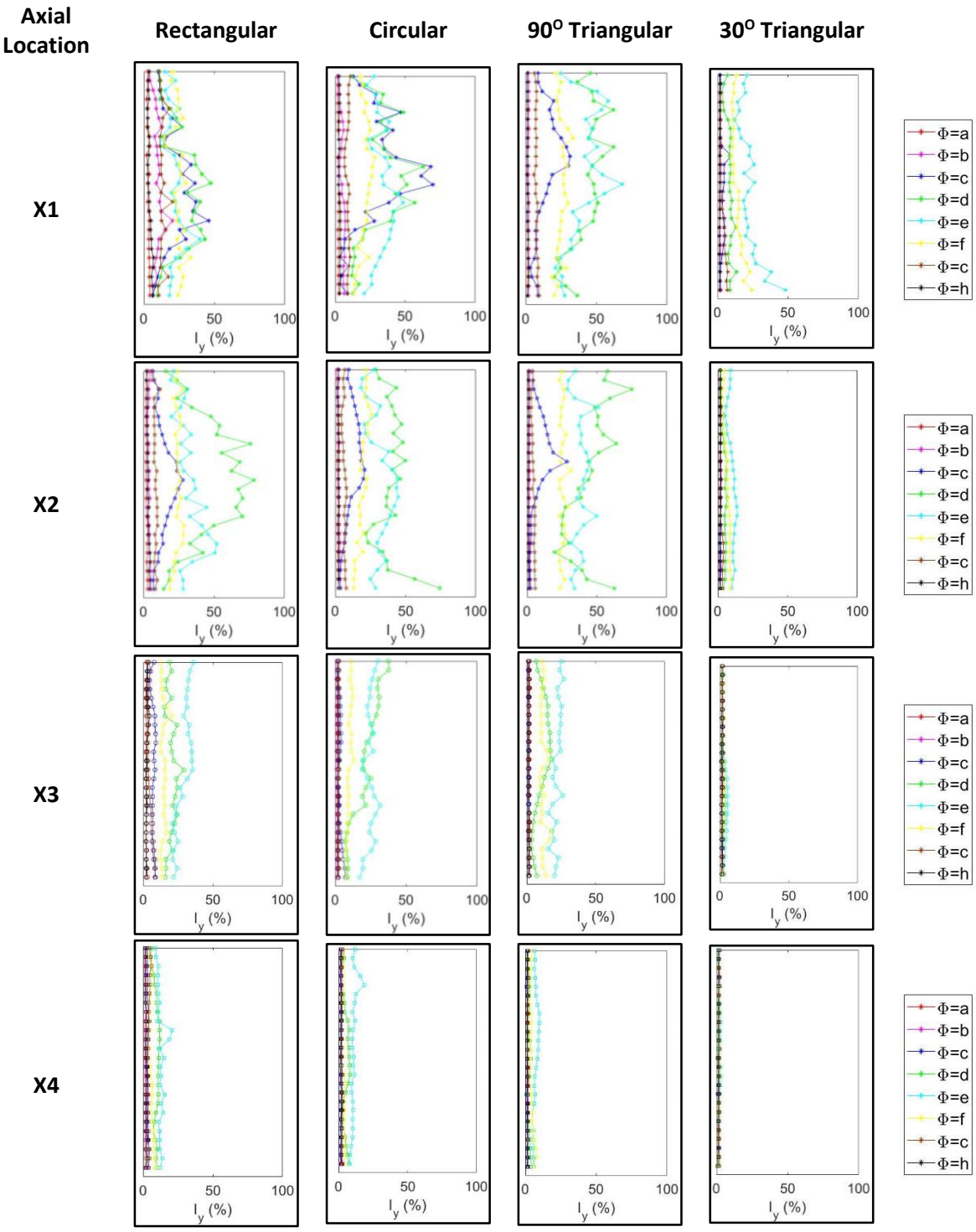

Figure 4.18: Turbulence intensity (I_y) distribution at different phases (a-h, see Fig. 4.3) at four different axial locations (X1, X2, X3 and X4) and for different plate-end shapes at Reynolds number (Re_δ) of 70.

4.3.2.B. Effects of Reynolds number

As shown in Fig. 4.19 and Fig. 4.20, the cycle-average turbulence intensities profiles at the same axial location for the same plate-end shape do not change a lot with the change of the Reynolds number. There are two reasons for this phenomena. First, as explained previously, the calculated value of the turbulence intensities takes into account both the large structures (i.e. vortices) and the small incoherent structures. So, the value of the turbulence intensities is mainly dependent on the large flow structures. As explained in the previous sections, the vorticity patterns do not change significantly with the Reynolds number (i.e. the dominant patterns are elongated vortices) and hence the turbulence intensities do not change with the Reynolds number. Second, the investigated range of the Reynolds number in the current study is much higher than the previous studies and hence the lowest Reynolds number investigated in this work is higher than the values in the previous studies. It is known that the turbulence intensities level becomes constant after a certain Reynolds number in the case of pulsatile flow [38]. So, it seems that the same phenomenon occurs with the pure oscillating flow, however, further investigations are required to confirm this finding.

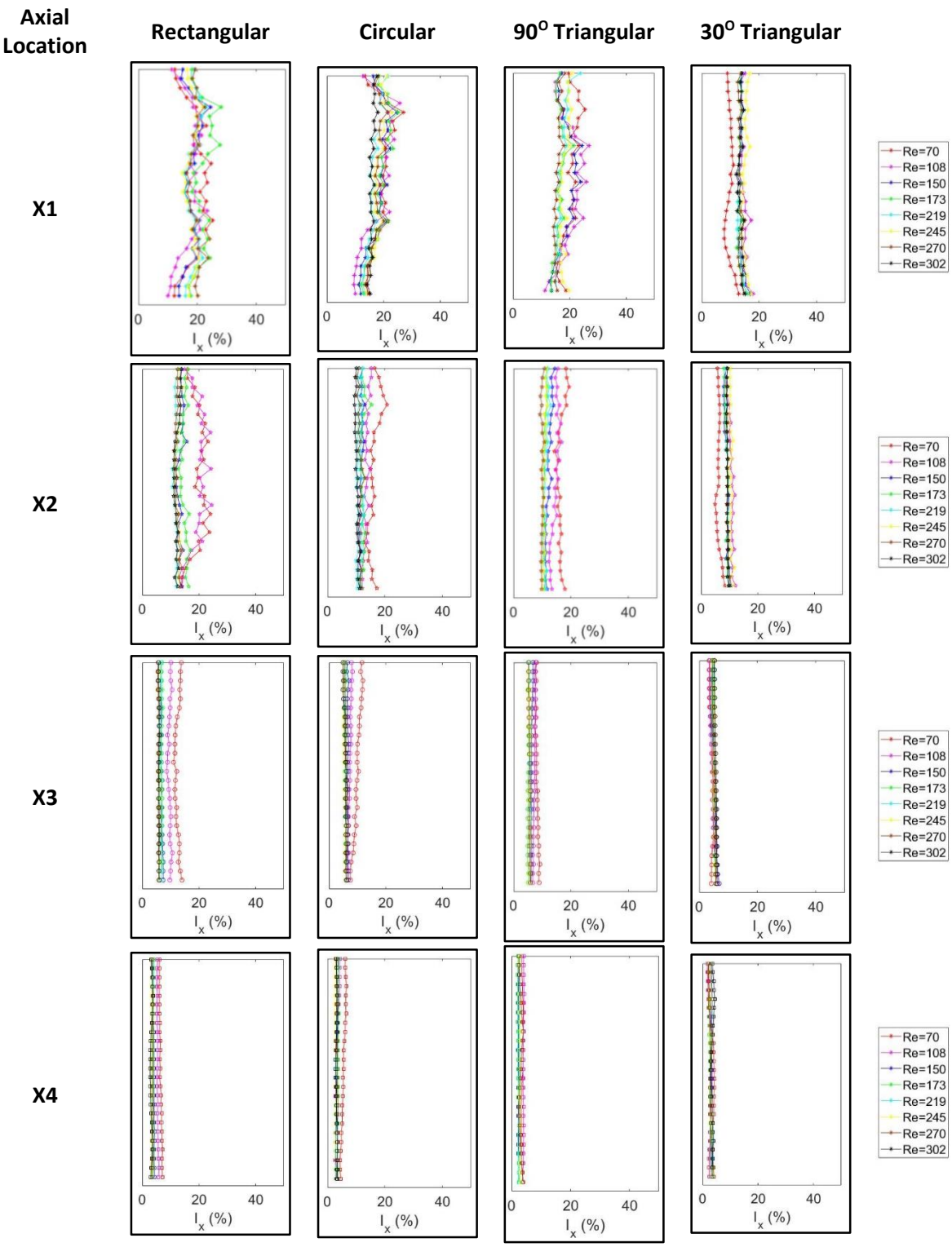

Figure 4.19: Cycle-average turbulence intensity (I_x) distribution at four different axial locations (X1, X2, X3 and X4) and for different plate-end shapes at different Reynolds numbers.

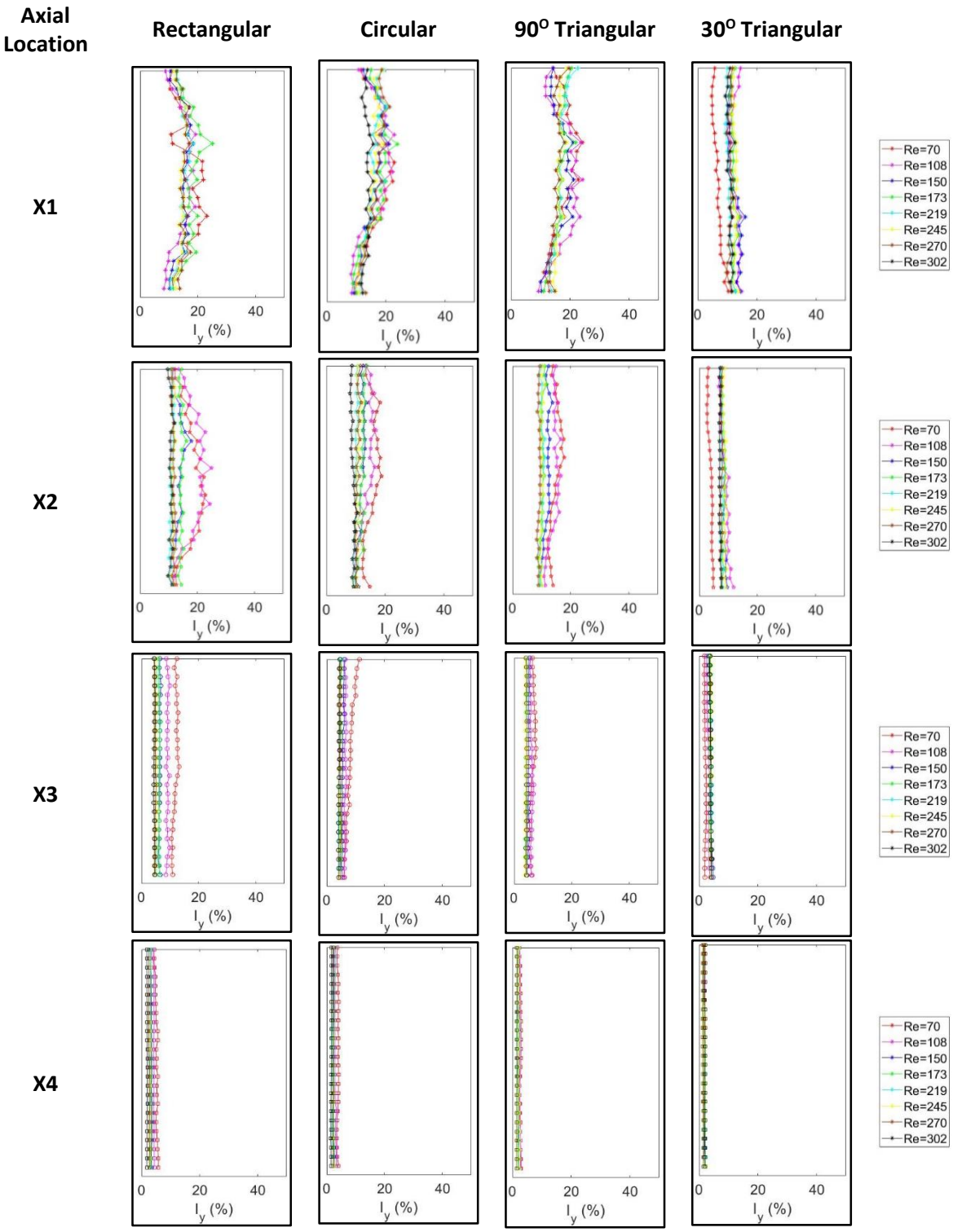

Figure 4.20: Cycle-average turbulence intensity (I_y) distribution at four different axial locations (X1, X2, X3 and X4) and for different plate-end shapes at different Reynolds numbers.

4.3.2.C. Effects of plate-end-shape

As shown in Fig. 4.21, the cycle-average turbulence intensities distributions are plotted at the same Reynolds number for different plate-end shapes. For low Reynolds number and near to the plates (i.e. axial locations X1 and X2), the turbulence intensities for rectangular, circular and 90^{O} triangular are nearly similar. The cycle-average turbulence intensity (I_x) for the 30^{O} triangular plate-end shape decreases significantly. However, at further axial locations (i.e. X3 and X3), the turbulence intensities for all plate-end shapes are nearly similar.

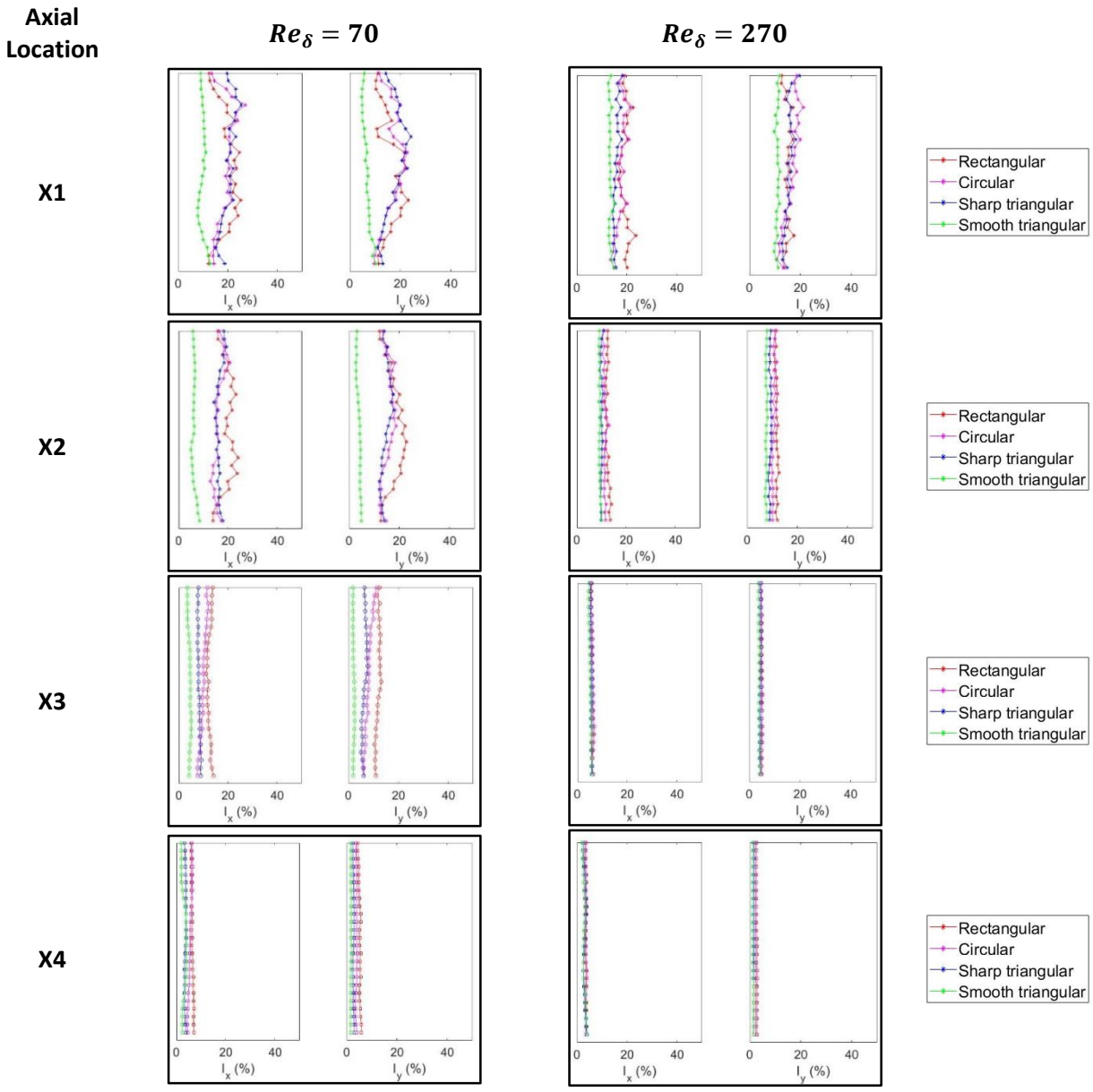

Figure 4.21: Cycle-average turbulence intensities (I_x *and* I_y) distribution at four different axial locations (X1, X2, X3 and X4) and for different plate-end shapes at two different Reynolds numbers.

4.4. Conclusions

In this part of the study, the effects of the plate-end shapes on the flow morphology at high velocity amplitudes have been investigated experimentally using PIV system. Four plate-end shapes are used namely rectangular, circular, 90^O triangular and 30^O triangular. The evolution of the vorticity field with time over a complete acoustic cycle has been described. The vorticities originate near the walls of the plates at the beginning of the ejection stage and then move to an axial distance of approximately one acoustic displacement amplitude. Afterwards, the vortices move back into the plates during the suction stage. As the Reynolds number increases, the vortices transformed into two-elongated vortices. Also, the same phenomena occur with all other plate-end shapes. However, for the 30^O triangular plate-end shape, the disturbances of the flow extend to an axial distance less than the acoustic displacement amplitude.

The turbulence intensities distributions are investigated for different plate-end shapes at different Reynolds numbers. The evolution of the turbulence intensities with time over a complete acoustic cycle has been reported. At the beginning of the ejection stage, the turbulence intensities are almost zero in the whole field of view. Afterwards, the turbulence intensities values increase near the plates and then the turbulence intensities spread over an axial distance of about one acoustic displacement amplitude. During the suction stage, the generated turbulence moves with the main flow inwards to the plates. The increase of the Reynolds number does not significantly change the turbulence intensities because the calculated values of the turbulence intensities are mainly dependent on the large flow structures which do not change significantly with the Reynolds number. It is found that the 30^O triangular plate-end shape reduces the cycle-average turbulence intensity near to the plate end whereas the other shapes have nearly the same turbulence level.

4.5. Recommendations for future work

In the current study, the investigation of the flow morphology is implemented for fixed plate thickness and plate separation. These two parameters have significant effects on the vortex patterns at mentioned in previous studies. However, the effects of these parameters on the turbulence intensities (or non-periodicity) have not been investigated yet. Also, in the current study the investigated Strouhal numbers are small and hence it is recommended to study the effects of the large Strouhal numbers on the non-periodicity of the flow.

In the current study, the effects of different parameters on the flow morphology have been investigated in the vicinity of the parallel plates. However, during the suction stage the generated vortices affect the flow characteristics between the plates. The effects extend to a certain axial distance in the channels formed by the parallel plate. So, it is important to investigate the effects of the vortices on the flow characteristics between the plates during the suction stage.

In the real thermoacoustic systems, the spacing of the stack plates is less than 1 mm and also, the plate thickness is usually a fraction of mm. Hence, the study of the flow morphology between plates have similar configuration of the real stack is important to understand the flow behavior.

Chapter 5: Summary and conclusions

In order to make the thermoacoustic devices economically competitive to the conventional systems of power generation or refrigeration, both the efficiency and the power density of the thermoacoustic systems should be improved. In order to improve the power density of the thermoacoustic devices, the velocity and pressure amplitudes of the oscillations should be increased. By increasing the oscillation amplitude, the linear theory is no longer valid to predict the performance of thermoacoustic systems and hence understanding of the non-linear phenomena that occur at high amplitudes will help in improving the performance of these systems. The current study focuses on some of the non-linear phenomena in the thermoacoustic systems. These phenomena are streaming, turbulence generation and entrance effects.

In chapter 2, the effects of the natural convection flow on the Rayleigh streaming flow in a simple standing-wave thermoacoustic system have been investigated experimentally. Streaming is a second order steady flow superimposed on the oscillating flow. This steady flow convects a certain amount of heat with no contribution to the thermoacoustic conversion process and hence it is considered as a loss. The effects of different parameters on the Rayleigh streaming in an empty resonator have been the focus of many researchers. However, the Rayleigh steaming in a real thermoacoustic system was not investigated. In the current study, the distribution of the mean flow velocity inside a simple standing-wave thermoacoustic engine is measured using PIV and LDV systems. The measurements are conducted along the axis of the resonator covering an axial distance from the cold side of the stack to the termination of the resonator duct. The measurements reveal that the mean velocity patterns changes over three different regions, namely the “cold streaming” region, the “hot streaming region” and the “end-effects” region. In the cold streaming region, the measured axial mean velocity agrees with the theoretical expectations of Rayleigh streaming at low acoustic level, whereas it deviates from theoretical expectations as the acoustic level is increased due to high amplitude effects, which agrees with the literature. Also, measurements performed when the engine is turned off showed that the natural convection velocity is almost zero over this region, explaining the reason for agreement between the measured mean velocity and the theoretical expectations of Rayleigh streaming. In the hot streaming region, the measured mean velocity disagrees with Rayleigh streaming expectation. Measurements performed when the engine is turned off showed that one reason for this disagreement is the non-uniformity of the temperature over the cross section, generating a natural convection flow that superimposes the acoustic streaming. The natural convection flow has a magnitude comparable to the magnitude of Rayleigh streaming but in the opposite direction. Hence, the measured mean velocity (in some cases) is almost zero which means the natural convection flow can be utilized to cancel the streaming flow. However, more studies are still needed to understand how the natural convection flow can be controlled in order to cancel the streaming flow. In the last region, the measurements do not agree with the theoretical expectations due to the combined effect of both natural convection and end-effects at the exit of the stack.

In chapter 3, the characteristics of the oscillating flow inside an empty resonator are investigated for two different frequency ranges, namely sub-acoustic (low) frequency range and acoustic (high) frequency range. In the sub-acoustic frequency range, the transition the turbulence has been investigated experimentally using PIV measurements. The axial velocity distribution in a square duct is measured at different Reynolds numbers and Womersley numbers and compared with the theoretical expectations. At low Reynolds number, the measured values are in agreement with the theoretical expectations. As the Reynolds number is increased; the agreement is violated in the deceleration phase first and then in more phases in the cycle. At the critical Reynolds number around 500, it is observed that there is a jump in the level of the axial turbulence intensity. These findings comply with the previous literature and hence using the PIV system to study the transition to turbulence in oscillating flow is validated. Therefore, the work is extended to high (i.e. acoustic) frequency range. At high (acoustic) frequency range, the transition to turbulence has been investigated using PIV measurements. The Reynolds stress distribution is utilized as a criterion for the occurrence of turbulence. At low Reynolds number, it is observed that the Reynolds stress distribution is flat and equals to zero. At Reynolds number of 272, a sudden increase in the Reynolds stress value is observed at traverse location of around $1.5\delta_{\nu}$. This sudden increase is due to the occurrence of turbulence. As the Reynolds number increases, the location of the peak in the Reynolds stress distribution moves gradually away from the wall. At Reynolds number higher than 418, another sudden increase in the level of the Reynolds stress is observed which may indicate the end of the transition to turbulence Regime and start of fully turbulent oscillating flow. Also, the spatial energy spectra of the flow are investigated. It shows an increase in the turbulent kinetic energy level as the Reynolds number increases. Also, at a given Reynolds number, the decay of the turbulent kinetic energy with the wavenumber complies with the universal slope (-5/3).

In chapter 4, the flow characteristics in the vicinity of a parallel plate stack with different plate-end shapes are investigated experimentally using PIV measurements. Four plate-end shapes are used namely rectangular, circular, 90^{O} triangular and 30^{O} triangular. The evolution of the vorticity field with time over a complete acoustic cycle has been described. The vorticities originate near the walls of the plates at the beginning of the ejection stage and then move to an axial distance of an approximately one acoustic displacement amplitude. Afterwards, the vortices move back into the plates during the suction stage. As the Reynolds number increases, the vortices transformed into two-elongated vortices. Also, the same phenomena occur with all other plate-end shapes. However, for the 30^{O} triangular plate-end shape, the disturbances of the flow extend to an axial distance less than the acoustic displacement amplitude.

The turbulence intensities distributions are investigated for different plate-end shapes at different Reynolds numbers. The turbulence intensities also represent the non-periodicity of the oscillating flow in the vicinity of the stack. The evolution of the turbulence intensities with time over a complete acoustic cycle has been reported. At the beginning of the ejection stage, the turbulence intensities are almost zero in the whole field of view. Afterwards, the turbulence intensities values

increase near the plates and then the turbulence intensities spread over an axial distance of about one acoustic displacement amplitude. During the suction stage, the generated turbulence moves with the main flow inwards to the plates. The increase of the Reynolds number does not significantly change the turbulence intensities because the calculated values of the turbulence intensities are mainly dependent on the large flow structures which do not change significantly with the Reynolds number. It is found that the 30^{O} triangular plate-end shape reduces the cycle-average turbulence intensity near to the plate end whereas the other shapes have nearly the same turbulence level. Finally, the results of this work reveal that the flow in the vicinity of the stack is a non-periodic flow. However, the available numerical models assume that the oscillating flow is a periodic flow and hence the current numerical models should be improved to account for the non-periodicity of the flow around the stack.

References

[1] N. Rott, "Thermoacoustics," *Adv. Appl. Mech.,* vol. 20, pp. 135-175, 1980.

[2] M. P. Telesz, "Design and Testing of a Thermoacoustic Power Converter," 2006.

[3] K. J. Bastyr, "The design, construction, and performance of a high–frequency, high–power thermoacoustic–stirling engine," 2004.

[4] J. R. Olson and G. W. Swift, "Acoustic streaming in pulse tube refrigerators: tapered pulse tubes," *Cryogenics,* vol. 37, no. 12, pp. 769-776, 1997.

[5] G. Swift, Thermoacoustics: a unifying perspective for some engines and refrigerators, Los Alamos National Laboratory, 2002.

[6] V. Dvořák, "Ueber die akustische anziehung und abstossung (On the acoustic attraction and repulsion)," *Ann. Phys.,* vol. 233, no. 1, pp. 42-73, 1876.

[7] L. Rayleigh, "On the circulation of air observed in Kundt's tubes, and on some allied acoustical problems," *Philos. Trans. R. Soc. London,* vol. 175, pp. 1-21, 1884.

[8] L. Menguy and J. Gilbert, "Non-linear acoustic streaming accompanying a plane stationary wave in a guide," *Acta Acust united Ac,* vol. 86, no. 2, pp. 249-259, 2000.

[9] I. Reyt, H. Bailliet and J.-C. Valiere, "Experimental investigation of acoustic streaming in a cylindrical wave guide up to high streaming Reynolds numbers," *J. Acoust. Soc. Am.,* vol. 135, no. 1, pp. 27-37, 2014.

[10] I. Reyt, V. Daru, H. Bailliet, S. Moreau, J.-C. Valiere, C. Weisman and D. Baltean-Carles, "Fast acoustic streaming in standing waves: generation of an additional outer streaming cell," *J. Acoust. Soc. Am.,* vol. 134, pp. 1791-1801, 2013.

[11] M. W. Thompson, A. A. Atchley and M. J. Maccarone, "Influences of a temperature gradient and fluid inertia on acoustic streaming in a standing wave," *J. Acoust. Soc. Am.,* vol. 117, no. 4, pp. 1839-1849, 2005.

[12] A. Gubaidullin and A. Yakovenko, "Effects of heat exchange and nonlinearity on acoustic streaming in a vibrating cylindrical cavity," *J. Acoust. Soc. Am.,* vol. 137, no. 6, 2015.

[13] V. Daru, I. Reyt, H. Bailliet, C. Weisman and D. Baltean-Carls, "Acoustic and streaming velocity components in a resonant wave guide at high acoustic levels," *J. Acoust. Soc. Am.,* vol. 141, no. 1, 2017.

[14] N. Rott, "The influence of heat conduction on acoustic streaming," *J. Appl. Math. Phys.,* vol. 25, pp. 417-421, 1974.

[15] J. R. Olson and G. W. Swift, "Acoustic streaming in pulse tube refrigerators: tapered pulse tubes," *Cryogenics,* vol. 37, pp. 769-776, 1997.

[16] H. Bailliet, V. Gusev, R. Raspet and R. A. Hiller, "Acoustic streaming in closed thermoacoustic devices," *J. Acoust. Soc. Am.,* vol. 110, no. 4, pp. 1808-1821, 2001.

[17] S. Moreau, H. Bailliet and J.-C. Valiere, "Effect of a stack on Rayleigh streaming cells investigated by laser doppler velocimetry for application to thermoacoustic devices," *J. Acoust. Soc. Am.,* vol. 125, no. 6, pp. 3514-3517, 2009.

[18] P. Debesse, D. Baltean-Carles, F. Lusseyran and M.-X. Francois, "Oscillating and streaming flow identification in a thermoacoustic resonator from undersampled PIV Measurements," *Meas. Sci. Technol.,* vol. 25, pp. 1-16, 2014.

[19] I. Ramadan, H. Bailliet and J.-C. Valière, "Experimental Investigation of Acoustic streaming in A simple Thermoacoustic Engine," in *ICSV24*, London, 2017.

[20] H. Babaei and K. Siddiqui, "Investigation of streaming flow patterns in a thermoacoustic device using PIV," in *Proceedings of the ASME*, Montreal, Canada, 2010.

[21] N. Pan , S. Wang and C. Shen, "Visualization investigation of the flow and heat transfer in thermoacoustic engine driven by loudspeaker," *Int. J. Heat and Mass Transfer,* vol. 55, pp. 7737-7746, 2012.

[22] E. Saint Ellier, Y. Bailly, L. Girardot, D. Ramel and P. Nika, "Temperature gradient effects on acoustic and streaming velocities in standing acoustic waves resonator," *Exp. Therm. Fluid Sci.,* vol. 66, pp. 1-6, 2015.

[23] M. K. Aktas and T. Ozgumus, "The effect of acoustic streaming on thermal convection in an enclosure with differentially heated horizontal walls," *Int. J. Heat and Mass Transfer,* vol. 53, 2010.

[24] Y. Lin and B. Farouk, "Heat transfer in a rectangular chamber with differentially heated horizontal walls: effect of a vibrating side wall," *Int. J. Heat Mass Transfer,* vol. 51, 2008.

[25] E. G. Richardson and E. Tyler, "The transverse velocity gradient near the mouths of pipes in which an alternating or continuous flow of air is established," in *The proceedings of physical scoiety*, 1929.

[26] J. I. Collins, "Inception of turbulence at the bed under periodic gravity waves," *Journal of Geophysical Research,* vol. 68, no. 21, pp. 6007-6014, 1963.

[27] S. I. Sergeev, "Fluid oscillations in pipes at moderate Reynolds numbers," *Fluid Mechanics ,* vol. 1, no. 1, pp. 121-122, 1966.

[28] M. Ohmi and M. Iguchi, "Critical Reynolds number in an oscillating pipe flow," *Bulletin of JSME,* vol. 25, no. 200, 1982.

[29] T. S. Zhao and P. Cheng, "Experimental studies on the onset of turbulenceand frictional losses in an oscillatory turbulent pipe flow," *International journal of heat and fluid flow,* vol. 17, pp. 356-362, 1996.

[30] P. Merkli and H. Thomann, "Transition to turbulence in oscillating pipe flow," *Journal of fluid mechanics,* vol. 68, no. 3, pp. 567-575, 1975.

[31] M. Ohmi and M. Iguchi, "Flow patterns and frictional losses in an oscillating pipe flow," *Bulletin of JSME,* vol. 25, no. 202, 1982.

[32] M. Hino, M. Sawamoto and S. Takasu, "Experiments on transition to turbulence in an oscillatory pipe flow," *Journal of fluid mechanics,* vol. 75, no. 2, pp. 193-207, 1976.

[33] M. Hino, M. Kashiwayanagi, A. Nakayama and T. Hara, "Experiments on the turbulence statistics and the structure of a reciprocating oscillatory flow," *Journal of fluid mechanics,* vol. 131, pp. 363-400, 1983.

[34] M. Clamen and P. MINTON, "An experimental investigation of flow in an oscillating pipe," *Journal of Fluid Mechanics,* vol. 81, no. 3, pp. 421-431, 1977.

[35] M. Eckmann and J. B. Grotberg, "Experiments on transition to turbulence in oscillatory pipe flow," *Journal of Fluid Mechanics,* vol. 222, pp. 329-350, 1991.

[36] L. S. Fishler and R. S. Brodkey, "Tansition, turbulence and oscillating flow in a pipe," *Experiments in fluids,* vol. 11, pp. 388-398, 1991.

[37] R. Akhavan, R. D. Kann and A. H. Shapiro, "An investigation to turbulence in bounded oscillatory stokes flows part 1. experiments," *Journal of fluid mechanics ,* vol. 225, pp. 398-422, 1991.

[38] R. Trip, D. J. Kuik, J. Westerweel and C. Poelma, "An experimental study of transitional pulsatile pipe flow," *Physics of Fluids,* vol. 24, 2012.

[39] O. M. Carpinliohlu and E. Ozahi, "An updated portriat of transition to turbulence in laminar pipe flows with periodic time dependence (a correlation study)," *Flow turbulence combust,* vol. 89, pp. 691-711, 2012.

[40] K. H. Ahn and M. B. Ibrahim, "Laminar/turbulent oscillating flow in circular pipes," *International journal of heat and fluid flow,* vol. 13, no. 4, pp. 340-346, 1992.

[41] R. Akhavan, R. D. Kann and A. H. Shapiro, "An investigation to turbulence in bounded oscillatory stokes flows part 2. numerical simulations," *Journal of fluid mechanics,* vol. 225, pp. 423-444, 1991.

[42] J. R. Womersley, "Method for the calculation of velocity , rate of flow and viscous drag in arteries when the pressure gradient is unknown," *Journal of Physiol,* vol. 127, pp. 553-563, 1955.

[43] D. G. Drake , "On the flow in the channel due to a periodic pressure gradient," *Quart. Jonrn. Mech and Applied Math.,* vol. XVIII, 1963.

[44] S. Tsangaris, "Exact solution of the Navier-stokes equations for the fully developed, pulsating flow in a rectangular duct with a constant cross-sectional velocity," *Journal of fluids engineering ,* vol. 125, pp. 382-392, 2003.

[45] C. FAN, "Unsteady, laminar, incompressible flow through rectangular ducts," *Journal of Applied Mathematics and Physics,* vol. 16, pp. 351-360, 1965.

[46] C. Kerczek and S. H. Davis, "The stability of oscillatory stokes layers," *Studies in applied mathematics ,* vol. Li, no. 3, pp. 239-252, 1972.

[47] I. Ramadan, A. Abd El-Rahman, A. Ibrahim and E. Abdel-Rahman, "Transition To Turbulence in Oscillating Flows," in *ICSV25*, London, 2017.

[48] G. W. Swift, "Analysis and performance of a large thermoacoustic engine," *J. Acoust. Soc. Am.,* vol. 92, no. 3, 1992.

[49] P. J. Storch, R. Radebaugh and J. E. Zimmerman, "Analytical model for the refrigeration power of the orifice pulse tube refrigerator," International Institute of Standards and Technology , 1990.

[50] P. Blanc-Benon, E. Besnoin and O. Knio, "Experimental and computational visualization of the flow field in a thermoacoustic stack," vol. 331, pp. 17-24, 2003.

[51] A. Berson, M. Michard and P. Blanc-Benon, "Vortex identification and tracking in unsteady flows," *C. R. Mecanique,* no. 337, p. 61–67, 2009.

[52] P. Debesse, D. Baltean-Carlès, F. Lusseyran and M. X. François, "Experimental analysis of nonlinear phenomena in a thermoacoustic system," in *18th International Symposium Nonlinear Acoustics*, 2008.

[53] X. Mao, L. Shi and A. J. Jaworski, "Non-dimensional parameters controlling the behavior of oscillatory flows around stacks of parallel plates in thermoacoustic devices," in *16th International Congress on Sound and Vibration*, Kraków, Poland, 2009.

[54] M. Nabavi, K. Siddiqui and J. Dargahi, "Measurement of the acoustic velocity field of nonlinear standing waves using the synchronized PIV technique," *Experimental Thermal and Fluid Science,* no. 33, p. 123–131, 2008.

[55] A. Berson, M. Michard and P. Blanc-Benon, "Measurement of acoustic velocity in the stack of a thermoacoustic refrigerator using particle image velocimetry," *Heat Mass Transfer,* p. 1015–1023, 2008.

[56] A. Berson and P. Blanc-Benon, "Nonperiodicity of the flow within the gap of a thermoacoustic couple at high amplitudes," *J. Acoust. Soc. Am.,* vol. 122, no. 4, 2007.

[57] X. Mao, D. Marx and A. Jaworski, "PIV measurement of coherent structures and turbulence created by an oscillating flow at the end of a thermoacoustic stack," in *Progress in Turbulence II*, 2007.

[58] L. Shi, Z. Yu and A. J. Jaworski, "Vortex shedding flow patterns and their transitions in oscillatory flows past parallel-plate thermoacoustic stacks," *Experimental Thermal and Fluid Science,* pp. 954-965, 2010.

[59] M. Rezk, A. H. Ibrahim, T. Nigim, A. I. Abd El-Rahman, A. A. Elbeltagy and E. Abdel-Rahman, "Particle-image-velocimetry investigation of flow morphology at sudden expansion and contraction in oscillating flows," in *22nd International Congress on Acoustics* , Buenos Aires, 2016.

[60] L. Shi, Z. Yu and A. J. Jaworski, "Investigation into the strouhal numbers associated with vortex shedding from parallel-plate thermoacoustic stacks in oscillatory flow conditions," *European Journal of Mechanics B/Fluids,* pp. 206-217, 2011.

[61] A. J. Jaworski, X. Mao, X. Mao and Z. Yu, "Entrance effects in the channels of the parallel plate stack in oscillatory flow conditions," *Experimental Thermal and Fluid Science,* vol. 33, p. 495–502, 2009.

[62] P. C. Aben, P. R. Bloemen and J. C. H. Zeegers, "2D PIV measurements of oscillatory flow around parallel plates," *Exp Fluids,* no. 46, p. 631–641, 2009.

[63] I. Ramadan, A. Ibrahim and E. Abdel-Rahman, "PIV Investigation of the Flow Patterns around Plates with Various Plate-End Shapes in Oscillating Flows," in *ICSV25*, Hiroshima, 2018.

[64] S. Moreau, H. Bailliet and J.-C. Valiere, "Measurements of inner and outer streaming vortices in a standing waveguide using laser doppler velocimetry," *J. Acoust. Soc. Am.,* vol. 123, no. 2, pp. 640-647, 2008.

[65] M. Nabavi, K. Siddiqui and J. Dargahi, "Analysis of regular and irregular acoustic streaming patterns in a rectangular enclosure," *Wave Motion,* vol. 46, p. 312–322, April 2009.

[66] A. Bejan and C. L. Tien, "Laminar natural convection heat transfer in a horizontal cavity with different end temperatures," *Journal of Heat Transfer,* vol. 100, pp. 641-647, 1978.

[67] J. H. Gerrard and M. D. Hughes, "The flow due to an oscillating piston in a cylindrical tube: a comparison between experiment and a simple flow theory," *Journal of fluid mechanics,* vol. 50, no. 1, pp. 97-106, 1971.

[68] J. Haertig, "Introductory lecture on particle behaviour," in *ISL/AGARD Workshop on Laser Anemometry*, 1976.

[69] I. Reyt, H. Bailliet, E. Foucault and J.-C. Valière, "Oscillating viscous boundary layer at high Reynolds number: Experiments and numerical calculations," in *AIP Conference Proceedings* , 2013.

[70] F. Durst and B. Unsal, "Forced laminar-to-turbulent transition of pipe flows," *J. Fluid Mech.,* vol. 560, p. 449, 2006.

[71] H. UEDA and J. O. HINZE, "Fine-structure turbulence in the wall region of a turbulent boundary layer," *J . Fluid Mech.,* vol. 67, pp. 125-143, 1975.

[72] D. Xu and J. Chen, "Accurate estimate of turbulent dissipation rate using PIV data," *Experimental Thermal and Fluid Science,* vol. 44, p. 662–672, 2013.

[73] J. Grue, G. Pedersen and P. Liu, PIV and water waves (advances in coastal and ocean engineering), Wspc, 2004, pp. 73-75.

[74] G. I. Taylor, "The Spectrum of Turbulence," *Proceedings of the Royal Society ,* vol. A164, no. 919, pp. 476-490, 1938.

[75] B. Preben and V. Clara Marika, "Measurement of turbulent spatial structure and kinetic energy spectrum by exact temporal-to-spatial mapping," *Physics of Fluids,* vol. 29, no. 8, 2017.

[76] P. DORON, I. BERTUCCIOLI and J. KATZ, "Turbulence characteristics and dissipation estimates in the coastal ocean bottom boundary layer from PIV data," *Journal of Physical Oceanography,* vol. 31, pp. 2108-2134, 2001.

[77] X. Mao and A. Jaworski, "Application of particle image velocimetry measurement techniques to study turbulence characteristics of oscillatory flows around parallel-plate structures in thermoacoustic devices," *Meas. Sci. Technol.,* vol. 21, 2010.

Appendices (A): DeltaEc Codes

A.1 DeltaEc code for the thermoacoustic engine

```
Engine_Exp#2
  0 BEGIN       Initial
                1.0132E+5 a Mean P Pa
Gues              244.23 b Freq   Hz
                  300.00 c TBeg   K
Gues             1950.6 d |p|     Pa
                  0.0000 e Ph(p)  deg
                  0.0000 f |U|    m^3/s
                  0.0000 g Ph(U)  deg
Optional Parameters
air             Gas type
   1 RPN          Pressure ratio (%)
                  0.0000 a G or T                    1.9252  A %
0d 0a / 100 *
   2 SURFACE      Ambient End
    Same  3a   1.1946E-3 a Area   m^2                1950.6 A |p|    Pa
                                                     0.0000 B Ph(p)  deg
                                                  8.5755E-7 C |U|    m^3/s
                                                     180.00 D Ph(U)  deg
                                                     0.0000 E Htot   W
ideal           Solid type                       -8.3636E-4 F Edot   W
   3 DUCT         Ambient Duct
                1.1946E-3 a Area   m^2      Mstr     1489.3 A |p|    Pa
                  0.12252 b Perim  m        3a       179.35 B Ph(p)  deg
                  0.5490 c Length m                 3.6780E-3 C |U|    m^3/s
Master-Slave Links                                   -88.981 D Ph(U)  deg
Optional Parameters                                  0.0000 E Htot   W
ideal           Solid type                       -7.9760E-2 F Edot   W
   4 RPN          Ambient end temperature
Gues              385.53 a G or T                   385.53    A K
4a =Tm
   5 RPN          Heat rate
                  -13.35 a G or T                   -13.35    A watss
5a =H2k
   6 STKRECT      Stack
    Same  3a   1.1946E-3 a Area   m^2                1893.0 A |p|    Pa
                  0.6400 b GasA/A          6def      171.61 B Ph(p)  deg
                6.0000E-2 c Length m                3.3509E-3 C |U|    m^3/s
                5.0000E-4 d aa     m      Mstr      -98.858 D Ph(U)  deg
                1.2500E-4 e Lplate m      Mstr      -13.35 E Htot   W
    Same  6d    5.0000E-4 f bb     m      Mstr    2.5975E-2 F Edot   W
Master-Slave Links                                   385.53 G TBeg   K
celcor          Solid type                           651.00 H TEnd   K
```

```
    7 RPN          Hot end temperature
Targ               651.00 a =A?                    651.00   A K
6H
    8 DUCT         Hot Duct
    Same  3a   1.1946E-3 a Area    m^2     Mstr     2047.7 A |p|     Pa
                0.12252 b Perim   m       8a        171.51 B Ph(p)   deg
                 0.1290 c Length  m                1.5496E-18 C |U|    m^3/s
Master-Slave Links                                   -78.395 D Ph(U)   deg
Optional Parameters                                  -13.35 E Htot    W
ideal          Solid type                         -5.4500E-16 F Edot    W
    9 HARDEND      Hot End
Targ               0.0000 a R(1/z)                   2047.7 A |p|     Pa
Targ               0.0000 b I(1/z)                   171.51 B Ph(p)   deg
                                                  1.5496E-18 C |U|    m^3/s
                                                     -78.395 D Ph(U)   deg
Possible targets                                     -13.35 E Htot    W
                                                  -5.4500E-16 F Edot    W
                                                  -6.0350E-17 G R(1/z)
                                                   1.6498E-16 H I(1/z)
```

A.2 DeltaEc code for the oscillating flow driven by the Scotch-yoke mechanism.

```
Scotch Yoke
  0 BEGIN
                1.0133E+5 a Mean P Pa
                   1.2500 b Freq   Hz
                   300.00 c TBeg   K
Gues               508.37 d |p|    Pa
Gues               35.884 e Ph(p)  deg
Gues            9.6384E-3 f |U|    m^3/s
                   0.0000 g Ph(U)  deg
Optional Parameters
air             Gas type
   1 RPN           Piston Amplitude
                   0.1000 a G or T                    9.6384E-3  A m^3/s
4a 1a * w *
   2 RPN           Calculate the volume flow rate ampitude
TargSame  1A    9.6384E-3 a =A?                       9.6384E-3  A m^3/s
0f
   3 ANCHOR        Change Me
   4 SURFACE       Piston Area
                1.2272E-2 a Area   m^2                  508.37 A |p|    Pa
                                                        35.884 B Ph(p)  deg
                                                     9.6383E-3 C |U|    m^3/s
                                                    -5.7224E-4 D Ph(U)  deg
                                                        1.9849 E Htot   W
ideal           Solid type                          1.9849 F Edot   W
   5 DUCT          Exit Port of the cylinder
                1.2668E-4 a Area   m^2      Mstr       465.57 A |p|    Pa
                3.9898E-2 b Perim  m        5a         39.094 B Ph(p)  deg
                1.0000E-2 c Length m                 9.6383E-3 C |U|    m^3/s
                5.0000E-4 d Srough                  -7.9831E-4 D Ph(U)  deg
Master-Slave Links                                      1.7413 E Htot   W
Optional Parameters                                     1.7413 F Edot   W
ideal           Solid type
   6 RPN           Mach number
                   0.0000 a G or T                     0.21912 A ChngeMe
5C 5a / a /
   7 CONE          Adjusting Cone (1/2'' - 1'')
                1.2668E-4 a AreaI  m^2      Mstr       409.27 A |p|    Pa
                3.9878E-2 b PerimI m        7a         43.218 B Ph(p)  deg
                5.0000E-2 c Length m                 9.6386E-3 C |U|    m^3/s
    Same  8a    4.9087E-4 d AreaF  m^2      Mstr      -2.8989E-3 D Ph(U)  deg
                7.8538E-2 e PerimF m        7d         1.4373 E Htot   W
                5.0000E-4 f Srough                     1.4373 F Edot   W
Master-Slave Links
Optional Parameters
ideal           Solid type
```

```
    8 DUCT        Connection pipe (1'')
              4.9087E-4 a Area    m^2      Mstr          44.908 A |p|     Pa
              7.8538E-2 b Perim   m        8a            80.471 B Ph(p)   deg
                 1.5000 c Length  m                   9.6471E-3 C |U|     m^3/s
              5.0000E-4 d Srough                     -5.7138E-2 D Ph(U)   deg
Master-Slave Links                            3.5649E-2 E Htot    W
Optional Parameters                           3.5649E-2 F Edot    W
ideal         Solid type
    9 DUCT        Half of the Resonator
              2.0250E-3 a Area    m^2        6.8368E-14 A |p|     Pa
                 0.1760 b Perim   m             -151.27 B Ph(p)   deg
                 1.0000 c Length  m           9.6498E-3 C |U|     m^3/s
              5.0000E-4 d Srough             -6.0714E-2 D Ph(U)   deg
Master-Slave Links                          -2.8909E-16 E Htot    W
Optional Parameters                         -2.8909E-16 F Edot    W
ideal         Solid type
   10 RPN         Womersly number - Reynolds number
                 0.0000 a G or T                11.257 A Wo
                                               607.11 B Re_dn
9C rho * dn * 9a / mu / ; 9a w * rho * mu / 2 / sqrt 2 /
   11 SOFTEND     Line of symmetry
Targ             0.0000 a Re(z)             6.8368E-14 A |p|     Pa
Targ             0.0000 b Im(z)                -151.27 B Ph(p)   deg
                                             9.6498E-3 C |U|     m^3/s
                                            -6.0714E-2 D Ph(U)   deg
                                           -2.8909E-16 E Htot    W
                                           -2.8909E-16 F Edot    W
                                           -3.0775E-17 G Re(z)
                                           -1.6912E-17 H Im(z)
                                                300.00 I T       K
```

A.3 DeltaEc code for the oscillating flow driven by the speakers.

```
Speakers
  0 BEGIN
              1.0133E+5 a Mean P Pa
                 23.300 b Freq   Hz
                 300.00 c TBeg   K
Gues             1623.1 d |p|    Pa
Gues             437.93 e Ph(p)  deg
                 0.0000 f |U|    m^3/s
                 0.0000 g Ph(U)  deg
Optional Parameters
air           Gas type
   1 DUCT       Rear Speaker Enclosure
              3.6300E-2 a Area   m^2          1615.4 A |p|     Pa
                 0.8600 b Perim  m            77.928 B Ph(p)   deg
                 0.2300 c Length m         1.3999E-2 C |U|     m^3/s
                 0.0000 d Srough             -12.222 D Ph(U)   deg
Master-Slave Links                            0.0000 E Htot    W
Optional Parameters                       -2.9717E-2 F Edot    W
ideal         Solid type
   2 VESPEAKER  Massive (TORO 104)
              3.6300E-2 a Area   m^2          3724.3 A |p|     Pa
                 1.8000 b R      ohms         65.549 B Ph(p)   deg
              6.8200E-4 c L      H         1.3996E-2 C |U|     m^3/s
                 11.280 d BLProd T-m          -12.311 D Ph(U)   deg
                 0.1613 e M      kg           16.062 E Htot    W
              2.7039E+4 f K      N/m          5.4812 F Edot    W
                 15.180 g Rm     N-s/m        16.062 G WorkIn  W
                 10.000 h |V|    V            10.000 H Volts   V
                 180.00 i Ph(V)  deg          3.2298 I Amps    A
                                              354.05 J Ph(V/I) deg
                                              2174.2 K |Px|    Pa
ideal         Solid type                      56.383 L Ph(Px)  deg
   3 RPN        enforce Resonance
                 0.0000 a G or T           77.859    A ChngeMe
2B 2D -
   4 ANCHOR     Change Me
   5 CONE       Cone
              7.8400E-2 a AreaI  m^2          3609.8 A |p|     Pa
                 1.1200 b PerimI m            65.433 B Ph(p)   deg
                 0.2200 c Length m         4.0011E-2 C |U|     m^3/s
    Same  8a  2.0250E-3 d AreaF  m^2          -20.327 D Ph(U)   deg
    Same  8b     0.1800 e PerimF m            5.3390 E Htot    W
              5.0000E-4 f Srough              5.3390 F Edot    W
Master-Slave Links
Optional Parameters
ideal         Solid type
```

```
47        6 STKRECT     Screen
48        Same   8a   2.0250E-3 a Area    m^2                    3407.4 A |p|     Pa
49                      0.59711 b GasA/A          6def            67.867 B Ph(p)  deg
50                    2.5000E-2 c Length m                    4.0130E-2 C |U|     m^3/s
51                    8.5000E-4 d aa      m       Mstr          -20.337 D Ph(U)  deg
52                    2.5000E-4 e Lplate  m       Mstr           5.3390 E Htot    W
53                    8.5000E-4 f bb      m       Mstr           2.1434 F Edot    W
54    Master-Slave Links                                         300.00 G TBeg    K
55    stainless     Solid type                                   299.73 H TEnd    K
56        7 DUCT        Resonator (location of pressure microphone)
57        Same   8a   2.0250E-3 a Area    m^2       Mstr         3059.6 A |p|     Pa
58                      0.15952 b Perim   m         7a             67.827 B Ph(p)  deg
59                       0.1000 c Length  m                    4.0813E-2 C |U|     m^3/s
60                    5.0000E-4 d Srough                        -20.378 D Ph(U)  deg
61    Master-Slave Links                                           1.9555 E Htot    W
62    Optional Parameters                                          1.9555 F Edot    W
63    ideal         Solid type
64        8 DUCT        Resonator (1st part)
65                    2.0250E-3 a Area    m^2                    972.46 A |p|     Pa
66                       0.1800 b Perim   m                      67.821 B Ph(p)  deg
67                       0.5750 c Length  m                    4.3278E-2 C |U|     m^3/s
68                    5.0000E-4 d Srough                        -20.525 D Ph(U)  deg
69    Master-Slave Links                                         0.60732 E Htot    W
70    Optional Parameters                                        0.60732 F Edot    W
71    ideal         Solid type
72        9 RPN         Total length of the 1st part
73                       0.0000 a G or T                         0.6750  A ChngeMe
74    8c 7c +
75        10 DUCT       Resonator (2nd part)
76        Same   8a   2.0250E-3 a Area    m^2                    972.00 A |p|     Pa
77        Same   8b      0.1800 b Perim   m                     -112.1 B Ph(p)  deg
78                       0.5200 c Length  m                    4.3278E-2 C |U|     m^3/s
79                       0.0000 d Srough                        -20.526 D Ph(U)  deg
80    Master-Slave Links                                         -0.5771 E Htot    W
81    Optional Parameters                                        -0.5771 F Edot    W
82    ideal         Solid type
83        11 RPN        Re delta and Womersely number
84                       0.0000 a G or T                        0.46259 A dn (mm)
85                                                               48.640  B Wo
86                                                              631.17   C Re dn
87    rho 10C * 10a / dn * mu / ; 10a sqrt 2 / dn / ; dn 1000 *
88        12 DUCT       Resonator (3rd part)
89        Same   8a   2.0250E-3 a Area    m^2                   3407.2 A |p|     Pa
90        Same   8b      0.1800 b Perim   m                    -112.13 B Ph(p)  deg
91        Same   9A      0.6750 c Length  m                    4.0129E-2 C |U|     m^3/s
92        Same   8d   5.0000E-4 d Srough                        -20.339 D Ph(U)  deg
93    Master-Slave Links                                         -2.1416 E Htot    W
94    Optional Parameters                                        -2.1416 F Edot    W
95    ideal         Solid type
```

```
96        13 STKRECT     screen
97          Same   6a   2.0250E-3 a Area    m^2                3609.7 A |p|     Pa
98                      0.59711 b GasA/A          13def        -114.57 B Ph(p)  deg
99          Same   6c   2.5000E-2 c Length  m                4.0009E-2 C |U|     m^3/s
100         Same   6d   8.5000E-4 d aa      m         Mstr      -20.327 D Ph(U)  deg
101         Same   6e   2.5000E-4 e Lplate  m         Mstr      -2.1416 E Htot   W
102         Same   6f   8.5000E-4 f bb      m         Mstr      -5.3391 F Edot   W
103     Master-Slave Links                                      299.73 G TBeg    K
104     stainless     Solid type                                299.98 H TEnd    K
105        14 CONE        Cone
106         Same   8a   2.0250E-3 a AreaI   m^2                3724.1 A |p|     Pa
107         Same   8b      0.1800 b PerimI  m                 -114.45 B Ph(p)  deg
108         Same   5c      0.2200 c Length  m                1.3995E-2 C |U|     m^3/s
109         Same   5a   7.8400E-2 d AreaF   m^2                -12.31 D Ph(U)  deg
110         Same   5b      1.1200 e PerimF  m                 -5.4812 E Htot   W
111         Same   5f   5.0000E-4 f Srough                     -5.4812 F Edot   W
112     Master-Slave Links
113     Optional Parameters
114     ideal         Solid type
115        15 VESPEAKER  Massive (TORO 104)
116         Same   2a   3.6300E-2 a Area    m^2                1615.4 A |p|     Pa
117         Same   2b      1.8000 b R       ohms               -102.07 B Ph(p)  deg
118         Same   2c   6.8200E-4 c L       H                1.3998E-2 C |U|     m^3/s
119         Same   2d      11.280 d BLProd  T-m                -12.221 D Ph(U)  deg
120         Same   2e      0.1613 e M       kg               2.9713E-2 E Htot   W
121         Same   2f   2.7039E+4 f K       N/m              2.9713E-2 F Edot   W
122         Same   2g      15.180 g Rm      N-s/m               16.062 G WorkIn W
123         Same   2h      10.000 h |V|     V                   10.000 H Volts  V
124         Same   2i      180.00 i Ph(V)   deg                 3.2299 I Amps   A
125                                                             354.06 J Ph(V/I) deg
126                                                             2174.1 K |Px|    Pa
127     ideal         Solid type                                56.381 L Ph(Px)  deg
128        16 DUCT        Rear Speaker Enclosure
129         Same   1a   3.6300E-2 a Area    m^2                1623.0 A |p|     Pa
130         Same   1b      0.8600 b Perim   m                 -102.07 B Ph(p)  deg
131         Same   1c      0.2300 c Length  m               5.1096E-17 C |U|     m^3/s
132         Same   1d      0.0000 d Srough                     -6.7631 D Ph(U)  deg
133     Master-Slave Links                                  -3.8373E-15 E Htot   W
134     Optional Parameters                                 -3.8373E-15 F Edot   W
135     ideal         Solid type
136        17 HARDEND     Rigid termination
137     Targ              0.0000 a R(1/z)                       1623.0 A |p|     Pa
138     Targ              0.0000 b I(1/z)                     -102.07 B Ph(p)  deg
139                                                         5.1096E-17 C |U|     m^3/s
140                                                            -6.7631 D Ph(U)  deg
141                                                         -3.8373E-15 E Htot   W
142                                                         -3.8373E-15 F Edot   W
143                                                         -3.2792E-17 G R(1/z)
144                                                          3.5282E-16 H I(1/z)
```

Appendices (B): Connection diagrams

B.1 Connection diagram for streaming PIV measurements

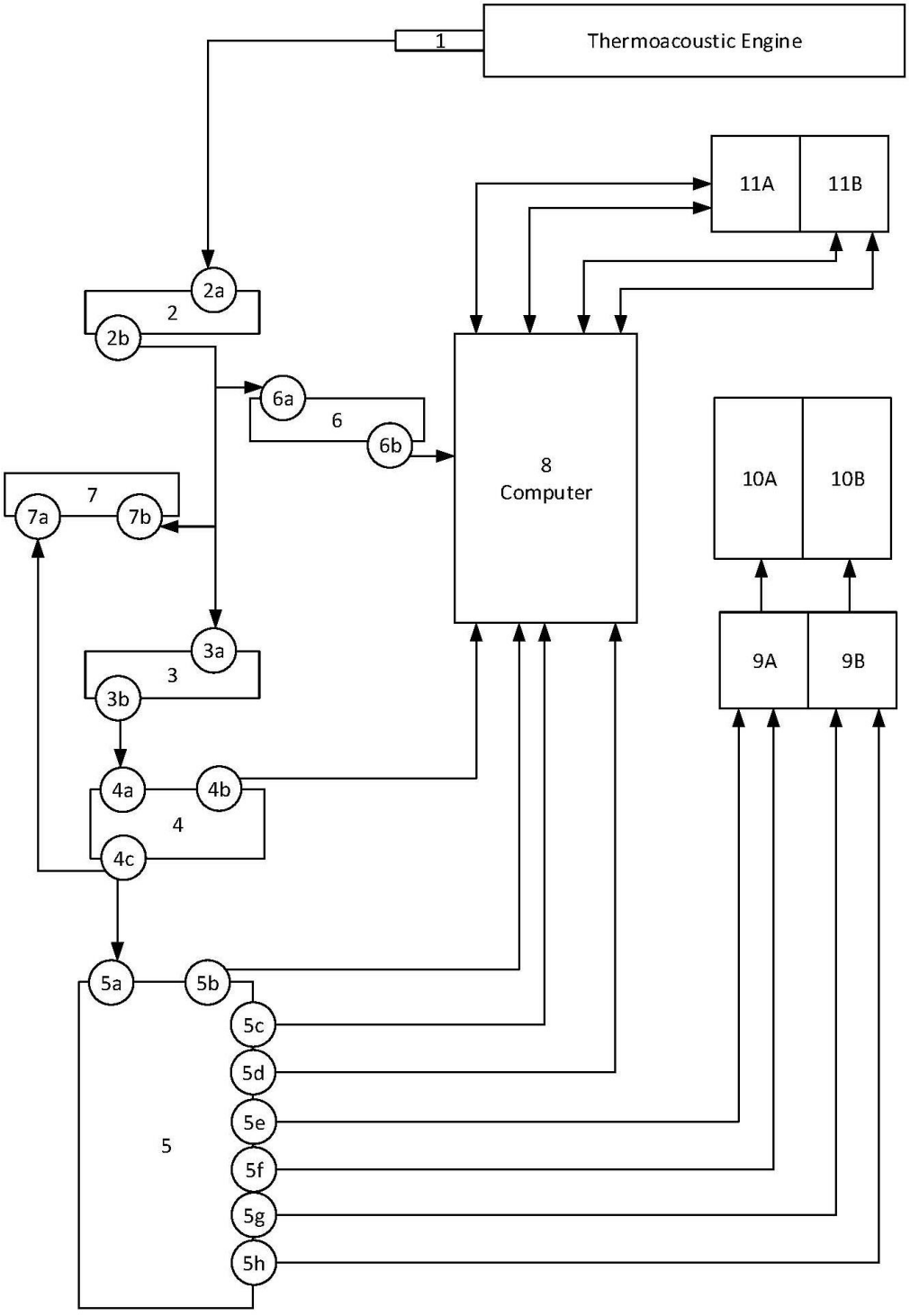

List of the devices used in the diagram are mentioned below:

Device # 1: Microphone screwed into Pre-amplifier

Device # 2: Signal Ampilifier

Device # 3: Lock-in Ampilifier

Device # 4: Delay Generator

Device # 5: Synchronizer

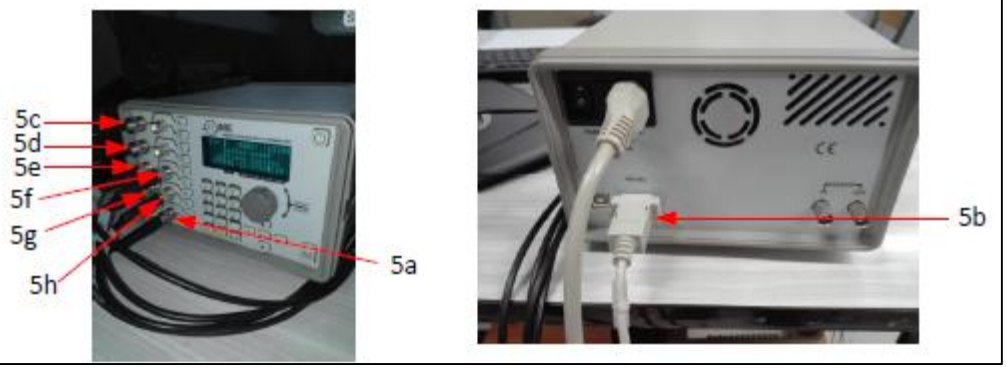

Device # 6: DAQ card

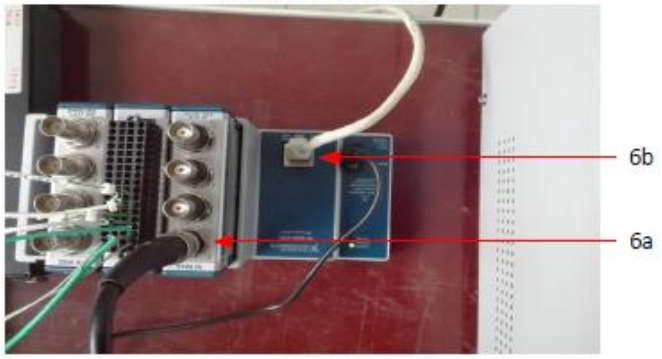

Device # 7: Oscilloscope

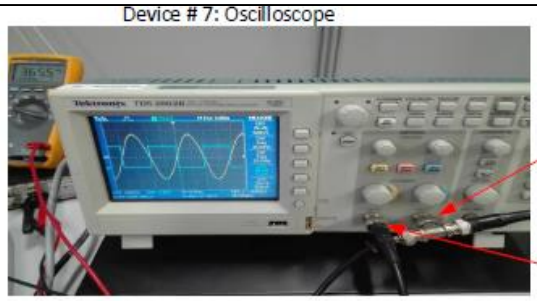

Device # 8: Computer

Device # 9: Laser Controllers and Chillers

Device # 10: Laser Heads

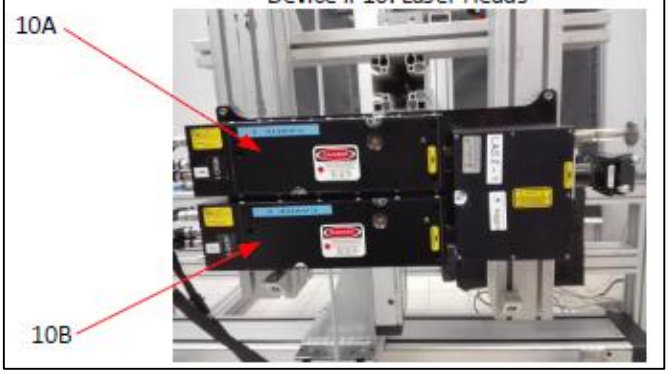

Device # 11: PIV Cameras

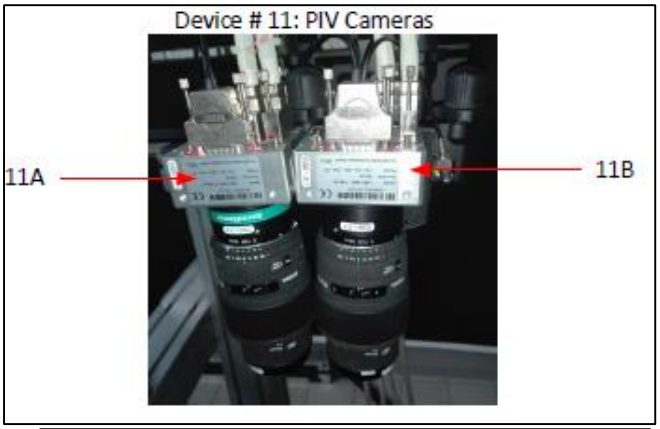

Device # 12: Function Generator

Device # 13: de-Phaser

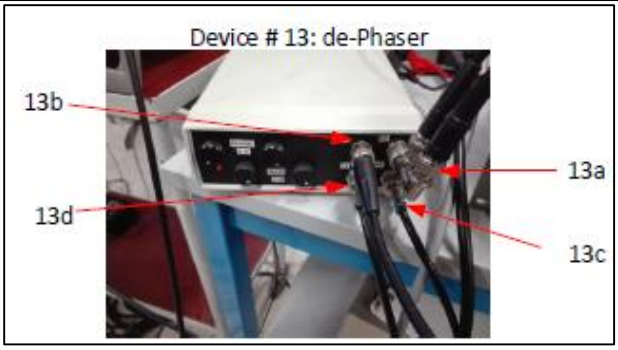

Device # 14: Power Amplifier

Device # 15: Power-meter

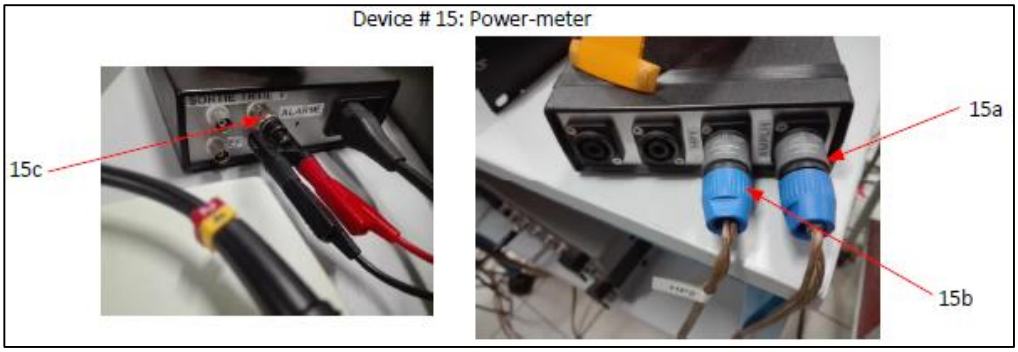

Device # 16: Multi-meter

B.2 Connection diagram for the experimental setup in Chapter 3: (Oscillating flow is generated by Scotch-yoke mechanism)

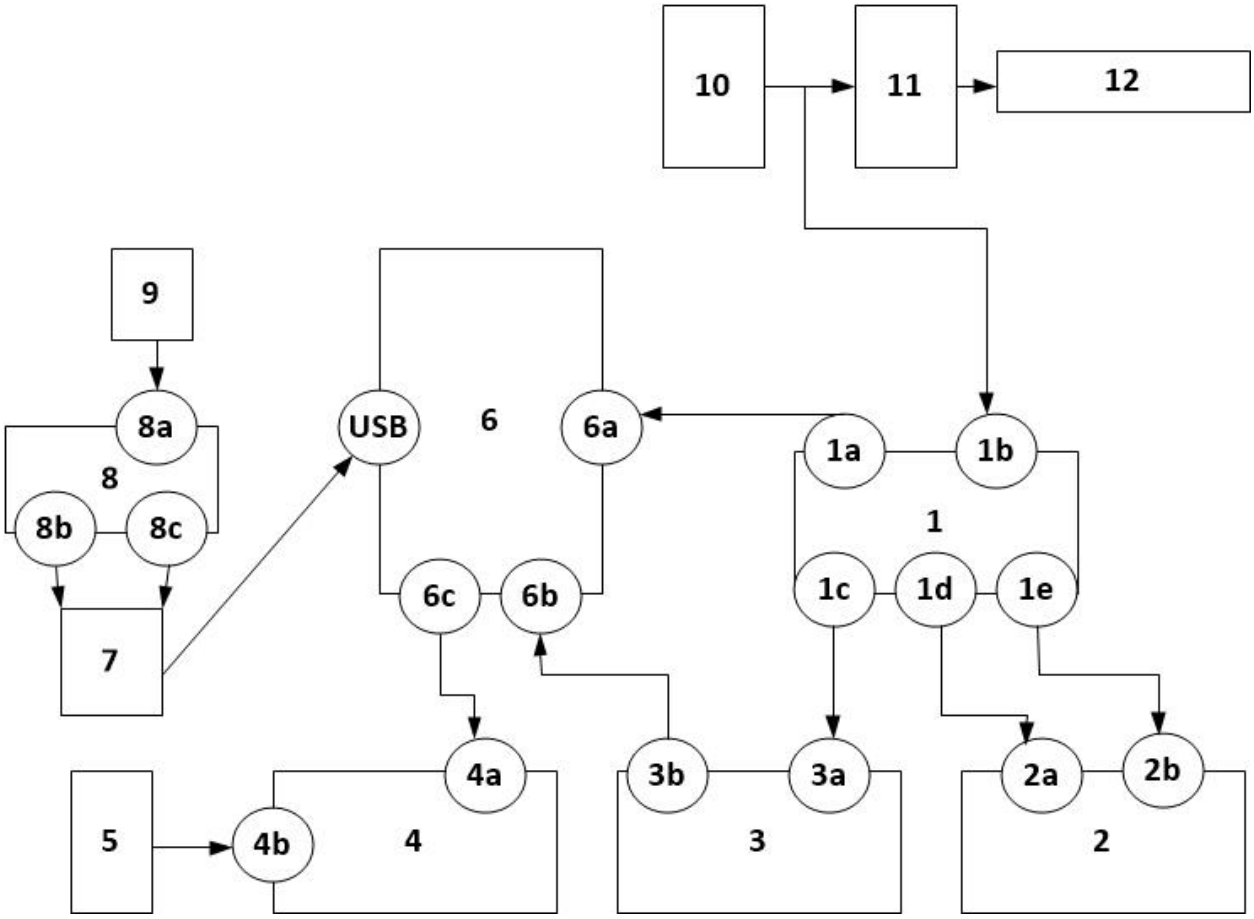

List of the devices used in the diagram are mentioned below:

Device# 1: Synchronization box

Device# 2: Laser head controller

Device# 3: Camera

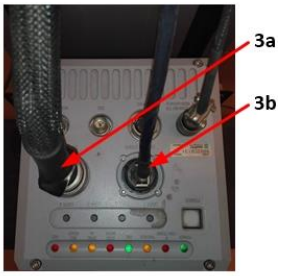

Device# 4: Traverse controller

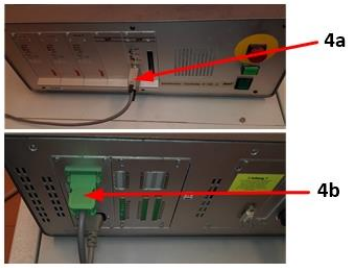

Device# 5: Emergency button

Device# 6: Computer

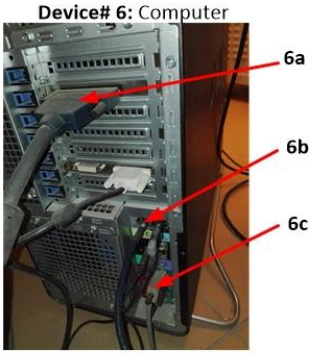

Device# 7: DAQ-Card

Device# 8: Demodulator

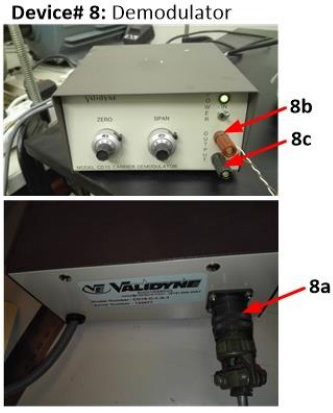

Device# 9: Pressure sensor

Device# 10: Line-tracker sensor

Device# 11: Micro-Controller

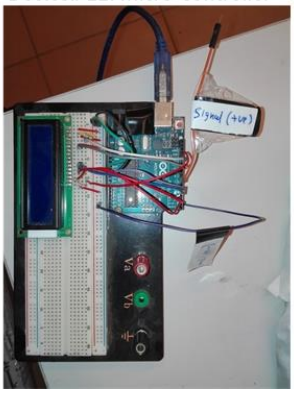

Device# 12: LCD screen

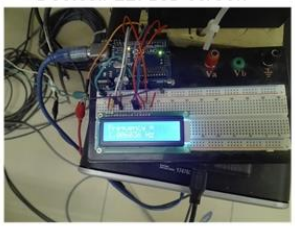

B.3 Connection diagram for the experimental setup in Chapter 3: (Oscillating flow is generated by two opposite speakers)

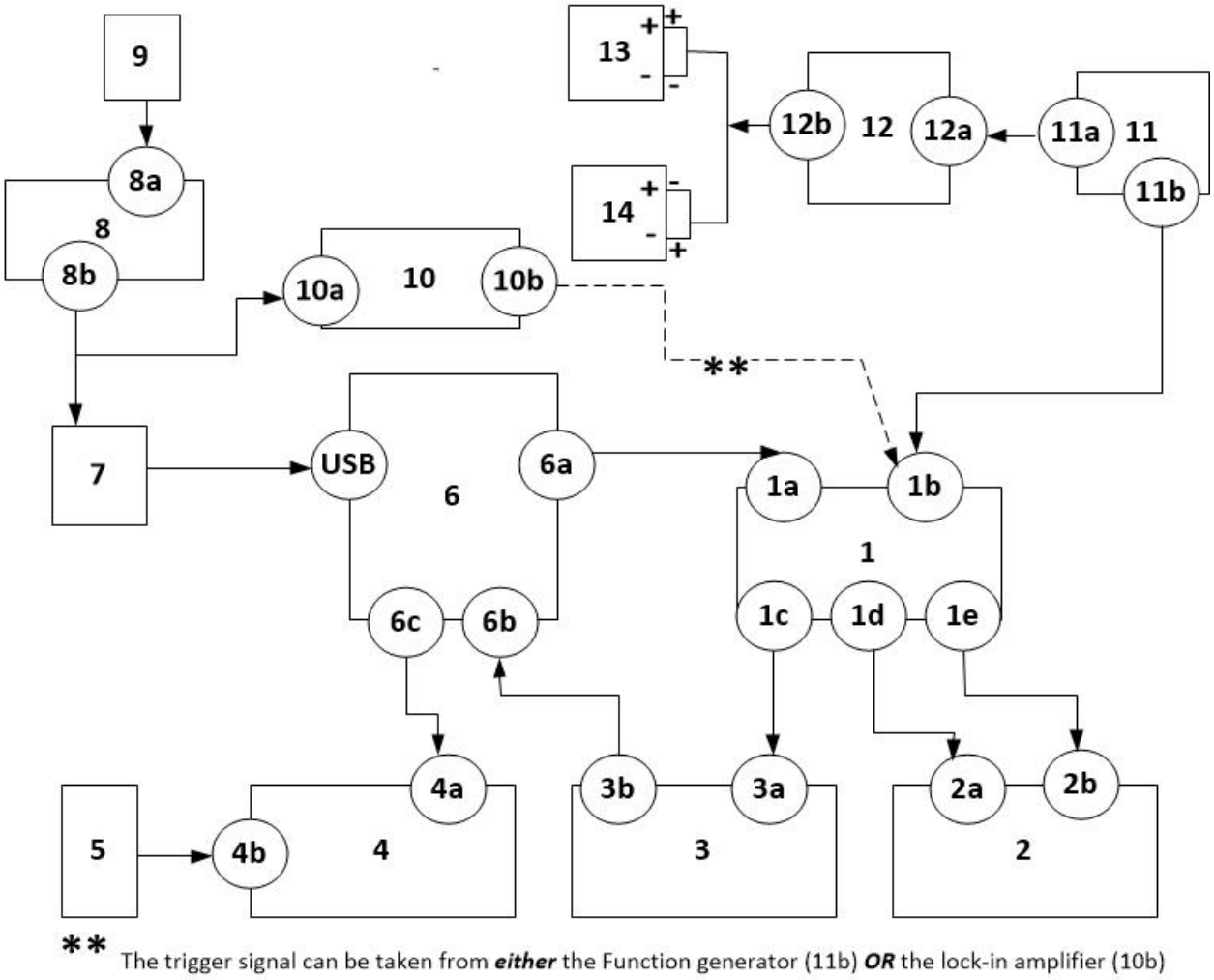

List of the devices used in the diagram are mentioned below:

Device# 1: Synchronization box

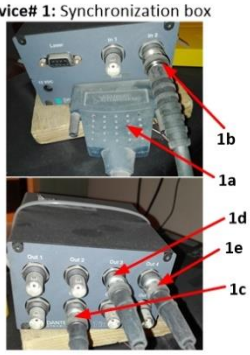

Device# 2: Laser head controller

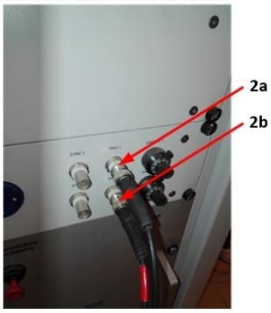

Device# 3: Camera

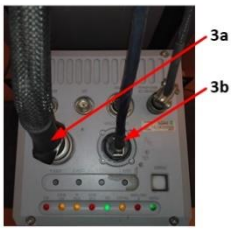

Device# 4: Traverse controller

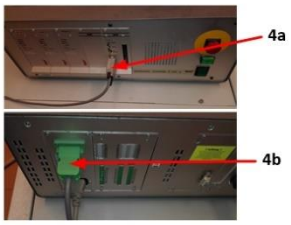

Device# 5: Emergency button

Device# 6: Computer

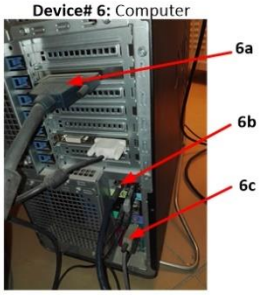

Device# 7: DAQ-Card

Device# 8: Signal amplifier

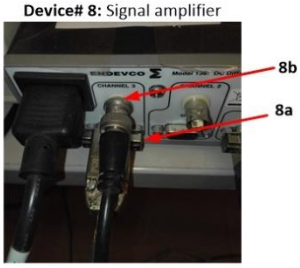

Device# 9: Pressure microphone

Device# 10: Lock-in amplifier

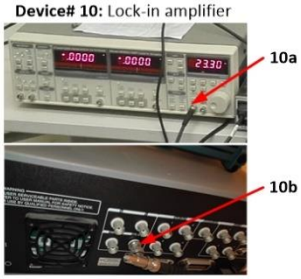

Device# 11: Function generator

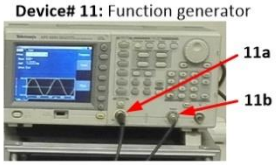

Device# 12: Power amplifier

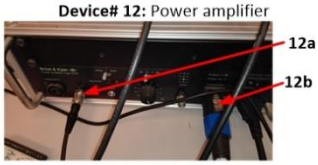

Device# 13: Right Speaker

Device# 14: Left Speaker

Appendices (C): Matlab Codes

C.1 Plot the acoustic velocity and the streaming velocity distributions from LDV data and compare them with the theoretical distributions

```
                %%%%The function of this code is to plot both the acoustic
and the streaming axial velocity distribution from LDV data%%%%%
% clear the memory
clear All
clear
clc
% Read the data file
N_files=input('The total number of axial locations (files)=');
F_pos=input('The axial position of the first location in mm (x-value)=');
L_pos=input('The axial position of the last location in mm (x-value)=');
S_pos=input('The axial step in mm=');
Freq_Imposee=input('Enter a value for the expected frequency (Hz)='); %%Hz
sp=input('The speed of sound (m/s)=');
pos=F_pos:S_pos:L_pos;
pos=[pos, -175]; %% If you have more points; they must be added to the
vector.
for FF=1:1:N_files
    if FF<10
    indx=['0' num2str(FF)];
    else
      indx=num2str(FF);
    end
fid = fopen(['test30_3.0000',indx,'.txt'],'rt');
Data = textscan(fid, '%f %f %f %f', 'HeaderLines',6);
fclose(fid);
RIEN=Data{1};
AT=Data{2};
TT=Data{3};
LDA1=Data{4};
AT=AT*10^-3; %% time (s)
n=size(LDA1,1);           %number of points
nn=0;
% plotting the raw data to determine the maximum and minimum velocity
% limits
plot(AT,LDA1,'*g');
xlabel('Time (seconds)'); ylabel('U_a_c (m/s)');
grid on
grid minor
% Input parameters
ST=n;
VLp=input('Enter the positive velocity limit (m/s)=');
VLn=input('Enter the negative velocity limit (m/s)=');
% toff=input('The time offset for this set of data=');
%Discretizing the data
%
for NST=0:ST:n-ST
T=AT((nn*ST+1):(nn+1)*ST,1)'; %% time (s)
V=LDA1((nn*ST+1):(nn+1)*ST,1)'; %% velocity (m/s)
Nb_pt=length(T);

if n>10                     %   criterion for the number of points
```

```
%%Frequency

%     Vmoyf=zeros(1,2001);

    choix=2;

    if(choix==1)
       f=Freq_Imposee-1:0.001:Freq_Imposee+1;
       size_f=size(f,2);
%        Vmoyf=zeros(1,size_f);
       for i=1:size_f;
          Xf=mean(V.*cos(2*pi*f(i)*T));
          Yf=mean(V.*sin(2*pi*f(i)*T));
          Vmoyf(i)=2*sqrt(Xf^2+Yf^2);
       end
       %plot(Vmoyf)
       [MaxV,K]=max(Vmoyf);
       freq=f(K);

    elseif(choix==2)
       %%%PASS 1
       f=Freq_Imposee-5:0.1:Freq_Imposee+5; %+/- 5
       size_f=size(f,2);
       Vmoyf=zeros(1,size_f);
       for i=1:size_f;
          Xf=mean(V.*cos(2*pi*f(i)*T));
          Yf=mean(V.*sin(2*pi*f(i)*T));
          Vmoyf(i)=2*sqrt(Xf^2+Yf^2);
       end
       [MaxV,K]=max(Vmoyf);
       freq=f(K);

       %%%PASS 2
       f=freq-0.1:0.01:freq+0.1;
       size_f=size(f,2);
       Vmoyf=zeros(1,size_f);
       for i=1:size_f;
          Xf=mean(V.*cos(2*pi*f(i)*T));
          Yf=mean(V.*sin(2*pi*f(i)*T));
          Vmoyf(i)=2*sqrt(Xf^2+Yf^2);
       end
       [MaxV,K]=max(Vmoyf);
       freq=f(K);

       %%%PASS 3
       f=freq-0.01:0.001:freq+0.01;
       size_f=size(f,2);
       Vmoyf=zeros(1,size_f);
       for i=1:size_f;
          Xf=mean(V.*cos(2*pi*f(i)*T));
          Yf=mean(V.*sin(2*pi*f(i)*T));
          Vmoyf(i)=2*sqrt(Xf^2+Yf^2);
       end
       [MaxV,K]=max(Vmoyf);
```

```
        freq=f(K);

    end

end

periode=1/freq;

V1=V;
T1=T;
for i=1:ST
    nb_periode=floor(T1(i)/periode);
    T1(i)=T1(i)-nb_periode*periode;
end
%% Sorting the data
% j=0;
[T2,kc]=sort(T1);
T2=T2';
% V2=zeros(n,1);
for i=1:ST
    V2(i,1)=V1(kc(i));
end

%                 pos_BZ=find(abs(V2)>0.1 & abs(V2)<3);
                pos_BZ=find(VLn<V2&V2<VLp);
                T2_BZ=T2(pos_BZ);
                V2_BZ=V2(pos_BZ);
 plot(T2_BZ,V2_BZ,'*k');
% ylim([-1*ceil(abs(VL)*1.01), ceil(abs(VL)*1.01)]);
 xlabel('Time (seconds)'); ylabel('U_ac (m/s)');
 hold on
m=length(T2_BZ);
Vitesse=zeros(m,2);
Vitesse(:,1)=T2_BZ;
Vitesse(:,2)=V2_BZ;
T6=Vitesse(:,1);
V6=Vitesse(:,2);
[m,kk]=size(T6);

%% Averaging the data over the interval : (T3,V3)
for i=1:m-1
    DT(i)=T6(i+1,1)-T6(i,1);
end
Dt=max(DT);
NbInt=floor(periode/Dt);  % number of intervals per cycle
Nb=zeros(NbInt,1);
p=periode/NbInt;
for j=1:NbInt
    T3(j)=(2*j-1)*p/2;
    ii=0;
    for i=1:m;
        if or(T6(i) < (j-1)*p,j*p <= T6(i))
%             ;
%          if T6(i) < (j-1)*p
%          elseif j*p <= T6(i)
         else
```

```
            ii=ii+1;
            Nb(j)=Nb(j)+1;
            SV(j,ii)=V6(i);
        end
    end
    if and(Nb(j)==0,j==1);
        V3(j)=V6(j);
    elseif and(Nb(j)==0,j>1);
         V3(j)=V3(j-1);
    else
    V3(j)=median(SV(j,:));
    end
%     V33(j)=mean(SV(j,:));
    P3(j)=Nb(j)/m;
    clear SV
end
plot(T3,V3,'og');
hold on
% plot(T3,V33,'-r');
pn=num2str(FF);
saveas(gcf,[pn '.jpg']);
hold off
close
    nn=nn+1;
    Fr(nn)=freq;
    Aac(nn)=(max(V3)-min(V3))/2;
    Us(nn)=mean(V3);
    Ti(nn)=AT(NST+ST);
clear T3 p Nb NbInt V3 V33 V2
end
Fr_F(FF)=Fr(nn);
Aac_F(FF)=Aac(nn);
Us_F(FF)=Us(nn);
end
%Theoretical curves
pos_theo=F_pos:(S_pos/100):L_pos;
pos_max=find(pos==0); %%% find the velocity at the center of the resonator
(zero position).
uac_theo=Aac_F(pos_max)*cos(0.5*pi*pos_theo/369);
ustr_theo=(3*Aac_F(pos_max)^2/(8*sp))*sin(1*pi*pos_theo/369);
% Plotting
subplot(3,1,1)
plot(pos,Fr_F,'*k');
xlabel('Position (mm)'); ylabel('Frequency(Hz)');
grid on
grid minor
% xlim([-150 360]);ylim([237 242]);
subplot(3,1,2)
plot(pos,Aac_F,'*g',pos_theo,uac_theo,'-k');
xlabel('Position (mm)'); ylabel('U_a_c (m/s)');
legend('Measured','theoretical');
grid on
grid minor
% xlim([-150 360]);
subplot(3,1,3)
plot(pos,Us_F,'*r',pos_theo,ustr_theo,'-k');
xlabel('Position (mm)'); ylabel('U_s_t_r_e_a_m_i_n_g (m/s)');
```

```
legend('Measured','theoretical');
grid on
grid minor
% xlim([-150 360]); ylim([-.05 .05]);
saveas(gcf,'Axial_Distribution.fig');
```

C.2 Plot the pressure signal and energy density of the pressure signal

```
%%%%%This functions of this codes are:%%%%%
%%%%%1- Removes the negative part of the signal because the sensor was
%%%%%connected to the positive pressure port and hence the negative values
%%%%%are not correct;%%%%%
%%%%%2- Plots the pressure signal with time%%%%%
%%%%%3- Calculates the Energy Density of the signal to make sure that there
%%%%%is no harmonics or at least they are negligible%%%%%
clear all;
clc;
A=xlsread('Data divided by 2.xlsx');
samprate= 200; %Hz
OF=0.5; %Hz
time=A([2:end],1);
volt=2*A([2:end],2);
volto=volt; %%%original voltage signal

%%% Removing the negative part from the signal because the pressure signal
%%%was connected to the positive pressure port and hence the negative
%%% data are not reliable.
pv=find(volt>=0);
timep=time(pv);
voltp=volt(pv);
volt=-1*volt;
nv=find(volt<0);
timen=time(nv)+0.5/OF;
voltn=volt(nv);
time=[timep;timen];
volt=[voltp;voltn];
[b m]=sort(time);
volt=volt(m);
[r c]=size(volt);
time=0:1/samprate:(r-1)/samprate;
time=time';

%%%Convert the voltage signal to pressure signal using calibration data
Pressure = volt*85.48-1.9; %%%% Pressure signal after removing the negative
part
Pressureo= volto*85.48-1.9;
%%%% Calculate standard dev., mean and effective bandwidth
numens = 1; %%% number of ensemble average
samples = length(Pressureo);
delta = 1/samprate;
nyquist = samprate/2;
reclength = samples/samprate;
avg = mean(Pressureo);
stddev = std(Pressureo);
bndwdth = 1/(reclength);
%%%% Data Standardization %%%%
x = Pressureo - avg;
%%%% Autospectrum Estimate %%%%
% clear ilng N nd j T specest
N = 2^floor(log2(samples/numens));
% 'N' is the number of points per ensemble.
% It is coerced to be power of 2
nd = floor(samples/N);
```

```
disp('For efficiency (i.e. power of 2 algorithm),')
disp(['the actual number of ensembles is ',num2str(nd),'.'])
disp(' ')
% 'nd' is the number of ensembles based on
% 'N' and total samples
q = 0.5;
% 'q' is the overlap parameter. Overlapping
% is done to minimize random error induced
% by Hanning tapering

ilng = nd/q;
j = (1:1:ilng);
T = N*delta;
frqres = 1/T;
rnderr = 1/(nd)^(1/2);

for count = 1:nd/q-1
    specmat(:,count) = x(q*(count-1)*N+1:(q*(count-1)+1)*N);
end
% apply Hanning window
t = (0:delta:T-delta)';
hann = 1 - (cos(t*pi/T)).^2;
clear count
for count = 1:nd/q-1
    specdata(:,count) = specmat(:,count).*hann;
end
specint = abs(delta*(8/3)^(1/2)*fft(specdata));
specest = 2/(N*nd*delta)*sum(specint.^2,2);
k = (0:1:N/2)';
fk = k/(N*delta);
srtspecf = sortrows([fk(2:N/2+1)';specest(2:N/2+1)']',2);
%%%% Plotting %%%%
subplot(3,1,1)
f=fit(time,Pressure,'fourier2');
plot(f,'-k',time,Pressure,'r.')
% axis([-0.03  0.03  -100 100 ])
title(['\bf Voltage Signal'])
% set(gca,'YTick',[-3000,-1500,0,1500,3000])
grid on
xlabel('\bf Time (second)');
ylabel( '\bf Pressure (Pa)');
subplot(3,1,2)
plot(fk, specest(1:N/2+1));
axis([0 max(fk) 0 max(specest(1:N/2+1))]);
xlabel('Frequency (Hz) -- Linear Scale');
ylabel('Energy. Density (Pa^2.s)');
grid on
subplot(3,1,3)
axis([0 1 0 1])
text(0.25,7/8,'Max. Autospectral Density Location (Hz)')
text(0.25,5/8,['1) ',num2str(srtspecf(N/2,1))])
text(0.25,3/8,['2) ',num2str(srtspecf(N/2-1,1))])
text(0.25,1/8,['3) ',num2str(srtspecf(N/2-2,1))])
text(0.5,5/8,['4) ',num2str(srtspecf(N/2-3,1))])
text(0.5,3/8,['5) ',num2str(srtspecf(N/2-4,1))])
text(0.5,1/8,['6) ',num2str(srtspecf(N/2-5,1))])
```

```
text(0.75,5/8,['7) ',num2str(srtspecf(N/2-6,1))])
text(0.75,3/8,['8) ',num2str(srtspecf(N/2-7,1))])
text(0.75,1/8,['9) ',num2str(srtspecf(N/2-8,1))])
saveas(gcf,'FFT_Pressure.fig');
saveas(gcf,'FFT_Pressure.jpg');
```

C.3 Calculate auto correlation and Energy density of the pressure signal

```
%%%%%This functions of this codes are:%%%%%
%%%%%1- plots the pressure signal and fit the data
%%%%%2- Removes the fitted curve from the original data to get the
%%%%%fluctuating component
%%%%%3- Calculates the auto correlation of the original signal and of the
%%%%%fluctuating signal as well
%%%%%4- Calculates the Energy density of the original signal and of the
%%%%%fluctuating signal as well
clear
clc
close
disp('Please make sure that the file names in lines and are changed');
de=0.045; %% diameter of the duct (m);
nu=1.57*10^-5; %%kinematic viscosity of the working fluid (m^2/s);
fs=9320; %% The sampling frequency Hz
f=23.3; %% The oscillating frequency Hz
dv=sqrt(2*nu/(2*pi*f)); %%% Viscous penetration depth
s=input('The sensitivity of the microphone (mv/kPa)='); %%% The sensitivity
of the microphones are as follows
G=50;%%% The gain of the signal conditioner
%%%% Microphone#1 (close to measurement section SN#23619)=16.49 mv/Kpa
%%%% Microphone#2 (close to the speaker SN#23749)=19.315 mv/Kpa
P=xlsread('1.xlsx'); %%% Pressure Signal from microphone
P=1000*(P-mean(P))*1000/(50*s); %%% value in Pa
[L a]=size(P);
t=(0:1:L-1)/fs;
%%% fitting the signal on sine wave
F=fit(t',P,'fourier2');
M=F(t);
Pf=P-M; %%%% Removing the fitted signal from the original one.
subplot(2,4,1)
plot(F,'-k',t,P,'.r');
legend('measured','fitted data');
xlim([0 0.1]);
xlabel('time (s)');
ylabel('Pressure (Pa)');
subplot(2,4,5)
plot(t,Pf,'.r');
legend('Fluctuating pressure');
xlim([0 0.1]);
xlabel('time (s)');
ylabel('Pressure (Pa)');
%%%Calculate the autocorrelation of the original signal
ho=xcorr(P,'coeff');
subplot(2,4,2)
plot((1:2*L-1)/round(fs/f),ho);
xlabel('Time/Time of cycle');
title('Autocorr for original signal');
%%%Calculate the autocorrelation of the signal after removing the fitted
%%%data
h=xcorr(Pf,'coeff');
subplot(2,4,6)
plot((1:2*L-1)/round(fs/f),h);
```

```
xlabel('Time/Time of cycle');
title('Autocorr for the fluctuating component');

%%%% Calculating the FFT and energy density spectrum for the original
%%%% signal
aFData=fft(P); % Take FFT of P signal
N=L/2; % FFT will yield half the number of unique points
aFreq=fs*(1:N)/N; % Frequency array (half the length of signal)
aFMag=abs(aFData(1:N)/L); % Normalized Magnitude array (half the length of
signal)
subplot(2,4,3)
semilogx(aFreq(2:N)/2,aFMag(2:N)) % Plot frequency against magnitude
title('Single-Sided Amplitude Spectrum of P(t)')
xlabel('Frequency (Hz)')
ylabel('|P(f)| (Pa)')
% Plot the energy density spectrum
Power=abs(fft(P)).^2/L; %Power is the magnitude squared by L
Energy=Power/fs;
subplot(2,4,4)
loglog(aFreq/2,Energy(2:L/2+1))
title('Energy Density Spectrum')
xlabel ('Frequency (Hz)')
ylabel ('Energy, E(f) (=Power/frequency) (Pa^2.s)')

%%%% Calculating the FFT and energy density spectrum for the signal after
removing the fitted
%%%data
aFData=fft(Pf); % Take FFT of P signal
N=L/2; % FFT will yield half the number of unique points
aFreq=fs*(1:N)/N; % Frequency array (half the length of signal)
aFMag=abs(aFData(1:N)/L); % Normalized Magnitude array (half the length of
signal)
subplot(2,4,7)
semilogx(aFreq(2:N)/2,aFMag(2:N)) % Plot frequency against magnitude
title('Single-Sided Amplitude Spectrum of P(t)')
xlabel('Frequency (Hz)')
ylabel('|P(f)| (Pa)')
% Plot the energy density spectrum
Power=abs(fft(Pf)).^2/L; %Power is the magnitude squared by L
Energy=Power/fs;
subplot(2,4,8)
loglog(aFreq/2,Energy(2:L/2+1))
title('Energy Density Spectrum')
xlabel ('Frequency (Hz)')
ylabel ('Energy, E(f) (=Power/frequency) (Pa^2.s)')

%%% saving the data
saveas(gcf,'P1.fig');
saveas(gcf,'P1.jpg');
```

C.4 Calculate the spatial average velocity distribution for each vector map

```
%%%% This code plots the spatial average of velocity distribution for each
velocity vector%%%
clear
clc
close
disp('Please make sure that the file names in line 27 are changed');
de=0.045; %% diameter of the duct (m);
nu=1.57*10^-5; %%kinematic viscosity of the working fluid (m^2/s);
fs=582.5; %% The sampling frequency Hz
f=23.3; %% The oscillating frequency Hz
dv=sqrt(2*nu/(2*pi*f)); %%% Viscous penetration depth
n=input('The number of files to be read=');
video=VideoWriter('output.avi');
video.FrameRate=1;
open(video);
for i=1:1:n;
    t(i)=(i-1)/fs; %%% time of each velocity map
    if i<11
    pointn = ['000' num2str(i-1)];
    elseif i<101
    pointn = ['00' num2str(i-1)];
    elseif i<1001
    pointn = ['0' num2str(i-1)];
    else
    pointn = num2str(i-1);
    end
fid = fopen(['Amp_2.5vpp_Fre23.3Hz_SF_582.5Hz_TbP_30_Amplifier(-
20and0).53k0nrjz.00',pointn,'.csv'],'rt');   %%%%%%%%% Enter numeric file
name
  A = textscan(fid,'%f %f %f %f %f %f %f
%f','delimiter',',','Multipledelimsasone',1,'Headerlines',10);
  A = ([A{1,1} A{1,2} A{1,3} A{1,4} A{1,5} A{1,6}]);
  fclose(fid); %% close file
 ncount=numel(A);
   for k = 1:ncount/6
      XP(k)=A(k,1); %Interrogation area number in x-direction
      YP(k)=A(k,2); %Interrogation area number in y-direction
      X(1+XP(k),1+YP(k))=A(k,3);  %True value of x in mm
      Y(1+XP(k),1+YP(k))=A(k,4);  %True value of y in mm
      u(1+XP(k),1+YP(k))=A(k,5); %True value of u in m/s
      v(1+XP(k),1+YP(k))=A(k,6); %True value of v in m/s
   end
    %% Spatial Averaging for the data in x-direction
    for y=1:1:127
     Ya(i,y)=mean(Y(:,y));
     ua(i,y)=median(u(:,y)); %%% here the median is used instead of mean to
eliminate the effect of spurious vectors.
     va(i,y)=median(v(:,y)); %%% here the median is used instead of mean to
eliminate the effect of spurious vectors.
    end

end
```

```
%% getting the velocity amplitude at the center of the duct and the phase of
the starting point
 for j=1:1:n
     uac(j)=ua(j,round(127/2));
 end
 ff=fit(t',uac','fourier2');
 tf=0:(1/((360)*f)):1/f; %%% The precision of the phase is about 0.5 deg
 Fc=ff(tf);
 [Amp Phsn]= max(Fc);
 Amp=(max(Fc)-min(Fc))/2; %%Amplitude of the wave at the center of the duct
 [zz tnPh]=size(tf);
 Phr=Phsn/tnPh*360;
 Phs=360+90-Phr;
 xx=floor(Phs/360);
 Phase=Phs-xx*360; %%% The phase of the starting point
%  plot(ff,t,uac,'-*g');
%  ylabel('Acoustic Velocity (m/s)');
%  xlabel('Time (sec)');
name=num2str(round(n/(fs/f)));
save(['Spatial Average
dis_',name,'cycles'],'Ya','ua','va','Phase','Amp','t','n');
clear i
break
 %% Plotting the measured data versus the theoretical values
 for Ph=1:1:n
   %%%% Calculating the theoretical distribution in a circular pipe (Reyt's
work 2013)
   tc=t(Ph)+(Phase/360)*(1/f)-0.25*(1/f);  %%% The last term is added because
the phase is measured from the time at which the velocity is zero (sine
wave),
   %%% Whereas the starting time of the theoretical equation is at
   %%% maximum velocity (Cos wave).
   for D = 0:0.0001:1 %% D: dimensionless depth. This "For-loop" is to
calculate the velocity at different depths.
   y = round(D*100+1);
   PsI(y)=D*de/2;
   wI(y)=Amp*exp(i*2*pi*f*tc)*(1-(besselj(0,PsI(y)*sqrt(-
1*i*2*pi*f/nu))/besselj(0,(de/2)*sqrt(-1*i*2*pi*f/nu))));
   end
    %%%% Calculating the theoretical distribution in a square duct (Fan's
work 1965)

for D = 0:0.01:1 %% D: dimensionless depth. This "For-loop" is to calculate
the velocity at different depths.
    y = round(D*100+1);
    PsF(y)=D/2;
    k=1;
    wt=t(Ph)*f*2*pi+(Phase/360)*2*pi;
    W=0; %% dimensionless width;
    P=1; %% aspect ratio of the rectangular duct (width/depth);
    FP=de*de*(2*pi*f)/(4*nu); %% dimensionless frequency parameter =
(width*depth*omega)/(4*Dynamic viscosity);
 for m=0:1:100; %% these "For-loops" are to calculate the double summation in
equation (17)
    for  n=0:1:100;
  t1=(-1)^(m+n)/((2*m+1)*(2*n+1)); %% first term of equ (17)
  t2=cos((2*m+1)*(pi*W/2)); %% second term of equ (17)
```

```
  t3=cos((2*n+1)*(pi*D/2)); %% third term of equ (17)
  t4n=(FP*pi^2*[((2*m+1)^2/P)+((2*n+1)^2*P)]*cos(wt)/4)+(FP^2*sin(wt)); %%
numerator of the fourth term of equ (17)
  t4d=(pi^4*([((2*m+1)^2/P)+((2*n+1)^2)*P]^2)/16)+FP^2; %% denominator of the
fourth term of equ (17)
  vv(k)=t1*t2*t3*(t4n/t4d);
  k=k+1;
    end
 end
 wF(y)=Amp*16*sum(vv)/pi^2; %% dimensionless velocity (%% equation # 17);
end

   %%%%% Plotting the theoretical values of both Fan and Reyt versus the
measured values
   Sh=-0.002; %%% This value is used to shift the data to get the wall
position by trial
   plot(ua(Ph,:),(Ya(Ph,:)/(1000)+Sh)/dv,'*r',wI,(-1*PsI+(de/2))/dv,'-
k',wF,(-1*PsF+0.5)*de/dv,'-g')
   legend('Measured','Reyt,2013','Fan,1965','Location','northeast');
   xlim([-1.2*Amp 1.2*Amp]);
   ylim([0.0 10]);
   xlabel('Acoustic Velocity (m/s)');
   ylabel('width/\delta_v');
   name=num2str(Ph);
   saveas(gcf,['Phase#',name,'.jpg']);
   saveas(gcf,['Phase#',name,'.fig']);
   img = imread(['Phase#',name,'.jpg']);
   writeVideo(video,img);
 end
 close
 clear
```

C.5 Calculate the ensemble average velocity distribution at different phases

```
%%%% This code plots the ensemble average velocity distribution at
%%%% different phases over one acoustic cycle
clear
clc
close
load('Spatial Average dis_100cycles'); This file is created by the code in
Appendix C.4
de=0.045; %% diameter of the duct (m);
nu=1.57*10^-5; %%kinematic viscosity of the working fluid (m^2/s);
fs=582.5; %% The sampling frequency Hz
f=23.3; %% The oscillating frequency Hz
dv=sqrt(2*nu/(2*pi*f)); %%% Viscous penetration depth
nPh=round(fs/f);%%% the number of phases in each cycle
% n=input('The number of files to be read=');
NOC=round(n/nPh); %%% The total number of cycles
video=VideoWriter('Ensemble_Average.avi');
video.FrameRate=1;
open(video);
for P=1:1:nPh;
    YEA(P,:)=Ya(P,:);
    uEA(P,:)=ua(P,:);
    vEA(P,:)=va(P,:);
    for g=nPh+P:nPh:n
        YEA(P,:)=YEA(P,:)+Ya(g,:);
        uEA(P,:)=uEA(P,:)+ua(g,:);
        vEA(P,:)=vEA(P,:)+va(g,:);
    end
     YEA(P,:)= YEA(P,:)/NOC;
     uEA(P,:)= uEA(P,:)/NOC;
     vEA(P,:)= vEA(P,:)/NOC;
end
save('Ensemble Average dis','YEA','uEA','vEA');
 % Plotting the measured data versus the theoretical values
 for Ph=1:1:nPh
   %%%% Calculating the theoretical distribution in a circular pipe (Reyt's
work 2013)
   tc=t(Ph)+(Phase/360)*(1/f)-0.25*(1/f);  %%% The last term is added because
the phase is measured from the time at which the velocity is zero (sine
wave),
   %%% Whereas the starting time of the theoretical equation is at
   %%% maximum velocity (Cos wave).
   for D = 0:0.0001:1 %% D: dimensionless depth. This "For-loop" is to
calculate the velocity at different depths.
   y = round(D*100+1);
   PsI(y)=D*de/2;
   wI(y)=Amp*exp(i*2*pi*f*tc)*(1-(besselj(0,PsI(y)*sqrt(-
1*i*2*pi*f/nu))/besselj(0,(de/2)*sqrt(-1*i*2*pi*f/nu))));
   end
    %%%% Calculating the theoretical distribution in a square duct (Fan's
work 1965)

for D = 0:0.01:1 %% D: dimensionless depth. This "For-loop" is to calculate
the velocity at different depths.
```

```
    y = round(D*100+1);
    PsF(y)=D/2;
    k=1;
    wt=t(Ph)*f*2*pi+(Phase/360)*2*pi;
    W=0; %% dimensionless width;
    P=1; %% aspect ratio of the rectangular duct (width/depth);
    FP=de*de*(2*pi*f)/(4*nu); %% dimensionless frequency parameter =
(width*depth*omega)/(4*Dynamic viscosity);
 for m=0:1:100; %% these "For-loops" are to calculate the double summation in
equation (17)
    for  n=0:1:100;
  t1=(-1)^(m+n)/((2*m+1)*(2*n+1)); %% first term of equ (17)
  t2=cos((2*m+1)*(pi*W/2)); %% second term of equ (17)
  t3=cos((2*n+1)*(pi*D/2)); %% third term of equ (17)
  t4n=(FP*pi^2*[((2*m+1)^2/P)+((2*n+1)^2*P)]*cos(wt)/4)+(FP^2*sin(wt)); %%
numerator of the fourth term of equ (17)
  t4d=(pi^4*([((2*m+1)^2/P)+((2*n+1)^2)*P]^2)/16)+FP^2; %% denominator of the
fourth term of equ (17)
  vv(k)=t1*t2*t3*(t4n/t4d);
  k=k+1;
    end
 end
 wF(y)=Amp*16*sum(vv)/pi^2; %% dimensionless velocity (%% equation # 17);
end
  Phs=Phase+(Ph-1)*360/nPh;
if Phs>360
    Phs=round(Phs-360);
else
    Phs=round(Phs);
end
subplot(1,2,1,'position',[0.1 0.35 0.25 0.3]);
th=0:1:360;
ampl=sin(th*pi/180);
plot(th,ampl,'-k',Phs,sin(Phs*pi/180),'*r','markersize',15);
set(gca,'fontsize',14)
xlabel('Phase, deg');
ylabel('U/Amp');
ylim([-1.2 1.2])
grid on
   %%%%% Plotting the theoretical values of both Fan and Reyt versus the
measured values
   Sh=-0.0021; %%% This value is used to shift the data to get the wall
position by trial
   subplot(1,2,2,'position',[0.45 0.1 0.45 0.8]);
   plot(uEA(Ph,:),(YEA(Ph,:)/(1000)+Sh)/dv,'*r',wI,(-1*PsI+(de/2))/dv,'-
k',wF,(-1*PsF+0.5)*de/dv,'-g')
   set(gca,'fontsize',14)
   legend('Measured','Reyt,2013','Fan,1965','Location','northeast');
   xlim([-1.2*Amp 1.2*Amp]);
   ylim([0.0 10]);
   name=num2str(Phs);
   xlabel('Acoustic Velocity (m/s)');
   ylabel('width/\delta_v');
   title(['Phase=',name,'deg']);
   saveas(gcf,['Phase#',name,'deg.jpg']);
   saveas(gcf,['Phase#',name,'deg.fig']);
   img = imread(['Phase#',name,'deg.jpg']);
```

```
  writeVideo(video,img);
end
close
clear
```

C.6 Calculate the turbulence intensities and Reynold Stress

```
%%%% This code plots the turbulence intensities based on both velocity
%%%% components and the Reynold Stress
clear
clc
close
load('Ensemble Average dis'); %%% This file is generated by the code in
Appendix C.5
load('Spatial Average dis_100cycles'); %%% This file is generated by the code
in Appendix C.4
de=0.045; %% diameter of the duct (m);
nu=1.57*10^-5; %%kinematic viscosity of the working fluid (m^2/s);
fs=582.5; %% The sampling frequency Hz
f=23.3; %% The oscillating frequency Hz
dv=sqrt(2*nu/(2*pi*f)); %%% Viscous penetration depth
nPh=round(fs/f);%%% the number of phases in each cycle
% n=input('The number of files to be read=');
NOC=round(n/nPh); %%% The total number of cycles
% video=VideoWriter('output_Tur_In.avi');
% video.FrameRate=1;
% open(video);
for P=1:1:nPh;
    Fx(P,:)=(ua(P,:)-uEA(P,:)).^2; %%%% fluctuations in x-direction
    Fy(P,:)=(va(P,:)-vEA(P,:)).^2; %%%% fluctuations in y-direction
    Re(P,:)=(ua(P,:)-uEA(P,:)).*(va(P,:)-vEA(P,:)); %%%% Reynolds stress
    for g=P+nPh:nPh:n
        Fx(P,:)=Fx(P,:)+(ua(g,:)-uEA(P,:)).^2;
        Fy(P,:)=Fy(P,:)+(va(g,:)-vEA(P,:)).^2;
        Re(P,:)=Re(P,:)+(ua(g,:)-uEA(P,:)).*(va(g,:)-vEA(P,:));
    end
    Ix(P,:)=sqrt(Fx(P,:)/NOC);
    Iy(P,:)=sqrt(Fy(P,:)/NOC);
    Res(P,:)=abs(Re(P,:))/NOC;
end
save('Turbulence intenesities','YEA','Ix','Iy','Res');

%%%%% Plotting the turbulence intensities distribution at different
%%%%% phases
 for Ph=1:1:nPh
Phs(Ph)=Phase+(Ph-1)*360/nPh;
if Phs(Ph)>360
    Phs(Ph)=round(Phs(Ph)-360);
else
    Phs(Ph)=round(Phs(Ph));
end
   %%%%% Plotting the turbulence intensities distribution at different
   %%%%% phases
   Sh=-0.002; %%% This value is used to shift the data to get the wall
position by trial
   subplot(1,2,1);
   plot(100*Ix(Ph,:)/Amp,(YEA(Ph,:)/(1000)+Sh)/dv,'-
*r',100*Iy(Ph,:)/Amp,(YEA(Ph,:)/(1000)+Sh)/dv,'-ok')
   legend('Ix','Iy','Location','northeast');
   xlim([0 40]);
   ylim([0.0 10]);
```

```
   xlabel('Turbulent Intensity, %');
   ylabel('width/\delta_v');
   set(gca,'fontsize',14)
   subplot(1,2,2);
   plot(100*Res(Ph,:)/(Amp^2),(YEA(Ph,:)/(1000)+Sh)/dv,'-*r')
   legend('Re_s_t_r_e_s_s','Location','northeast');
   xlim([0 0.15]);
   ylim([0.0 10]);
   xlabel('Reynolds stress/U^2, (%)');
   ylabel('width/\delta_v');
   set(gca,'fontsize',14)
   name=num2str(Phs(Ph));
   saveas(gcf,['Phase#',name,'deg.jpg']);
   saveas(gcf,['Phase#',name,'deg.fig']);
%    img = imread(['Phase#',name,'deg.jpg']);
%    writeVideo(video,img);
 end
 close
 [v o]=sort(Phs); %%% Sorting the phases
 %%%% Plotting the turbulence intensities versus the phase at different
 %%%% widths
 for W=23:1:100 %% Here we started from 23 NOT 1 because the first 22 points
were located outside/on the wall of the duct
   %%%%% Plotting the turbulence intensities distribution at different
   %%%%% phases
   subplot(1,2,1);
   plot(v,100*Ix(o,W)/Amp,'-*r',v,100*Iy(o,W)/Amp,'-ok')
   legend('Ix','Iy','Location','northeast');
   ylim([0 40]);
   xlim([0 360]);
   ylabel('Turbulent Intensity, %');
   xlabel('Phase, deg');
   set(gca,'fontsize',14)
   subplot(1,2,2);
   plot(v,100*Res(o,W)/(Amp^2),'-*r')
   legend('Re_s_t_r_e_s_s','Location','northeast');
   ylim([0 0.15]);
   xlim([0 360]);
   ylabel('Reynolds stress/U^2, (%)');
   xlabel('Phase, deg');
   set(gca,'fontsize',14)
   name=num2str((W-22)*(.076/1000)/dv);
   saveas(gcf,['Width',name,'dv.jpg']);
   saveas(gcf,['Width',name,'dv.fig']);
   img = imread(['Width',name,'dv.jpg']);
%    writeVideo(video,img);
 end
```

C.7 Calculate the vorticity field at different phases

```
%%%% This code plots the vorticity field at different phases
clear
clc
close
disp('Please make sure that the file names in line 32 are changed');
load('Spatial Average dis_100cycles.mat'); %%% This file is generated by the
code in Appendix C.4
de=0.045; %% diameter of the duct (m);
nu=1.57*10^-5; %%kinematic viscosity of the working fluid (m^2/s);
fs=582.5; %% The sampling frequency Hz
f=23.3; %% The oscillating frequency Hz
dv=sqrt(2*nu/(2*pi*f)); %%% Viscous penetration depth
n=input('The number of files to be read=');
NOC=round(n*f/fs); %%Total number of cycles
PPC=round(fs/f); %%% Number of points per cycle
video=VideoWriter('Vorticity.avi');
video.FrameRate=1;
open(video);
for jj=1:1:PPC;
    l=0;
    for j=jj:PPC:n
        l=l+1;
    t(l)=(l-1)/fs; %%% time of each velocity map
    if j<10
    pointn = ['000' num2str(j)];
    elseif j<100
    pointn = ['00' num2str(j)];
    elseif j<1000
    pointn = ['0' num2str(j)];
    else
    pointn = num2str(j);
    end
fid = fopen(['Amp_0.85vpp_Fre23.3Hz_SF_582.5Hz_TbP_55_Amplifier(-
20and0).53u1xaad.00',pointn,'.csv'],'rt');   %%%%%%%%% Enter numeric file
name
  A = textscan(fid,'%f %f %f %f %f %f %f
%f','delimiter',',','Multipledelimsasone',1,'Headerlines',10);
  A = ([A{1,1} A{1,2} A{1,3} A{1,4} A{1,5} A{1,6}]);
  fclose(fid); %% close file
  [c d]=size(A(:,1));
  xp(:,l)=A(:,1);
  yp(:,l)=A(:,2);
  x(:,l)=A(:,3);
  y(:,l)=A(:,4);
  up(:,l)=A(:,5);
  vp(:,l)=A(:,6);
    end
    for d=1:1:c
    XP(d)=median(xp(d,:));
    YP(d)=median(yp(d,:));
    X(d)=median(x(d,:));
    Y(d)=median(y(d,:));
    u(d)=median(up(d,:));
    v(d)=median(vp(d,:));
```

```
    end
    for k=1:1:c
      Px(k)=XP(k); %Interrogation area number in x-direction
      Py(k)=YP(k); %Interrogation area number in y-direction
      xx(1+Px(k),1+Py(k))=X(k)/1000;  %True value of x in m
      yy(1+Px(k),1+Py(k))=Y(k)/1000;  %True value of y in m
      U(1+Px(k),1+Py(k))=u(k); %True value of u in m/s
      V(1+Px(k),1+Py(k))=v(k); %True value of v in m/s
    end
    Ph(jj)=Phase+(jj-1)*(360/PPC);
    if Ph(jj)>360
        Ph(jj)=Ph(jj)-360;
    else
        Ph(jj)=Ph(jj);
    end
   name=num2str(round(Ph(jj)));
   save(['Vor_Phase_',name,'deg'],'Px','Py','xx','yy','U','V');

   %%%% Plotting the vorticity field
   clear j
   [g h]=size(U);
   for i = 1:g
       for j = 1:h
             if or(and(i==1,j<h),and(j==1,i<g))   %%bottom and left borders
, Forward technique is used
              dudy(i,j)=(U(i,j+1)-U(i,j))/(yy(i,j+1)-yy(i,j));
              dvdx(i,j)=(V(i+1,j)-V(i,j))/(xx(i+1,j)-xx(i,j));
              vort(i,j)=dvdx(i,j)-dudy(i,j);
          elseif or(and(i==g,j>1),and(j==h,i>1)) %%top and right borders ,
backward technique is used
              dudy(i,j)=(U(i,j)-U(i,j-1))/(yy(i,j)-yy(i,j-1));
              dvdx(i,j)=(V(i,j)-V(i-1,j))/(xx(i,j)-xx(i-1,j));
              vort(i,j)=dvdx(i,j)-dudy(i,j);
          elseif and(i==g,j==1) %%bottom and right corner , forward and
backward techniques are used respectively.
              dudy(i,j)=(U(i,j+1)-U(i,j))/(yy(i,j+1)-yy(i,j));
              dvdx(i,j)=(V(i,j)-V(i-1,j))/(xx(i,j)-xx(i-1,j));
              vort(i,j)=dvdx(i,j)-dudy(i,j);
           elseif and(i==1,j==h) %%top and left corner ,  backward and
forward techniques are used respectively.
              dudy(i,j)=(U(i,j)-U(i,j-1))/(yy(i,j)-yy(i,j-1));
              dvdx(i,j)=(V(i+1,j)-V(i,j))/(xx(i+1,j)-xx(i,j));
              vort(i,j)=dvdx(i,j)-dudy(i,j);
             else %%All internal points , central difference technique is
used
              dudy(i,j)=(U(i,j+1)-U(i,j-1))*0.5/(yy(i,j+1)-yy(i,j-1));
              dvdx(i,j)=(V(i+1,j)-V(i-1,j))*0.5/(xx(i+1,j)-xx(i-1,j));
              vort(i,j)=dvdx(i,j)-dudy(i,j);
          end

       end
   end
subplot(1,2,1,'position',[0.07 0.35 0.25 0.3]);
th=0:1:360;
ampl=sin(th*pi/180);
plot(th,ampl,'-k',Ph(jj),sin(Ph(jj)*pi/180),'*r','markersize',15);
```

```
set(gca,'fontsize',14)
xlabel('Phase, deg');
ylabel('U/Amp');
ylim([-1.2 1.2])
grid on
% Plot the vector map and vorticity contour levels
% in dimensionless form (Amp/dv = 1381499.02 s^-1)
subplot(1,2,2,'position',[0.45 0.1 0.5 0.85]);
 Sh=-2/1000; %%%(m) This value is used to shift the data to get the wall
position by trial
pcolor(xx/dv,(yy+Sh)/dv,vort); hold on
set(gca,'fontsize',14)
xlim([0 20])
ylim([0 10])
xlabel('x/\delta_v');
ylabel('width/\delta_v');
% title(['Phase=',name,'deg']);
% quiver(xx/(1000*dv),(yy+Sh)/(1000*dv),U,V,'Color',[0 0
0],'AutoScaleFactor',3.);
colorbar('southoutside');
shading interp;
set(gca, 'clim', [-25000 25000]);
colormap([0 0 0; jet]);
set(gca,'fontsize',14)
saveas(gcf,['Vor_Phase_',name,'deg.fig']);
saveas(gcf,['Vor_Phase_',name,'deg.jpg']);
img = imread(['Vor_Phase_',name,'deg.jpg']);
writeVideo(video,img);
close
end
clear
```

C.8 Calculate the Kolmogorov length scale at different phases

```
%%%% This code calculates the Kolmogorov length scale
clear
clc
close
disp('Please make sure that the file names in line 32 are changed');
load('Spatial Average dis_100cycles.mat'); %%% This file is generated by the
code in Appendix C.4
de=0.045; %% diameter of the duct (m);
nu=1.57*10^-5; %%kinematic viscosity of the working fluid (m^2/s);
fs=582.5; %% The sampling frequency Hz
f=23.3; %% The oscillating frequency Hz
dv=sqrt(2*nu/(2*pi*f)); %%% Viscous penetration depth
n=input('The number of files to be read=');
NOC=round(n*f/fs); %%Total number of cycles
PPC=round(fs/f); %%% Number of points per cycle
video=VideoWriter('kolmogorov.avi');
video.FrameRate=1;
open(video);
for jj=1:1:PPC;
    l=0;
    for j=jj:PPC:n
        l=l+1;
    t(l)=(l-1)/fs; %%% time of each velocity map
    if j<10
    pointn = ['000' num2str(j)];
    elseif j<100
    pointn = ['00' num2str(j)];
    elseif j<1000
    pointn = ['0' num2str(j)];
    else
    pointn = num2str(j);
    end
fid = fopen(['Amp_1.3vpp_Fre23.3Hz_SF_582.5Hz_TbP_44_Amplifier(-
20and0).53irros5.00',pointn,'.csv'],'rt');   %%%%%%%%% Enter numeric file
name
  A = textscan(fid,'%f %f %f %f %f %f %f
%f','delimiter',',','Multipledelimsasone',1,'Headerlines',10);
  A = ([A{1,1} A{1,2} A{1,3} A{1,4} A{1,5} A{1,6}]);
  fclose(fid); %% close file
  [c d]=size(A(:,1));
  xp(:,l)=A(:,1);
  yp(:,l)=A(:,2);
  x(:,l)=A(:,3);
  y(:,l)=A(:,4);
  up(:,l)=A(:,5);
  vp(:,l)=A(:,6);
    end
    for d=1:1:c
    XP(d)=median(xp(d,:));
    YP(d)=median(yp(d,:));
    X(d)=median(x(d,:));
    Y(d)=median(y(d,:));
    u(d)=median(up(d,:));
    v(d)=median(vp(d,:));
    end
```

```
    for k=1:1:c
      Px(k)=XP(k); %Interrogation area number in x-direction
      Py(k)=YP(k); %Interrogation area number in y-direction
      xx(1+Px(k),1+Py(k))=X(k)/1000;  %True value of x in m
      yy(1+Px(k),1+Py(k))=Y(k)/1000;  %True value of y in m
      U(1+Px(k),1+Py(k))=u(k); %True value of u in m/s
      V(1+Px(k),1+Py(k))=v(k); %True value of v in m/s
    end
    Ph(jj)=Phase+(jj-1)*(360/PPC);
    if Ph(jj)>360
        Ph(jj)=Ph(jj)-360;
    else
        Ph(jj)=Ph(jj);
    end
    %%%%removing the mean velocity
    Um=mean(U'); Vm=mean(V');
    Um=Um'; Vm=Vm';
    Um=repmat(Um, [1, 1+Px(k)]); Vm=repmat(Vm, [1, 1+Px(k)]);
    U=U-Um;  V=V-Vm;
   name=num2str(round(Ph(jj)));
   save(['Phase_',name,'deg'],'Px','Py','xx','yy','U','V');
   %%%% Plotting the Kolmogorov length scale field
   clear j
   [g h]=size(U);
   for i = 1:g
       for j = 1:h
             if or(and(i==1,j<h),and(j==1,i<g))   %%bottom and left borders
, Forward technique is used
                dudx(i,j)=(U(i,j+1)-U(i,j))/(xx(i+1,j)-xx(i,j));
                dvdy(i,j)=(V(i+1,j)-V(i,j))/(yy(i,j+1)-yy(i,j));
                dudy(i,j)=(U(i,j+1)-U(i,j))/(yy(i,j+1)-yy(i,j));
                dvdx(i,j)=(V(i+1,j)-V(i,j))/(xx(i+1,j)-xx(i,j));
                dis(i,j)= 3*nu*(dudx(i,j)^2+
dvdy(i,j)^2+dudy(i,j)^2+dvdx(i,j)^2+2*(dudy(i,j)*
dvdx(i,j))+(2*(dudx(i,j)*dvdy(i,j))/3)); %%%% energy dissipation rate
                KL(i,j)=(nu^3/dis(i,j))^0.25; %%Kolmogorov length scale
            elseif or(and(i==g,j>1),and(j==h,i>1)) %%top and right borders ,
backward technique is used
                dudx(i,j)=(U(i,j)-U(i,j-1))/(xx(i,j)-xx(i-1,j));
                dvdy(i,j)=(V(i,j)-V(i-1,j))/(yy(i,j)-yy(i,j-1));
                dudy(i,j)=(U(i,j)-U(i,j-1))/(yy(i,j)-yy(i,j-1));
                dvdx(i,j)=(V(i,j)-V(i-1,j))/(xx(i,j)-xx(i-1,j));
                dis(i,j)= 3*nu*(dudx(i,j)^2+
dvdy(i,j)^2+dudy(i,j)^2+dvdx(i,j)^2+2*(dudy(i,j)*
dvdx(i,j))+(2*(dudx(i,j)*dvdy(i,j))/3)); %%%% energy dissipation rate
                KL(i,j)=(nu^3/dis(i,j))^0.25; %%Kolmogorov length scale
            elseif and(i==g,j==1) %%bottom and right corner , forward and
backward techniques are used respectively.
                dudx(i,j)=(U(i,j+1)-U(i,j))/(xx(i,j)-xx(i-1,j));
                dvdy(i,j)=(V(i,j)-V(i-1,j))/(yy(i,j+1)-yy(i,j));
                dudy(i,j)=(U(i,j+1)-U(i,j))/(yy(i,j+1)-yy(i,j));
                dvdx(i,j)=(V(i,j)-V(i-1,j))/(xx(i,j)-xx(i-1,j));
                dis(i,j)= 3*nu*(dudx(i,j)^2+
dvdy(i,j)^2+dudy(i,j)^2+dvdx(i,j)^2+2*(dudy(i,j)*
dvdx(i,j))+(2*(dudx(i,j)*dvdy(i,j))/3)); %%%% energy dissipation rate
                KL(i,j)=(nu^3/dis(i,j))^0.25; %%Kolmogorov length scale
```

```
            elseif and(i==1,j==h) %%top and left corner ,  backward and
forward techniques are used respectively.
                dudx(i,j)=(U(i,j)-U(i,j-1))/(xx(i+1,j)-xx(i,j));
                dvdy(i,j)=(V(i+1,j)-V(i,j))/(yy(i,j)-yy(i,j-1));
                dudy(i,j)=(U(i,j)-U(i,j-1))/(yy(i,j)-yy(i,j-1));
                dvdx(i,j)=(V(i+1,j)-V(i,j))/(xx(i+1,j)-xx(i,j));
                dis(i,j)= 3*nu*(dudx(i,j)^2+
dvdy(i,j)^2+dudy(i,j)^2+dvdx(i,j)^2+2*(dudy(i,j)*
dvdx(i,j))+(2*(dudx(i,j)*dvdy(i,j))/3)); %%%% energy dissipation rate
                KL(i,j)=(nu^3/dis(i,j))^0.25; %%Kolmogorov length scale
               else %%All internal points, central difference technique is
used
                dudx(i,j)=(U(i,j+1)-U(i,j-1))*0.5/(xx(i+1,j)-xx(i-1,j));
                dvdy(i,j)=(V(i+1,j)-V(i-1,j))*0.5/(yy(i,j+1)-yy(i,j-1));
                dudy(i,j)=(U(i,j+1)-U(i,j-1))*0.5/(yy(i,j+1)-yy(i,j-1));
                dvdx(i,j)=(V(i+1,j)-V(i-1,j))*0.5/(xx(i+1,j)-xx(i-1,j));
                dis(i,j)= 3*nu*(dudx(i,j)^2+
dvdy(i,j)^2+dudy(i,j)^2+dvdx(i,j)^2+2*(dudy(i,j)*
dvdx(i,j))+(2*(dudx(i,j)*dvdy(i,j))/3)); %%%% energy dissipation rate
                KL(i,j)=(nu^3/dis(i,j))^0.25; %%Kolmogorov length scale
            end
        end
    end
subplot(1,2,1,'position',[0.07 0.35 0.25 0.3]);
th=0:1:360;
ampl=sin(th*pi/180);
plot(th,ampl,'-k',Ph(jj),sin(Ph(jj)*pi/180),'*r','markersize',15);
set(gca,'fontsize',14)
xlabel('Phase, deg');
ylabel('U/Amp');
ylim([-1.2 1.2])
grid on
% Plot the Kolmogorov length scale contour
subplot(1,2,2,'position',[0.45 0.1 0.5 0.85]);
 Sh=-1.8/1000; %%%(m) This value is used to shift the data to get the wall
position by trial
pcolor(xx/dv,(yy+Sh)/dv,KL*1000); hold on %%%% values of Length scale in mm
set(gca,'fontsize',14)
xlim([0 20])
ylim([0 10])
xlabel('x/\delta_v');
ylabel('width/\delta_v');
% title(['Phase=',name,'deg']);
% quiver(xx/(1000*dv),(yy+Sh)/(1000*dv),U,V,'Color',[0 0
0],'AutoScaleFactor',3.);
colorbar('southoutside');
shading interp;
set(gca, 'clim', [0 1]);
colormap([0 0 0; jet]);
set(gca,'fontsize',14)
saveas(gcf,['KL_Phase_',name,'deg.fig']);
saveas(gcf,['KL_Phase_',name,'deg.jpg']);
img = imread(['KL_Phase_',name,'deg.jpg']);
writeVideo(video,img);
close
end
clear
```

C.9 Calculate the spatial energy density spectra at different phases

```
%%%% This code calculates the spatial energy spectra of the signal in
%%%% y-direction
clear
clc
close
disp('Please make sure that the file names in line 33 are changed');
load('Spatial Average dis_100cycles.mat'); %%% This file is generated by the
code in Appendix C.4
de=0.045; %% diameter of the duct (m);
nu=1.57*10^-5; %%kinematic viscosity of the working fluid (m^2/s);
fs=582.5; %% The sampling frequency Hz
f=23.3; %% The oscillating frequency Hz
dv=sqrt(2*nu/(2*pi*f)); %%% Viscous penetration depth
n=input('The number of files to be read=');
NOC=round(n*f/fs); %%Total number of cycles
PPC=round(fs/f); %%% Number of points per cycle
video=VideoWriter('Spatial Energy Spectra.avi');
video.FrameRate=1;
open(video);
for jj=1:1:PPC;
    l=0;
    for j=jj:PPC:n
        l=l+1;
    t(l)=(l-1)/fs; %%% time of each velocity map
    if j<10
    pointn = ['000' num2str(j)];
    elseif j<100
    pointn = ['00' num2str(j)];
    elseif j<1000
    pointn = ['0' num2str(j)];
    else
    pointn = num2str(j);
    end
fid = fopen(['Amp_0.85vpp_Fre23.3Hz_SF_582.5Hz_TbP_55_Amplifier(-
20and0).53u1xaad.00',pointn,'.csv'],'rt');   %%%%%%%%% Enter numeric file
name
  A = textscan(fid,'%f %f %f %f %f %f %f
%f','delimiter',',','Multipledelimsasone',1,'Headerlines',10);
  A = ([A{1,1} A{1,2} A{1,3} A{1,4} A{1,5} A{1,6}]);
  fclose(fid); %% close file
  [c d]=size(A(:,1));
  xp(:,l)=A(:,1);
  yp(:,l)=A(:,2);
  x(:,l)=A(:,3);
  y(:,l)=A(:,4);
  up(:,l)=A(:,5);
  vp(:,l)=A(:,6);
    end
    for d=1:1:c
    XP(d)=median(xp(d,:));
    YP(d)=median(yp(d,:));
    X(d)=median(x(d,:));
    Y(d)=median(y(d,:));
    u(d)=median(up(d,:));
    v(d)=median(vp(d,:));
```

```
    end
    for k=1:1:c
      Px(k)=XP(k); %Interrogation area number in x-direction
      Py(k)=YP(k); %Interrogation area number in y-direction
      xx(1+Px(k),1+Py(k))=X(k)/1000;  %True value of x in m
      yy(1+Px(k),1+Py(k))=Y(k)/1000;  %True value of y in m
      U(1+Px(k),1+Py(k))=u(k); %True value of u in m/s
      V(1+Px(k),1+Py(k))=v(k); %True value of v in m/s
    end
    Ph(jj)=Phase+(jj-1)*(360/PPC);
    if Ph(jj)>360
        Ph(jj)=Ph(jj)-360;
    else
        Ph(jj)=Ph(jj);
    end
   name=num2str(round(Ph(jj)));
   save(['Phase_',name,'deg'],'Px','Py','xx','yy','U','V');
   %%% Calculating the spatial energy spectra
   clear j k
   %%%% removing the data outside the duct (The first 22 IA)
   xx=xx(:,23:end);
   yy=yy(:,23:end)-(22*0.076423/1000);
   U=U(:,23:end);
   V=V(:,23:end);
   [g h]=size(U);
   for j = 1:1:g
      for L=1:1:h
          k(L)=2*pi/yy(j,L);
          fu(L)=sum(abs(U(j,:)-mean(U(j,:))).*exp(-1*i*k(L)*yy(j,:)));
          fv(L)=sum(V(j,:).*exp(-1*i*k(L)*yy(j,:)));
          Eu(j,L)=yy(j,end)*(fu(L)*conj(fu(L)))/(2*pi*h^2); %%% energy
spectra based on axial velocity component
          Ev(j,L)=yy(j,end)*(fv(L)*conj(fv(L)))/(2*pi*h^2); %%% energy
spectra based on traverse velocity component
      end
   end
   %%% Averaging the energy spectra on the axial direction
   s=127; %%%step for averaging
   for m=1:s:g-s+1
       EuA(jj,:)=mean(Eu(m:m+s-1,:));
       EvA(jj,:)=mean(Ev(m:m+s-1,:));
       %%%%Plotting
      subplot(1,2,1)
      %%%plotting line with slope of -5/3
        x1=k(3);y1=EuA(jj,3);x2=300;
        ss=-5/3; %%%slope
        y2=10^(ss*(log10(x2)-log10(x1))+log10(y1));
        Lx=[x1 x2];Ly=[y1 y2];
      loglog(k,EuA(jj,:),':*r',Lx,Ly,'k')
      legend('Measured','slope=-5/3');
      xlabel('wave number (k), radians/m','fontsize', 14);
      ylabel('E_u(k), (m^2/s^2)/(rad/m)','fontsize', 14);
%       title(['Phase=',name,'deg'],'fontsize', 14);
      xlim([100 4e4])
      grid on;
      set(gca,'fontsize', 14)
      subplot(1,2,2)
```

```
        x1=k(3);y1=EvA(jj,3);x2=300;
        ss=-5/3; %%%slope
        y2=10^(ss*(log10(x2)-log10(x1))+log10(y1));
        Lx=[x1 x2];Ly=[y1 y2];
      loglog(k,EvA(jj,:),':*r',Lx,Ly,'k')
      legend('Measured','slope=-5/3');
      xlabel('wave number (k), radians/m','fontsize', 14);
      ylabel('E_v(k), (m^2/s^2)/(rad/m)','fontsize', 14);
%       title(['Phase=',name,'deg'],'fontsize', 14);
      xlim([100 4e4])
      grid on;
      set(gca,'fontsize', 14)
       saveas(gcf,['Phase',name,'deg.fig']);
       saveas(gcf,['Phase',name,'deg.jpg']);
       img = imread(['Phase',name,'deg.jpg']);
       writeVideo(video,img);
       close
   end
end
 %%% calculating the cycle average energy spectra
EuCA=mean(EuA);%%%cycle Average energy spectra;
EvCA=mean(EvA);%%%cycle Average energy spectra;
EUCA=sqrt(EuCA.*EvCA);%%%% The product of both energy spectra
%%%plotting
subplot(1,3,1)
x1=k(1);y1=EuCA(1);x2=300;
        ss=-5/3; %%%slope
        y2=10^(ss*(log10(x2)-log10(x1))+log10(y1));
        Lx=[x1 x2];Ly=[y1 y2];
      loglog(k,EuCA,':*b',Lx,Ly,'k')
      legend('Cycle Average','slope=-5/3');
      xlabel('wave number (k), radians/m','fontsize', 14);
      ylabel('E_u(k), (m^2/s^2)/(rad/m)','fontsize', 14);
%       title('Cycle average','fontsize', 14);
      xlim([100 4e4])
      grid on;
      set(gca,'fontsize', 14)
subplot(1,3,2)
x1=k(1);y1=EvCA(1);x2=300;
        ss=-5/3; %%%slope
        y2=10^(ss*(log10(x2)-log10(x1))+log10(y1));
        Lx=[x1 x2];Ly=[y1 y2];
      loglog(k,EvCA,':*b',Lx,Ly,'k')
      legend('Cycle Average','slope=-5/3');
      xlabel('wave number (k), radians/m','fontsize', 14);
      ylabel('E_v(k), (m^2/s^2)/(rad/m)','fontsize', 14);
%       title('Cycle average','fontsize', 14);
      xlim([100 4e4])
      grid on;
      set(gca,'fontsize', 14)
      subplot(1,3,3)
x1=k(1);y1=EUCA(1);x2=300;
        ss=-5/3; %%%slope
        y2=10^(ss*(log10(x2)-log10(x1))+log10(y1));
        Lx=[x1 x2];Ly=[y1 y2];
      loglog(k,EUCA,':*b',Lx,Ly,'k')
      legend('Cycle Average','slope=-5/3');
```

```
      xlabel('wave number (k), radians/m','fontsize', 14);
      ylabel('E_U_V(k), (m^2/s^2)/(rad/m)','fontsize', 14);
%       title('Cycle average','fontsize', 14);
      xlim([100 4e4])
      grid on;
      set(gca,'fontsize', 14)
saveas(gcf,'Cycle Average.fig');
saveas(gcf,'Cycle Average.jpg');
%  quiver(xx/(dv),(yy)/(dv),U,V,'Color',[0 0 0],'AutoScaleFactor',1.)
clear
```

C.10 Calculate the velocity amplitude and the starting phase of the freestream (away from the plates)

```
%%%% This code gets the velocity amplitude and starting phase of the
oscilating flow away from the plates
clear
clc
close
disp('Please make sure that the file name in line 22 is changed');
nu=1.57*10^-5; %%kinematic viscosity of the working fluid (m^2/s);
fs=582.5; %% The sampling frequency Hz
f=23.3; %% The oscillating frequency Hz
dv=sqrt(2*nu/(2*pi*f)); %%% Viscous penetration depth
n=input('The number of files to be read=');
for i=1:1:n;
    t(i)=(i-1)/fs; %%% time of each velcoity map
    if i<11
    pointn = ['000' num2str(i-1)];
    elseif i<101
    pointn = ['00' num2str(i-1)];
    elseif i<1001
    pointn = ['0' num2str(i-1)];
    else
    pointn = num2str(i-1);
    end
fid = fopen(['Rect_0.4vpp_test.56nbq7z4.00',pointn,'.csv'],'rt');   %%%%%%%%%
Enter numeric file name
  A = textscan(fid,'%f %f %f %f %f %f %f
%f','delimiter',',','Multipledelimsasone',1,'Headerlines',10);
  A = ([A{1,1} A{1,2} A{1,3} A{1,4} A{1,5} A{1,6}]);
  fclose(fid); %% close file
 ncount=numel(A);
   for k = 1:ncount/6
      XP(k)=A(k,1); %Interrogation area number in x-direction
      YP(k)=A(k,2); %Interrogation area number in y-direction
      X(1+XP(k),1+YP(k))=A(k,3);  %True value of x in mm
      Y(1+XP(k),1+YP(k))=A(k,4);  %True value of y in mm
      u(1+XP(k),1+YP(k))=A(k,5); %True value of u in m/s
      v(1+XP(k),1+YP(k))=A(k,6); %True value of v in m/s
   end
    %% Spatial Averaging for the data in x-direction away from the the plates
(columns 125 to 127)
    for y=1:1:127
     Ya(i,y)=mean(Y(125:127,y));
     ua(i,y)=median(u(125:127,y)); %%% here the median is used instead of
mean to eleminate the effect of spurious vectors.
     va(i,y)=median(v(125:127,y)); %%% here the median is used instead of
mean to eleminate the effect of spurious vectors.
    end

end
%% getting the velocity amplitude at the center of the duct and the phase of
the starting point
 for j=1:1:n
     uac(j)=ua(j,round(127/2));
 end
```

```
 ff=fit(t',uac','fourier2');
 plot(ff,t',uac','*k');
 tf=0:(1/((360)*f)):1/f; %%% The precision of the phase is about 0.5 deg
 Fc=ff(tf);
 [Amp Phsn]= max(Fc);
 Amp=(max(Fc)-min(Fc))/2; %%Amplitude of the wave at the center of the duct
 [zz tnPh]=size(tf);
 Phr=Phsn/tnPh*360;
 Phs=360+90-Phr;
 xx=floor(Phs/360);
 Phase=Phs-xx*360; %%% The phase of the starting point
%  plot(ff,t,uac,'-*g');
%  ylabel('Acoustic Velocity (m/s)');
%  xlabel('Time (sec)');
name=num2str(round(n/(fs/f)));
save(['Spatial Average dis_',name,'cycles'],'Ya','ua','va','t','n','Phase');
close
save('Amplitude','Amp');
```

C.11 Calculate the vorticity field and plot vector maps around the plates

```
%%%% This code plots the vorticity field at different phases
clear
clc
close
disp('Please make sure that the file name in line 37 is changed');
load('Spatial Average dis_100cycles.mat'); %%%obtained from code in appendix
C.10.
load('Amplitude.mat'); %%%obtained from code in appendix C.10.
de=0.045; %% diameter of the duct (m);
nu=1.57*10^-5; %%kinematic viscosity of the working fluid (m^2/s);
fs=582.5; %% The sampling frequency Hz
f=23.3; %% The oscillating frequency Hz
%%%%%%Parameters to be changed for each case
SL=0; %%% the starting location in the axial direction in mm
Shx=-0.4; %%% This value is used to make the zero location at the plate end
(it can be obtained by trial)
PHsh=15; %%% this value is added to the value of the starting phase to fine
tune its value because the synchronizer is not precise enough.
%%%%
dv=sqrt(2*nu/(2*pi*f)); %%% Viscous penetration depth
Xa=Amp/(2*pi*f); %%%Displacement amplitude in m
n=input('The number of files to be read=');
NOC=round(n*f/fs); %%Total number of cycles
PPC=round(fs/f); %%% Number of points per cycle
for jj=1:1:PPC;
    l=0;
    for j=jj:PPC:n
        l=l+1;
    t(l)=(l-1)/fs; %%% time of each velcoity map
    if j<10
    pointn = ['000' num2str(j)];
    elseif j<100
    pointn = ['00' num2str(j)];
    elseif j<1000
    pointn = ['0' num2str(j)];
    else
    pointn = num2str(j);
    end
fid = fopen(['Rect_0.4vpp_test.56nbq7z4.00',pointn,'.csv'],'rt');   %%%%%%%%%
Enter numeric file name
  A = textscan(fid,'%f %f %f %f %f %f %f
%f','delimiter',',','Multipledelimsasone',1,'Headerlines',10);
  A = ([A{1,1} A{1,2} A{1,3} A{1,4} A{1,5} A{1,6}]);
  fclose(fid); %% close file
  [c d]=size(A(:,1));
  xp(:,l)=A(:,1);
  yp(:,l)=A(:,2);
  x(:,l)=A(:,3);
  y(:,l)=A(:,4);
  up(:,l)=A(:,5);
  vp(:,l)=A(:,6);
    end
    for d=1:1:c
    XP(d)=median(xp(d,:));
    YP(d)=median(yp(d,:));
```

```
    X(d)=median(x(d,:));
    Y(d)=median(y(d,:));
    u(d)=median(up(d,:));
    v(d)=median(vp(d,:));
    end
    for k=1:1:c
      Px(k)=XP(k); %Interrogation area number in x-direction
      Py(k)=YP(k); %Interrogation area number in y-direction
      xx(1+Px(k),1+Py(k))=(X(k)+SL)/1000;  %True value of x in m
      yy(1+Px(k),1+Py(k))=Y(k)/1000;  %True value of y in m
      U(1+Px(k),1+Py(k))=u(k); %True value of u in m/s
      V(1+Px(k),1+Py(k))=v(k); %True value of v in m/s
    end
    Ph(jj)=Phase+PHsh+(jj-1)*(360/PPC); %%% constant is added to adjust the
phase
    if Ph(jj)>360
        Ph(jj)=Ph(jj)-360;
    else
        Ph(jj)=Ph(jj);
    end
   %%%% Averaging the data in axial direction (x-dir) to improve the
apperance
%%%% of vector map in the plot
for ii=1:1:127
    pp=1;
    for dd=1:3:127-1
    xxa(pp,ii)=mean(xx(dd:dd+3,ii));
    yya(pp,ii)=mean(yy(dd:dd+3,ii));
    Ua(pp,ii)=mean(U(dd:dd+3,ii));
    Va(pp,ii)=mean(V(dd:dd+3,ii));
%     xxa(ii,pp)=mean(xx(ii,dd:dd+1));
%     yya(ii,pp)=mean(yy(ii,dd:dd+1));
%     Ua(ii,pp)=mean(U(ii,dd:dd+1));
%     Va(ii,pp)=mean(V(ii,dd:dd+1));
    pp=pp+1;
    end
end
   %%%% Calculating the vorticity field
   clear j
   [g h]=size(U);
   for i = 1:g
       for j = 1:h
             if or(and(i==1,j<h),and(j==1,i<g))    %%bottom and left borders
, Forward technique is used
               dudy(i,j)=(U(i,j+1)-U(i,j))/(yy(i,j+1)-yy(i,j));
               dvdx(i,j)=(V(i+1,j)-V(i,j))/(xx(i+1,j)-xx(i,j));
               vort(i,j)=dvdx(i,j)-dudy(i,j);
           elseif or(and(i==g,j>1),and(j==h,i>1)) %%top and right borders ,
backward technique is used
               dudy(i,j)=(U(i,j)-U(i,j-1))/(yy(i,j)-yy(i,j-1));
               dvdx(i,j)=(V(i,j)-V(i-1,j))/(xx(i,j)-xx(i-1,j));
               vort(i,j)=dvdx(i,j)-dudy(i,j);
           elseif and(i==g,j==1) %%bottom and right corner , forward and
backward techniques are used respectively.
               dudy(i,j)=(U(i,j+1)-U(i,j))/(yy(i,j+1)-yy(i,j));
               dvdx(i,j)=(V(i,j)-V(i-1,j))/(xx(i,j)-xx(i-1,j));
               vort(i,j)=dvdx(i,j)-dudy(i,j);
```

```
            elseif and(i==1,j==h) %%top and left corner ,  backward and
forward techniques are used respectively.
                dudy(i,j)=(U(i,j)-U(i,j-1))/(yy(i,j)-yy(i,j-1));
                dvdx(i,j)=(V(i+1,j)-V(i,j))/(xx(i+1,j)-xx(i,j));
                vort(i,j)=dvdx(i,j)-dudy(i,j);
               else %%All internal points , central difference technique is
used
                dudy(i,j)=(U(i,j+1)-U(i,j-1))*0.5/(yy(i,j+1)-yy(i,j-1));
                dvdx(i,j)=(V(i+1,j)-V(i-1,j))*0.5/(xx(i+1,j)-xx(i-1,j));
                vort(i,j)=dvdx(i,j)-dudy(i,j);
            end
        end
    end
    Phr(jj)=round(Ph(jj));
       name=num2str(Phr(jj));
    save(['Vor_Phase_',name,'deg'],'xxa','yya','Ua','Va','xx','yy','vort');
%%%%% plotting
figure('units','normalized','outerposition',[0 0 1 1])
subplot(1,2,1);
subplot('position',[0.07 0.35 0.25 0.3]);
th=0:1:360;
ampl=sin(th*pi/180);
plot(th,ampl,'-k',Ph(jj),sin(Ph(jj)*pi/180),'*r','markersize',15);
set(gca,'fontsize',14)
xlabel('Phase, deg');
ylabel('U/Amp');
ylim([-1.2 1.2])
grid on
% Plot the vector map and vorticity contour levels
subplot(1,2,2);
subplot('position',[0.45 0.1 0.5 0.85]);
Shy=0/1000; %%%(m) This value is used to shift the data to get the wall
position by trial
pcolor(xx/Xa+Shx,(yy+Shy)/Xa,vort);
% set(e1,'facealpha',0.5)
hold on
set(gca,'fontsize',14)
% xlim([0 118.4])
ylim([0.95 2.25])
xlabel('x/X_A_m_p');
% ylabel('width/\delta_v');
% title(['Phase=',name,'deg']);
colorbar('southoutside');
shading interp;
% set(gca, 'clim', [-7000 7000]);
colormap(b2r(-5000,5000))
set(gca,'fontsize',14)
hold on
quiver(xxa/Xa+Shx,(yya+Shy)/Xa,Ua,Va,'Color',[0 0 0],'AutoScaleFactor',2);
hold off
set(gca,'YTickLabel',{' '})
saveas(gcf,['Vor_Phase_',name,'deg.fig']);
saveas(gcf,['Vor_Phase_',name,'deg.jpg']);
close
end
save('Phases_vor','Phr');
clear
```

C.12 Calculate the turbulence intensities around the plates

```
clear
close
clc
disp('Please make sure that the file name in line 35 is changed');
load('Spatial Average dis_100cycles.mat');
load('Amplitude.mat');
nu=1.57*10^-5; %%kinematic viscosity of the working fluid (m^2/s);
fs=582.5; %% The sampling frequency Hz
f=23.3; %% The oscillating frequency Hz
dv=sqrt(2*nu/(2*pi*f)); %%% Viscous penetration depth
Xa=Amp/(2*pi*f); %%%Displacement amplitude in m
n=input('The number of files to be read=');
%%%%%%Parameters to be changed for each case
Shx=-0.4; %%%This value is used to make the zero location at the plate end
(it can be obtained by trial)
SL=0; %%% the starting location in the axial direction in mm
PHsh=15; %%% this value is added to the value of the starting phase to fine
tune its value because the synchronizer is not precise enough.
%%%%
NOC=round(n*f/fs); %%Total number of cycles
PPC=round(fs/f); %%% Number of points per cycle
for jj=1:1:PPC
    l=0;
    for j=jj:PPC:n
        l=l+1;
    t(l)=(l-1)/fs; %%% time of each velcoity map
    if j<10
    pointn = ['000' num2str(j)];
    elseif j<100
    pointn = ['00' num2str(j)];
    elseif j<1000
    pointn = ['0' num2str(j)];
    else
    pointn = num2str(j);
    end
fid = fopen(['Rect_0.4vpp_test.56nbq7z4.00',pointn,'.csv'],'rt');    %%%%%%%%%
Enter numeric file name
  A = textscan(fid,'%f %f %f %f %f %f %f
%f','delimiter',',','Multipledelimsasone',1,'Headerlines',10);
  A = ([A{1,1} A{1,2} A{1,3} A{1,4} A{1,5} A{1,6}]);
  fclose(fid); %% close file
      ncount=numel(A);
        for k = 1:ncount/6
      XP(k)=A(k,1); %Interrogation area number in x-direction
      YP(k)=A(k,2); %Interrogation area number in y-direction
      X(1+XP(k),1+YP(k))=(A(k,3)+SL)/1000;  %True value of x in m
      Y(1+XP(k),1+YP(k))=A(k,4)/1000;  %True value of y in m
      u(1+XP(k),1+YP(k))=A(k,5); %True value of u in m/s
      v(1+XP(k),1+YP(k))=A(k,6); %True value of v in m/s
        end
    U(:,:,l)=u;
    V(:,:,l)=v;
    end
    %%% Calculating the phase
```

```
        Ph(jj)=Phase+PHsh+(jj-1)*(360/PPC); %%% constant is added to adjust
the phase
    if Ph(jj)>360
        Ph(jj)=Ph(jj)-360;
    else
        Ph(jj)=Ph(jj);
    end
%%% Calculate the turbulence intensities
for ii=1:1:127
    for bb=1:1:127
        for dd=1:1:l
       Uv(dd)=U(ii,bb,dd);
       Vv(dd)=V(ii,bb,dd);
        end
       Um(ii,bb)=mean(Uv);
       Vm(ii,bb)=mean(Vv);
       SU(ii,bb)=sqrt((l-1)/l)*std(Uv);%%/A(i,j)*100;
       SV(ii,bb)=sqrt((l-1)/l)*std(Vv);
    end
end
%%%%Plotting
%%%%% plotting
Phr(jj)=round(Ph(jj));
name=num2str(Phr(jj));
figure('units','normalized','outerposition',[0 0 1 1])
subplot(1,3,1);
subplot('position',[0.05 0.4 0.25 0.3]);
th=0:1:360;
ampl=sin(th*pi/180);
plot(th,ampl,'-k',Ph(jj),sin(Ph(jj)*pi/180),'*r','markersize',15);
set(gca,'fontsize',14)
xlabel('Phase, deg');
ylabel('U/Amp');
ylim([-1.2 1.2])
grid on
% Plot the turbulence intensity vector map based on x-velocity component
subplot(1,3,2);
subplot('position',[0.35 0.2 0.28 0.6]);
Shy=0/1000; %%%(m) This value is used to shift the data to get the wall
position by trial
pcolor(X/Xa+Shx,(Y+Shy)/Xa,SU/Amp*100);
% set(e1,'facealpha',0.5)
set(gca,'fontsize',14)
% xlim([0 118.4])
ylim([0.95 2.25])
xlabel('x/X_A_m_p');
% ylabel('width/\delta_v');
title('I_x (%)');
colorbar('southoutside');
shading interp;
% set(gca, 'clim', [-100 100]);
% colormap([0 0 0; jet]);
colormap(b2r(0,100))
set(gca,'fontsize',14)
set(gca,'YTickLabel',{' '})
% Plot the turbulence intensity vector map based on y-velocity component
subplot(1,3,3);
```

```
subplot('position',[0.7 0.2 0.28 0.6]);
Shy=0/1000; %%%(m) This value is used to shift the data to get the wall
position by trial
pcolor(X/Xa+Shx,(Y+Shy)/Xa,SV/Amp*100);
set(gca,'fontsize',14)
% xlim([0 118.4])
ylim([0.95 2.25])
xlabel('x/X_A_m_p');
% ylabel('width/\delta_v');
title('I_y (%)');
colorbar('southoutside');
shading interp;
% set(gca, 'clim', [-100 100]);
% colormap([0 0 0; jet]);
colormap(b2r(0,100))
set(gca,'fontsize',14)
set(gca,'YTickLabel',{' '})
saveas(gcf,['Tur_Phase_',name,'deg.fig']);
saveas(gcf,['Tur_Phase_',name,'deg.jpg']);
close
end
save('Phases_Tur','Phr');
clear
```

Appendices (D): Miscellaneous

D.1 Image for the experimental setup and the measurement system (Oscillating flow is driven by Scotch Yoke mechanism

D.2 Image for the experimental setup and the measurement system (Oscillating flow is driven by two opposite speakers)

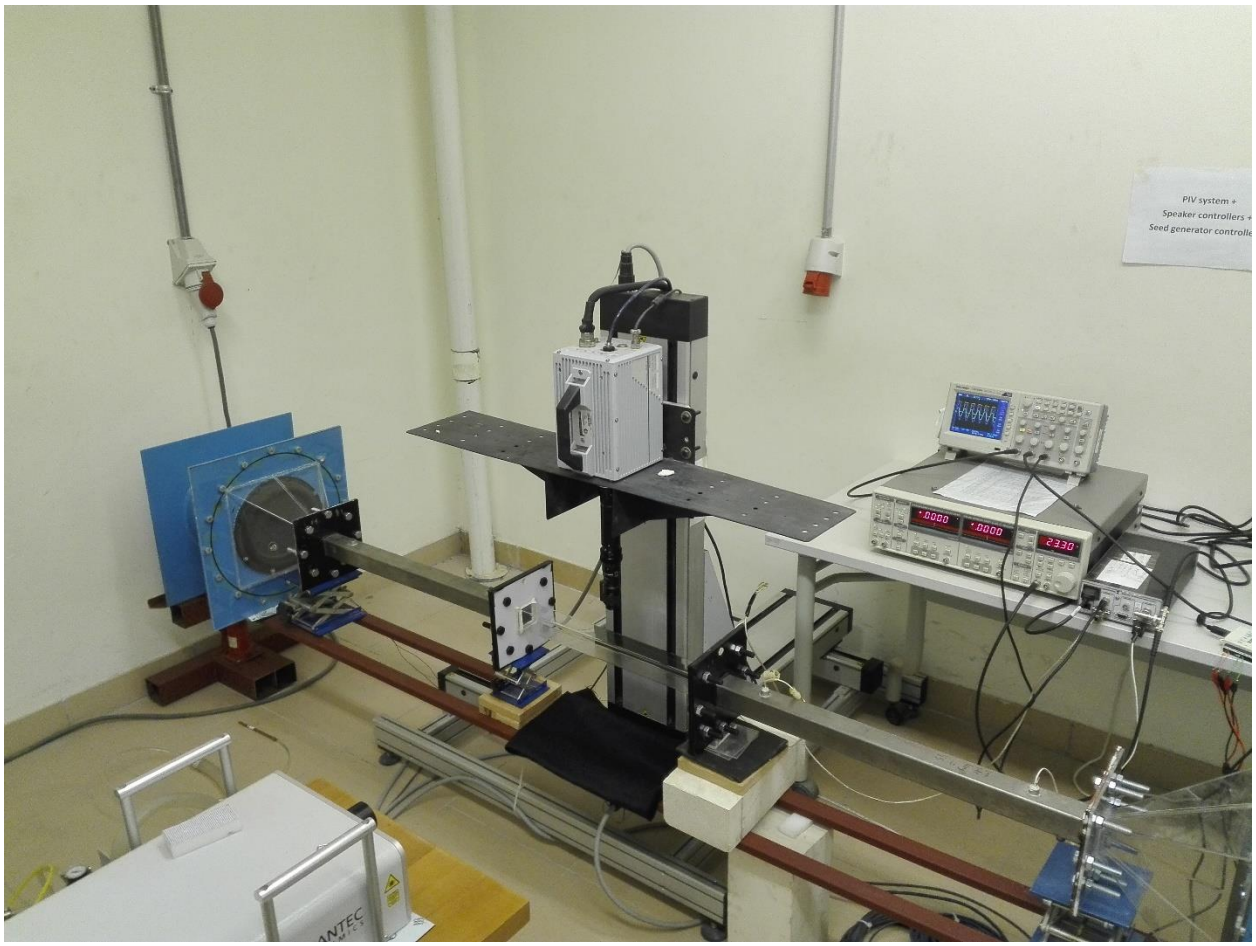

D.3 Images for the prime lens and zoom lens used with the CMOS camera

Prime lens

Zoom lens

D.4 Image for the calibration plate used for calibration of the PIV imaging system

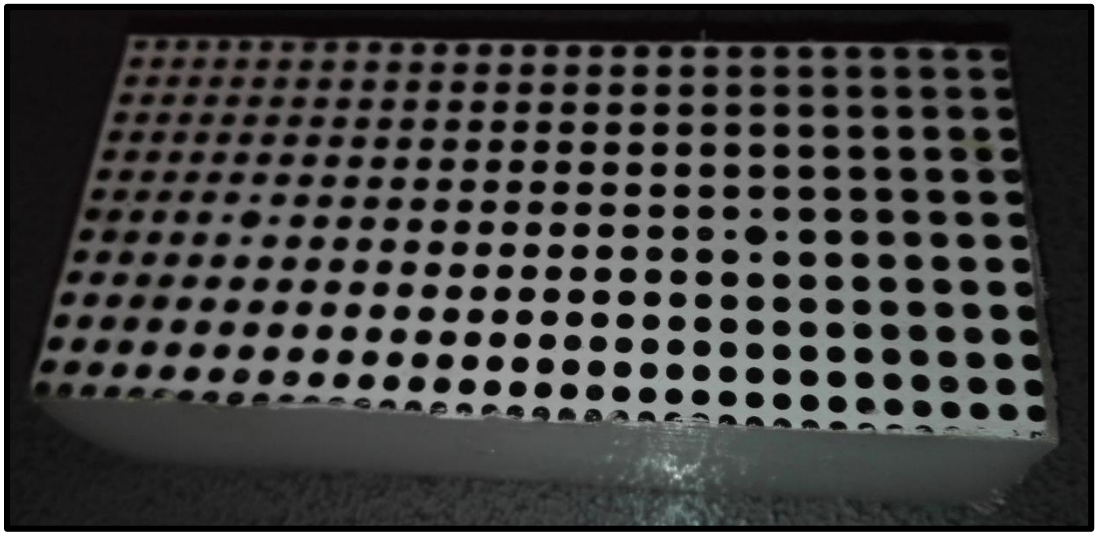

D.5 Example for the parameters of the PIV system.

Input data		
Camera		
Sensor size	20	mm
Focal length	60	mm
F#	8	
Actual size of the FOV	55	mm
Number of Pixels in x-direction	1024	pixel
Number of Pixels in y-direction	1024	pixel
Laser		
wave length	0.000000527	m
Measurement duration	4.3	s
seeding particles		
Average particle diameter	0.0000006	m
Particle density	900	Kg/m^3
Flow parameters		
Maximum velocity of the flow	5.8	m/s
Maximum acceleration of the flow	850	m/s^2
Fluid density	1.17	Kg/m^3
Fluid viscosity	0.00001846	kg/m.s
Frequency of turbulence fluctuations	1000	Hz (rough estimation)
Analysis parameters		
Random error constant	0.07	Ranged from **0.05** to **0.1** based on experiment conditions
size of intrrogation windows in one direction	16	
Overlap ratio	0.5	
Calculated data		
Magnification	0.363636364	camera sensor size / actual size of the measurement plane
Object distance (mm)	225	The distance between the camera sensor and the measurement plane
Total number of intrrogation windows in one direction	64	
Side length of the intrrogation window (mm)	0.859375	
Depth of field (mm)	1.8972	
Diffraction spot-size (mm)	0.014027782	
Effective particle image diameter (mm)	0.014027782	**the particle size can be increased**
Particle reponse time (s)	9.75081E-07	
Velocity lag (m/s)	0.000827742	difference between flow velocity and particle velocity in an accelerating flow
Characterisitc frequency of particle motion (Hz)	1025555.556	
Ratio between the turbulent flow fluctuations and particle fluctuations	0.993910691	**This value should be near 1**
Settling velocity (m/s)	9.55311E-06	
Ratio between the settling velocity and (the DOF divided by the measurement duration)	0.021652109	**This value should be less than 1**
Random error (mm)	0.000981945	
the recommended time between pulses to make sure the maximum particle displacement does not exceed 25% of the interrogation area (μs)	37.04202586	
Minimum velocity that can be measured (m/s)	0.757398198	
theoretical number of velocity vectors	16384	

D.6 Methods used to reduce the light reflections, physically.

In order to reduce the light reflections during the PIV measurement, a black sheet is placed below the measurement section and a black adhesive tape is stuck on the side of the measurement section, as shown below.

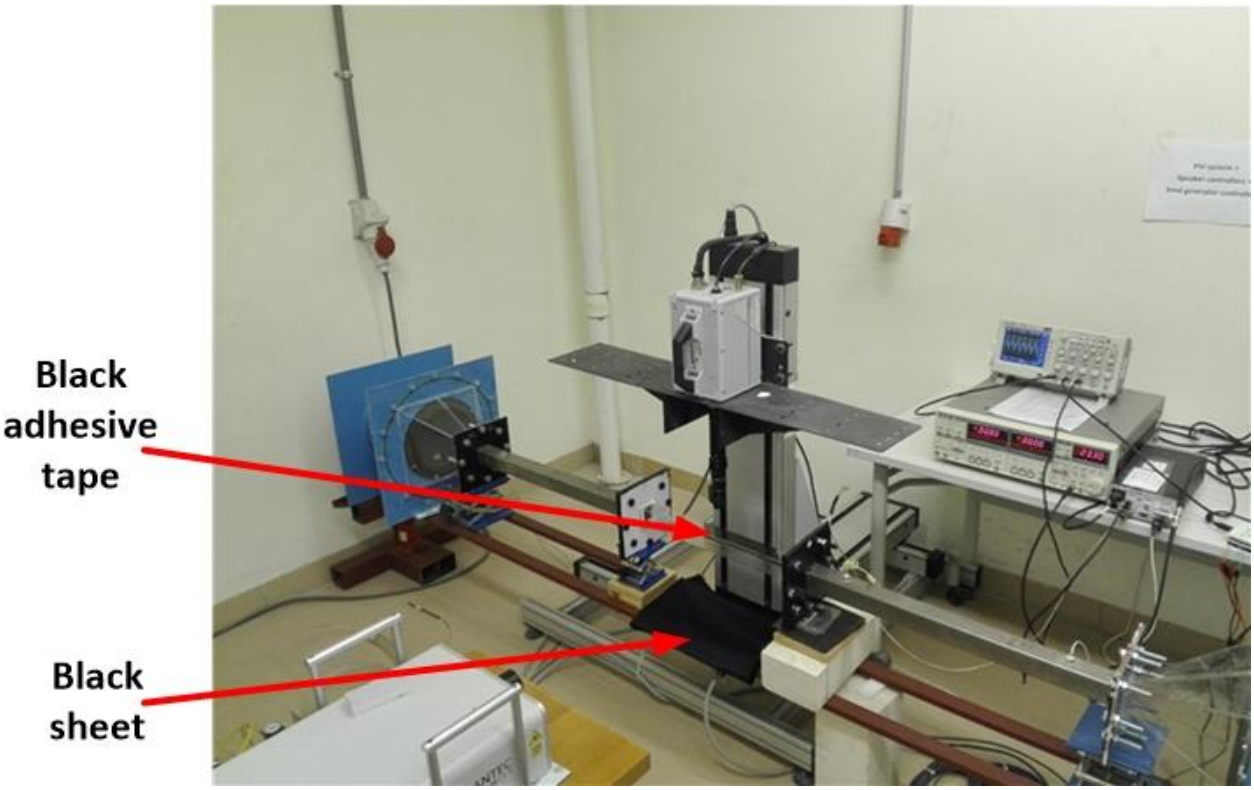

D.7 Mechanical drawings of different parts of the Scotch-Yoke mechanism

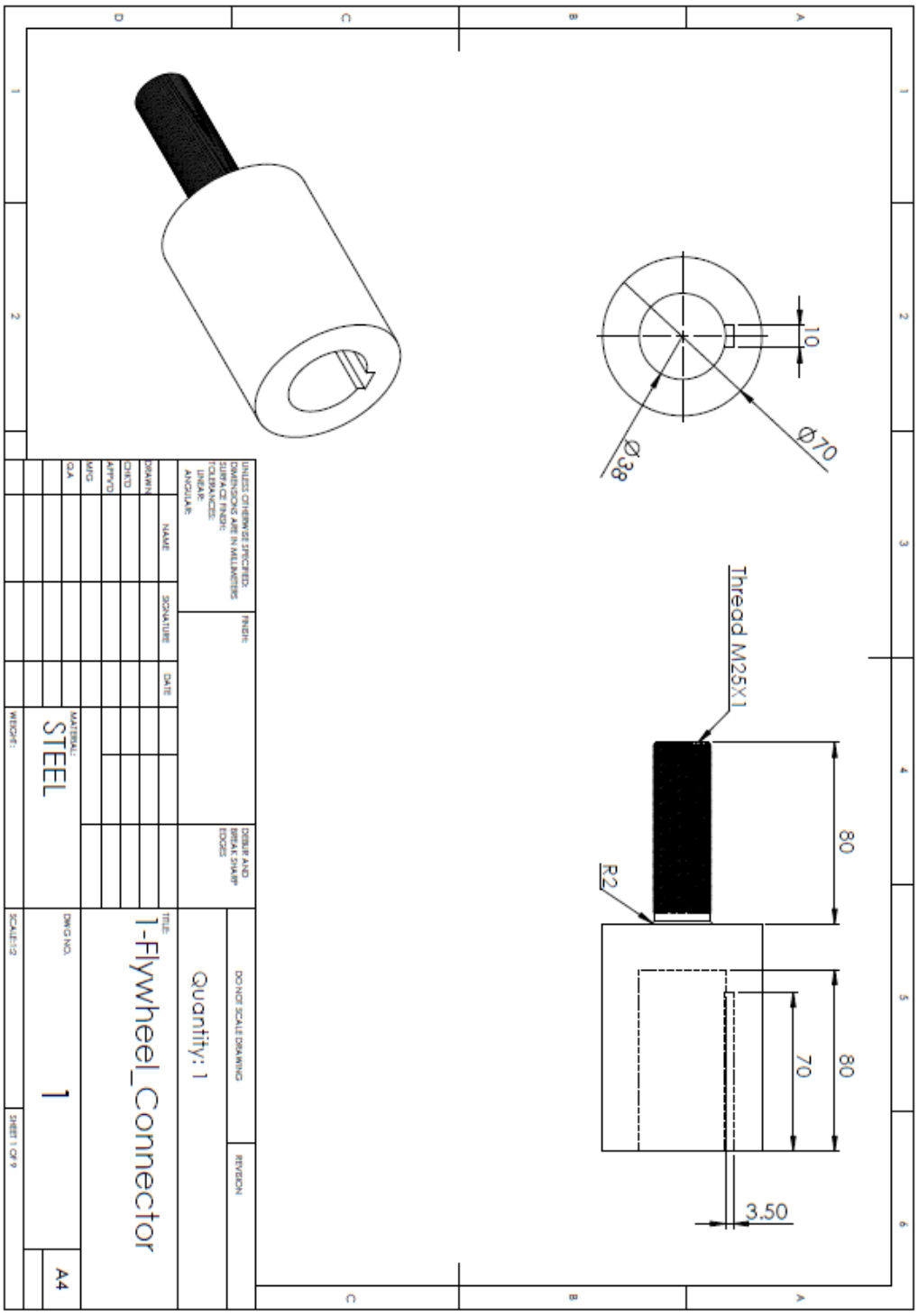

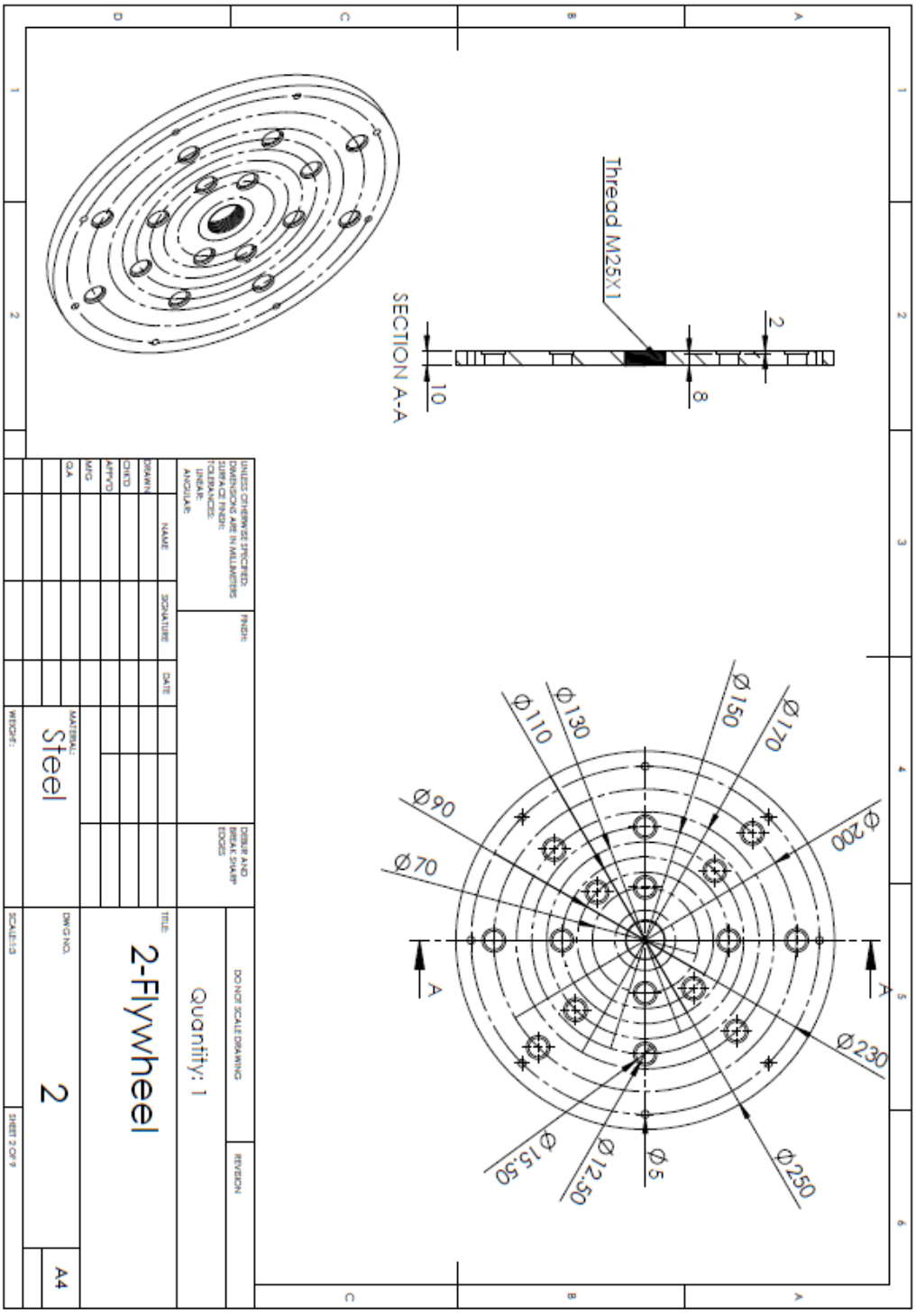
Thread M25X1
SECTION A-A
2
8
10
Ø70
Ø90
Ø110
Ø130
Ø150
Ø170
Ø200
Ø230
Ø250
Ø5
Ø12.50
Ø15.50
A
A
UNLESS OTHERWISE SPECIFIED:
DIMENSIONS ARE IN MILLIMETERS
SURFACE FINISH:
TOLERANCES:
LINEAR:
ANGULAR:
FINISH:
DEBUR AND BREAK SHARP EDGES
NAME
SIGNATURE
DATE
DRAWN
CHKD
APPV'D
MFG
Q.A.
MATERIAL:
Steel
WEIGHT:
DO NOT SCALE DRAWING
REVISION
TITLE:
2-Flywheel
Quantity: 1
DWG NO.
2
A4
SCALE:1:3
SHEET 2 OF 9

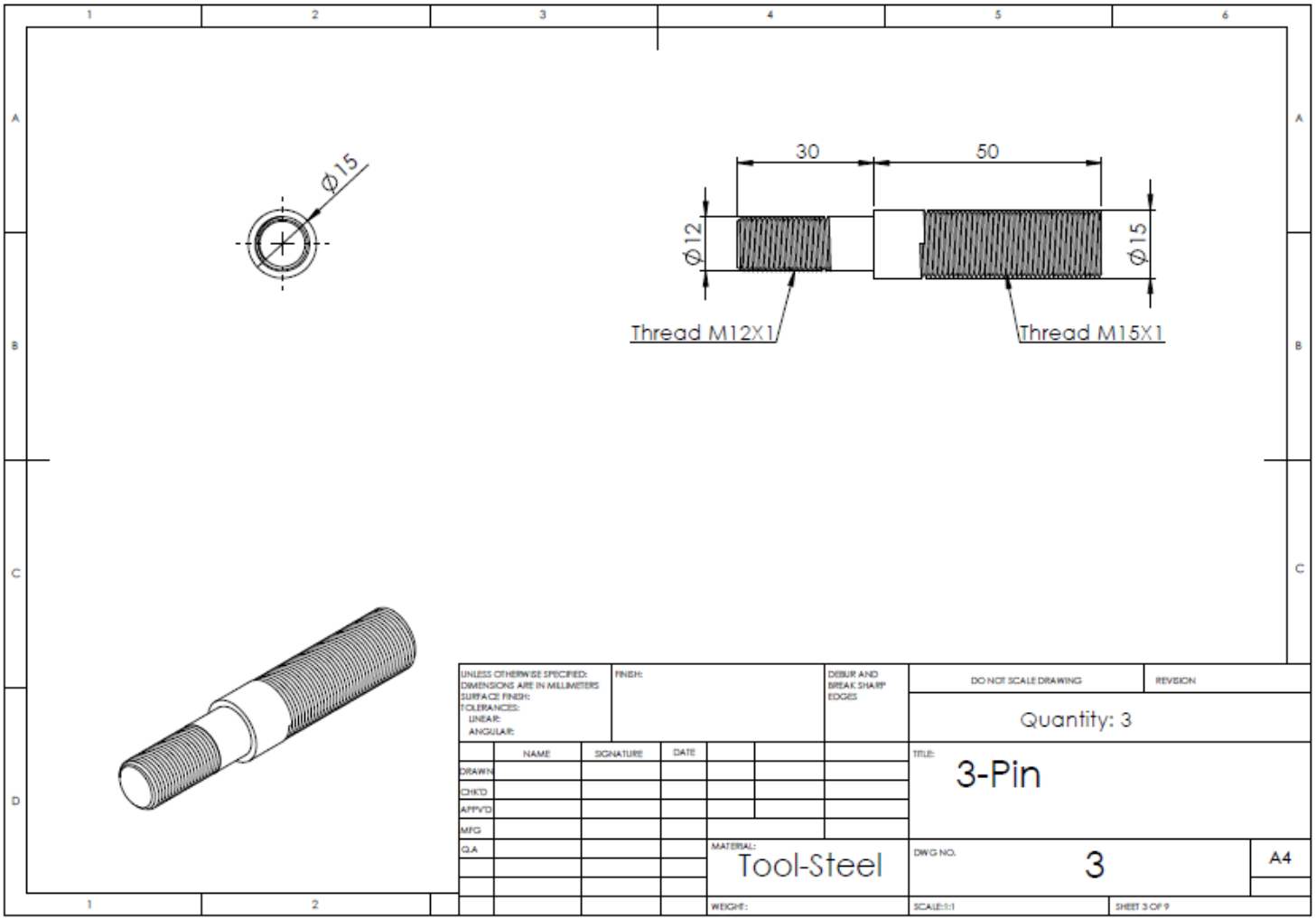
Ø15
30
50
Ø12
Ø15
Thread M12X1
Thread M15X1
UNLESS OTHERWISE SPECIFIED:
DIMENSIONS ARE IN MILLIMETERS
SURFACE FINISH:
TOLERANCES:
LINEAR:
ANGULAR:
FINISH:
DEBUR AND BREAK SHARP EDGES
DO NOT SCALE DRAWING
REVISION
Quantity: 3
NAME
SIGNATURE
DATE
DRAWN
CHK'D
APP'VD
MFG
QA
TITLE:
3-Pin
MATERIAL:
Tool-Steel
DWG NO.
3
A4
WEIGHT:
SCALE:1:1
SHEET 3 OF 9

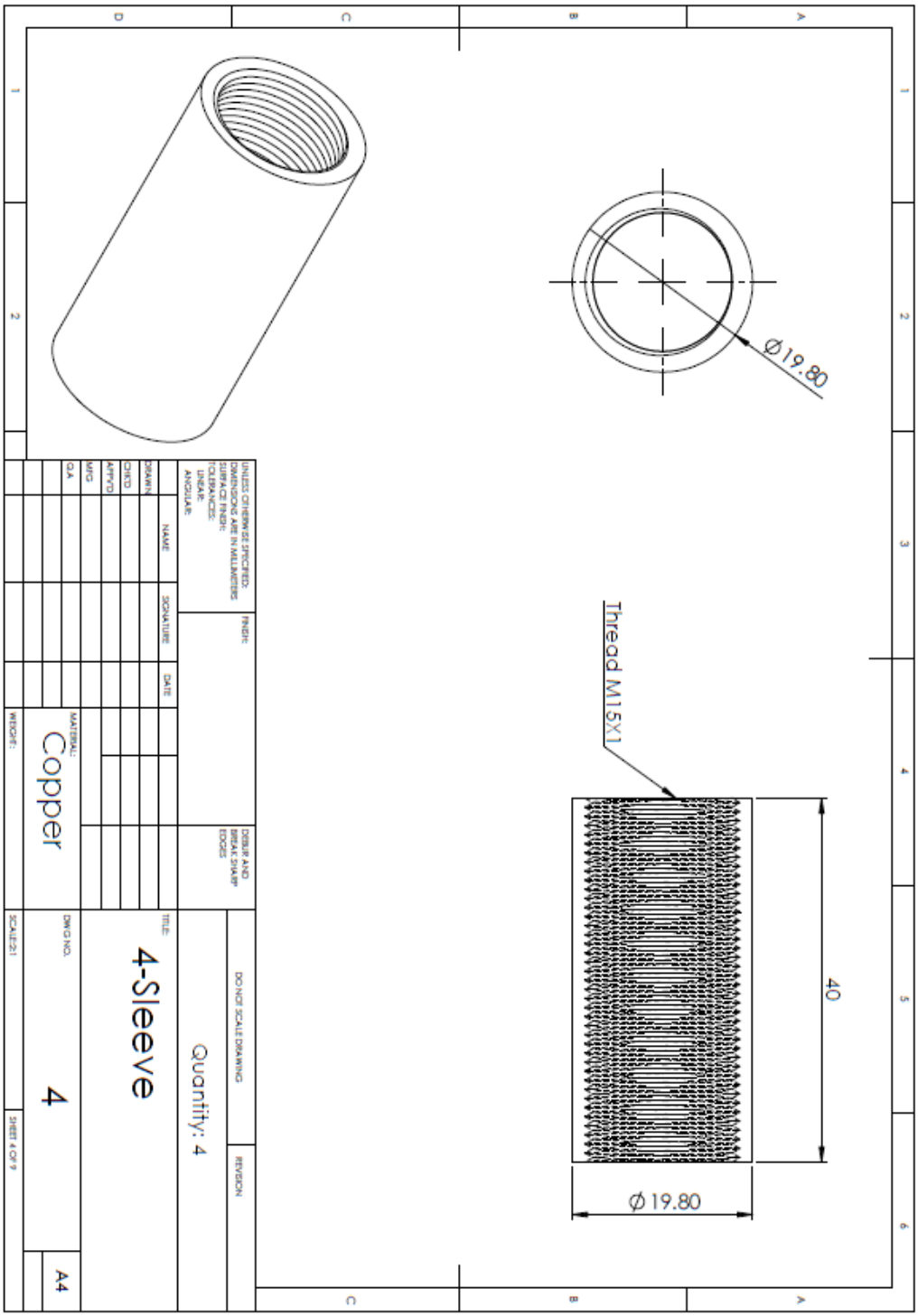
Ø19.80
Thread M15X1
40
Ø 19.80
UNLESS OTHERWISE SPECIFIED:
DIMENSIONS ARE IN MILLIMETERS
SURFACE FINISH:
TOLERANCES:
LINEAR:
ANGULAR:
NAME
SIGNATURE
DATE
DRAWN
CHKD
APPVD
MFG
Q.A
FINISH:
DEBUR AND BREAK SHARP EDGES
MATERIAL:
Copper
WEIGHT:
TITLE:
4-Sleeve
DWG NO.
4
A4
SCALE:2:1
SHEET 4 OF 9
DO NOT SCALE DRAWING
REVISION
Quantity: 4

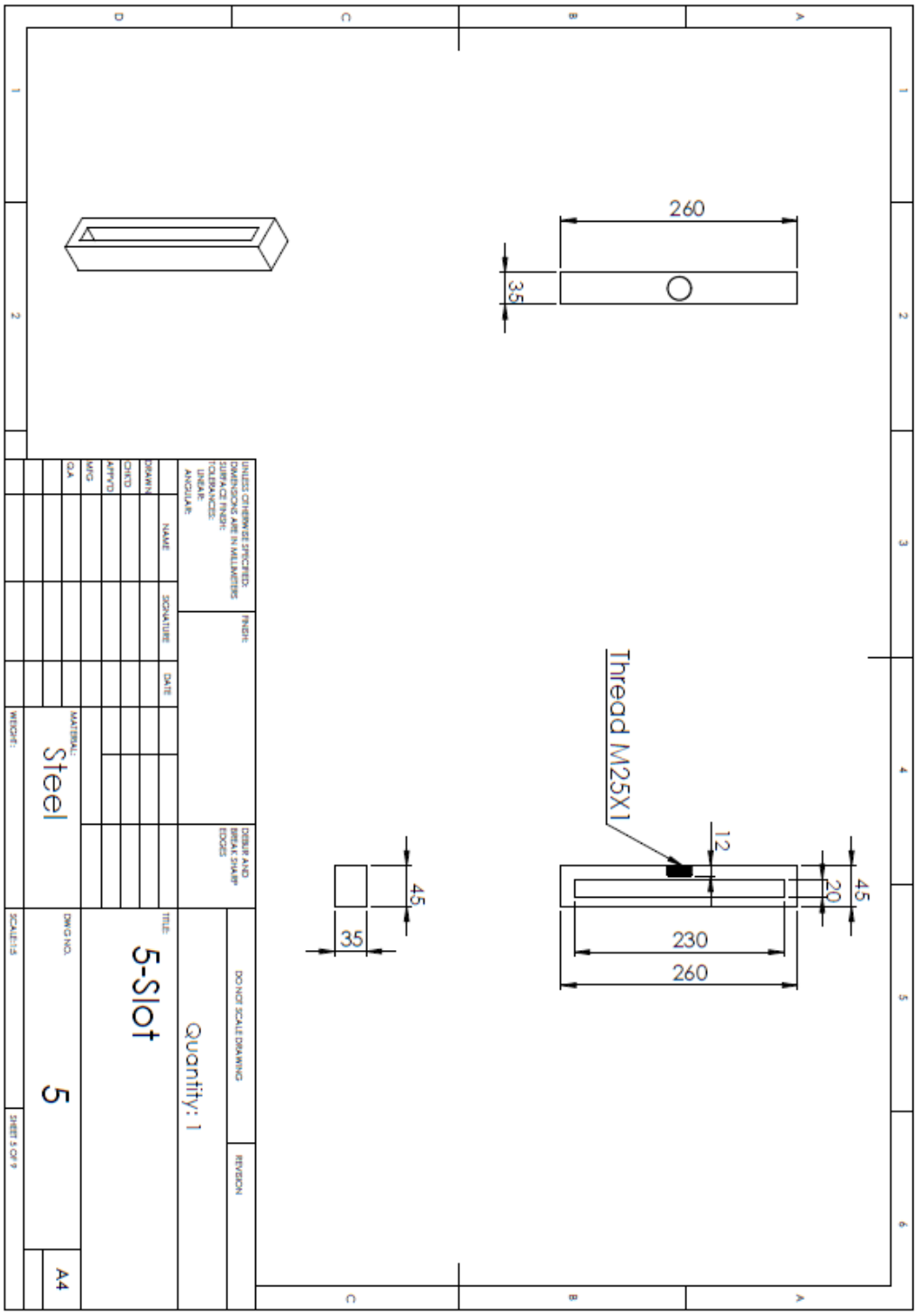
260
35
Thread M25X1
12
20
45
230
260
45
35
UNLESS OTHERWISE SPECIFIED:
DIMENSIONS ARE IN MILLIMETERS
SURFACE FINISH:
TOLERANCES:
LINEAR:
ANGULAR:
NAME
SIGNATURE
DATE
DRAWN
CHK'D
APP'D
MFG
Q.A
FINISH:
DEBUR AND
BREAK SHARP
EDGES
MATERIAL:
Steel
WEIGHT:
TITLE:
5-Slot
Quantity: 1
DO NOT SCALE DRAWING
REVISION
DWG NO.
5
A4
SCALE:1:5
SHEET 5 OF 9

Appendices (E): Additional measurement data

E.1 Pressure measurements at high frequency range

The dynamic pressure of the system at the resonance frequency (i.e. 23.3 Hz) is measured at two different axial locations for different experimental conditions to make sure that the flow exhibits an oscillating behavior over the entire range of the study. As shown in the figures below, the dynamic pressure at different Reynolds number shows a sinusoidal behavior. Also, the Auto-correlation for the pressure signal shows a typical result of the sinusoidal signal. Moreover, the amplitude spectrum shows a peak at the resonance frequency while the amplitude of the harmonics is much lower than the value at the resonance frequency. Therefore, the system doesn't produce any significant harmonics.

Preliminary trials were performed to investigate the transition to turbulence in the oscillating flow using the pressure signals. In order to do so, the fluctuating component of the pressure signal is obtained by subtracting the original pressure signal from the fitted data. Then the spectral analysis is performed on the fluctuating component of the pressure signal, as shown in the figures below. At the same Reynolds number, the maximum value of the fluctuating component of the pressure signal is roughly the same at both axial locations. As the Reynolds number is increased the maximum value of the fluctuating component of the pressure signal increases. Also, the energy density spectrum for the fluctuating component of the pressure signal at all Reynolds number shows a decay for the signal at higher frequencies. However, there is no significant phenomena (e.g. sharp increase in the maximum value of the fluctuating component of the pressure) observed at a certain Reynolds number to indicate the occurrence of turbulence.

The matlab codes used to perform the spectral analysis for the pressure signal are presented in appendices C.2 and C.3.

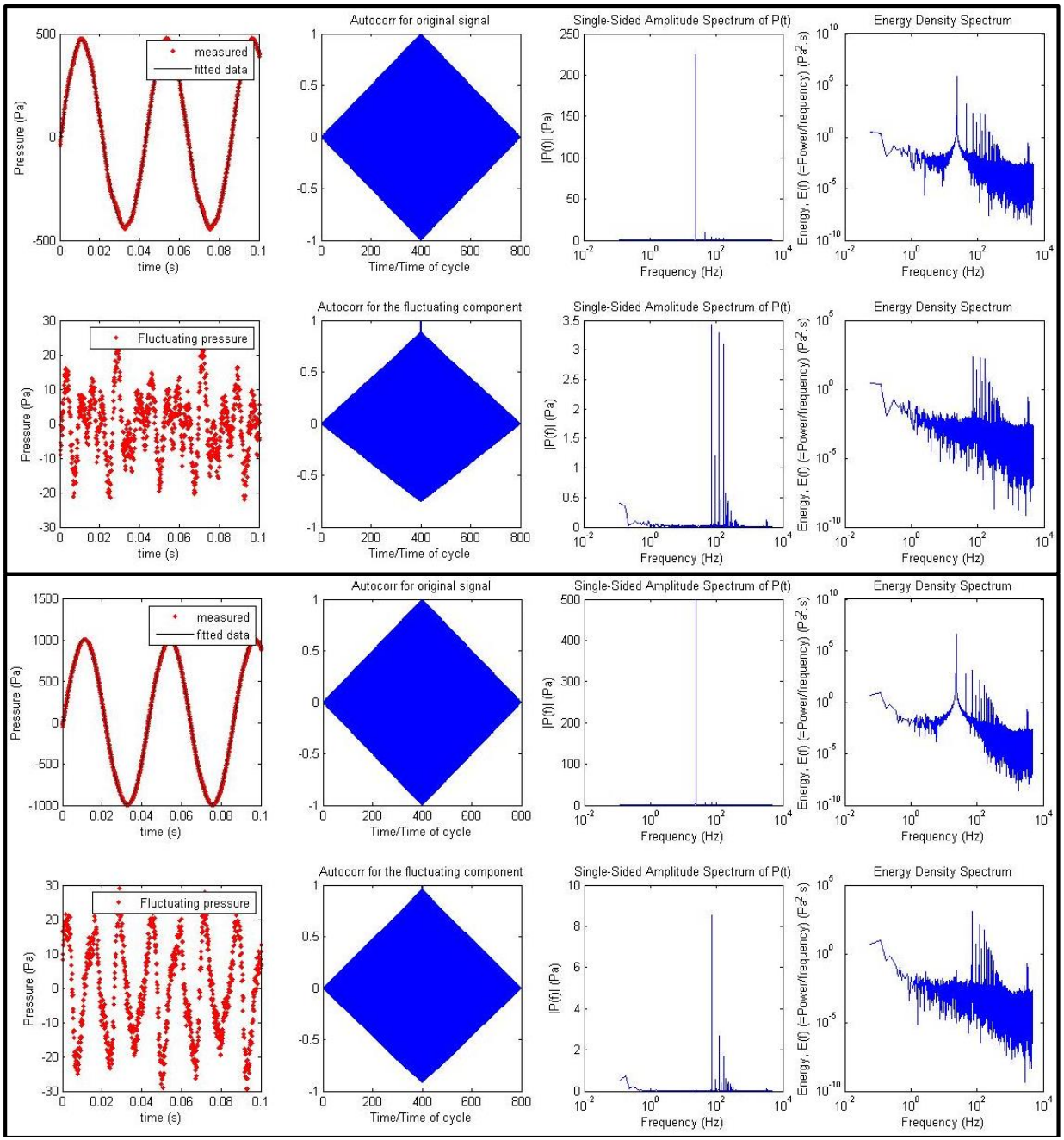

(a)

(b)

Fig 1: Auto correlation, Amplitude spectrum and Energy density of the original pressure signal and the fluctuating component of the pressure signal for $\boldsymbol{Re_{\delta} = 205}$ at two different points: (a) P1, (b) P2.

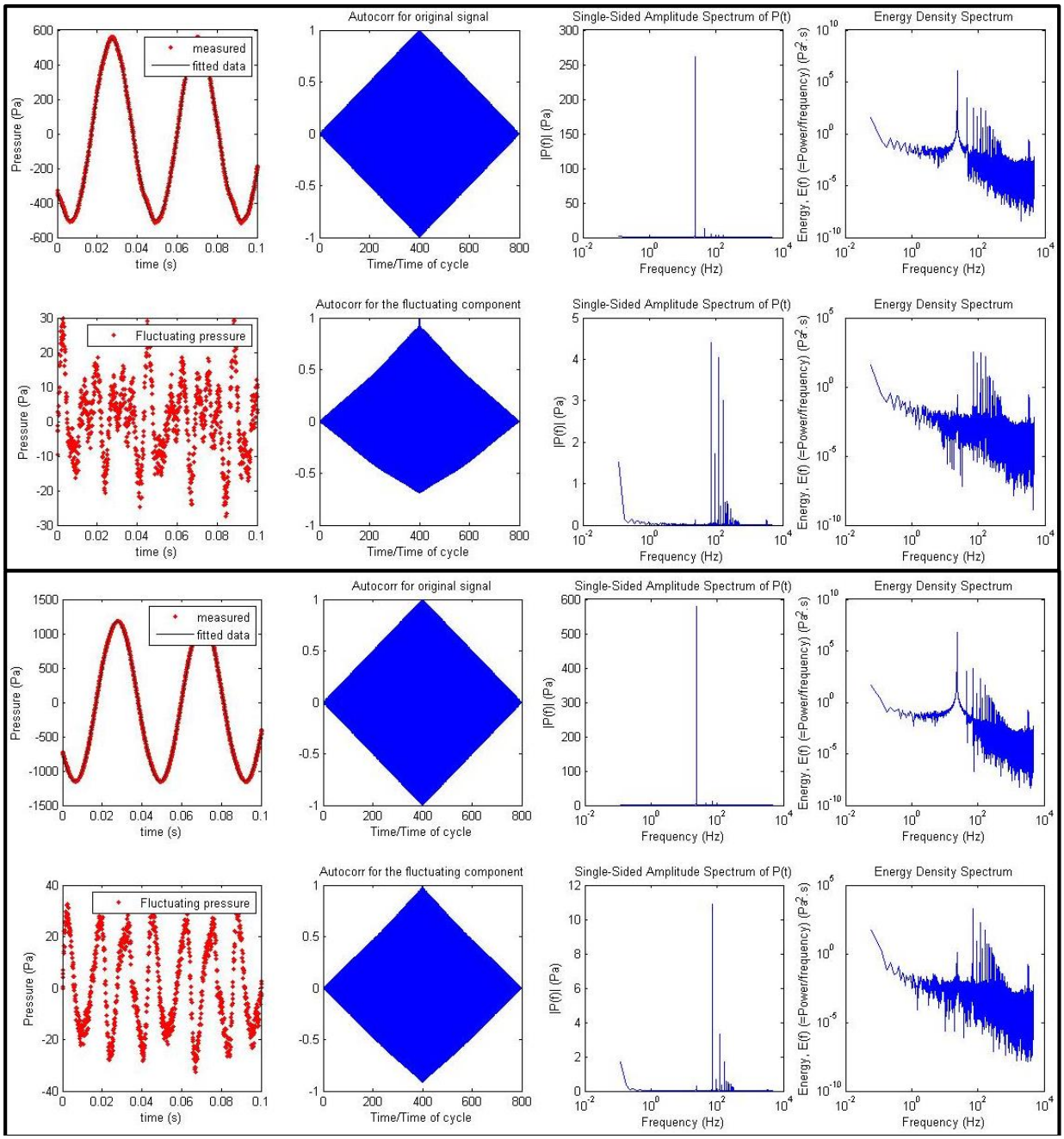

(a)

(b)

Fig 2: Auto correlation, Amplitude spectrum and Energy density of the original pressure signal and the fluctuating component of the pressure signal for $\boldsymbol{Re_{\delta} = 240}$ at two different points: (a) P1, (b) P2.

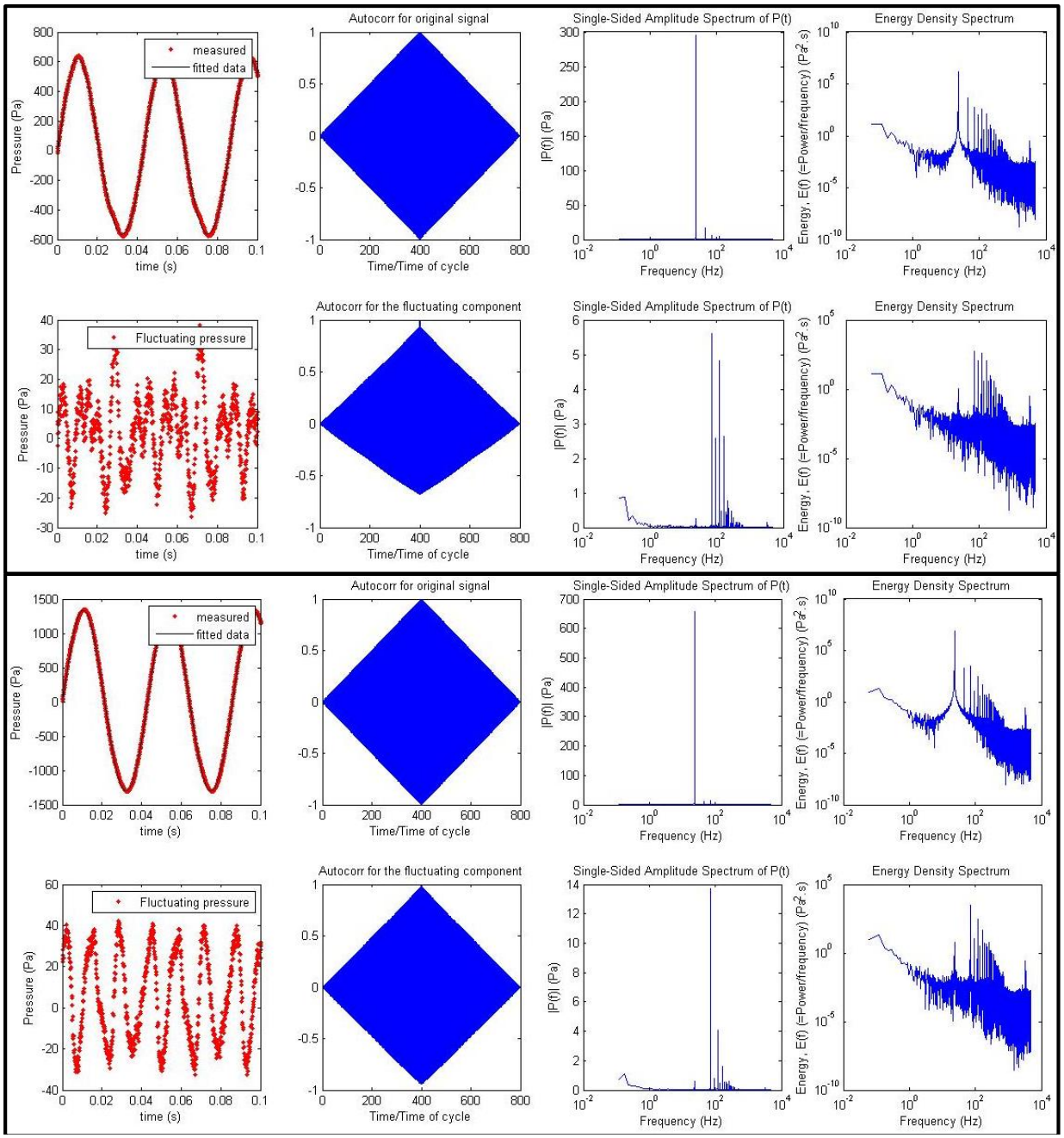

(a)

(b)

Fig 3:Auto correlation, Amplitude spectrum and Energy density of the original pressure signal and the fluctuating component of the pressure signal for $\boldsymbol{Re_{\delta} = 272}$ at two different points: (a) P1, (b) P2.

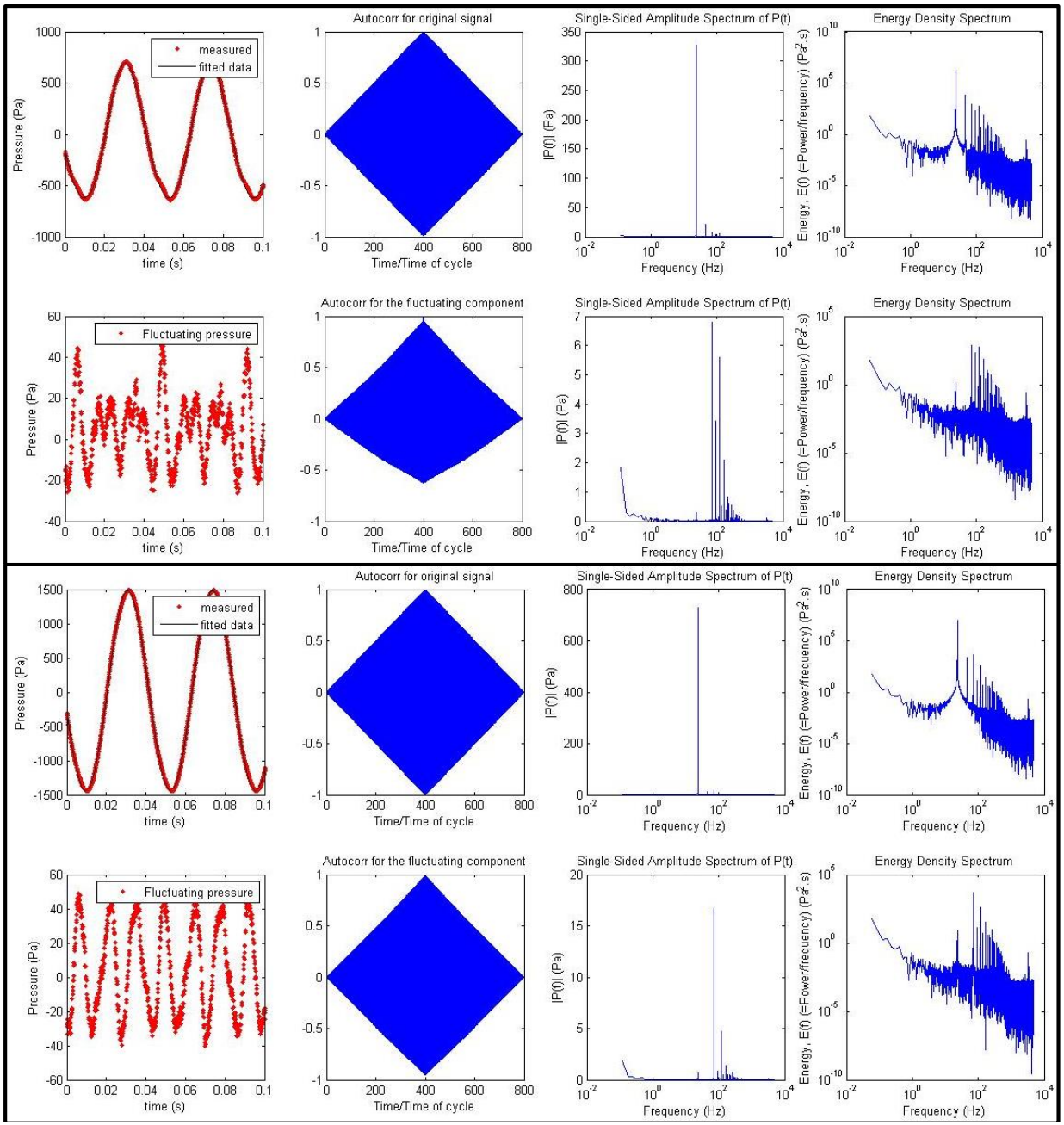

(a)

(b)

Fig 4: Auto correlation, Amplitude spectrum and Energy density of the original pressure signal and the fluctuating component of the pressure signal for $\boldsymbol{Re_{\delta} = 302}$ at two different points: (a) P1, (b) P2.

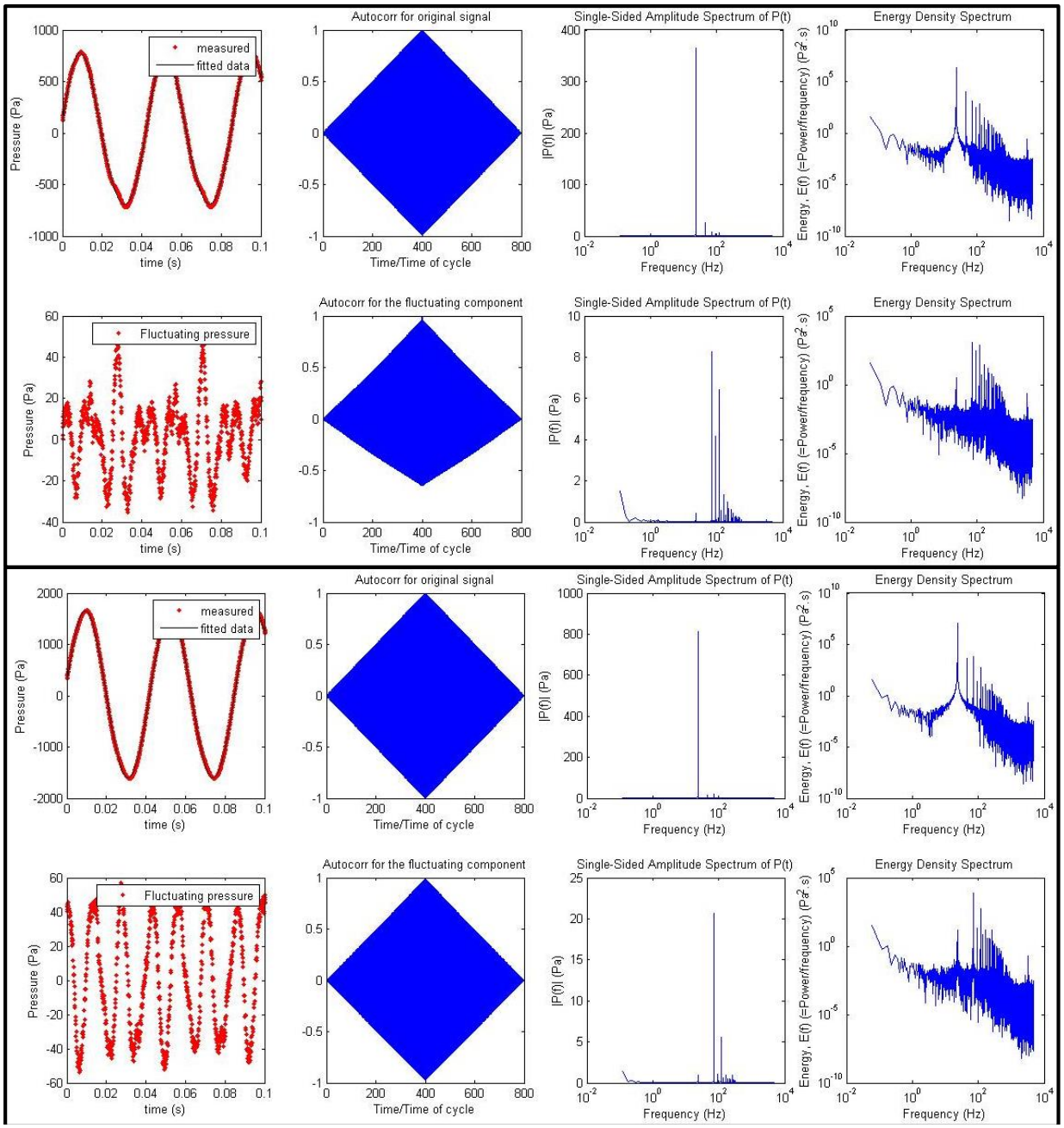

(a)

(b)

Fig 5: Auto correlation, Amplitude spectrum and Energy density of the original pressure signal and the fluctuating component of the pressure signal for $\boldsymbol{Re_\delta = 336}$ at two different points: (a) P1, (b) P2.

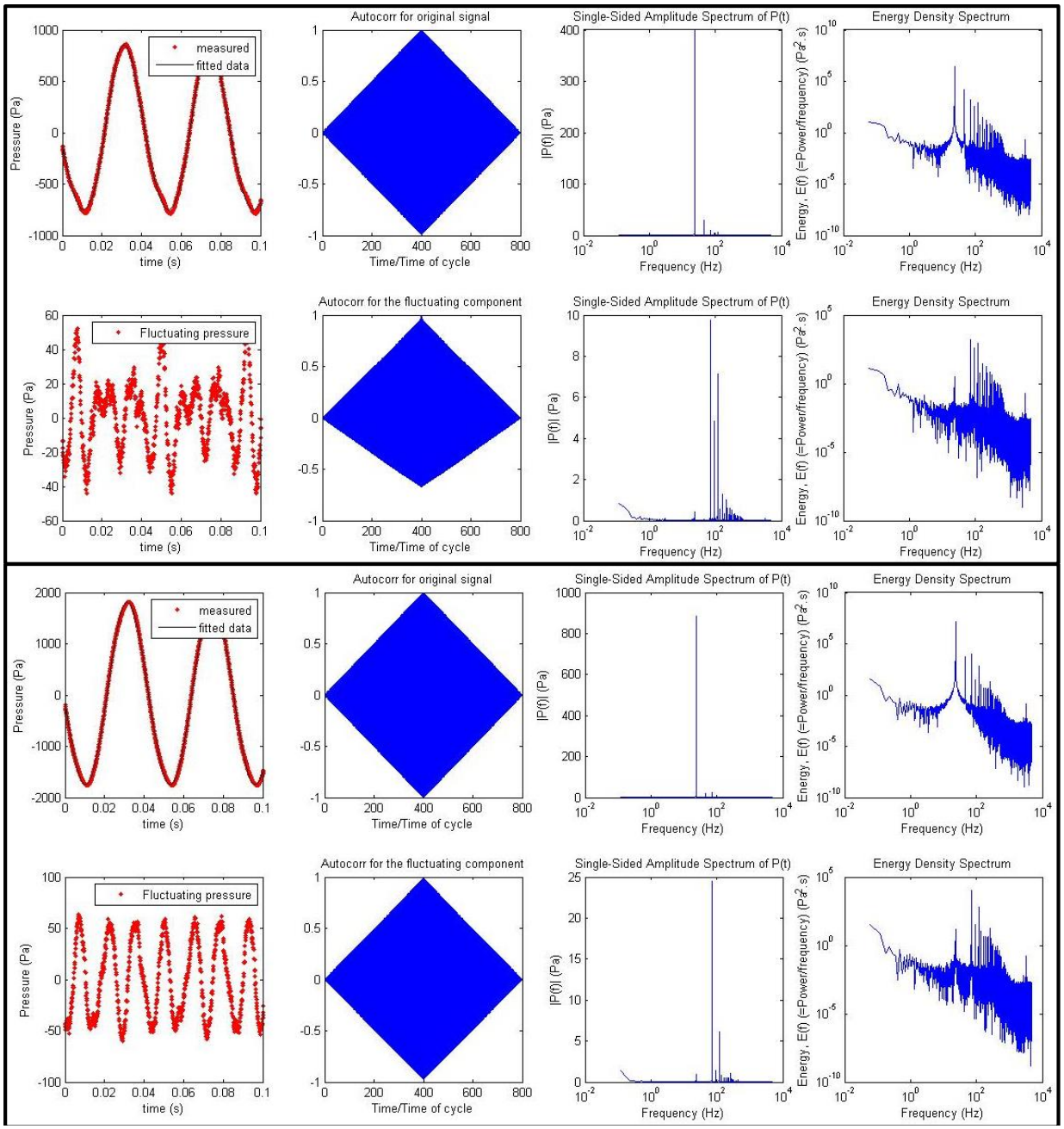

(a)

(b)

Fig 6: Auto correlation, Amplitude spectrum and Energy density of the original pressure signal and the fluctuating component of the pressure signal for $\boldsymbol{Re_\delta = 375}$ at two different points: (a) P1, (b) P2.

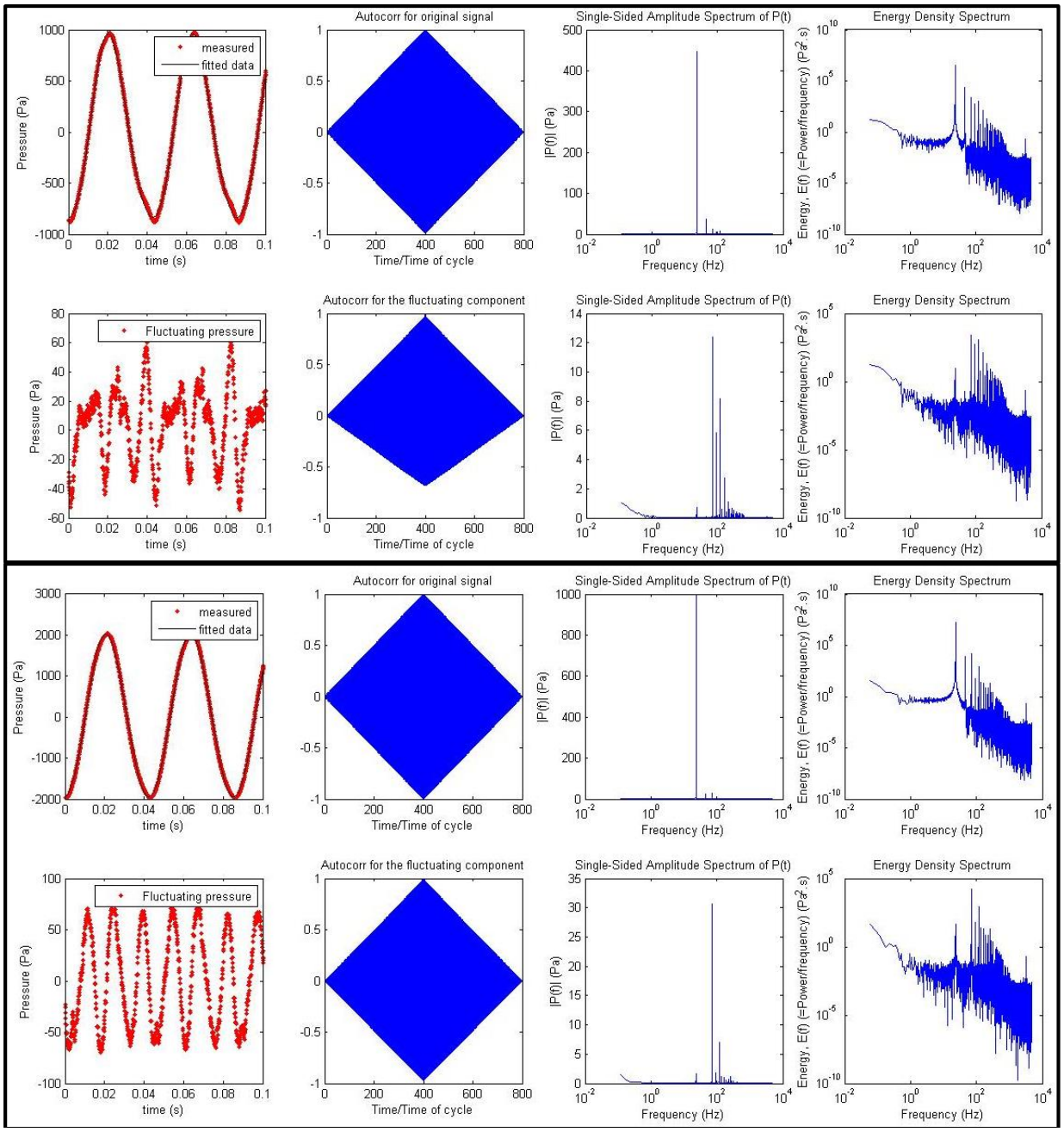

(a)

(b)

Fig 7: Auto correlation, Amplitude spectrum and Energy density of the original pressure signal and the fluctuating component of the pressure signal for $\boldsymbol{Re_\delta = 418}$ at two different points: (a) P1, (b) P2.

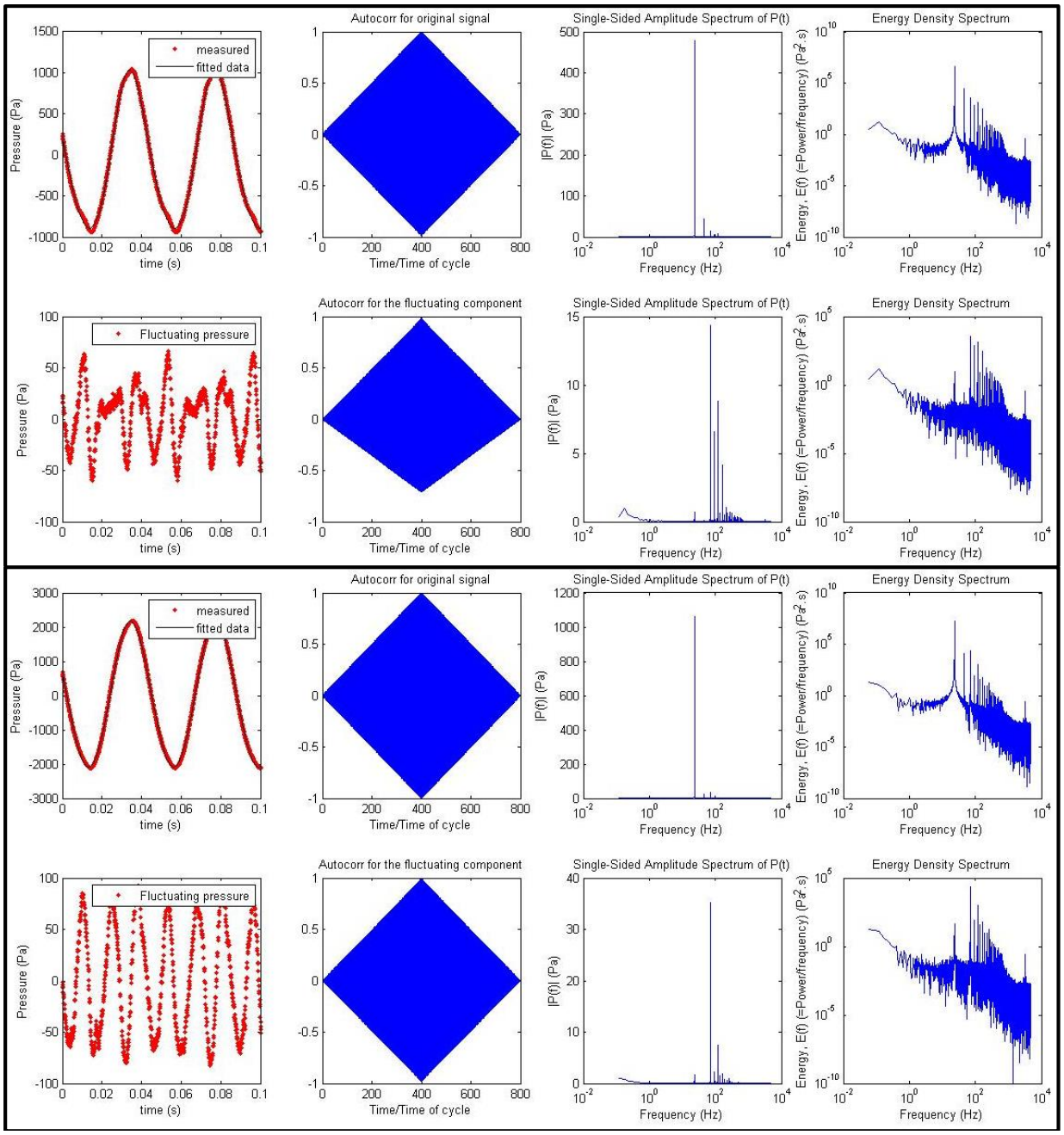

(a)

(b)

Fig 8: Auto correlation, Amplitude spectrum and Energy density of the original pressure signal and the fluctuating component of the pressure signal for $\boldsymbol{Re_{\delta} = 445}$ at two different points: (a) P1, (b) P2.

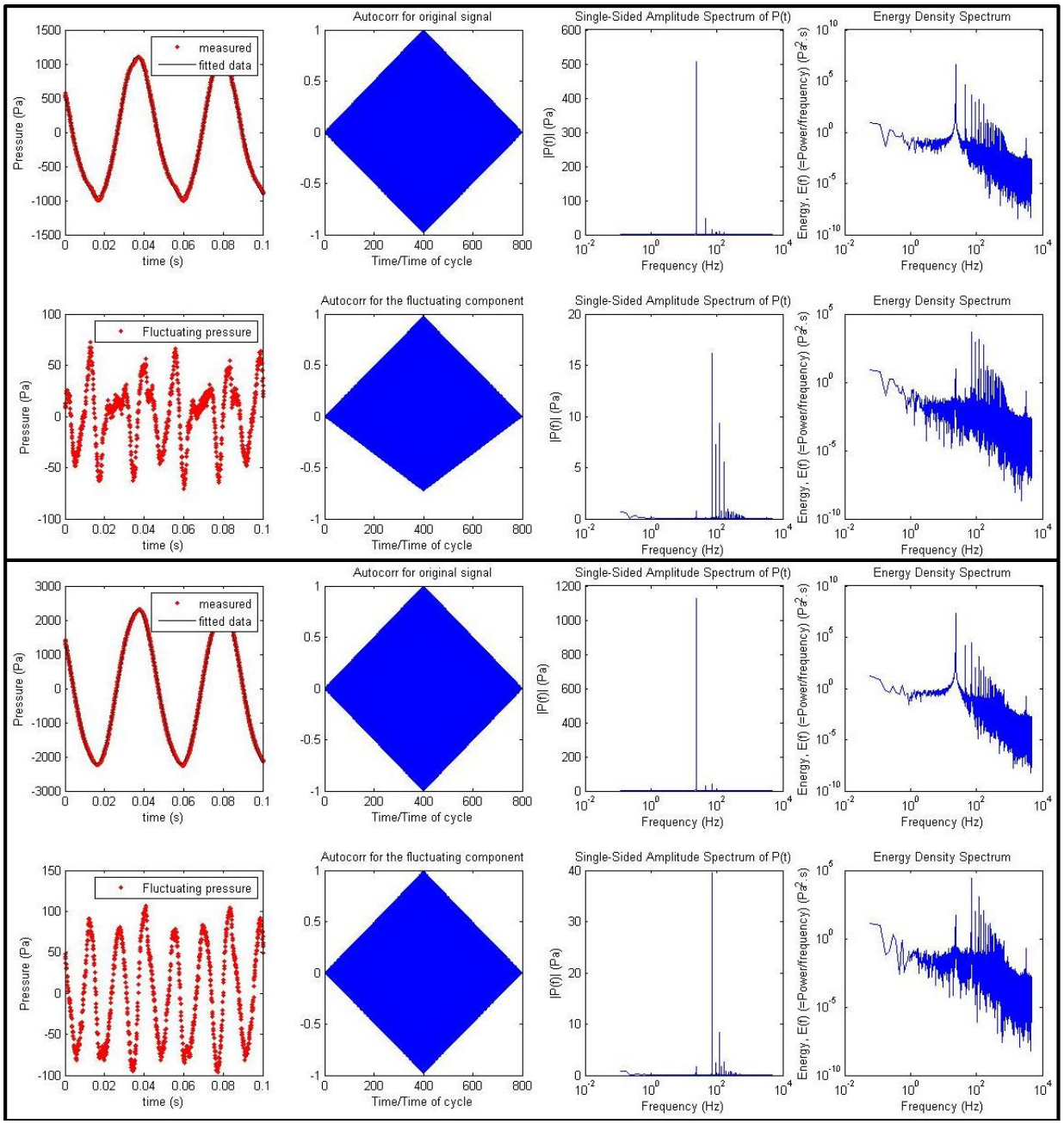

(a)

(b)

Fig 9: Auto correlation, Amplitude spectrum and Energy density of the original pressure signal and the fluctuating component of the pressure signal for $\boldsymbol{Re_{\delta} = 466}$ at two different points: (a) P1, (b) P2.

E.2 Links for the videos of the vorticity field and turbulence intensity fields around the plates with different end-plate shapes

The link below contains Microsoft PowerPoint Presentation (*.pptx) files and categorized as following:

1- "Rectangular Plates.pptx": This file includes videos for the vorticity field and turbulence intensities for rectangular plate-end shape at different Reynolds numbers.

2- "Circular Plates.pptx": This file includes videos for the vorticity field and turbulence intensities for circular plate-end shape at different Reynolds numbers.

3- "Sharpe Triangular Plates.pptx": This file includes videos for the vorticity field and turbulence intensities for 90^{O} triangular plate-end shape at different Reynolds numbers.

4- "Smooth Triangular Plates.pptx": This file includes videos for the vorticity field and turbulence intensities for 30^{O} triangular plate-end shape at different Reynolds numbers.

Download from here:

https://drive.google.com/drive/folders/1bfGkhYUaAloKo5x_yBBRon4fiTe1iLO4?usp=sharing

Appendices (F): Uncertainty analysis

F.1 Uncertainty evaluation

The uncertainty of measurements can be divided into two types namely, type A and type B. The former type of uncertainty gives a value for the repeatability of the measurement process whereas the latter type represents the systematic components of the uncertainty. In the current work, only type A uncertainty is considered.

According to M3003*, type A uncertainty is evaluated by statistical analysis of a series of observations and is calculated as follows:

$$U_A = \frac{\sigma_{n-1}}{\sqrt{n}}$$

Where, n is the number of samples.

σ_{n-1} is the standard deviation of measurement.

$$\sigma_{n-1} = \sqrt{\frac{1}{n-1}\sum_{i=1}^{n}(q_i - \bar{q})^2}$$

Where, q_i is the value of measured quantity.

$\bar{q}$ is the mean value of repeated measurements.

$$\bar{q} = \frac{q_1 + q_1 + q_1 + \cdots + q_n}{n}$$

The reported uncertainty is based on a standard uncertainty U_A multiplied by a coverage factor k = 2 to provide a coverage probability (or confidence interval) of approximately 95%.

* M3003: The Expression of Uncertainty and Confidence in Measurement, United Kingdom Accreditation Service (UKAS), edition 3, 2012.